Development of a 108 MHz 4-Rod CW RFQ-Design for High Duty Cycle Acceleration of Heavy Ion Beams at the GSI-HLI

von

Daniel Koser

geboren in Offenbach a.M.

vom Fachbereich Physik der
Johann Wolfgang Goethe-Universität als Dissertation angenommen.

Dekan:
Prof. Dr. Michael Lang

Gutachter:
Prof. Dr. Holger Podlech
Prof. Dr. Oliver Kester

Datum der Disputation:
22.03.2021

Zusammenfassung

Diese Dissertation beschreibt die Entwicklung einer neuen Radio-Frequenz-Quadrupol (RFQ-) Struktur des 4-Rod-Typs mit einer Betriebsfrequenz von $108\,\mathrm{MHz}$ für die Beschleunigung schwerer Ionen mit Masse-zu-Ladungsverhältnissen von bis zu 8,5 bei hohen Tastverhältnissen bis hin zum CW-Betrieb („Continuous Wave") am Hochladungsinjektor (HLI) des GSI Helmholtzzentrums für Schwerionenforschung in Darmstadt.

Neben der Hochfrequenzauslegung durch mit dem Programm CST Microwave Studio durchgeführten HF-Simulationen, fiel der Schwerpunkt der Untersuchungen auf die mechanische Analyse der durch den HF-Betrieb hervorgerufenen Vibrationen an den Elektroden-Stäben, wofür auf die ANSYS Workbench Software zurückgegriffen wurde. Aufgrund der im CW-Betrieb hohen thermischen Belastung der RFQ-Struktur von mehr als $30\,\mathrm{kW/m}$ ist ebenso eine akkurate Analyse der thermischen Effekte auf die Elektrodendeformation sowie die daraus resultierende Frequenzverstimmung des Resonators erforderlich, was im Rahmen der Möglichkeiten von CST Mphysics Studio durch Simulationen untersucht wurde.

Basierend auf den Ergebnissen der mittels Simulationen durchgeführten Design-Studien und daraus erzielter Optimierungen wurde ein entsprechender 4-Rod-RFQ Prototyp mit 6 Stützen gefertigt, an dem durch Messungen der HF-Eigenschaften sowie des Vibrationsverhaltens die aus den Simulationen erwarteten Eigenschaften verifiziert werden konnten.

Die Notwendigkeit zur Entwicklung eines komplett neuen RFQs für den HLI ergibt sich aus der Tatsache, dass mit der ursprünglich im Rahmen des geplanten HLI-Upgrades entworfenen und gebauten 4-Rod-Struktur, die im Jahr 2010 am HLI in Betrieb genommen wurde, auch nach mehrjähriger Betriebserfahrung und erheblichen Anstrengungen zur Behebung oder zumindest Reduzierung der schwerwiegenden Betriebsprobleme die angestrebten Betriebsmodi sowohl im gepulsten, als auch im CW-Betrieb nicht erreicht werden konnten. Problematisch erwiesen sich dabei vor allem mechanische Vibrationen der Elektroden, die eine starke modulierte Leistungsreflektion zur Folge haben, sowie die hohe thermische Sensitivität.

Der im Jahr 1991 in Betrieb genommene Hochladungsinjektor (HLI) ist neben dem Hochstrominjektor (HSI) einer der beiden Injektoren für den UNILAC-Beschleuniger („Universal Linear Accelerator"), der wiederum zusammen mit dem Schwerionensynchrotron SIS18 als Injektor für die neue geplante und bereits im Bau befindliche FAIR-Anlage („Facility for Antiproton and Ion Research") vorgesehen ist. Im Rahmen des internationalen Großforschungsprojektes FAIR sind vielfältige Experimente auf verschiedensten Forschungsgebieten geplant, wie etwa der Atom- und Plasmaphysik sowie deren Anwendung in Bio-, Medizin- und Materialwissenschaften (APPA), die Erforschung von komprimierter baryonischer Materie (CBM) sowie der Struktur und Reaktionen exotischer Atomkerne in Sternen (NuSTAR), als auch Forschung mit Antiprotonen (PANDA). Weil der UNILAC dementsprechend für die Anforderungen von FAIR umgerüstet werden soll, wobei nur geringe Tastverhältnisse $< 1\,\%$ erforderlich sind, ist der Bau eines neuen dedizierten (supraleitenden) CW-Linearbeschleunigers mit dem Namen „Helmholtz Linear Accelerator" (HELIAC)

geplant, der zur Weiterführung der Erforschung superschwerer Elemente an der GSI vorgesehen ist. Das Erfordernis des CW-Betriebs ergibt sich dabei aus den typischerweise sehr niedrigen Produktionsraten superschwerer Elemente.

Die künstliche Produktion und der Nachweis eines transuranen Elementes gelang erstmals im Jahr 1940 am Berkeley Radiation Laboratory mit der Erzeugung von Neptunium durch den Neutroneneinfang von Uran, wobei die dafür benötigten Neutronen durch den Beschuss eines Beryllium-Targets mit einem Deuteronen-Strahl aus einem Zyklotron generiert wurden. Nach ähnlichem Prinzip konnten so in den folgenden Jahren bis 1954 auch die transuranen Elemente bis zur Ordnungszahl 100 hergestellt werden, was maßgeblich durch die Entwicklung des Zyklotrons ermöglicht wurde. Ab 1955 bis 1974 gelang es dann mit Hilfe eines neuen Schwerionenbeschleunigers in Berkeley (HILAC) und der Entwicklung von Schwerionenzyklotrons am Joint Institute for Nuclear Research (JINR) in Dubna durch den Prozess der sogenannten „heißen Fusion" die Elemente bis zur Ordnungszahl 106 zu erzeugen.
Die nachfolgenden superschweren Elemente mit Ordnungszahlen von 107 bis 112 mit den Benennungen „Bohrium", „Hassium", „Meitnerium", „Darmstadtium", „Roentgenium" und „Copernicium" wurden in der Zeit von 1981 bis 1996 an der GSI in Darmstadt entdeckt, wobei hierfür das Prinzip der „kalten Fusion" angewendet wurde. Die dafür benötigten Schwerionenstrahlen mit Energien um die $5\,\mathrm{MeV/u}$ wurden vom 1975 in Betrieb genommenen UNILAC bereitgestellt und die neuen Elemente wurden im Schwerionenseparator SHIP erzeugt und nachgewiesen. Die Strahlen zur Erzeugung von Darmstadtium, Roentgenium und Copernicium wurden dabei vom Hochladungsinjektor in den UNILAC injiziert.
Die heute schwersten bekannten nachgewiesenen Elemente mit den Ordnungszahlen 113 bis 118 („Oganesson") wurden schließlich wieder mit dem Verfahren der heißen Fusion zwischen 1998 und 2006 in Dubna unter Verwendung des Schwerionenzyklotrons U-400 entdeckt.
Diese beträchtlichen Fortschritte wurden letztlich durch kontinuierliche Weiterentwicklungen sowie Innovationen auf dem Gebiet der Beschleuniger-Technologie ermöglicht.

Eine Grundproblematik bei der Vorbeschleunigung von niederenergetischen Ionenstrahlen aus der Ionenquelle für die Injektion in einen Driftröhrenbeschleuniger stellen die bei niedrigen Strahlgeschwindigkeiten hohen Raumladungskräfte dar, die eine effiziente transversale Strahlfokussierung nötig machen. Zudem muss der Gleichstromstrahl aus der Ionenquelle longitudinal in sogenannte Teilchen-Bunche komprimiert werden, um so viele Strahlteilchen wie möglich in die Phasenakzeptanz der nachfolgenden Driftröhrenstruktur zu bringen.
Nachdem die Beschränkungen der elektrostatischen Vorbeschleunigung und der dabei angewendeten Methoden zur longitudinalen Strahlfokussierung typischerweise den Flaschenhals von Ionenbeschleunigern hinsichtlich der erreichbaren Strahlströme sowie der Strahlqualität bildeten, wurde schließlich im Jahr 1969 von I. Kapchinsky und V. Teplyakov das Prinzip des Radio-Frequenz-Quadrupols vorgeschlagen. Dieses sieht die gleichzeitige transversale Fokussierung, das longitudinale Bunchen sowie die Beschleunigung des Ionenstrahls in einem mit hoher Frequenz alternierendem elektrischen Quadrupolfeld vor. Die für das Bunchen und Beschleunigen benötigte longitudinale Feldkomponente wird dabei durch eine sinusförmige Modulation der Elektrodenform erreicht. Die transversal geschwindigkeitsunabhängige elektrische Fokussierung folgt dem Prinzip der alternierenden Gradienten-Fokussierung.
Nachdem das grundlegende Konzept des RFQ-Beschleunigers erstmals im Jahr 1974 am Institute of High Energy Physics (IHEP) in Protwino, sowie nochmals 1980 am Los Alamos

National Laboratory (LANL) mit deutlich erhöhter Transmissionseffizienz erfolgreich getestet werden konnte, werden RFQ-Strukturen bis heute standardmäßig für die (Vor-)Beschleunigung von niederenergetischen Ionenstrahlen verwendet. Mit der Zeit wurden neben den ursprünglich verwendeten 4-Vane-Strukturen auch verschiedene andere Resonator-Konzepte für die Anwendung als RFQ eingesetzt. So wurde etwa ab Mitte der 1980er Jahre die sogenannte 4-Rod-Struktur vorwiegend am Institut für Angewandte Physik der Goethe-Universität Frankfurt unter Leitung von A. Schempp entwickelt. Aufgrund der besonderen Vorzüge von 4-Rod-Strukturen, wie etwa der flexible und vergleichsweise simple Mechanismus zum Frequenz- und Flatness-Tuning sowie die im Vergleich geringen Fertigungskosten und einfache Wartung, kann der 4-Rod Resonator-Typ trotz der auftretenden Probleme am aktuellen HLI-RFQ dennoch als praktikabelste Lösung bezüglich der Anforderungen des HLI-Betriebs betrachtet werden. Die wesentlichen im Rahmen dieser Dissertation erarbeiteten Verbesserungen der mechanischen Auslegung von 4-Rod-Strukturen im Hinblick auf den CW-Betrieb im HLI, sowie die Methoden und Ergebnisse der durchgeführten experimentellen Untersuchungen an dem 6-Stützen-Prototyp sind im Folgenden zusammengefasst.

Vor der Auslegung des neuen RFQ-Designs wurde zunächst eine umfangreiche simulationsbasierte Analyse der an dem bestehenden HLI-RFQ auftretenden mechanischen und thermischen Probleme durchgeführt. Ausgangspunkt und Referenzfall waren dabei die zuvor an der GSI gemachten Beobachtungen während des HF-Betriebs sowie die dort durchgeführten Vibrationsmessungen. Ausgehend von einer mechanischen Modalanalyse mit ANSYS konnten die zuvor gemessenen mechanischen Schwingungsmoden bei $350\,\mathrm{Hz}$ und $500\,\mathrm{Hz}$ schnell identifiziert und klassifiziert werden, woraus zwei Kriterien für die Anregung mechanischer Elektrodenmoden durch das elektrische Quadrupolfeld abgeleitet werden konnten: Zum einen muss die Vibrationsebene der betreffenden Eigenmodenschwingung eine radiale Komponente relativ zum Quadrupolzentrum aufweisen, d.h. die Schwingung muss zumindest teilweise parallel zum Vektor der elektrischen Kraft auf die Elektrode verlaufen. Zum anderen muss das Verformungsprofil der Eigenmode unidirektional in eine Richtung der Schwingungsebene zeigen, da auch die Richtung der Anregung durch die elektrische Kraft entlang der Elektrode homogen ist. Diese Schlussfolgerungen konnten auch durch eine harmonische Analyse des mechanischen Antwortspektrums bestätigt werden, bei der zudem gezeigt werden konnte, dass nur die radiale Mode bei $500\,\mathrm{Hz}$ durch das Quadrupolfeld angeregt wird, wohingegen die Anregung der tangentialen Mode (in senkrechter Schwingungsebene zur radialen Richtung) eindeutig auf eine Asymmetrie der Quadrupolfeldverteilung zurückzuführen ist, die durch die für 4-Rod-Strukturen charakteristische elekrische Dipolkomponente hervorgerufen wird. Aus einer Analyse der HF-Sensitivität gegenüber den identifizierten problematischen Elektrodeneigenmoden mittels CST MWS, konnte schließlich auch die Tatsache aufgeklärt werden, dass die tangentiale Schwingung bei $350\,\mathrm{Hz}$ nicht im reflektierten HF-Signal beobachtet werden kann, was darauf zurückzuführen ist, dass ihr Einfluss auf die Frequenzverstimmung nur etwa $5\,\%$ von dem der radialen Mode beträgt. Der aus diesen Simulationen abgeleitete Wert der Schwingungsamplitude von etwa $2\,\mu\mathrm{m}$ zeigt eine gute Übereinstimmung mit den entsprechenden Messwerten aus den vorangegangenen Vibrationsmessungen. Dies wurde zusätzlich durch transiente Schwingungssimulationen mit ANSYS bestätigt, bei denen auch der zuvor vermutete Anregungsmechanismus durch die Flanken der HF-Pulse reproduziert werden konnte.

Aus den mit CST Mphysics Studio durchgeführten thermischen Simulationen konnte schließlich auch die zunächst unerwartet hohe thermische Sensitivität des HLI-RFQ reproduziert werden. Dafür erwies es sich als unbedingt notwendig, neben der Wärmeleitung im Material auch zusätzlich ausschlaggebende thermische Prozesse in der Simulation zu berücksichtigen, wie z.B. die Erwärmung des Kühlwassers entlang der Kühlkanäle sowie der endliche Wärmeübertrag vom Kupfer in das strömende Kühlwasser. Da in der aktuellen Software-Version von CST diese Effekte jedoch nicht in die Simulation einbezogen werden können, wurde ein semi-analytisches Modell zur Berechnung der thermischen Randbedingungen angewendet. Dadurch konnte gezeigt werden, dass beide Prozesse einen erheblichen und nicht zu vernachlässigenden Einfluss auf die Temperaturverteilung und die daraus resultierende Frequenzverstimmung haben. Im Fall von 4-Rod-Strukturen haben zudem die Eigenschaften der mechanischen Kopplung zwischen den thermischen Verformungen der einzelnen Bauteile an den Schraubverbindungen zwischen den Elektroden und den Stems einen signifikanten Einfluss auf den Wert der simulierten Frequenzverstimmung, was durch die Betrachtung verschiedener mechanischer Randbedingungen genauer untersucht wurde. Schlussendlich konnte die beobachtete Frequenzverstimmung von $-200\,\mathrm{kHz}$ bei einer Verlustleistung von $30\,\mathrm{kW}$ mit einem mittleren Wärmeübergangskoeffizienten von $\alpha = 9250\,\mathrm{W/m^2K}$ und vollständig unterdrückter mechanischer Kopplung zwischen den Elektroden und Stems reproduziert werden, bei einem Wasserdurchfluss von $2\,\mathrm{l/min}$ wie bei dem Betrieb des realen HLI-RFQs.

Für eine zuverlässigere thermische Analyse wäre es jedoch empfehlenswert eine leistungsfähigere Simulationssoftware wie ANSYS oder COMSOL einzusetzen, die in der Lage ist, die Erwärmung des Kühlwassers und die Fluiddynamik in den Kühlkanälen sowie die Eigenschaften der Wärmeübertragung an Materialübergängen zu berücksichtigen.

Die Auslegung des Prototypen erfolgte auf der Grundlage der bereits im CW-Betrieb bei hohen Leistungen erfolgreich getesteten RFQs für das FRANZ- und MYRRHA-Projekt. Die geometrischen Parameter der HF-Struktur wurden dabei durch HF- und mechanische Designstudien angepasst und optimiert, um die Soll-Betriebsfrquenz von $108.408\,\mathrm{MHz}$ zu erreichen und eine maximale mechanische Steifigkeit bei möglichst geringer Verminderung der Shunt-Impedanz zu erlangen. Dafür wurde der maßgebliche Parameter des Stützenabstandes auf einen Wert von $120\,\mathrm{mm}$ festgelegt, nahe dem Maximum der entsprechenden Shunt-Impedanzkurve (als Funktion des Stützenabstandes). Dies machte es möglich, trotz einer deutliche höheren Kapazität durch die strukturelle Verstärkung der HF-Struktur nahezu den gleichen Wert der Shunt-Impedanz von etwa 105–$110\,\mathrm{k\Omega m}$ wie beim bestehenden HLI-RFQ zu erzielen. In ähnlicher Weise wurden auch alle anderen geometrischen Eigenschaften der HF-Struktur optimiert, was sowohl die Geometrie der Elektroden sowie deren Halterungen, als auch die Stützengeometrie betrifft. Die Zielparameter der durchgeführten Optimierung waren die resultierende Stützenhöhe, die Shunt-Impedanz, der Einfluss auf das Dipolverhältnis und die Frequenz der unidirektionalen radialen mechanischen Elektrodeneigenmode, mit dem Ziel diese soweit wie möglich anzuheben. Schließlich konnten die mechanischen Eigenfrequenzen auf Werte ähnlich denen des FRANZ- und MYRRHA-RFQs erhöht werden und liegen damit um einen Faktor von etwa $1,5$ bis 2 deutlich über den entsprechenden Werten des bestehenden HLI-RFQ. Zudem konnte eine vollständige Dipolkompensation erreicht werden, bei einer vergleichsweiße großen aber tolerierbaren Stützenhöhe von über $250\,\mathrm{mm}$.

Basierend auf den Ergebnissen der durchgeführten Designstudien wurde der 6-Stützen-Prototyp mit einer Elektrodenlänge von $702\,\mathrm{mm}$ bei der NTG GmbH gefertigt, wobei zunächst

noch Optimierungen des Kühlkonzepts erarbeitet wurden. Insgesamt konnte dadurch die simulierte thermische Sensitivität (Frequenzverstimmung pro Einheit Verlustleistung) im Vergleich zum bestehenden HLI-RFQ um einen Faktor von etwa 5 bis 6 deutlich reduziert werden (von 6,7 auf 1,1–1,3 Hz/W). Der mit einem voll funktionsfähigen Wasserkühlsystem ausgestattete und damit für Hochleistungs-HF-Tests ausgelegte Prototyp verfügt außerdem über einzigartige Möglichkeiten zur experimentellen thermischen und Vibrationsanalyse, wie etwa Sensorschächte in den Stützen zur Messung deren Innentemperatur während dem Betrieb, sowie vier dedizierte Diagnosefenster im Tank für Messungen mit einem Laservibrometer.

Am fertigen Prototyp wurden sodann zum Vergleich mit den simulierten Eigenschaften vor den geplanten Hochleistungstests umfangreiche HF- und mechanische Vormessungen durchgeführt. Durch Anwendung verschiedener Messmethoden konnte schließlich die simulierte Güte ($Q \approx 5000$) sowie die antizipierte Shunt-Impedanz ($R_{\mathrm{pL}} \approx 110\,\mathrm{k\Omega m}$) validiert werden. Auch das Erreichen von nahezu vollständiger Dipolkompensation auf ein Dipolverhältnis von unter 1 % wurde durch Messungen der Spannungsverteilung am oberen und unteren Elektrodenpaar bestätigt. Zur Untersuchung des mechanischen Eigenmodenspektrums der Prototypenstruktur wurden verschiedene Methoden zur Messung und Anregung von Vibrationen angewandt. Dabei wurde die Anregung entweder akustisch durch einen PA-Lautsprecher oder mechanisch durch einen Piezoaktor oder einen Schonhammer induziert, während die Messung mittels eines Mikrofons, eines Piezosensors oder des Laservibrometers erfolgte, mit dem zuvor bereits die Vibrationsmessungen am bestehenden HLI-RFQ durchgeführt wurden. Insgesamt zeigten die so gemessenen Spektren eine gute Übereinstimmung mit den entsprechenden Simulationen. Zusätzlich wurde eine experimentelle Modalanalyse mit einem 3D-Laservibrometer durchgeführt, wodurch die Eigenmoden-Verformungsprofile der Elektroden experimentell untersucht aber auch die mechanischen Dämpfungszeiten genauer bestimmt werden konnten. Nachdem die RFQ-Struktur auf die HLI-Frequenz von 108,408 MHz abgestimmt, der Tank vakuumdicht gemacht und die Diagnosegeräte installiert wurden, konnte am IAP eine Vorkonditionierung bis 200 W durchgeführt werden, bei der neben einer unerheblichen Konditionierungsschwelle zwischen 140 und 240 mW im typischerweise kritischen Niederleistungsbereich die Kavität das Hochfahren der Leistung ohne merkliche Probleme akzeptierte. Nach Abschluss der Vormessungen sowie der Vorkonditionierung wurde der Prototypen-Tank für den Transport zur GSI vorbereitet, wo in Kürze Hochleistungstests mit thermischen Belastungen von mehr als 30 kW/m und weitere Vibrationsmessungen während dem HF-Betrieb durchgeführt werden sollen.

Basierend auf einem von C. Zhang neu entwickelten vorläufigen Strahldynamik-Konzept, was für die CW-Beschleunigung eines Schwerionenstrahls mit $A/q = 6$ bei einem Strahlstrom von 1 mA (entsprechend den HELIAC-Spezifikationen) eine Elektrodenlänge von etwa 2,8 m vorsieht, wurde ausgehend von dem Prototypen-Entwurf ein entsprechendes HF-Design für einen möglichen neuen HLI-RFQ angepasst. Durch die vom neuen Strahldynamik-Konzept vorgesehene Herabsetzung der Elektrodenspannung auf 40 kV konnte die Gesamtleistungsaufnahme auf nur 43 kW reduziert werden. Dies verringert außerdem die elektrische Kraft auf die Elektroden und trägt daher zur Minderung der Elektrodenvibration bei. Aus dem simulierten Vergleich zwischen dem bestehenden HLI-RFQ und dem neuen Design geht hervor, dass allein durch die machanische Versteifung der Struktur die Vibrationsamplituden voraussichtlich um den Faktor 100 bis 200 reduziert werden konnten.

Während die ursprünglich für den MYRRHA-RFQ entwickelte Methode zur Dipolkompensation mittels einer lateralen Verschiebung der unteren Stützenarme und der damit einhergehenden Verlängerung des Strompfades zu den unteren Elektroden direkt auf das entwickelte Prototypen-Design angewendet werden konnte, wurde im Rahmen der vorliegenden Dissertation ein vollkommen neuer Ansatz zur Kompensation eines weiteren für 4-Rod-Strukturen typischen Feldfehlers, den sogenannten longitudinalen Endfeldern, entwickelt. Die mittels Simulationen durchgeführten Studien zur Entstehung der Endfelder zeigten deutlich, dass die zur longitudinalen elektrischen Feldkomponente führende ungleichmäßige Potentialverteilung an den Quadrupolelektrodenenden auf ungleiche Längen der zu diesen führenden Strompfade sowie auf deutlich geringere induzierte Ladeströme an den End-Stützen im Vergleich zur vorletzten Stütze zurückzuführen ist. Beide Effekte konnten schließlich durch Modifikationen der Elektrodenhalter an den End-Stützen sowie durch sogenannte Seiten-Stützen erfolgreich kompensiert werden. Dies ermöglichte eine Reduktion des Endfeldes von anfänglich etwa 50 % (Verhältnis der Spannung im Endfeld zur Elektrodenspannung) auf nahezu Null, wobei der Wert der Shunt-Impedanz erhalten werden konnte.

Contents

(1) Introduction & Motivation

This thesis presents the development of a new radio frequency quadrupole (RFQ) accelerator structure of the 4-rod type for the acceleration of heavy ion beams, according to the requirements set by the future planned operation modes of the High Charge State Injector (HLI[1]) at the GSI Helmholtz Centre for Heavy Ion Research in Darmstadt, Germany.

After all, a strong focus was put on the investigation and optimization of the structural-mechanical properties, such as vibration behavior and thermal deformation, in order to minimize the resulting frequency detuning and finally enable stable RF operation of the RFQ. Besides its continuing function as injector for the existing GSI facility, thus also being relevant for the new FAIR project[2], the HLI is also planned to be used as a dedicated injector for a new superconducting CW[3] linear accelerator, with regard to which special attention was hence given to the design for RF operation with high duty cycles up to CW mode.

Ultimately, the presently installed 4-rod RFQ at the HLI cannot be operated in pulsed mode without major restrictions due to considerable problems caused by mechanical vibrations, nor can it be operated reliably in CW mode due to a severe thermal operational instability.

Eventually, the requirement for the capability of CW operation mainly results from the aim to study particle interaction processes with very low reaction cross sections, e.g. as in the field of super-heavy elements (SHE) research, which has been a major focus at GSI for decades and where further advances shell now be pursued.

This chapter summarizes the history of the exploration of heavy and super-heavy elements since the 1940s and outlines the concept of the yet unexplored "Island of Stability" beyond the limits of the nuclides chart known by today. In this context, also the current and planned scope of the GSI facility and the FAIR project, the HLI as well as the CW linac, which is termed as HELIAC (Helmholtz Linear Accelerator), are being briefly presented.

The basic operating principle and applications of RFQs, different types of applicable RF resonator structures and their properties, as well as the principles of RFQ beam dynamics and electrode design are explained in chapter (2). An emphasis was made here on 4-rod RFQ resonator structures, which have been primarily developed at the Institute for Applied Physics (IAP) of the Goethe University Frankfurt since the mid 1980s.

An extensive simulation-based mechanical analysis of the existing problematic HLI-RFQ is then given in chapter (3), which was followed by the development and test of a completely newly designed RFQ prototype structure, as shown in chapter (4). Based on the developed prototype and the results of its mechanical and RF tests, finally, a design concept for a new full-length HLI-RFQ was derived, the properties of which are presented in chapter (5).

A developed new method to compensate the longitudinal electric end-fields in 4-rod RFQs is discussed in chapter (6), thus providing an applicable strategy to eliminate one of the major field errors typically occurring at RFQ structures of the 4-rod type.

---

[1] *Ger.*: "Hochladungsinjektor"
[2] Facility for Antiproton and Ion Research
[3] continuous wave

1.1 History of the Exploration of (Super-) Heavy Elements

Besides uranium, which is present in comparatively large quantities, the heaviest naturally occurring element on earth is arguably plutonium, which however is extremely rare and can be found in the earth's crust with only an almost negligible abundance [1, 2, 3]. Whereas the $^{244}_{94}$Pu isotope was created by the rapid neutron-capture process ("r-process") either during supernova explosions or the merging of neutron stars before the formation of the solar system or after, thus having a primordial or interstellar origin, the $^{239}_{94}$Pu isotope can be naturally produced on earth in concentrated ores of uranium by the capture of fission neutrons. However, a much larger amount of anthropogenically produced plutonium exists today, mainly as a result of nuclear reactor operation and the production of nuclear weapons.

The historically first-ever artificial production and detection of a transuranium element was accomplished in 1940 at the Berkeley Radiation Laboratory, producing $^{239}_{93}$Np (neptunium) [4] by irradiation of uranium with neutrons which again were produced by bombarding a beryllium target with a deuteron beam extracted from a cyclotron. Within the following years until 1954, isotopes of all further transuranium elements up to a proton number of $Z = 100$ could be produced at Berkeley by irradiating uranium, plutonium or respectively lighter transuranium elements with neutrons or alpha particles [5, 6, 7, 8, 9]. These advances benefited greatly from the continuous development of new cyclotron accelerators [10], for the invention of which Ernest Lawrence was already awarded the Nobel Prize in 1939. Eventually, the applied mechanism of neutron capture by a heavy nuclei to form neutron-rich isotopes which then undergo beta decay to an element with a higher proton number $\left(^{A}_{Z}X + n \rightarrow {}^{A+1}_{Z}X + \gamma \rightarrow {}^{A+1}_{Z+1}Y + \beta^{-}\right)$ reached its limits at the element fermium. This owes to the fact that isotopes of larger nuclei with $Z \geq 100$ become more prone to spontaneous fission as the neutron number increases, which results in very short corresponding half-lives [11]. For this reason, fermium is the heaviest element with the highest proton number that can typically be found in reactor or thermonuclear-produced materials. The production of elements beyond fermium can only be obtained by nuclear fusion reactions from the irradiation of less heavy target nuclei with charged particle beams provided by accelerators. During the period from 1955 to 1974, further heavy elements up to a proton number of $Z = 106$ could be produced in Berkeley as well as at the Joint Institute for Nuclear Research (JINR) in Dubna by irradiation of the previously discovered transuranium elements of proton numbers $Z = 94$–99 with ion beams of increasingly heavier projectile particles starting from $^{4}_{2}$He over $^{10/11}_{5}$B, $^{12}_{6}$C, $^{15}_{7}$N, $^{16}_{8}$O, $^{22}_{10}$Ne up to $^{54}_{24}$Cr [12], for the acceleration of which a heavy-ion linear accelerator (HILAC) was installed at Berkeley whereas in Dubna the development of heavy-ion cyclotrons was pushed forward. Using a comparatively light projectile particle and a heavy transuranium target nucleus results in a so-called hot fusion reaction which is characterized by high excitation energies of the formed "hot" compound system of about 40–50 MeV and a subsequent de-excitation down to the ground state by a cascaded evaporation of multiple neutrons and emission of gamma radiation [13]. In order to yield a sufficiently high production rate of newly formed heavier nuclei, there has to be a low probability for the hot compound nucleus to undergo fission during the process of de-excitation, which at highly excited states far above the ground state eventually requires high enough fission barriers [14].

With the aim to reduce the energy deposited in the excitation of the fused compound system, thus allowing to advance to the production of heavier elements, Yuri Oganessian of JINR finally proposed the concept of cold fusion, according to which the compound nucleus can be cooled down to 10–15 MeV by choosing collision partners with a more symmetrical mass distribution and high nuclear binding energies (shell-stabilized) while accelerating the projectile particle to an energy just high enough to overcome the coulomb barrier. The reduction of steps required for de-excitation, corresponding to a decreased probability for fission, is characterized by the number of evaporated neutrons reducing to a few or even none at all.

Following the concept of cold fusion, six further super-heavy elements with the proton numbers 107–112 could be discovered from 1981 to 1996 at the GSI Helmholtz Centre for Heavy Ion Research in Darmstadt, Germany, by irradiating $^{209}_{83}$Bi or $^{207/208}_{82}$Pb targets with heavy ion beams of $^{54}_{24}$Cr, $^{58}_{26}$Fe, $^{62/64}_{28}$Ni and $^{70}_{30}$Zn [15]. Whereas the required beams with typical energies between 4.5 and 5.5 MeV/u were provided by the Universal Linear Accelerator (UNILAC), which was put into operation at GSI during 1975 [16], the newly discovered super-heavy elements were produced and analyzed at the Separator for Heavy Ion Reaction Products (SHIP). The elements with proton numbers 108 ("hassium") and 110 ("darmstadtium") were named after the German state of Hesse and after the city of Darmstadt, respectively.

$^{262}_{107}$**Bh**	$^{265}_{108}$**Hs**	$^{266}_{109}$**Mt**	$^{269}_{110}$**Da**	$^{272}_{111}$**Rg**	$^{277}_{112}$**Cn**
Bohrium	*Hassium*	*Meitnerium*	*Darmstadtium*	*Roentgenium*	*Copernicium*
(1981)	(1984)	(1982)	(1994)	(1994)	(1996)

Figure 1.1: Overview of super-heavy elements discovered at GSI with name and year of discovery.

After all, the production of super-heavy elements by the cold fusion method however seemed to be limited by a steep decrease of the production cross-sections with increasing proton number, which is assumed to be caused by an increasing probability for the occurrence of "quasi-fission", where the compound system re-separates in two fragments without forming a compound nucleus [17, 13]. Whereas compared to this, the hot fusion cross-sections decrease even stronger for the production of elements with proton numbers ≤ 110, due to the increase of fission losses at high excitation energies and decreasing fission barriers, the cross-section curve however increases again starting from a proton number of about 111 and seems to form a bump with a maximum at roughly around 115 before starting to fall again[4]. Eventually, this behavior results from an analogous evolution of the fission barriers[5].

Finally, returning to hot fusion, the heaviest elements known today with proton numbers from 113 to 118 were discovered between 1998 and 2006 at JINR in Dubna [18], which was accomplished by irradiating transuranium target materials like $^{244}_{94}$Pu, $^{243}_{95}$Am, $^{248}_{96}$Cm, $^{249}_{97}$Bk and $^{249}_{98}$Cf with an ion beam of $^{48}_{20}$Ca extracted from the U-400 cyclotron. This specific calcium isotope was chosen as projectile due to its doubly magic nuclide property (see explanation in section 1.2), in analogy to the choice of doubly magic (or close to being doubly magic) target nuclei like $^{208}_{82}$Pb in case of cold fusion. The heaviest ever produced and detected element to date, $^{294}_{118}$Og "oganesson", was named after Yuri Oganessian in honor of his pioneering contributions to the research of super-heavy elements. Ultimately, the synthesis of super-heavy elements as carried out at JINR, using calcium projectile beams, is limited to proton numbers ≤ 118 by californium being the heaviest target material available in sufficient quantities.

---

[4]see [13, Fig. 25]
[5]see [17, Fig. 8]

1.2 Limits of the Nuclides Chart & the "Island of Stability"

The protons and neutrons which form an atomic nucleus are bound together by the so-called nuclear force which counteracts the repulsive electric force caused by the proton charge [19]. In principle, the nuclear force itself is a residual effect of the fundamental strong interaction between the quarks which constitute the nucleons. The stability of an atomic nucleus relating to the decay probability is characterized by its binding energy, which is basically given by Bohr's and Wheeler's generalization of the semi-empirical Bethe-Weizsäcker formula [20], where the atomic nucleus is considered to behave like a deformable charged liquid drop. Based on the magnitudes of the fission barriers calculated from the liquid drop model, it was expected that actually observable atomic nuclei with proton numbers higher than about 103 cannot exist due to correspondingly short half-lives for spontaneous fission. Today, the elements with proton numbers of 104 and above are termed as "super-heavy elements" (SHE). In general, the existence of an element is defined by its lifetime exceeding 10^{-14} s, which is about the duration necessary to reach an atomic electron shell structure [21].
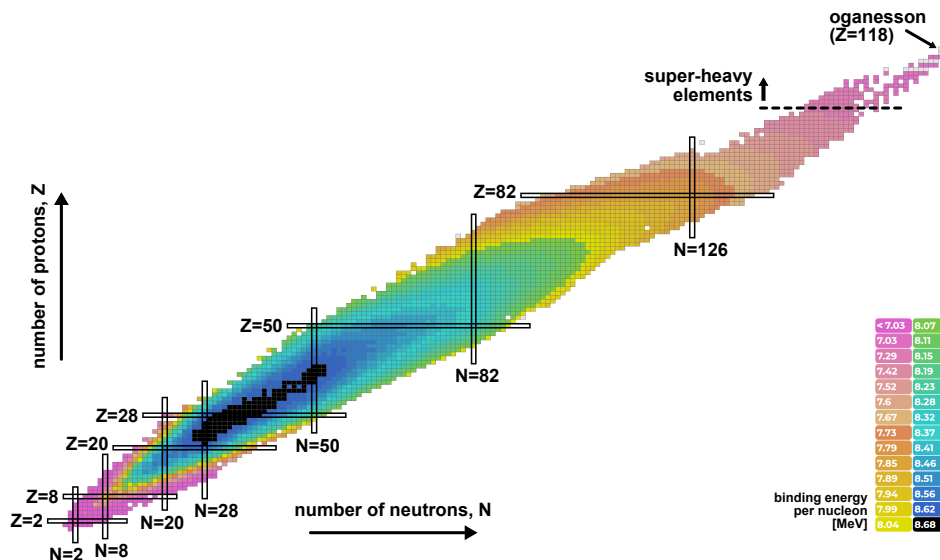

Figure 1.2: Chart of known and experimentally confirmed nuclides by nuclear binding energy[6].

Looking at the nuclides chart, reflecting the nuclide properties as function of the proton and neutron number, the so-called line of beta stability extends in the immediate vicinity of the isotopes with the respective maximum binding energy per element, as predicted by the Bethe-Weizsäcker formula. While nuclides on the line of beta stability are completely stable against beta decay, which is an effect of the fundamental weak interaction, neutron-rich isotopes tend to decay to nuclei with increased proton and decreased neutron number by β^- emission, whereas neutron-poor isotopes vice versa decay by β^+ emission. The corresponding maximum and minimum neutron-proton ratios beyond which no nuclides can exist anymore form the borders of the "valley of stability" (as can be seen in Fig. 1.2), with the line of beta stability at its bottom, whereas the outside area is referred to as "sea of instability". Towards super-heavy nuclei with very high proton and neutron numbers, the valley of stability is limited mainly by spontaneous fission, as mentioned above, but also by alpha decay.

[6]diagram taken from the IAEA (International Atomic Energy Agency) Nuclear Data Services: LiveChart of Nuclides, http://www-nds.iaea.org/

To obtain a more accurate description of the nuclear properties than provided by the macroscopic liquid drop model, modern single-particle models have been developed since the 1950s with the aim to describe the behavior of the nuclear system at quantum levels[7], which in principle would correspond to a many-body Schrödinger equation with the potential being determined by the nuclear forces. In analogy to the discrete arrangement of the energy levels found in the atomic electron shell, hence also the energy levels occupied by the nucleons exhibit a shell-like structure, with the complete closure of the respective highest shell resulting in an increased nuclear binding energy relative to the number of nucleons. The numbers of protons or neutrons, respectively, at which a shell is completed are termed as "magic numbers". Confirmed values of magic numbers are today considered to be 2, 8, 20, 28, 50 and 82 for both protons and neutrons, and additionally 126 for neutrons. Nuclides with both the proton and neutron number being magic are called "doubly magic" and are ultimately known to be the most stable existing elements, with decay being prevented by their typically spherically shaped nuclei providing a high resistance against deformation.

The stabilizing effects due to the shell-structure become more significant towards larger and heavier nuclei at the upper end of the valley of stability, which eventually allows super-heavy elements to exist, contrary to the predictions from the liquid drop model. While the next magic numbers are predicted to be in the range of 114–126 for protons and 184–196 for neutrons [22], a larger region of spherical super-heavy nuclei with enhanced stability is expected to be located near the presumably doubly magic $^{298}_{114}$Fl, which so far could not be artificially produced. After all, estimates for the half-lives of nuclei at the peak of this so-called "island of stability" range up to thousands and even millions of years [21, 23].

1.3 GSI & FAIR

The GSI Helmholtz Centre for Heavy Ion Research (original German title: "Gesellschaft für Schwerionenforschung") was first founded as a national research institution back in 1969 [24]. To this day, the centerpiece of the GSI facility is formed by the UNILAC accelerator, which is capable to provide beams of all ion species from protons to uranium with a maximum end energy of 11.4 MeV/u. As shown schematically in Fig. 1.3, today the UNILAC is fed either by the High Current Injector (HSI[8]), or by the High Charge State Injector (HLI). The HSI is designed for providing a high current heavy ion beam to the post-stripper UNILAC accelerator of up to $I = A/q \cdot 1.76$ mA with a maximum mass-to-charge ratio of $A/q = 8.5$ [25], corresponding to a pre-stripper beam current of $I = A/q \cdot 0.25$ mA with $A/q \leq 65$ [26]. Following its two existing source terminals and the high current LEBT section, the HSI consists of an IH-RFQ[9] with a length of 9 m [27], the "Super Lens" with a 0.8 m long bunching-RFQ [28], and two IH-DTL[9] cavities which implement the KONUS beam dynamics concept [29]. At the gas stripper [30], the low-charged beam from the HSI is stripped to charge states which enable efficient acceleration in the post-stripper accelerator section. The already highly charged beam from the HLI, as further described in section 1.4, is injected to the UNILAC behind the stripper. Finally, the beam acceleration from the injector output energy of 1.4 MeV/u to the variable end energy between 3.4 and 11.4 MeV/u is accomplished by four DTL cavities of the Alvarez type [25] and an additional array of 10 separately controlled single-gap resonators [31], with the entire post-stripper accelerator being operated at 108.408 MHz.

---

[7]from this, single-particle shell effects could also be included as corrections in the liquid drop model, resulting in the macroscopic-microscopic model as further discussed in [20]

[8]*Ger.*: "Hochstrominjektor", [9]IH → Interdigital H-mode

The beam from the UNILAC can then either be used directly at the adjoining low energy physics experimental area with experiments like SHIP [22] and TASCA [32] for super-heavy elements research, or injected through a transfer channel including another stripper to the heavy ion synchrotron SIS18 (also see Fig. 1.4), which was commissioned in 1990. With a circumference of 216 m and a magnetic bending power of 18 Tm, the SIS18 can provide acceleration up to the GeV range[10] for experimental programs in numerous scientific fields like nuclear, atomic, plasma, astro- and biophysics, material sciences or even newly developed medical applications like cancer therapy [33].
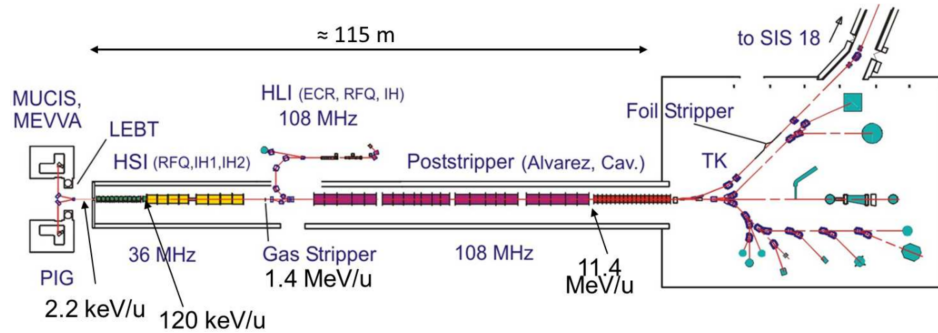

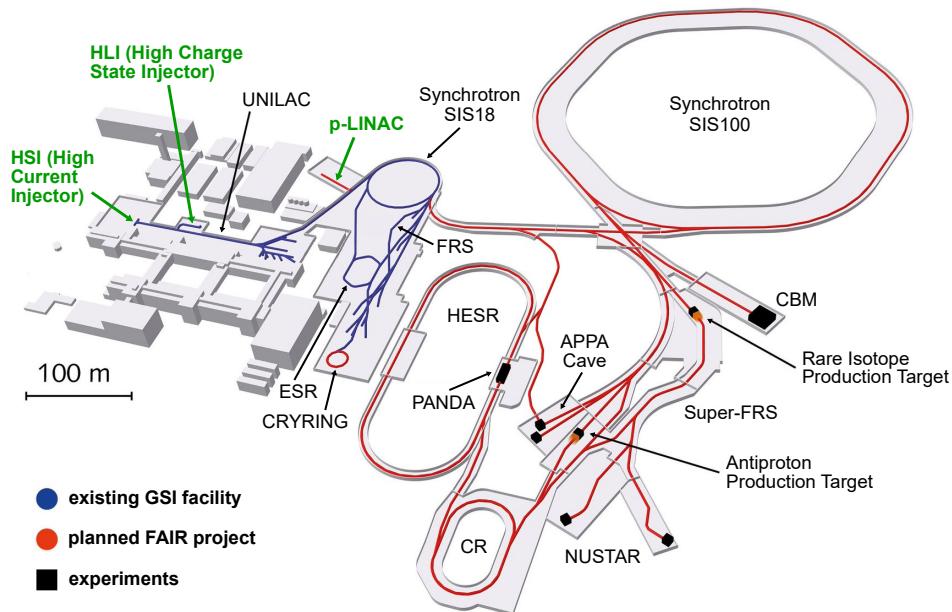**Figure 1.3:** Layout of the UNILAC [25].

Figure 1.4: Schematic overview of the existing GSI facility and the planned start version of the FAIR complex[11] (the injector linacs are highlighted in green) [34].

In 2003, the German Federal Ministry of Education and Research approved the construction of the new FAIR accelerator facility, which as a large-scale international research project is supported by a collaboration of 11 partner countries[12]. As an extension of the existing GSI accelerator, the double-ring synchrotron SIS100/300 planned for FAIR will use the SIS18 as its injector (Fig. 1.4 shows the start version of FAIR, only including the SIS100).

---

[10]from 4.5 GeV for protons to 1 GeV/u for highly charged uranium ions
[11]figure courtesy of GSI/FAIR, [12]Finland, France, Germany, India, Poland, Romania, Russia, Slovenia, Sweden, United Kingdom and Czech Republic

For this purpose, all parts of the GSI accelerator facility, including the SIS18 [35], the UNILAC [25], the HSI [36, 37] and the ion sources [38], are being upgraded to meet the requirements of FAIR operation. Additionally, a new dedicated proton injector linac ("p-Linac") [39] will be installed at the SIS18 to provide the FAIR facility with a high-intensity proton beam as required for the production of anti-protons for the PANDA experiment.

After all, the SIS100 with a circumference of about 1100 m and a magnetic bending power of 100 Tm is planned to deliver beams of protons with up to 29 GeV, U^{28+} with 1.5 GeV/u and U^{92+} with 11 GeV/u for the four main experimental programs APPA (**A**tomic and **P**lasma **P**hysics, and **A**pplications in bio, medical and material sciences), CBM (physics of **C**ompressed **B**aryonic **M**atter), NuSTAR (**Nu**clear **ST**ructure, **A**strophysics and **R**eactions) and PANDA (Anti-**P**roton **AN**nihilation at **DA**rmstadt) [34].

1.4 High Charge State Injector (HLI)

The High Charge State Injector was commissioned at GSI in 1991 as a second injector to the post-stripper UNILAC accelerator in order to allow the pulse-to-pulse time-shared acceleration of beams with different ion species and currents, being extracted from two different injectors [40]. This was required to enable the operation of the SIS18 injection simultaneously to providing beam for the experiments at the low energy physics experimental area.
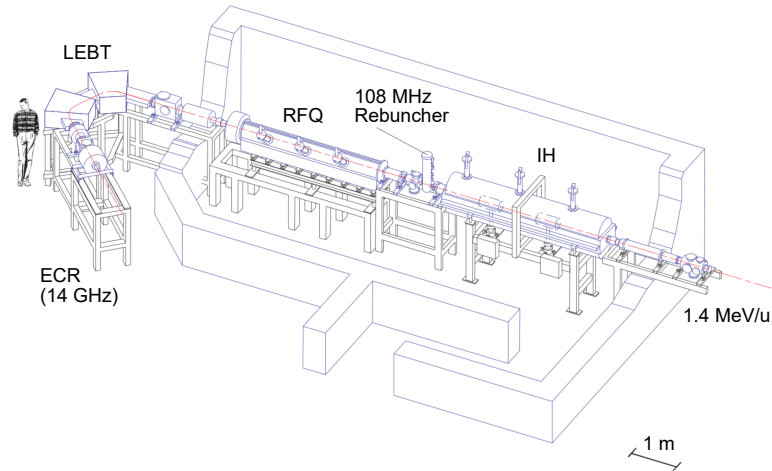

Figure 1.5: Overview of the High Charge State Injector (HLI) [41].

Fig. 1.5 shows the current layout of the HLI: The ion source is followed by a high resolution 135° double magnet spectrometer for charge and mass analysis, behind which the 2.5 keV/u heavy ion beam with A/q up to 8.5 is matched transversely for the injection to the RFQ by a magnetic quadrupole triplet and a solenoid. The RFQ, which is operated at the HLI/UNILAC frequency of 108.408 MHz, bunches and accelerates the beam to 300 keV/u before again being matched transversely and longitudinally by a transport section consisting of a magnetic quadrupole triplet, a doublet and a quarter-wave rebuncher for injection to the IH-DTL structure. At the IH output energy of 1.4 MeV/u, the beam is finally transported through a 180° bend to the post-stripper UNILAC section (also see Fig. 1.6).

Since the HLI, which was originally designed for a maximum duty cycle of 25 to 50 % (for A/q from 8.5 to 1), is intended to serve as injector for the planned new CW linac (see section 1.5), a major upgrade of most of the beamline components will be required to enable CW operation, concerning the ion source, the low level RF and the power amplifiers, beam diagnostics and the control system, the RFQ, the rebuncher and the IH cavity [41].

1.5 HELIAC Project

As the UNILAC is being primarily upgraded to the specifications for future injection to the FAIR facility, which requires only a comparatively low duty factor below 1 %, a new dedicated superconducting CW linac is planned to be built at GSI with the main purpose of providing intense heavy ion beams for super-heavy elements research near the coulomb barrier [42].

The HELIAC (Helmholtz Linear Accelerator) is designed to accelerate ion beams with mass-to-charge ratios of $A/q = 1$–6 to a variable end energy between 3.5 and 7.3 MeV/u at beam currents ≤ 1 mA, operating at an RF frequency of 218.816 MHz [43]. The currently proposed layout of the HELIAC with the HLI as injector is shown in Fig. 1.7 and includes a total of 12 superconducting multi-gap constant-beta CH-DTL[13] cavities in 4 cryomodules, each containing an additional superconducting 2-gap spoke cavity for longitudinal beam matching as well as two superconducting solenoids for transverse focusing. While the first type of superconducting CH structures designed for HELIAC operation (*CH0*) has already been successfully beam-tested in the CW linac demonstrator project [44], the scheme of which is depicted in Fig. 1.6, and cold-tests have been conducted on the second type (*CH1* and *CH2*) [45], the following CH cavities (*CH3–11*) are currently still in the design phase[14] [46].
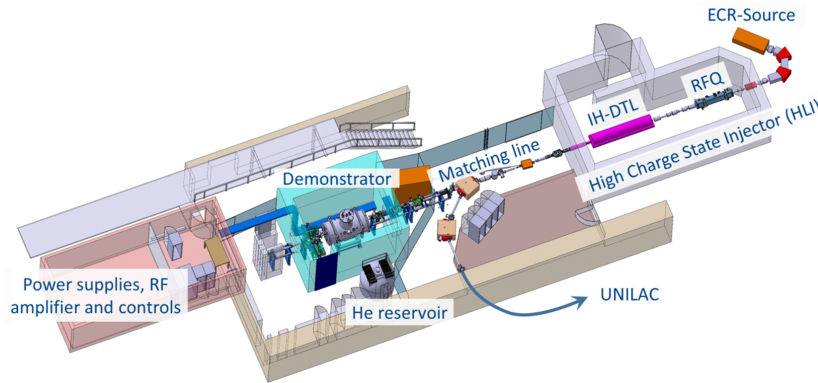

Figure 1.6: Overview of the CW linac demonstrator with connection to the HLI beamline [42].
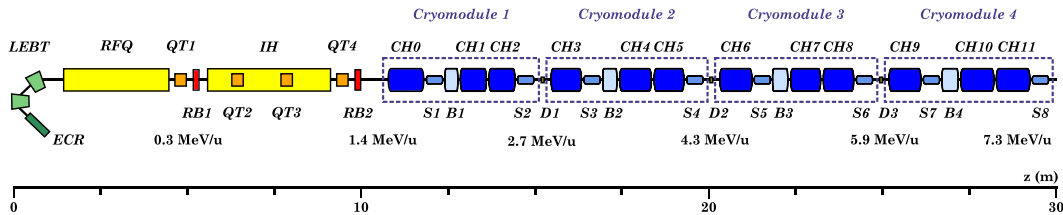

Figure 1.7: Conceptual layout of the HELIAC [43].

[13]CH → Crossbar H-mode
[14]all 12 superconducting CH cavities are developed at IAP

(2) Fundamentals of Radio Frequency Quadrupoles

In particle accelerators, beams of charged particles such as electrons or ions are accelerated by electric fields to kinetic energies which besides numerous practical irradiation applications allow the properties of matter to be studied by analyzing high energy particle interactions. After cathode-ray tubes had already existed since the end of the 19th century, providing a few tens of kV for the acceleration of electron beams, the first kind of particle accelerator by today's standards was developed by John Cockcroft and Ernest Walton around the beginning of the 1930s [47]. The original Cockcroft-Walton generator allowed to produce a static voltage of $800\,\mathrm{kV}$, using a voltage multiplier cascade of capacitors and diodes [48], and eventually enabled the historically first artificially induced nuclear reaction[1] to be observed in 1932 from irradiating a lithium target with a proton beam of up to $600\,\mathrm{keV}$ and beam currents in the range of a few $\mu\mathrm{A}$ [49]. For this achievement Cockcroft and Walton were awarded the Nobel Prize in 1951. At about the same time as the development of the Cockcroft-Walton accelerator in the early 1930s, also other accelerator types were already being developed, such as the electrostatic Van de Graaff accelerator [50], the cyclotron [10], or the Wideröe linac [51].

In fact, the principle of particle acceleration by high-frequency (RF) alternating electric fields as first proposed by Gustav Ising in 1925 and implemented in the Wideröe drift tube linac (DTL) is still applied today in modern linear accelerators[2]. Whereas with electrostatic acceleration the obtainable DC beam energies are ultimately limited by the maximum achievable static voltage, reaching up to about $30\,\mathrm{MV}$ [52], in RF linear accelerators a bunched beam is accelerated in the gaps between an array of drift tubes, which are being alternately oppositely charged by an electromagnetic standing wave generated by an RF resonator structure, basically allowing to use the resonator field multiple times for beam acceleration.

Therefor, the so-called Wideröe condition $\ell_c = \beta_c \lambda_{\mathrm{RF}}/2$ has to apply in order to obtain synchronicity of the bunch motion with velocity β_c between two adjacent gap centers in a distance of ℓ_c and the accelerating phase of the electric field with a corresponding shift of $180°(\pi\text{-mode})$[3]. Accordingly, the gap center distance ℓ_c has to be gradually adapted along the beamline to the increasing particle velocity.
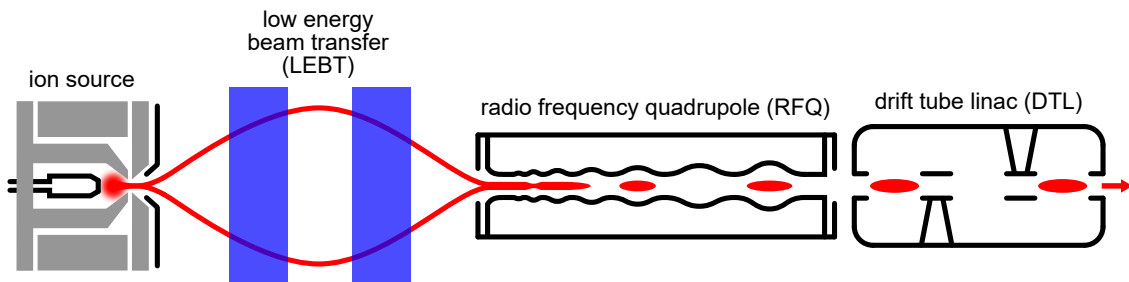

Figure 2.1: Schematic overview of a typical front-end of a linear accelerator for ions.

---

[1]$({}^{7}\mathrm{Li} + \mathrm{p} \rightarrow {}^{4}\mathrm{He} + {}^{4}\mathrm{He} + \gamma)$
[2]a comprehensive review of the history of RF particle accelerators can be found in [53]
[3]the Alvarez accelerator is operated in 0-mode, resulting in a Wideröe condition of $\ell_c = \beta_c \lambda_{\mathrm{RF}}$

However, the efficiency of ion beam acceleration in RF drift tube structures at the low-energy end after extraction from the ion source is compromised to a major extent by predominantly three aspects [54]:

- The transversally defocusing space charge force due to the repulsive Coulomb forces between the beam particles has a $1/\gamma^2$-dependency [55] and hence is maximum at low beam velocities (γ being the Lorentz factor). Also, the strength of magnetic focusing by Lorentz force is proportional to the particle velocity, thus being weak at low beam energies. Anyway, at accordingly short gap center distances ℓ_c, the corresponding small dimensions of the drift tubes would not provide enough longitudinal space for placing focusing elements like magnetic quadrupoles to yield efficient transversal focusing.

- Considering the acceleration of low-velocity beams, drift tube structures typically have a reduced RF efficiency, which is due to the fact that with short required gap lengths and at the same time comparatively large aperture diameters, the generated electric acceleration field is less concentrated onto the beam axis. Therefore, as high as practically achievable extraction voltages at the ion source or dedicated electrostatic pre-accelerators had to be used in order to increase the injection energy to the drift tube linac to the highest possible extent (see Fig. 2.2).

- Due to the requirement for synchronicity between particle motion and accelerating phase of the electric field, RF drift tube accelerators have a limited phase acceptance, corresponding to the fact that beam particles outside the so-called stable phase space "bucket" will be lost during RF acceleration. Although single-gap RF bunching cavities or multi-harmonic bunching systems have been used to increase the fraction of particles that are transferred into the stable bucket, the achieved transmission efficiency was however very limited, being in the range of about 50 to 80 %.
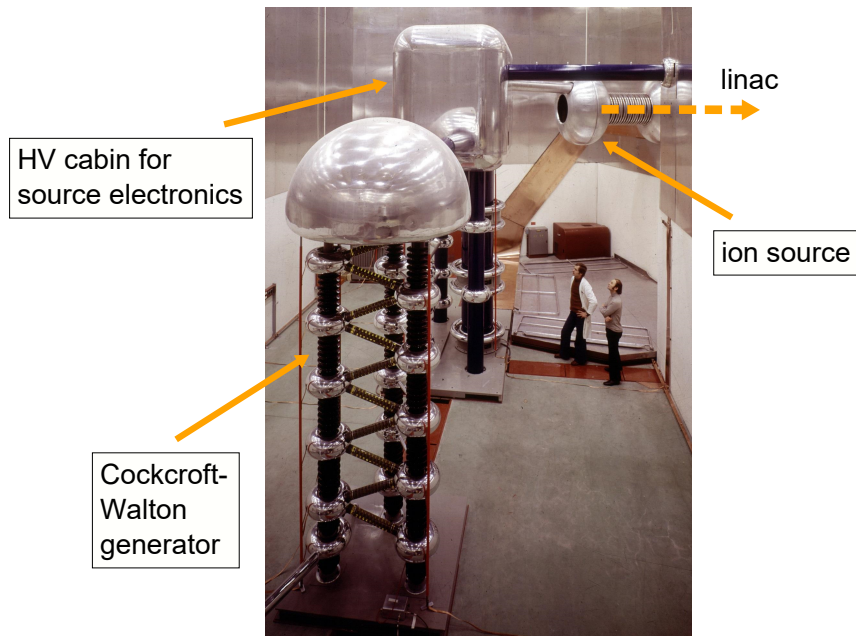

Figure 2.2: High-voltage installation of the CERN Linac2 with a 750 kV Cockcroft-Walton generator, which was replaced by a 90 kV pre-injector and a 1.8 m long 750 keV RFQ in 1993 [54][4].

[4]image © 1974–2020 CERN (CERN-AC-7602012)

After all, because of the low transversal focusing, lack of pre-acceleration and weak longitudinal pre-bunching, the low-energy section used to be a major bottleneck regarding the achievable beam quality and current, and additionally affected the overall operational reliability of the entire linac due to frequently occuring high voltage breakdowns. However, a solution to all of the problems outlined above was finally provided by the invention of the radio frequency quadrupole (RFQ) accelerator concept, which is standardly used in most of today's ion linacs to achieve efficient injection of the low-energy beam extracted from the ion source to the downstream drift tube accelerator, as schematically depicted in Fig. 2.1.

2.1 Operating Principle & Applications

The basic functional concept of the RFQ accelerator was first proposed in 1969 by Ilya Kapchinsky of the Institute for Theoretical and Experimental Physics (ITEP) in Moscow and Vladimir Teplyakov of the Institute of High Energy Physics (IHEP) in Protvino [56], whose idea was to combine the velocity-independent transversal focusing by a high-frequency alternating electric quadrupole field with the simultaneous acceleration and bunching effect due to a longitudinal field component created by a periodic modulation of the electrode shape.
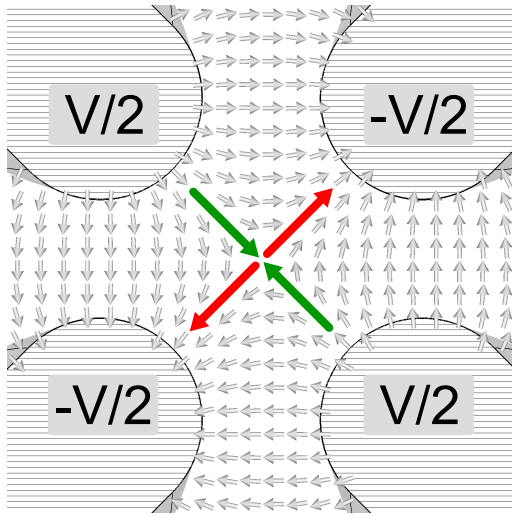

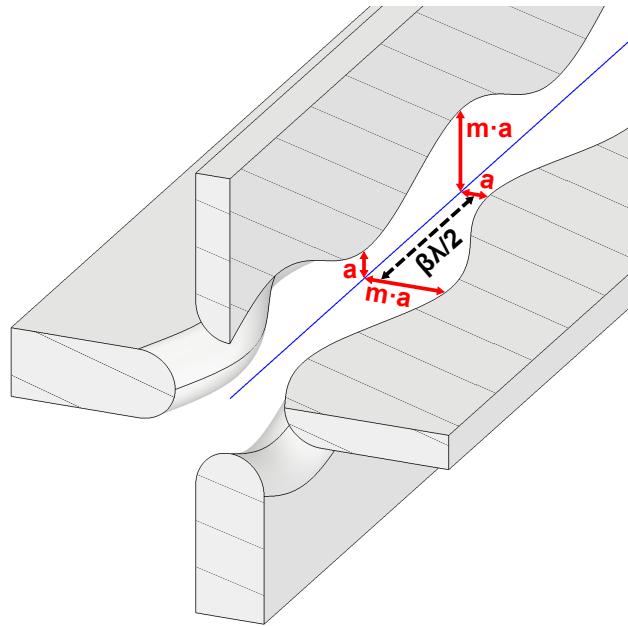**Figure 2.3:** Transversal electric quadrupole field in an RFQ (green: focusing plane, red: defocusing plane).

Figure 2.4: Modulation of the quadrupole electrodes (a = minimum distance from the beam axis, $m \cdot a$ = maximum distance from the beam axis, m = modulation factor) [57].

The arrangement of the quadrupole electrodes in the transverse plane with the corresponding potentials and resulting electric field distribution is depicted in Fig. 2.3. As can be seen, at each point in time the quadrupole field leads to a focusing force along one of the transverse

axes while perpendicular to which defocusing occurs. This also corresponds to the fact that according to the Laplace equation for the electric RF field between the electrode vane tips ($\Delta \vec{E} = 0$, see derivation of Eq. 2.55), focusing in all spatial directions at the same time is not possible. However, since the polarity of the quadrupole reverses periodically with the frequency of the applied RF field, the focusing axis thus changes to be defocusing and vice versa every time after half the duration of an RF period, corresponding to a distance traveled by the beam of $\beta\lambda_{\mathrm{RF}}/2$. Eventually, this forms an alternating gradient focusing channel with the same focusing properties as a corresponding FODO lattice of magnetic quadrupoles (F = focusing, D = defocusing, O = drift), as schematically depicted in Fig. 2.5.

Considering that the strength of the focusing/defocusing electric field increases with the distance of the respective particle position to the quadrupole center, which in the vicinity to the beam axis is in good approximation subject to a linear dependency, defocusing at one element (D) of the lattice results in stronger focusing at the following element (F), since there the initially increased divergence and the associated larger beam envelope causes the beam to experience higher focusing forces. In analogy to that, focusing at one element (F) leads to weaker defocusing at the following element (D), since there the initially increased convergence and the associated smaller beam envelope results in a lower defocusing force being applied. Following this principle, finally a net focusing of the particle beam on both transverse axes is achieved as it passes through the lattice of focusing elements with alternating gradients.
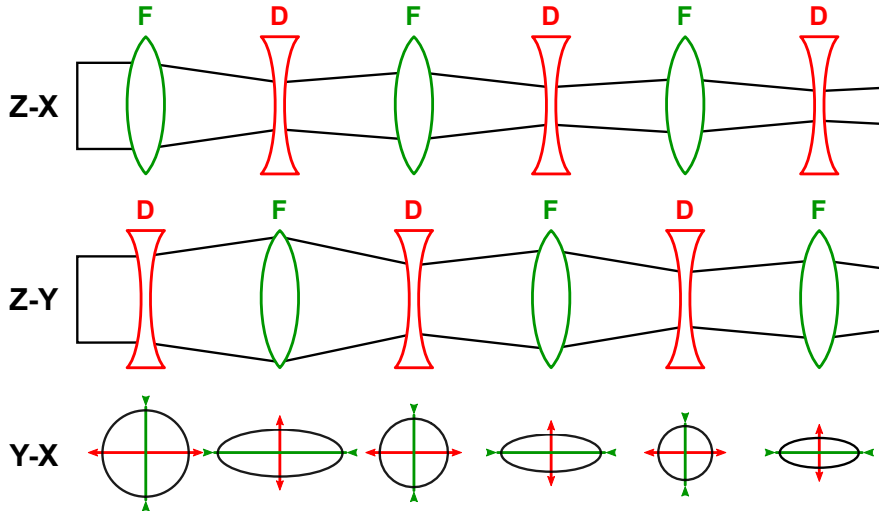

Figure 2.5: Alternating gradient focusing in a FODO lattice.

In order to achieve acceleration as well as longitudinal bunching in addition to the transverse focusing by the quadrupole field, according to Kapchinsky's and Teplyakov's idea the shape of the electrode vane tips is longitudinally modulated with a sinusoidal profile as shown in Fig. 2.6, with the minimum distance between the vane tip and the beam axis being specified by the cell aperture parameter a and the respective maximum distance being defined by its product $a \cdot m$ with the modulation factor m. Due to the boundary condition for the electric field at the conducting electrode surface, according to which the field vector points parallel to the surface normal at all times, eventually an electric field component parallel to the direction of the beam axis emerges. Since the opposite charging of the electrode

pairs arranged perpendicular to each other leads to opposite orientations of the respectively generated longitudinal field components, the modulation of the respective electrode pairs has to be shifted by half the modulation length (see Fig. 2.4) for yielding a net longitudinal electric field. Because the obtained electric field thus changes direction with the same spatial periodicity, the electrode modulation length is hence set to $\beta_c \lambda_{RF}$, effectively constituting acceleration cells with a length of $\ell_c = \beta_c \lambda_{RF}/2$, corresponding to the Wideröe condition derived for π-mode drift tube accelerator structures. In analogy to that, the lengths ℓ_c of the RFQ acceleration cells also have to be adapted to the particle velocity $\beta_c(z)$ along the beam axis z, whereas for each cell the overall strength of transverse focusing is determined by the respective aperture parameter a with the modulation factor m allowing to adjust the amount of the longitudinal field component which provides either acceleration and/or longitudinal bunching, depending on the synchronous phase ϕ_s.
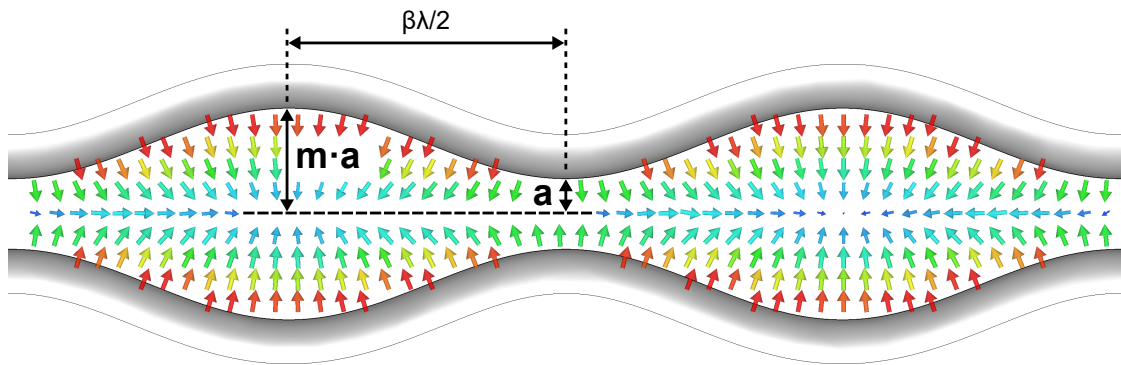

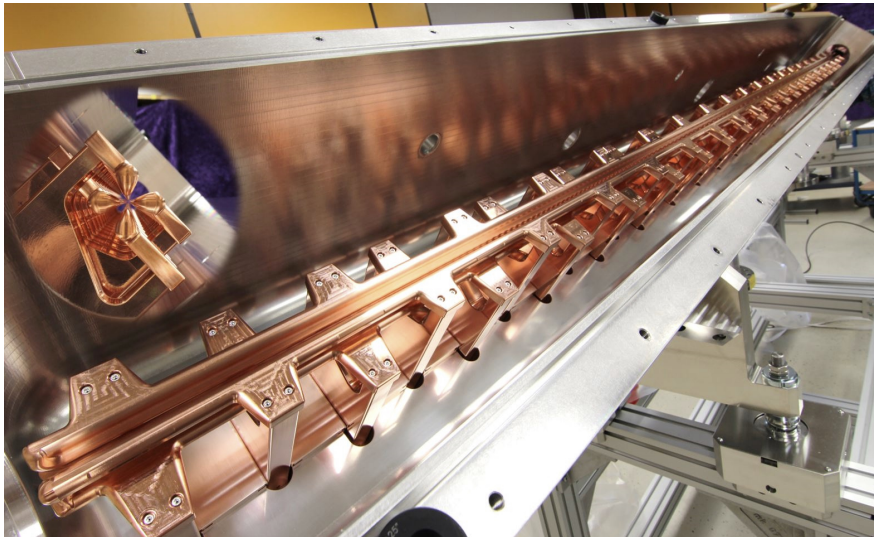**Figure 2.6:** Electric field between sinusoidally modulated opposite electrodes of the quadrupole.

Figure 2.7: 176 MHz 4-rod RFQ for CW acceleration of a 4 mA proton beam at the MYRRHA injector [58].

A first successful experimental test of the proposed RFQ concept for the acceleration of high-intensity low-energy ion beams was first conducted in 1974 at IHEP, where a proton beam was

accelerated by a 148.5 MHz RFQ from 100 to 620 keV with an efficiency of 50 % [59]. Later, in 1980, finally the acceleration of a proton beam from 100 to 640 keV with a high efficiency of 90 % could be demonstrated at the Los Alamos National Laboratory (LANL) with the developed 425 MHz proof-of-principle (POP) RFQ of the 4-vane type [60], which became a prototype for numerous following RFQ developments. Until today, hundreds of RFQs have been built and put into operation in laboratories all over the world for the preparation and acceleration of ion beams within a typical range of about $\beta = 0.01$ to 0.06 (input/output) and currents from almost zero to a few hundred mA, either for direct use of the beam for scientific or commercial irradiation applications, or for injection to another accelerator. Also, a variety of different applicable resonator concepts has been developed, with examples for the most significant types being given by Figs. 2.7–2.10. An extensive but by far not complete overview of developed RFQs for different projects and applications is provided by Tab. 2.1.
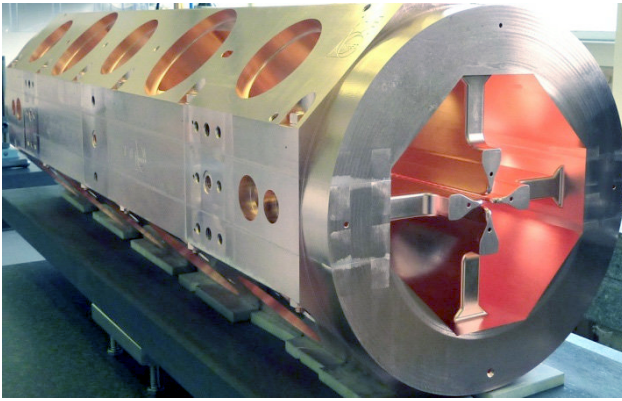

Figure 2.8: One of three modules of the 352 MHz 4-vane RFQ at the CERN Linac4 for the acceleration of a 70 mA H⁻ beam [61].
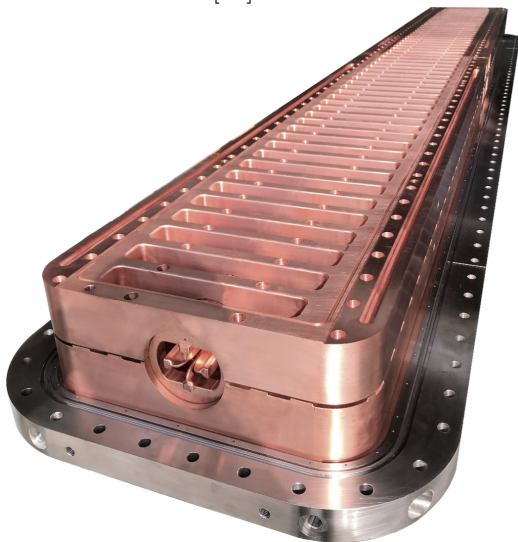

Figure 2.9: Assembly of the 325 MHz ladder-RFQ for the acceleration of a 100 mA proton beam at the FAIR p-Linac [62].
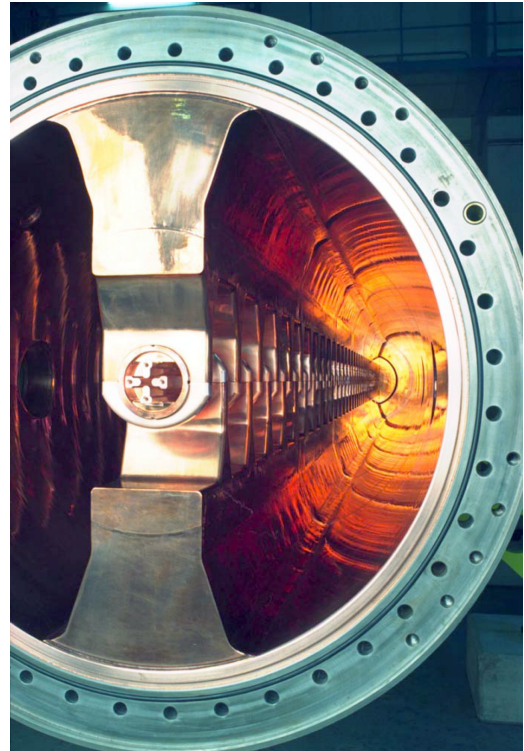

Figure 2.10: Interior view of the 36 MHz IH-RFQ at the GSI High Current Injector (HSI) for the acceleration of very heavy ion beams with mass-to-charge ratios of up to $A/q = 65$ and beam currents of up to 20 mA [63, p. 26].

facility / project	type	f [MHz]	L [m]	I [mA]	E_{in} [keV/u]	E_{out} [MeV/u]	A/q	D [%]
Spiral-RFQ (prototype)[64]	spiral	27.1	4.0	25	2.2	0.0176	119	1
TRIUMF ISAC[65]	split-ring	35.36	8.0	$<10^{-3}$	2	0.15	30	CW
GSI HSI[37]	IH	36.136	9.2	20	2.2	0.12	65	2
IMP SSC[66]	4-rod	53.667	2.5	0.5	3.7	0.143	7	CW
LNL PIAVE (SRFQ1+2)[67]	CH	80	2.1	0^*	37.1	0.585	8.5	CW
LANL FMIT[68]	4-vane	80	3.9	100	75	2	2	CW
MSU FRIB[69]	4-vane	80.5	5.0	0.45	12	0.5	7	CW
MSU ReA3[70]	4-rod	80.5	3.5	$\sim10^{-3}$	12	0.6	5	CW
IMP LEAF[71]	4-vane	81.25	6.0	2	14	0.5	7	CW
GANIL SPIRAL2[72]	4-vane	88.0525	5.1	5/1	20	0.75	2/3	CW
TUM MAFF[73]	IH	101.28	2.9	0.8	3	0.3	6.3	10
CERN REX-ISOLDE[74]	4-rod	101.28	3.0	0^*	5	0.3	4.5	10
CERN Linac3[75]	ladder	101.28	2.5	0.08	2.5	0.25	8.3	0.4
BNL EBIS[76]	4-rod	100.625	3.1	10	17	0.3	6.25	0.1
GSI HITRAP[77]	4-rod	108.408	1.9	0^*	500	0.006	3	<1
GSI HLI (new)[78]	**4-rod**	**108.408**	**2.0**	**5**	**2.5**	**0.3**	**6/8.5**	**CW/50**
MPI HCI (RFQ1+2)[79]	4-rod	108.48	6.0	10	4	0.478	9	25
GSI HLI (old)[80]	4-rod	108.5	3.0	0^*	2.5	0.3	8.5	25
GSI CRYRING[81]	4-rod	108.5	1.6	~0.1	10	0.3	4	0.1
JINR NICA[82]	4-vane	145.2	2.1	10	103	0.156	3.33	0.015
IMP Injector II[83]	4-vane	162.5	4.2	15	30	2.1	1	CW
FNAL PIP2IT[84]	4-vane	162.5	4.5	10	30	2.1	-1	CW
IAP FRANZ[85]	4-rod	175	1.7	140	120	0.7	1	CW
IFMIF EVEDA[86]	4-vane	175	9.8	130	100	5	2	CW
SNRC SARAF[87]	4-rod	176	3.8	5	20	1.5	2	CW
SCK-CEN MYRRHA[88]	4-rod	176.1	4.0	5	30	1.5	1	CW
LBL Bevatron[89]	4-vane	200	2.3	0.29	8.4	0.2	7	0.2
FNAL[90]	4-rod	201.25	1.3	50	35	0.75	-1	0.12
DESY HERA[91]	4-vane	202.56	1.2	20	18	0.75	-1	0.004
HERA-Prototype[92]	4-rod	202.56	1.2	20	18	0.75	-1	0.004
CERN Linac1[93]	4-vane	202.56	1.4	80	50	0.52	1	0.01
CERN Linac2[94]	4-vane	202.56	1.8	200	90	0.75	1	0.01
HIT[95]	4-rod	216.816	1.5	$2/\sim10^{-3}$	8	0.4	1/3	<1
CSNS[96]	4-vane	324	3.6	40	50	3	-1	1.05
J-PARC RFQ III[97]	4-vane	324	3.6	50	50	3	-1	3
CPHS[98]	4-vane	325	3.0	50	50	3	1	2.5
FAIR p-Linac[62]	ladder	325.224	3.4	100	95	3	1	0.08
LANL LEDA[99]	4-vane	350	8.0	100	75	6.7	1	CW
CERN Linac4[100]	4-vane	352.2	3.1	70	45	3	-1	10
ESS[101]	4-vane	352.2	4.6	70	75	3.6	1	4
IHEP Injector I[102]	4-vane	352.2	4.7	50	75	3.5	1	CW
CEA IPHI[103]	4-vane	352.2	6.0	100	95	3	1	CW
INFN TRASCO[104]	4-vane	352.2	7.1	30	80	5	1	CW
ORNL SNS[105]	4-vane	402.5	3.7	60	65	2.5	-1	8
LBL Bevalac[106]	4-vane	410	1.0	30	40	0.8	1	0.2
LANL BEAR[107]	4-vane	425	1.0	30	30	1	-1	0.025
LANL POP[60]	4-vane	425	1.1	26	100	0.64	1	0.72
LANL ATS[68]	4-vane	425	2.9	100	100	2	-1	1
CERN PIXE[108]	4-vane	749.48	1.1	$2\cdot10^{-4}$	20	2	1	2.5
ADAM LIGHT[109]	4-vane	750	2.0	0.3	40	5	1	5

Table 2.1: Overview of different RFQs for the acceleration of ion beams, listed by RF operating frequency f with the RFQ length L, design/typical beam current I (*for low beam currents $<1\,\mathrm{mA}$, typically the electrodes are designed for zero-current), injection energy E_{in}, extraction energy E_{out}, maximum mass-to-charge ratio A/q and corresponding duty cycle D.

2.2 Resonator Types

In general, different resonator types can be deployed to obtain the required alternating quadrupolar electrode potentials on which the operating principle of the RFQ is based on (see Fig. 2.11), with the same potential on opposing electrodes and opposite potentials on adjacent electrodes, respectively. In analogy to the resonance in an equivalent RLC circuit, which is further discussed in section 2.3.1, the RF resonance frequency $\omega_0 = \sqrt{1/LC}$ of the respective resonator structure is determined by its inductance L and the overall capacitance C. Whereas the capacitance is mainly given by the shape of the electrode vane tips, which are geometrically modulated according to the beam dynamics design, the inductance is mainly determined by the structure of the respective resonator type, the dimensions of which have to be adapted to yield the desired value of the resonance frequency.
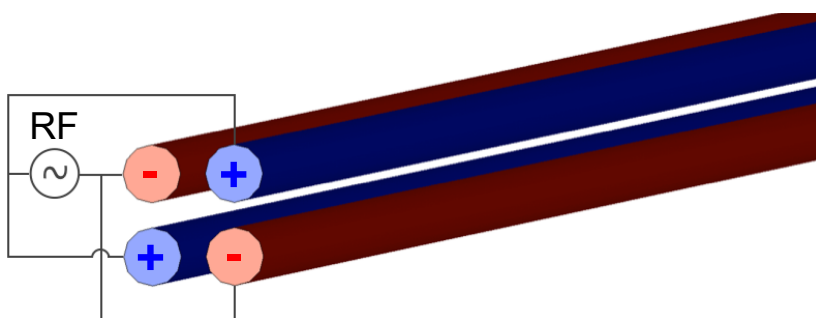

Figure 2.11: Time varying polarity of the quadrupole electrode potentials[5].

A general classification of RFQ resonator structures can be made based on the localization of the resonant current flows: On the one hand, in transmission-line type resonators the current flow occurs predominantly on a dedicated RF resonance structure, the geometry of which solely determines the obtained mode spectrum and frequencies. Besides these, also all other resonator properties are hence mostly independent of the surrounding tank geometry. On the other hand, in RF cavity type resonators the mode spectrum and frequencies are mostly determined by the geometry of the cavity walls (the tank), over which the entire current flows from one pair of electrodes to the other. The functional principle and main characteristics of the four most significant resonator types for RFQ applications, namely the cavity resonator type 4-vane and IH structures and the transmission-line type 4-rod and ladder resonators, are discussed and compared in this section.

Regarding the choice of a resonator type for a specific application, a decisive criterion is not only posed by the RF efficiency (power dissipation compared to the generated vane voltage, characterized by the shunt impedance following the definition provided in section 2.3.2), but also by the required manufacturing effort and related costs, the (transverse) geometric dimensions for the given nominal resonance frequency, technical feasibility of water cooling, and flexibility as well as handling of the available mechanisms for frequency and field adjustment.

---

[5]figure modified from [110, Fig. 2.4]

2.2.1 4-Vanes

In 4-vane type resonators the transverse electric TE_{210} resonant cavity mode is applied to generate the desired quadrupole potential on the tips of the four electrode vanes that are arranged rotationally symmetrically in each quadrant of the structure, as depicted in Fig. 2.13. The resulting current flow from one electrode to the respectively adjacent ones, which is induced by the alternately oppositely oriented longitudinal magnetic fields in the four quadrants, is shown in Fig. 2.14. Eventually, from the resulting charging of the electrode vane tips a concentration of the electric quadrupole field in the area close to the beam axis is achieved, which would not be the case for the original TE_{210} mode, the field distribution of which is schematically depicted in Fig. 2.12.
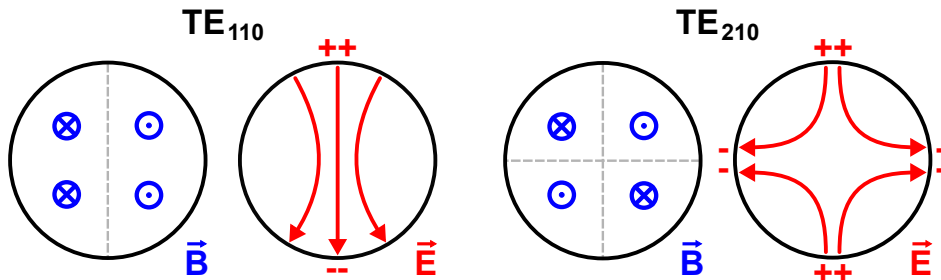

Figure 2.12: Field distribution of the dipole (TE_{110}) and quadrupole (TE_{210}) cavity modes.
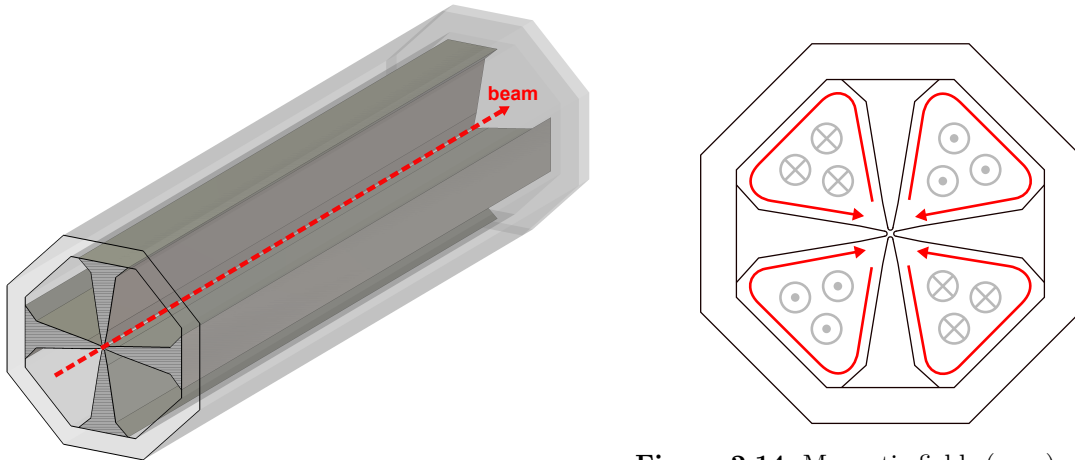

Figure 2.13: Basic structure of a 4-vane RFQ.

Figure 2.14: Magnetic fields (gray) and induced surface current (red) in a 4-vane RFQ.

The nomenclature of the transverse electric TE_{mnp} modes with the indexes m, n and p refers to the number of wave nodes of the longitudinal magnetic field component $B_z(\phi, r, z)$ in the azimuthal ($0 \leq \phi < \pi$), radial ($0 < r \leq R_c$) and longitudinal ($0 \leq z < \ell_c$) direction, respectively. The analytic solution for the components of the magnetic and electric field distribution of TE-modes in an idealized cylindrical "pillbox" type resonator are given by Eqs. 2.1–2.6, which can be calculated from Maxwell's equations, considering the electric and magnetic boundary conditions at the conducting cavity walls (also see [111, pp. 12–14]). $J_m(x)$ denotes the mth Bessel function of the first kind with $J'_m(x)$ being its first derivative and x_{mn} and x'_{mn} being

the nth zero, respectively, whereas the radial coordinate is parameterized by $\varrho = r/R_c$ and E_0 and B_0 being the electric and magnetic field amplitudes ($B_0^* = B_0/J_m(x'_{m1})$). The resonance frequency of TE-modes is given by Eq. 2.7.

$$B_z = B_0^* \, J_m(x'_{mn}\varrho) \, \cos(m\phi) \, \sin\left(\frac{p\pi z}{\ell_c}\right) \, e^{i\omega t} \tag{2.1}$$

$$B_r = \frac{p\pi R_c}{\ell_c x'_{mn}} \, B_0^* \, J'_m(x'_{mn}\varrho) \, \cos(m\phi) \, \cos\left(\frac{p\pi z}{\ell_c}\right) \, e^{i\omega t} \tag{2.2}$$

$$B_\phi = -\frac{p\pi m R_c^2}{\ell_c x'^2_{mn} r} \, B_0^* \, J_m(x'_{mn}\varrho) \, \sin(m\phi) \, \cos\left(\frac{p\pi z}{\ell_c}\right) \, e^{i\omega t} \tag{2.3}$$

$$E_z = 0 \tag{2.4}$$

$$E_r = i\omega \, \frac{m R_c^2}{x'^2_{mn} r} \, B_0^* \, J_m(x'_{mn}\varrho) \, \sin(m\phi) \, \sin\left(\frac{p\pi z}{\ell_c}\right) \, e^{i\omega t} \tag{2.5}$$

$$E_\phi = i\omega \, \frac{R_c}{x'_{mn}} \, B_0^* \, J'_m(x'_{mn}\varrho) \, \cos(m\phi) \, \sin\left(\frac{p\pi z}{\ell_c}\right) \, e^{i\omega t} \tag{2.6}$$

$$f_0^{\mathrm{TE}}(m,n,p) = c \cdot \sqrt{\left(\frac{x'_{mn}}{2\pi R_c}\right)^2 + \frac{1}{4}\left(\frac{p}{\ell_c}\right)^2} \tag{2.7}$$

Due to the electric boundary condition at the cavity end walls ($E_r = E_\phi = 0$, $p = 0$ results in all field components being zero in the above equations), the pursued ideal TE_{210} operating mode with a perfectly flat longitudinal electric field distribution is actually not a natural cavity mode but has to be created as a pseudo-mode from the TE_{211} mode by artificially raising the field level towards the electrode ends, which for example can be accomplished by fitting undercuts to the vane-ends (similar to the girder undercuts shown in Fig. 2.16). According to the radius dependence of the pillbox TE-mode frequencies, the resonance frequency of the basic 4-vane RFQ structure is practically determined by the tank radius, but also by the overall capacitance between the installed electrodes, which due to the corresponding significant reduction in frequency however also results in a smaller tank radius compared to the capacitively unloaded case in order to obtain the nominal resonance frequency.

After all, 4-vane structures are the most commonly used type of RFQ resonator for the frequency range above 200 MHz, thus being usually applied for the acceleration of light ions and especially protons [112]. Whereas even for higher operating frequencies up to and above 450 MHz, 4-vane resonators typically have reasonable transversal dimensions regarding the feasibility of construction, they also provide a comparatively high RF efficiency (as can also be seen in Fig. 2.28), which is because the distribution of the surface currents on the structure is very uniform. The typical mode spectrum of a 4-vane RFQ is shown in Fig. 2.15.
One major general problem for the RF design and tuning of 4-vane resonators arises from the fact that the TE_{210} operating mode is not the zero mode of the cavity and hence some of the existing dipole modes TE_{11p} ($p \geq 1$) might actually be close to the operating frequency. As the gap in frequency $\Delta f = f_{\mathrm{mn}(p+1)} - f_{\mathrm{mn}p} \propto (\ell_c \, f_{\mathrm{mn}p})^{-2}$ between consecutive mode orders p and $p+1$ is inversely proportional to the square of both cavity length ℓ_c and frequency $f_{\mathrm{mn}p}$ [54], the probability for a disturbance of the quadrupole field stability by the influence of dipole modes increases significantly with the RFQ length and operating frequency. Whereas

in a geometrically ideal resonator driven at the exact frequency of the quadrupole mode the influence of nearby dipole modes is typically negligible due to the small resonance bandwidths at high quality factors, in reality the field stability of 4-vane structures can be highly sensitive to errors of the dimensional machining or the positioning of the vanes. On the one hand the accordingly resulting requirement for very low manufacturing tolerances can thus lead to a cost-intensive production, whereas on the other hand constructive measures have to be implemented to compensate field errors or yield an artificial mode separation. Commonly used methods are the attachment of coupling rings between opposing vanes, the use of movable plunger tuners being positioned along the structure for adjusting the inductance in the quadrants, the mounting of dipole stabilizer rods inside the cavity and longitudinally dividing the resonator in segments that are resonantly coupled with each other [112, 113].

A modified variation of the original 4-vane structure is the so-called "4-vane with windows" RFQ [112, pp. 276 ff.], which is fitted with coupling windows in the vanes. By accordingly increasing the coupling between adjacent quadrants, this can significantly reduce the frequency of the quadrupole operating mode below that of the dipole modes and also results in smaller transversal tank dimensions. Taking this approach further, the vanes can also be completely replaced by radial stems that support the electrodes which are then in form of rods, with the resulting stem configuration being reminiscent of crossbar H-mode (CH) DTL structures.
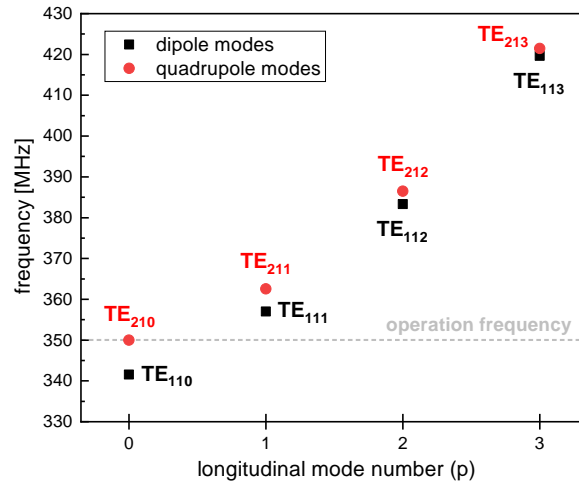

Figure 2.15: Mode spectrum of a 2 m long 350 MHz 4-vane RFQ.

2.2.2 IH

Similar to 4-vane structures, "interdigital" H-mode (IH-) RFQs also are cavity resonators, being operated in the TE_{110} dipole mode (also referred to as H_{110}-mode), the field distribution of which can be seen in Fig. 2.12. As shown in Fig. 2.16, the electrode mounting holders are attached interdigitally (*Latin*: "between fingers") to two opposite sides of the tank via so-called girders. Due to the oppositely oriented longitudinal magnetic fields in the half spaces of the transverse cavity cross-section, a charging current is induced from the electrode holders on one side of the cavity, over the tank wall, to the holders on the opposite side. In order to obtain a quadrupole potential distribution on the four electrode rods which are placed inside

the tank, each correspoding pair of opposite electrodes is connected to an opposite set of mounting holders and hence to a different charging polarity.
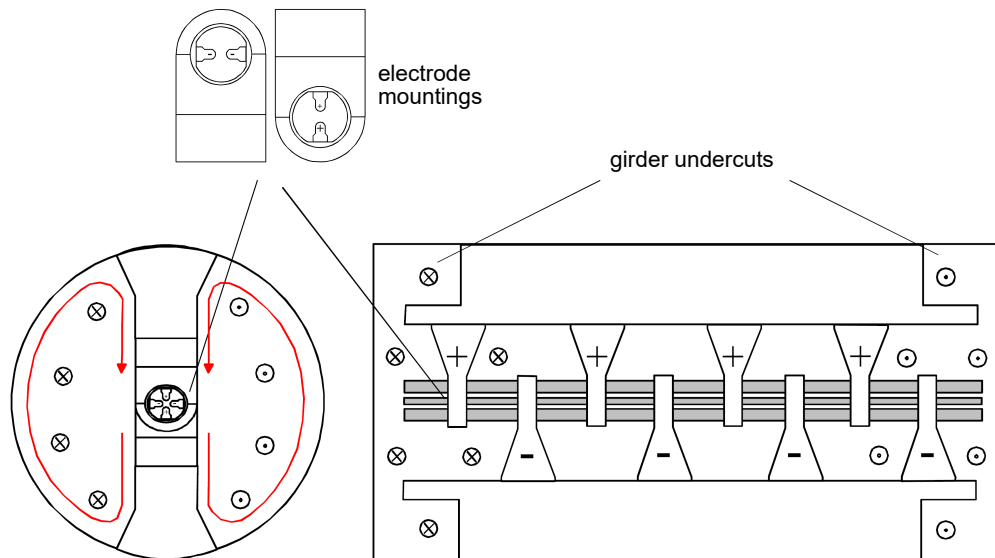
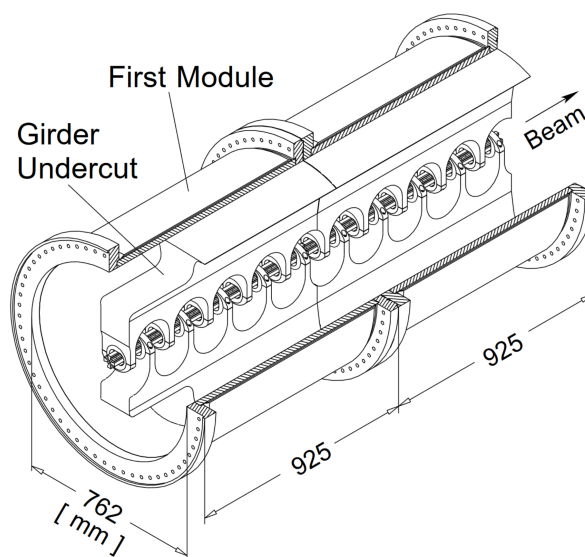**Figure 2.16:** Schematic construction and functional principle of an IH-RFQ[6].

Figure 2.17: Drawing of the first two out of ten modules of the 36 MHz IH-RFQ at the GSI HSI [115].

Because the length of the current path from one electrode pair to the other extends over half the tank circumference and is thus much longer than at 4-vane resonators, where the current only has to travel over one tank quadrant, IH-RFQs have comparatively small transverse dimensions. For this reason they are well suited for the low frequency range below 100 Hz, which makes them ideal structures for the acceleration of very heavy low-charged ion beams.

Again similar to 4-vane resonators, the distribution of the surface current and corresponding RF power losses is very homogeneous and a high RF efficiency is hence obtained. Due to the difference in length of the current paths to the vertically mounted electrodes, an electric dipole field emerges, which however results in a dipole ratio of typically less than 1 % as further discussed in [114], where also an analytic model for the calculation of the IH resonator properties is presented. A commonly applied method for the tuning of the field flatness is to fit undercuts to the girder ends, which leads to an increase of the local magnetic field density and thus higher charging currents to the outer electrode mounting holders.

In general, IH-type RFQs are far less common than 4-vane and 4-rod structures. Two examples are given by the 36 MHz HSI RFQ at GSI (see Fig. 2.17 and Fig. 2.10) [115, 37], as well as by the 101 MHz MAFF RFQ [114, 73].

2.2.3 4-Rods

The 4-rod RFQ whose basic structure and operating principle is depicted in Fig. 2.18 and Fig. 2.19, is a transmission-line type resonator that consists of a linear array of stems with each acting as a quarter-wave ($\lambda/4$)-resonator. However, the required height of the stems to accommodate a quarter-wave oscillation is significantly reduced due to the capacitive termination by the electrodes, as schematically shown in Fig. 2.33. Via the mutual capacitance at the intermediate electrode section and with the respective quarter-wave oscillations being in opposite phase, each pair of adjacent stems forms a separate resonant circuit, which is referred to as an "RF cell". While diagonally opposite quadrupole electrodes are connected to every second stem, respectively, providing the same polarity of charging current, the overall length of the current path in one RF cell is about half an RF wavelength, extending from one pair of electrodes via the stems and the tuning plate to the other (also see Fig. 2.20), with the zero point of the potential distribution being at the center of the tuning plate.
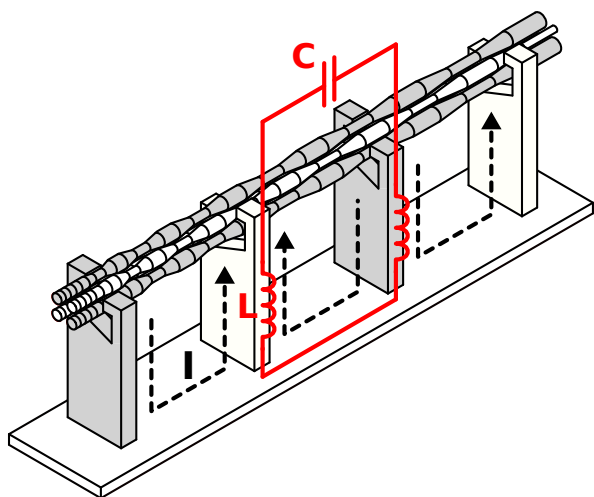

Figure 2.18: Current paths (black dashed lines) in a 4-rod RFQ and corresponding equivalent circuit diagram for one RF cell (red)[7].
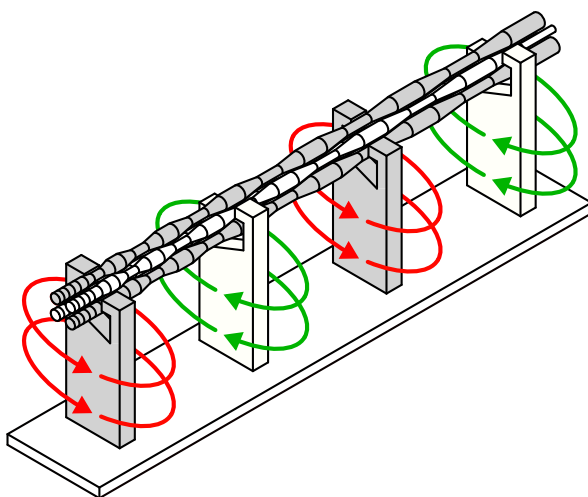
Figure 2.19: Orientation of the magnetic fields around the stems of a 4-rod RFQ[7].

---

[7]figure courtesy of A. Schempp

Since the entire charging current is concentrated on the stems and tuning plates, the resulting high surface current densities lead to increased ohmic losses and thus typically to a lower RF efficiency compared to cavity type resonators such as 4-vane or IH structures (see Fig. 2.28 for comparison). However, another consequence of being a transmission-line resonator is that the resonance frequency and RF efficiency barely depend on the geometry of the surrounding tank, provided that the tank walls are far enough away from the RF structure not to affect either inductance or capacitance. The length of the current path in each RF cell and hence its resonance frequency can simply be adjusted by changing the vertical position of the movable tuning plates between the stems, corresponding to a change in inductance.
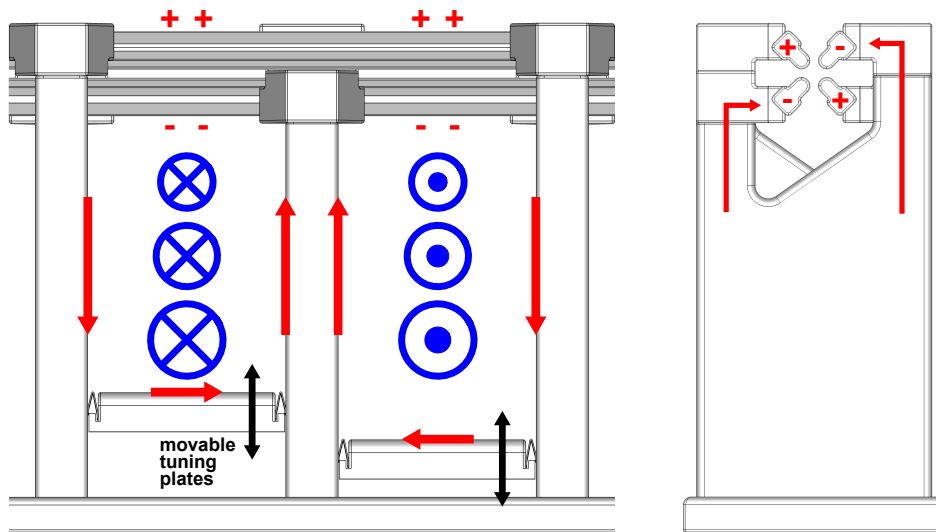

Figure 2.20: Magnetic field distribution between the stems of a 4-rod RFQ (blue) and charging currents to the electrode rods (red). Each pair of adjacent stems forms an RF cell, the inductance of which can be adjusted by movable tuning plates.

Eventually, the variation of the resonance frequency of an RF cell results in a change of the generated voltage amplitude at the respective cell electrode section, with an increase in frequency causing a decrease of the voltage amplitude and vice versa. After all, this leads to the characteristic tub-like shape of the untuned field flatness in 4-rod RFQs (see Fig. 6.17, but also section 2.3.4), since the surplus capacitance on the electrode overhangs of the RF end-cells lowers their RF resonance frequency, which in turn raises the voltage amplitude towards the electrode ends. Details on the properties of the longitudinal voltage distribution in 4-rod RFQs can be found in [116]. Due to the fact that the frequency and related field amplitude can be tuned independently for each RF cell after manufacturing and assembly of the RFQ structure, compared to almost all other conventional RFQ types the 4-rod resonator concept offers an outstanding flexibility of adjustment for reaching the nominal operating frequency and desired longitudinal voltage distribution. Even different sets of electrode rods with different modulation and therefore a different capacitance distribution can simply be retrofitted, with the rods typically being bolted to the stems. Due to accordingly low required manufacturing tolerances, 4-rod RFQs have comparatively cheap production costs.
While given the advantages discussed above of a flexible and simple frequency and field tuning mechanism as well as low acquisition costs, however, besides a generally higher power

consumption there are several additional problems specific to 4-rod structures: On the one hand, the inter-stem electrode rod sections are highly thermally loaded, especially at high RF duty cycles where adequately cooling must be provided, but also are prone to mechanical vibrations. Both problems gain in significance at lower operating frequencies and correspondingly longer inter-stem electrode sections. On the other hand, the intrinsically asymmetric geometry of the 4-rod structure causes two characteristic types of field errors, namely an electric dipole field component (see section 2.3.5) and longitudinal end-fields (see section 2.3.6). As a matter of fact, all of these problems have been subject to the studies for this thesis. Overall, the applicable frequency range of 4-rod type RFQs is considered to be limited to about 50 to 200 MHz due to the practicability of the required geometric dimensions of the stems and inter-stem electrode sections.
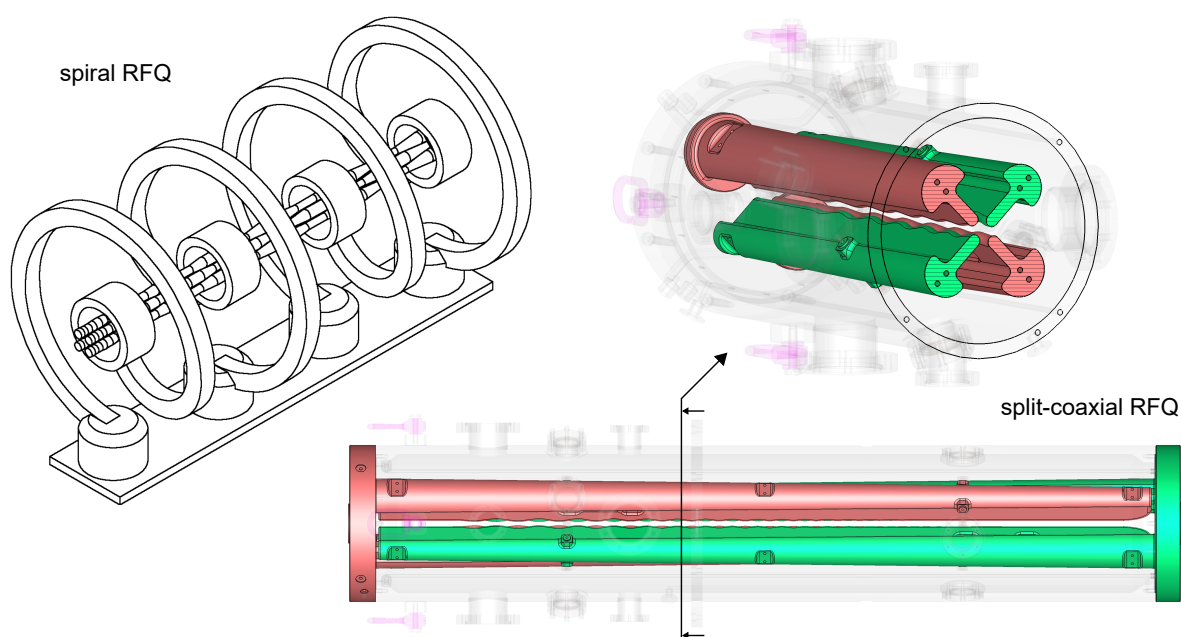
Figure 2.21: Schematic view of a spiral RFQ (*left*) [117] and the split-coaxial RFQ[8] for the IsoDAR RFQ-DIP (*right*, the components marked in red and green are connected to each other, respectively).

A variation of the original 4-rod concept is given by the spiral-RFQ (see Fig. 2.21), where basically the stems are formed as spiral arms in order to accommodate quarter-wave oscillations with larger wavelengths, thus allowing for very low operating frequencies of less than 30 MHz. A similar approach with the same objective is applied to the split-ring RFQ [65]. Another quarter-wave transmission-line RFQ resonator type for low-frequency applications is the so-called split-coaxial RFQ (Fig. 2.21), in which the quarter-wave oscillation extends over the entire length of the electrode rods.

Since the RF cells of the 4-rod RFQ form a chain of magnetically coupled single resonators, the typical mode spectrum of 4-rod type resonant structures can be derived from an analytical approach, considering each cell as an RLC circuit as schematically shown in Fig. 2.22.

---

[8]figure courtesy of Bevatech GmbH

With the coupling between adjacent cells being parameterized by the coupling factor k, which describes the mutual inductance $M = kL$ between two coupled inductances L, and ω_0 being the resonance frequency of the individual cells, the eigenmode frequencies ω_q of the coupled system are given by Eq. 2.8, following the derivation in [118].
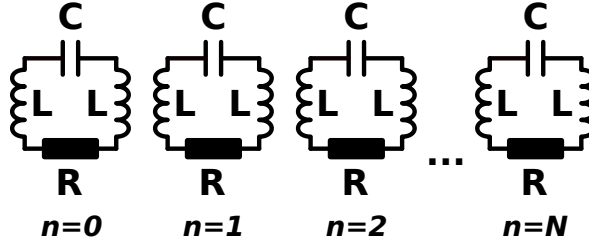

Figure 2.22: Chain of $N+1$ coupled resonant RLC circuits.

$$\omega_q^2 = \frac{\omega_0^2}{1 + k\,\cos\frac{\pi q}{N}} \qquad q = 0, ..., N \tag{2.8}$$

$$\Phi_q = \frac{\pi q}{N} \tag{2.9}$$

With a total number of $N+1$ RF cells, the eigenmodes with mode index $q = 0, ..., N$ of the coupled resonant system can also be classified by the phase $\Phi_q = 0...\pi$, according to Eq. 2.9. The 4-rod RFQ resonator with a number of $N+2$ stems is operated in the so-called π-0-mode, referring to a phase difference of π between the quarter-wave oscillations on adjacent stems to load the electrodes to the desired quadrupole potential and the RF cells oscillating in 0-mode ($\Phi_{q=0} = 0$) to obtain a homogeneous longitudinal potential distribution on the electrodes, as can be seen from Fig. 2.23. The corresponding dispersion relation is shown in Fig. 2.24, as is the simulated mode separation for a 2 m long 175 MHz 4-rod RFQ with 19 RF cells.
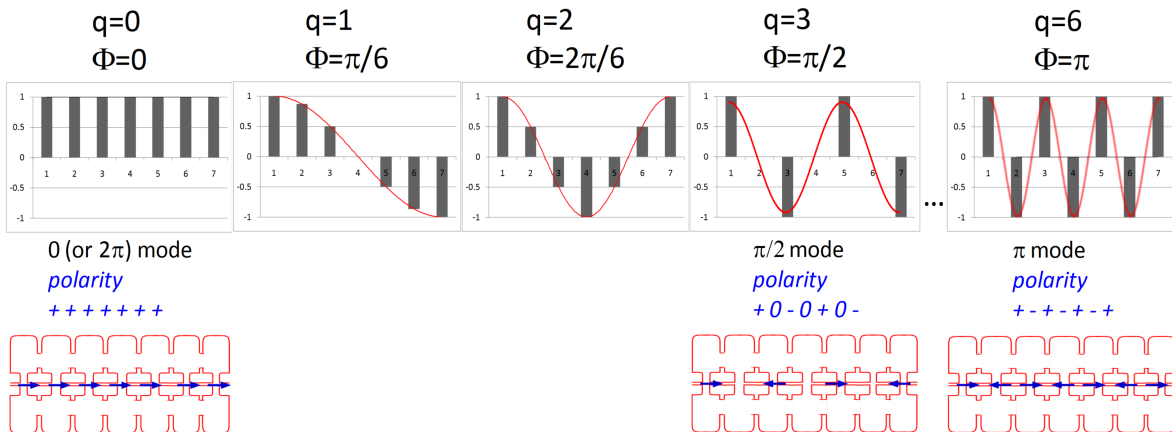

Figure 2.23: Mode spectrum of a seven-cell system of coupled resonators [118].
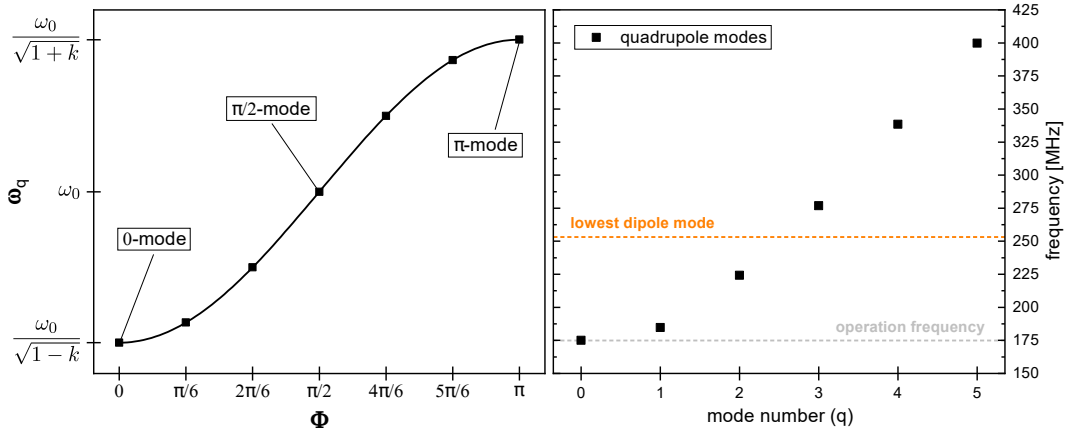
Figure 2.24: Dispersion relation of a seven-cell system of coupled resonators (*left*) and higher-order quadrupole modes in a 2 m long 175 MHz 4-rod RFQ with 19 RF cells (*right*).

2.2.4 Ladder

In contrast to the 4-rod structure, where each stem accommodates an RF quarter-wave oscillation, the ladder RFQ consists of a series of "ladder spokes", each acting as a half-wave resonator with the voltage antinode being located at the spoke center. As depicted in Fig. 2.26, every second spoke is connected to the same pair of opposite quadrupole electrodes and the charging mechanism as well as the mode of magnetic coupling between the RF cells constituted by adjacent spokes is similar to the 4-rod RFQ. Since due to the half-wave oscillation an overall larger volume is occupied with magnetic field around the ends of the spokes, the RF efficiency of ladder resonators is typically lower than of 4-rod structures. Also, the frequency and field tuning is not as flexible because usually the ladder structure is milled out of a solid copper block and the cell heights are basically fixed after manufacturing. However, due to the symmetric mounting of the electrode pairs on the spokes, there is no dipole component being generated.
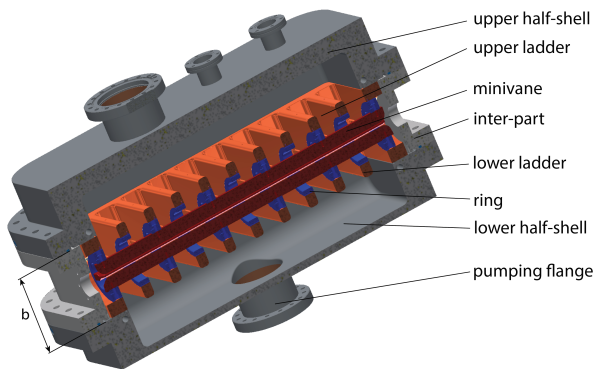

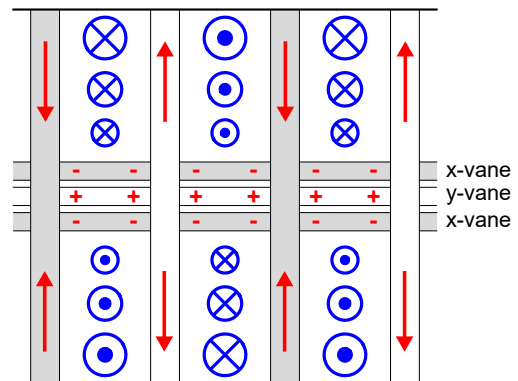**Figure 2.25:** Prototype model of the 325 MHz ladder-RFQ for the FAIR p-Linac [119].

Figure 2.26: Magnetic field distribution (blue) and corresponding charging currents (red) in a ladder structure (topview).

Similar to the case of IH-RFQs, also ladder structures are rare to find. However, two examples are given by the 101 MHz CERN Linac3-RFQ [75] and the newly developed 325 MHz ladder-RFQ for the FAIR p-Linac, a prototype of which is depicted in Fig. 2.25. Further details on ladder-RFQs are provided by [63].

2.3 Resonator Properties

In general, the RF performance of RFQ resonator structures can basically be characterized by the generated vane voltage U_0 in relation to the occurring power dissipation P_c with typical figures of merit being the resonator quality factor Q_0 and the shunt impedance R_{pL}. Besides that, the peak surface electric field on the electrodes, which relates to the probability for electric breakdowns and sparking, is usually specified in terms of the Kilpatrick limit E_K. Whereas the overall field distribution along the longitudinal axis of the quadrupole is described by the field flatness ϵ, typical field errors like the electric dipole component and longitudinal end-fields are quantified by the dipole ratio and the end-field voltage U_z, respectively. This section provides an overview and definitions of the basic RFQ resonator properties and describes methods for their experimental determination.

2.3.1 Quality Factor

The RF properties of an RFQ resonator can be described theoretically using an equivalent RLC circuit with a capacitance C and an inductance L, to which an ohmic resistance R is connected in parallel. Following Kirchhoff's voltage law $U_R + U_L + U_C = 0$, with $U_R = RI$, $U_L = L\dot{I}$ and $\dot{U}_C = I/C$, results in the differential equation of a damped harmonic oscillation as given in Eq. 2.10 with the damped resonance frequency ω_d (Eq. 2.11). By assuming a negligibly small ohmic resistance R, the expression finally reduces to the undamped resonance frequency $\omega_0 = \sqrt{1/LC}$, which is known as Thomson's formula.

$$\ddot{U} + \frac{R}{L}\dot{U} + \frac{1}{LC}U = 0 \tag{2.10}$$

$$\omega_d = \sqrt{\frac{1}{LC} - \frac{R^2}{4L^2}} \approx \omega_0 = \sqrt{\frac{1}{LC}} \tag{2.11}$$

A solution to Eq. 2.10 is provided by Eq. 2.12, with the voltage time constant $\tau_{\text{voltage}} = 2L/R$ denoting the time when the amplitude of the voltage $U(t)$ has reduced to $1/e$ of its initial value U_0. The stored energy $W(t)$ can thus be calculated according to Eq. 2.13 with the corresponding energy time constant $\tau_{\text{energy}} = \tau_{\text{voltage}}/2 = L/R$ and $W(\tau_{\text{energy}}) = W_0/e$.

$$U(t) = U_0\, e^{-t/\tau_{\text{voltage}}}\, e^{i\omega_0 t} \qquad (2.12) \qquad\qquad W(t) = W_0\left(\frac{U(t)}{U_0}\right)^2 \qquad (2.13)$$

From the energy time constant $\tau_{\text{energy}} = \tau$, the unloaded quality factor Q_0 is defined according to Eq. 2.14 [120, pp. 25 ff.]. Because the ratio L/R is equal to the stored energy $W = \frac{1}{2}LI_0{}^2$

divided by the power loss $P = RI_{\text{eff}}^2 = \frac{1}{2}RI_0{}^2$, the quality factor can also be expressed as stated in Eq. 2.15. Accordingly, Q_0 is inversely proportional to the energy loss TP during one RF period duration T and proportional to the number N of periods until the stored energy $W(t = NT) = W_0/e$ decreased to $1/e$ of its initial value.

$$Q_0 = \omega_0 \tau = \omega_0 \frac{L}{R} = \frac{1}{\omega_0 CR} = \frac{1}{R}\sqrt{\frac{L}{C}} \tag{2.14}$$

$$Q_0 = \frac{\omega_0 W}{P} = 2\pi \frac{W}{TP} = 2\pi N \tag{2.15}$$

The total amount W of stored energy inside an RFQ resonator can be calculated according to Eq. 2.16, considering the distribution of either the maximum magnetic or electric field ($\vec{H}_{\text{max}}(\vec{x})$ or $\vec{E}_{\text{max}}(\vec{x})$, respectively). The overall power dissipation P_{c} is given by Eq. 2.17 and depends mostly on the distribution of the magnetic field which induces eddy currents on the resonator surface S. At room temperature, the surface resistance $R_{\text{s}} = 1/(\sigma\delta) = \sqrt{\mu_0\omega/(2\sigma)}$ with the skin depth $\delta = \sqrt{2/(\sigma\omega\mu_0)}$ is proportional to the square root of the RF frequency ω and inversely proportional to the square root of the electrical conductivity σ [112, pp. 19 f.].

$$W = \frac{1}{2}\mu_0 \int_V |\vec{H}_{\text{max}}(\vec{x})|^2 \, dV = \frac{1}{2}\epsilon_0 \int_V |\vec{E}_{\text{max}}(\vec{x})|^2 \, dV \tag{2.16}$$

$$P_{\text{c}} = \frac{1}{2}R_{\text{s}} \int_S |\vec{H}_{\text{max}}(\vec{x})|^2 \, dA \tag{2.17}$$

Finally, the Fourier transform of $U(t)$ into the frequency domain $U(\omega)$ (Eq. 2.18) yields the root of a Lorentzian function and can be written as in Eq. 2.19 with $\Delta\omega = 2(\omega_0 - \omega)$ and $U_{\text{max}} = 2Q_0 U_0/(\omega_0\sqrt{2\pi})$. The corresponding function for the stored energy $W(\omega)$ is given by Eq. 2.20 with $W_{\text{max}} = \frac{1}{2}CU_{\text{max}}{}^2$ (also see [121, pp. 371 ff.]).

$$U(\omega) = \left| \frac{1}{\sqrt{2\pi}} \int_0^\infty U_0 \, e^{-t/\tau} \, e^{i\omega_0 t} \, e^{-i\omega t} \, dt \right| = \frac{2Q_0 U_0}{\omega_0\sqrt{2\pi}} \sqrt{\frac{1}{1 + 4Q_0{}^2 \left(\frac{\omega_0-\omega}{\omega_0}\right)^2}} \tag{2.18}$$

$$U(\omega) = \frac{U_{\text{max}}}{\sqrt{1 + Q_0{}^2 \left(\frac{\Delta\omega}{\omega_0}\right)^2}} \tag{2.19} \qquad W(\omega) = \frac{W_{\text{max}}}{1 + Q_0{}^2 \left(\frac{\Delta\omega}{\omega_0}\right)^2} \tag{2.20}$$

According to Eq. 2.21, the quality factor can thus also be determined from the voltage resonance curve $U(\omega)$ and equals the ratio of the resonance frequency ω_0 to the resonance width $\Delta\omega_{\text{-3 dB}}$ at an attenuation of the voltage amplitude by a factor of $1/\sqrt{2}$ ($\approx -3\,\text{dB}$), corresponding to the full width at half maximum of the energy resonance curve $W(\omega)$.

$$Q_0 = \frac{\omega_0}{\Delta\omega} \sqrt{\frac{U_{\text{max}}{}^2}{U(\omega)^2} - 1} = \frac{\omega_0}{\Delta\omega_{\text{-3 dB}}} \tag{2.21}$$
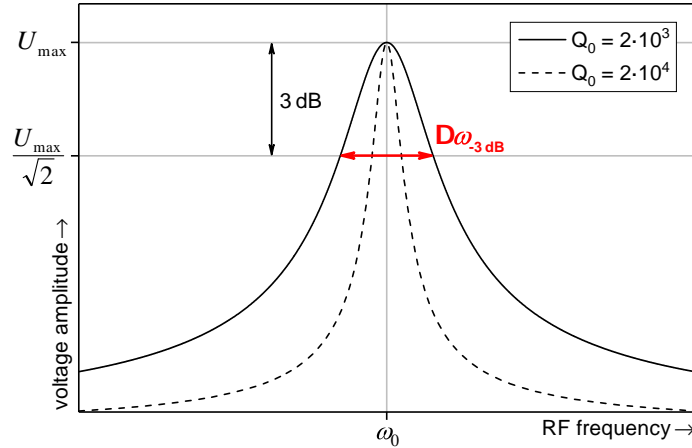
Figure 2.27: Resonance curves $U(\omega)$ of the voltage for different quality factors.

After all, an experimental determination of the quality factor can be achieved by measuring the resonance curve using a network analyzer and applying the 3 dB method as given by Eq. 2.21, provided that the resonance width $\Delta\omega_{\text{-3 dB}}$ is large enough to obtain adequate accuracy. Alternatively, also the time constant for the attenuation of the field amplitude can be measured, from which the quality factor $Q_0 = \omega_0 \tau_{\text{voltage}}/2$ can be derived according to Eq. 2.14. This however requires a pulsed RF signal. Regarding 4-rod RFQs, the value of the quality factor is typically in the range between $2 \cdot 10^3$ and $6 \cdot 10^3$, whereas 4-vane resonators usually have a higher quality factor that can exceed 10^4.

$$Q_{\text{L}} = \frac{\omega_0 W}{P_{\text{total}}} \qquad (2.22) \qquad\qquad Q_0 = Q_{\text{L}} \cdot (1 + \beta_{\text{e}} + \beta_{\text{t}}) \qquad (2.23)$$

$$\beta_{\text{e}} = \frac{Q_0}{Q_{\text{e}}} = \frac{P_{\text{e}}}{P_{\text{c}}} \qquad (2.24) \qquad\qquad \beta_{\text{t}} = \frac{Q_0}{Q_{\text{t}}} = \frac{P_{\text{t}}}{P_{\text{c}}} \qquad (2.25)$$

Considering that in an experimental setup there is also RF power dissipated in the power coupler (emitted power P_{e}) and through the pickup antennas (transmitted power P_{t}), the total power loss amounts to $P_{\text{total}} = P_{\text{c}} + P_{\text{e}} + P_{\text{t}}$, from which the loaded quality factor Q_{L} is defined according to Eq. 2.22. With the analogously defined external quality factors ($Q_{\text{e}} = \omega_0 W/P_{\text{e}}$, $Q_{\text{t}} = \omega_0 W/P_{\text{t}}$) and the coupling parameters β_{e} and β_{t} (Eq. 2.24 and Eq. 2.25), the unloaded quality factor is hence given by Eq. 2.23. In general, this reduces to $Q_0 \approx Q_{\text{L}} \cdot (1 + \beta_{\text{e}})$, assuming that the RF pickup is dimensioned and positioned so that coupling is only very weak ($\beta_{\text{t}} \approx 0$). After all, the unloaded quality factor Q_0 can be determined from a measurement of the loaded quality factor Q_{L} by two methods: On the one hand, the power coupler can be adjusted to very weak coupling ($\beta_{\text{e}} \approx 0$), in which case the unloaded and loaded quality factors are approximately equal ($Q_0 \approx Q_{\text{L}}$). However, in reality this method suffers from the fact that the reduction of the coupling β_{e} is limited by the minimum required signal amplitude in order to still allow a decent measurement of the resonance curve $U(\omega)$. Therefore, the determined values of Q_0 tend to be smaller than their actual magnitude. On the other hand, a more precise determination can be obtained by calculating the coupling parameter β_{e} from the ratio $P_{\text{r}}/P_{\text{f}}$ of reflected to forward power according to Eq. 2.26[9] with Γ being the reflection coefficient [120, pp. 92 ff.]. In case of critical coupling with $\beta_{\text{e}} = 1$ and $P_{\text{r}} = 0$, the unloaded

---

[9]The upper signs of $\pm/\mp$ correspond to overcoupling ($\beta_{\text{e}} > 1$), whereas the lower signs reflect the undercoupled case ($\beta_{\text{e}} < 1$). A method to determine whether coupling is strong or weak is described in [120, pp. 101 ff.].

quality factor is then simply given by $Q_0 = 2 \cdot Q_{\mathrm{L}}$.

$$\frac{P_{\mathrm{r}}}{P_{\mathrm{f}}} = |\Gamma|^2 = \left(\frac{\beta_{\mathrm{e}} - 1}{\beta_{\mathrm{e}} + 1}\right)^2 \quad \Longrightarrow \quad \beta_{\mathrm{e}} = \frac{1 \pm \sqrt{\frac{P_{\mathrm{r}}}{P_{\mathrm{f}}}}}{1 \mp \sqrt{\frac{P_{\mathrm{r}}}{P_{\mathrm{f}}}}} \tag{2.26}$$

2.3.2 Shunt Impedance

Whereas the quality factor Q_0 describes efficiency of energy storage within the resonator, the shunt impedance indicates the power consumption required to generate voltage between the electrodes. According to Eq. 2.27, the shunt impedance R_{p} is thus defined by the amplitude of the vane voltage U_0 and the power loss P_{c}. With $Q_0 = \omega_0 W/P_{\mathrm{c}}$ (Eq. 2.15) and the stored energy being $W = \frac{1}{2}CU^2$, the shunt impedance can also be expressed as function of the quality factor and the overall capacitance [63, pp. 31 f.], which is mainly determined by the geometry and length of the electrodes. Since accordingly the power consumption scales with the electrode length L, the shunt impedance is typically specified by the length-normalized expression R_{pL} (Eq. 2.28), which refers to the power loss per length P_{c}/L.

$$R_{\mathrm{p}} = \frac{{U_0}^2}{P_{\mathrm{c}}} = \frac{2Q_0}{\omega_0 C} \qquad (2.27) \qquad R_{\mathrm{pL}} = \frac{{U_0}^2}{P_{\mathrm{c}}/L} = \frac{{U_0}^2}{P_{\mathrm{c}}} \cdot L = R_{\mathrm{p}} \cdot L \qquad (2.28)$$
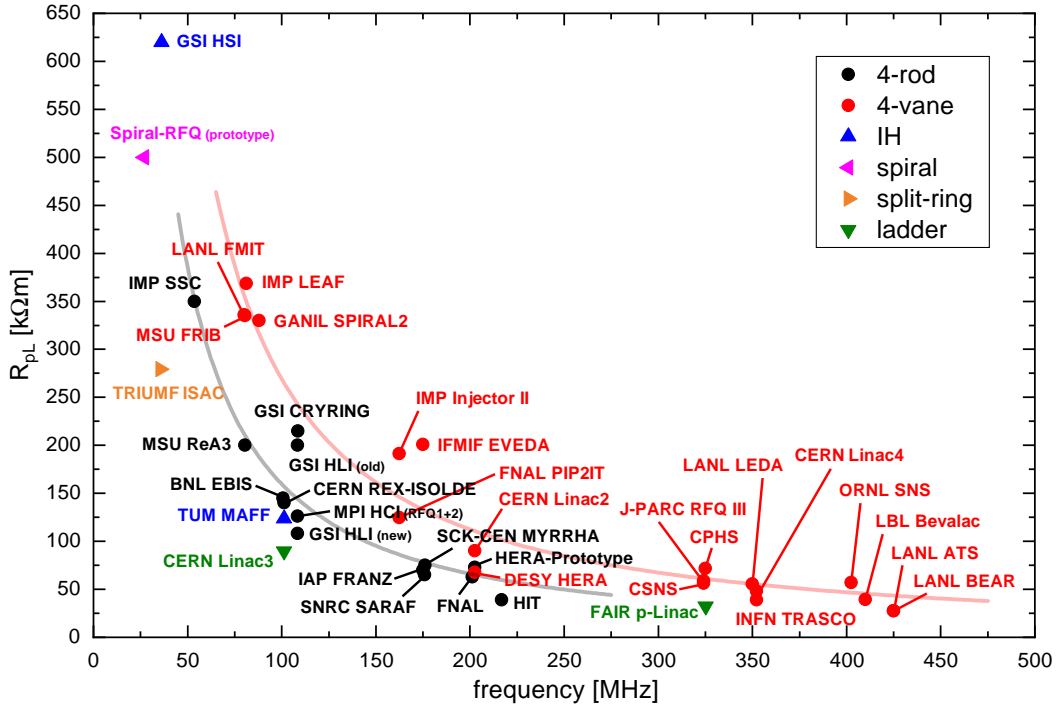

Figure 2.28: Shunt impedance of some of the RFQs from Tab. 2.1 plotted against the operating frequency (the fitted curves reflect the basic relation of $R_{\mathrm{pL}} \propto 1/P_{\mathrm{c}} \propto 1/R_{\mathrm{s}} \propto 1/\sqrt{f}$).

According to [110, pp. 31 ff.], there are several different methods for the experimental determination of the shunt impedance, which are briefly described in the following:

Capacitance Calculation

Based on Eq. 2.27, the shunt impedance can in principle be determined from a measurement of the quality factor Q_0, given the knowledge of the capacitance C. Regarding the simple case of flat electrodes without modulation, as typically found on RFQ prototype structures for RF tests, the electrodes can approximately be treated as ideal cylindrical rods in order to obtain an analytical solution for the calculation of the capacitance of the RFQ as given by Eq. 2.29 [122, pp. 13 ff.].

$$C_{\mathrm{RFQ}} = \frac{2\pi\epsilon}{\ln\left(\frac{r_{\mathrm{aperture}}}{r_{\mathrm{electrode}}} + 1\right)} \cdot L \tag{2.29}$$

Alternatively, the capacitance matrix which contains the separate capacitances C_{ij} between the potentials of the electrodes and ground can be numerically determined by an electrostatic solver such as CST EM Studio [123]. The total capacitance of a system with four potentials $V_{1...4}$, as depicted in Fig. 2.29, and a 4×4 capacitance matrix can then be calculated according to Eqs. 2.30–2.33 [116, pp. 73 f.]. Since the quadrupole is due to its potential symmetry basically just a two-potential system ($V_1 = V_3 = -V_2 = -V_4$), the capacitance matrix reduces to a size of 2×2 and the capacitance of the RFQ can be calculated according to Eq.2.34[10].
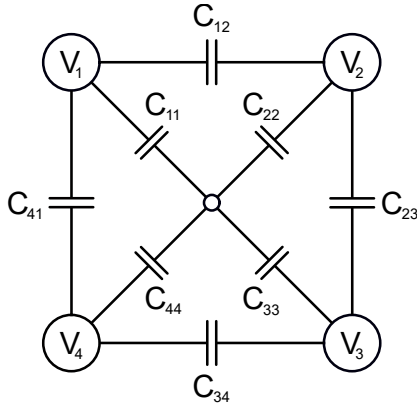

$$C_{\mathrm{A}} = C_{12} + C_{23} + C_{34} + C_{14} \tag{2.30}$$

$$C_{\mathrm{B}} = C_{11} + C_{33} \tag{2.31}$$

$$C_{\mathrm{C}} = C_{22} + C_{44} \tag{2.32}$$

$$C_{\mathrm{total}} = C_{\mathrm{A}} + \frac{C_{\mathrm{B}}C_{\mathrm{C}}}{C_{\mathrm{B}} + C_{\mathrm{C}}} \tag{2.33}$$

$$C_{\mathrm{RFQ}} = C_{12} + \frac{C_{11}C_{22}}{C_{11} + C_{22}} \tag{2.34}$$

Figure 2.29: Capacitances between the quadrupole electrodes and ground.

Perturbation Capacitance Method

In general, the capacitance of an RFQ structure can be derived from a measurement of the frequency shift Δf which is caused by a perturbation capacitor with a capacitance of ΔC that is placed between the electrodes. From Thomsons's formula (Eq. 2.11), the detuned resonance frequency f^* and the relative frequency shift $\Delta f/f$ can be calculated according to Eq. 2.35. As shown in Eq. 2.36, the relative frequency shift can alternatively be calculated by using Slater's perturbation theorem, considering a perturbation capacitance $\delta C \ll C$ that is

---

[10]if the simulation boundaries are located very far from the capacitive structure, this reduces further to $C_{\mathrm{RFQ}} = C_{12}$ as $C_{11}, C_{22} \to 0$

much smaller than the overall capacitance. Since in general the measurement of the frequency provides a value that is averaged over time, for the calculation of the deviation in electric field energy $\Delta W_{\text{electric}} = \frac{1}{2}\delta C\, U_{0,\text{eff}}{}^2$ the effective voltage $U_{0,\text{eff}} = U_0/\sqrt{2}$ must hence be used [124, pp. 36 ff.]. After rearranging Eq. 2.35 or Eq. 2.36 to $C(\Delta f)$ and inserting this into Eq. 2.27, the shunt impedance can finally be calculated from Eq. 2.37, given the measured values of Δf and Q_0 as well as an accurate knowledge of the perturbation capacitance ΔC (or δC).

$$f^* = \frac{1}{2\pi\sqrt{L(C+\Delta C)}} \quad \Longrightarrow \quad \frac{\Delta f}{f_0} = \frac{f_0 - f^*}{f_0} = 1 - \frac{1}{\sqrt{1 + \frac{\Delta C}{C}}} \tag{2.35}$$

$$\frac{\Delta f}{f_0} \approx \frac{\Delta W_{\text{electric}}}{W} = \frac{\frac{1}{2}\delta C\, U_{0,\text{eff}}{}^2}{W} = \frac{\frac{1}{4}\delta C\, U_0{}^2}{\frac{1}{2}C U_0{}^2} = \frac{\delta C}{2C} \tag{2.36}$$

$$R_{\text{p}} = \frac{Q_0(1-\kappa)}{\pi f_0 \kappa \Delta C} \approx \frac{2 Q_0 \Delta f}{\pi f_0{}^2 \delta C} \quad \text{with} \;\; \kappa = \left(1 - \frac{\Delta f}{f_0}\right)^2 \tag{2.37}$$

Because according to Eq. 2.36 the measured frequency shift $\Delta f(z)$ is proportional to the square of the electrode voltage $U_0(z)^2$ at the longitudinal position z where the perturbation capacitor is placed, the field flatness (see section 2.3.4) can be determined from measurements with the perturbation capacitance as described by Eq. 2.38. The mean value $\langle\sqrt{\Delta f_n}\rangle$ relates to a number n of equidistantly distributed measuring positions along the entire electrode length (typically corresponding to the centers of the RF cells).

$$\epsilon(z) = \frac{\sqrt{\Delta f(z)} - \langle\sqrt{\Delta f_n}\rangle}{\langle\sqrt{\Delta f_n}\rangle} \tag{2.38}$$

Gamma Spectroscopy

A method for the direct experimental determination of the electrode voltage U_0 is provided by the possibility to measure the energy spectrum of the emitted gamma radiation during RF operation [124, pp. 38 ff.]. Since the radiation is caused by bremsstrahlung of electrons that were emitted on the electrodes by field emission and accelerated towards an respectively adjacent electrode, the maximum electrode voltage U_0 is hence given by the maximum measured energy $E_{\gamma,\text{max}}$ in the gamma spectrum according to Eq. 2.39, provided that the time required for the electrons with maximum energy gain to reach the adjacent electrode is less than half an RF period duration. With the knowledge of U_0 and the power consumption P_{c} during operation, the shunt impedance can again be calculated according to Eq. 2.27.

$$U_0 = E_{\gamma,\text{max}}/e \tag{2.39}$$

R/Q-Comparison

According to Eq. 2.40, the shunt impedance can also be determined from the comparison to the simulated R/Q-value, which as so-called geometric impedance is independent of the frequency ω_0, the surface resistance R_{s} and the linear dimensions of the resonator structure

[120, pp. 31 f.]. Because the quality factor Q_0 of the real resonator can be measured comparatively precisely, and the (simulated) R/Q-value has no dependence on the magnitude of the power loss, the numerical calculation of which is known from experience to be subject to large errors of up to 25 %, especially regarding transmission-line resonators, eventually the method of R/Q-comparison provides a very reliable and simple possibility for an accurate determination of the shunt impedance.

$$\frac{R_{\text{p,measured}}}{Q_{0,\text{measured}}} = \frac{R_{\text{p,simulated}}}{Q_{0,\text{simulated}}} \implies R_{\text{p}} = \frac{R_{\text{p,simulated}}}{Q_{0,\text{simulated}}} \cdot Q_{0,\text{measured}} \tag{2.40}$$

2.3.3 Bravery Factor (Kilpatrick's Criterion)

After all, the magnitude of the electric field between metal electrodes of an RF resonator is limited by the occurrence of electric breakdowns and sparking [112, pp. 163 f.]. In order to obtain a criterion for the corresponding threshold of the surface electric field, empirical studies on the conditions for sparking were conducted [125], from which the so-called Kilpatrick limit E_{K} was derived as given by the formula for $f(E_{\text{K}})$ according to Eq. 2.41 ($E_0 = 1\,\text{MV/m}$). Since the found limit is valid over a large range of vacuum pressure from 10^{-3} to $10^{-7}\,\text{mbar}$ and also different electrode materials only cause minor deviations, the Kilpatrick limit $E_{\text{K}}(f)$ thus only has a dependence on the RF frequency f, which is depicted in Fig. 2.30.
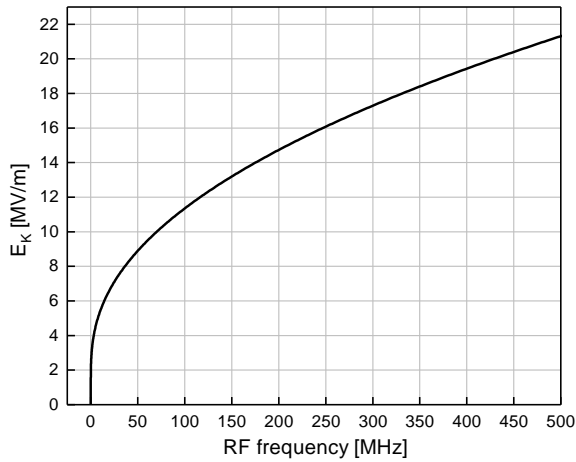
$$f = 1.64\,\text{MHz} \cdot \left(\frac{E_{\text{K}}}{E_0}\right)^2 e^{-8.5\,\frac{E_0}{E_{\text{K}}}} \tag{2.41}$$

$$b = \frac{E_{\text{s}}}{E_{\text{K}}} \tag{2.42}$$

Figure 2.30: Kilpatrick limit E_{K} as function of the RF frequency.

The fact that the formula for the Kilpatrick limit has a striking similarity to the Fowler-Nordheim equation for the calculation of the emitted current density due to electron field emission [112, p. 162] is not surprising, considering that the mechanism of sparking is presumably triggered by field emission which is intensified by secondary electron emission from incident energetic ions. The maximum energy of ions, originating from the cavity surface or the residual gas, is mainly limited by the timespan available for their acceleration in the RF field, which is determined by the applied RF frequency.

Whereas theoretically no sparking at all should occur at magnitudes of the surface electric field below the Kilpatrick limit, beyond that, the rate of sparking events increases exponentially with increasing field amplitude. In fact, the actual threshold for sparking is however determined by the condition of the electrode surface, concerning surface defects and contamination, and can thus be raised by the process of RF conditioning. With today's standards for surface preparation and clean vacuum systems, the threshold for sparking and RF breakdowns can be raised well above the comparatively conservative Kilpatrick limit by a factor of up to 2.0. The ratio of the maximum design surface electric field E_s to the Kilpatrick limit E_K is also referred to as bravery factor b (Eq. 2.42). In the end, the choice of the bravery factor determines the minimum applicable electrode radius, which in turn determines the electrode capacitance (see Eq. 2.29) and therefore also affects the shunt impedance of the RFQ.

2.3.4 Field Flatness

A requirement which is typically posed by the applied beam dynamics design concept of RFQs is a constant longitudinal distribution of the electrode vane voltage $U_\mathrm{vane}(z)$, which in case of 4-rod RFQs is given when each RF-cell of the resonator structure has the same resonance frequency. In the untuned case with all tuning plates being at the same height, the longitudinal voltage distribution of 4-rod structures has a characteristic tub-like shape (see [116, pp. 43 ff.] and [126]). This is mainly due to the additional capacitance of the electrode overhangs, which reduces the resonance frequency of the RF end-cells. Besides that, the local electrode voltage is also affected by the deviation of the capacitance due to the electrode modulation, which varies gradually along the beam axis. In order to characterize the longitudinal voltage distribution in an RFQ, the relative field flatness $\epsilon(z)$ is defined as given by Eq. 2.43. From the difference between the maximum and minimum relative field flatness, the absolute field flatness $\Delta\epsilon_\mathrm{max}$ is defined (Eq. 2.44), which is commonly considered as a figure of merit for the uniformity of the longitudinal voltage distribution. An experimental technique for measuring the distribution of the electric field in an RF resonator is provided by the well-established bead-pull measurement method as explained in the following.

$$\epsilon(z) = \frac{U_\mathrm{vane}(z) - \langle U_\mathrm{vane} \rangle}{\langle U_\mathrm{vane} \rangle} = \frac{|\vec{E}(z)| - \langle |\vec{E}| \rangle}{\langle |\vec{E}| \rangle} \tag{2.43}$$

$$\Delta\epsilon_\mathrm{max} = \epsilon_\mathrm{max} - \epsilon_\mathrm{min} \tag{2.44}$$

Bead-Pull Measurement Method

The frequency detuning of an RF cavity due to the field perturbation by an inserted spherical bead, whose diameter is small in comparison to the RF wavelength, is given by Eq. 2.45 with the bead volume ΔV_bead, the total stored energy W inside the resonator cavity and the unperturbed electric and magnetic field amplitude E and H, respectively, at the spatial position of the bead [112, pp. 165 ff.]. This relation can be derived either from Slater's perturbation theorem according to [127] or from the Boltzmann-Ehrenfest adiabatic theorem as shown in [128]. For a dielectric bead material with a relative magnetic permeability close to 1 ($\mu_\mathrm{r} \approx 1$), the resulting frequency shift $\Delta\omega_0$ is hence only proportional to the square of the electric field

magnitude at the position $\vec{x}$ of the bead in the cavity, which finally allows to determine the field distribution $E(\vec{x})$ from measurements of the corresponding frequency shifts $\Delta\omega_0(E(\vec{x}))$.

$$\frac{\Delta\omega_0}{\omega_0} = -\frac{3\Delta V_{\text{bead}}}{4W}\left(\frac{\epsilon_{\text{r}}-1}{\epsilon_{\text{r}}+2}\epsilon_0 E^2 + \frac{\mu_{\text{r}}-1}{\mu_{\text{r}}+2}\mu_0 H^2\right) \overset{\mu_{\text{r}}=1}{=} -\frac{3\Delta V_{\text{bead}}}{4W}\frac{\epsilon_{\text{r}}-1}{\epsilon_{\text{r}}+2}\epsilon_0 E^2 \quad (2.45)$$

However, due to the requirement for a small dimensioned bead, the resulting frequency detuning is hence very low, which eventually results in a poor measuring accuracy. After all, a quantity that can be measured more accurately is the phase shift $\Delta\phi$ between the emitted and transmitted RF signals, which for small values relates to the frequency detuning $\Delta\omega_0$ as given by Eq. 2.46 [128]. In principle, the absolute value of the electric field amplitude $E(\Delta V_{\text{bead}}, \epsilon_{\text{r}}, Q_{\text{L}}, W, \Delta\phi)$ can thus be calculated from a measurement of the phase shift according to Eq. 2.47, given the knowledge of the bead properties (ΔV_{bead}, ϵ_{r}) as well as of the resonator parameters (Q_{L}, W). Also, the proportionality $E \propto \sqrt{\tan(|\Delta\phi|)}$ allows to determine the relative field distribution without requiring information on the bead itself.
In an experimental setup, the bead is usually fixed on a nylon thread that moves through the inside of the resonator cavity by being pulled by a stepper motor.

$$\tan(\Delta\phi) = 2Q_{\text{L}}\frac{\Delta\omega_0}{\omega_0} = -Q_{\text{L}}\frac{3\Delta V_{\text{bead}}}{2W}\frac{\epsilon_{\text{r}}-1}{\epsilon_{\text{r}}+2}\epsilon_0 E^2 \quad (2.46)$$

$$E = \sqrt{\frac{2W}{3Q_{\text{L}}\epsilon_0\Delta V_{\text{bead}}}\frac{\epsilon_{\text{r}}+2}{\epsilon_{\text{r}}-2}\cdot\tan(|\Delta\phi|)} \quad \propto \quad \sqrt{\tan(|\Delta\phi|)} \quad (2.47)$$

2.3.5 Dipole Ratio

To obtain an ideal electric quadrupole field distribution in the area between the electrode vane tips, the electric potentials on the four electrodes, with adjacent electrodes being oppositely charged, must have the same absolute value. In case of an asymmetry between the potentials on the upper and the bottom electrode pair ($|V_{\text{top}}| \neq |V_{\text{bottom}}|$, see Fig. 2.32), the quadrupole symmetry of the electric field is violated and the position of the beam axis, where the transversal electric field components $E_{x,y}$ are zero, is effectively shifted downwards from the geometrical center of the quadrupole as depicted in Fig. 2.34. This corresponds to an unwanted dipole component of the electric field distribution that can be quantified by the value of the dipole ratio, for which a number of different definitions is given in [129].
Fig. 2.31 shows the dipole ratio according to the definitions provided by Eq. 2.48 and Eq. 2.49, as well as the displacement of the beam axis as function of the ratio $V_{\text{top}}/V_{\text{bottom}}$.

$$\text{dipole ratio}_1 = \frac{|\vec{E}_{\text{top}}| - |\vec{E}_{\text{bottom}}|}{|\vec{E}_{\text{top}}|} \quad (2.48) \qquad \text{dipole ratio}_2 = \frac{|\vec{E}_{\text{top}}| - |\vec{E}_{\text{bottom}}|}{\frac{|\vec{E}_{\text{top}}|+|\vec{E}_{\text{bottom}}|}{2}} \quad (2.49)$$
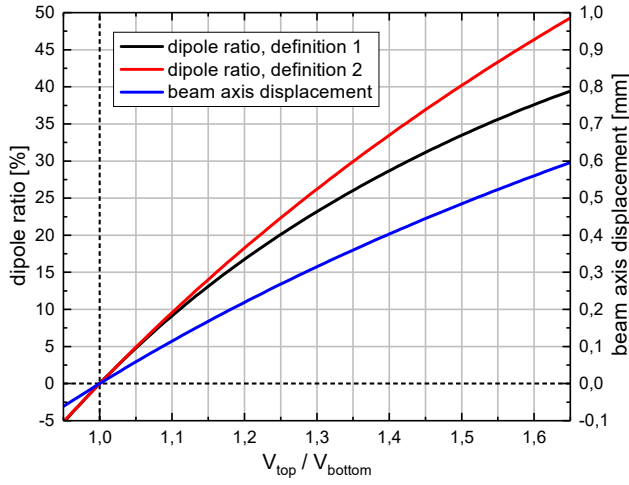
Figure 2.31: Dipole ratio and beam axis displacement as function of the asymmetry between the potentials on the upper and bottom electrode pair, characterised by the ratio $V_{\text{top}}/V_{\text{bottom}}$ ($r_{\text{electrode}}/r_{\text{aperture}} = 0.81$).
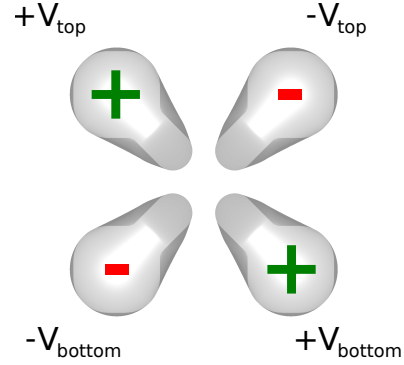

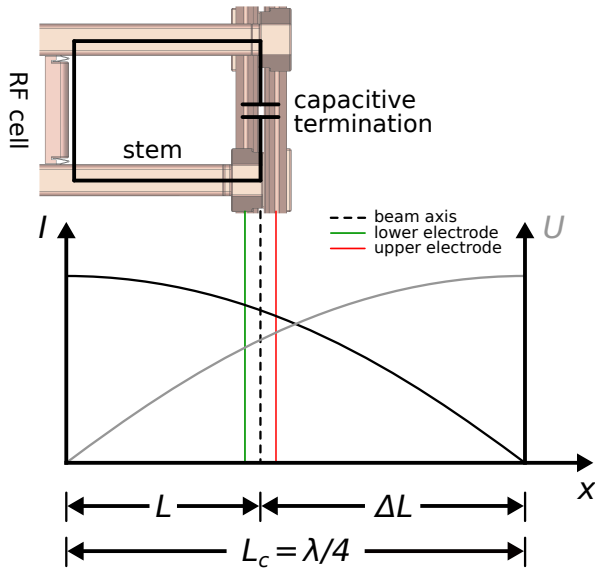**Figure 2.32:** Definition of the potentials on the upper and bottom electrodes.

Figure 2.33: Voltage and current distribution on one RFQ stem, corresponding to a quarter-wave resonator (courtesy of A. Schempp).
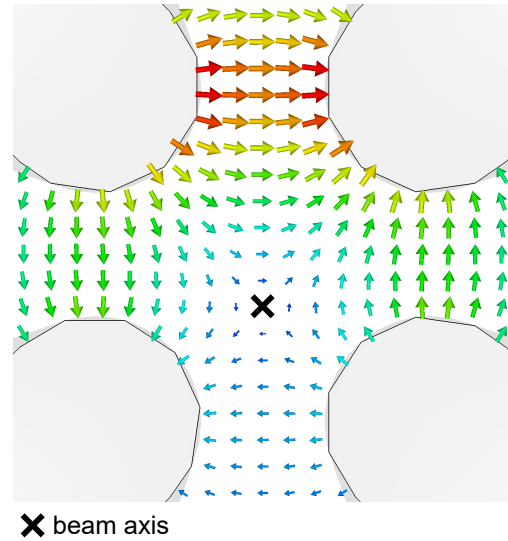

Figure 2.34: Displacement of the beam axis from the geometrical center (exaggerated depiction).
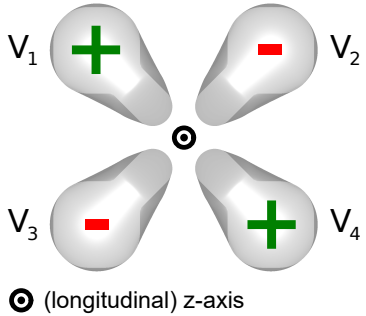
Whereas in 4-vane RFQs an electric dipole component can emerge from the proximity of the TE_{110} dipole mode to the TE_{210} quadrupole operation mode, in 4-rod RFQs the dipole is a consequence of the design inherent geometrical asymmetry of the stems, with the upper and lower electrode rods being mounted at different height. Because the current path from the stems to the lower electrodes is hence shorter than to the upper electrodes, the absolute

value of the potential at the lower electrode pair is less compared to the upper electrode pair, where the voltage curve $U(x)$ of the quarter-wave oscillation along the stem has its maximum (see Fig. 2.33). For higher RF frequencies the difference in length between the current paths to the lower and upper electrodes increases relative to the shorter wavelength and, accordingly, also the dipole ratio increases to typical values in the range of up to $40\,\%$ for what is conventionally considered the upper frequency range of 4-rod RFQs around $200\,\mathrm{MHz}$.

In principle, the dipole ratio can be experimentally determined either from the measurement of the electric field magnitudes $|\vec{E}_{\mathrm{top}}|$ and $|\vec{E}_{\mathrm{bottom}}|$ between the upper and lower electrode pair, respectively, using the bead-pull method as described in section 2.3.4, or by measuring the respective electrode voltages $U_{\mathrm{top}} = 2V_{\mathrm{top}} \propto |\vec{E}_{\mathrm{top}}|$ and $U_{\mathrm{bottom}} = 2V_{\mathrm{bottom}} \propto |\vec{E}_{\mathrm{bottom}}|$, which are proportional to the electric field magnitudes, using a perturbation capacitor according to section 2.3.2.

2.3.6 Longitudinal End-Field

At each of the four electrode ends of the quadrupole the generated electric field has a longitudinal component, with the fields associated with the single electrode ends exactly canceling each other out on the beam axis, given the case of a perfect quadrupolar potential symmetry and hence satisfying Eq. 2.50. If this condition is not fulfilled, in total an on-axis longitudinal field component emerges that alters the beam input and output properties at the low- and high-energy end of the RFQ, respectively. Typically, the longitudinal end-fields in 4-rod structures are caused by the corresponding potentials on the pairs of opposite electrodes being unequal, $|V_1| = |V_4| \neq |V_2| = |V_3|$, due to the difference in current path length to the long- and short-overhang ends (see chapter (6) for a detailed explanation and analysis). However, an electric dipole component resulting in $|V_1| = |V_2| \neq |V_3| = |V_4|$ does not affect the on-axis longitudinal end-field, since the potentials of horizontally adjacent electrodes balance each other out, as $|V_1| + |V_2| = |V_3| + |V_4| = 0$.

$$\sum_{n=1}^{4} V_n \stackrel{!}{=} 0 \qquad (2.50)$$

$$U_z = \int_{-\infty}^{z_{\mathrm{shaper}}} E_z \, dz \qquad (2.51)$$

Figure 2.35: General definition of the potentials at the electrode ends.

In general, the magnitude of the longitudinal end-field component at the low-energy RFQ-end can be characterized according to Eq. 2.51 by the on-axis voltage ranging from infinity to the beginning of the shaper-section at $z = z_{\mathrm{shaper}}$. From this, an "end-field ratio" U_z/U_{vane} can be defined, describing the magnitude of the longitudinal end-field independent of the applied vane voltage U_{vane}.

2.4 Beam Dynamics & Electrode Design

As discussed in the previous, the RFQ concept provides the possibility for simultaneous strong transversal focusing, longitudinal (adiabatic) bunching and acceleration of a low-velocity charged particle beam. After all, especially bunching can be a delicate procedure, given the high sensitivity of space-charge dominated beams to perturbations of the beam density, which eventually might result in emittance growth that affects the beam quality along the entire linac. However, since in each of the typically hundreds of modulation cells the corresponding aperture a (relating to the strength of transverse focusing), the modulation m (setting the longitudinal field strength) and the synchronous phase ϕ_s (setting the ratio between bunching and acceleration) can be adjusted individually, the effects on the beam can be applied very smoothly, thus allowing to yield very low emittance growth and high transmission [57, 54]. Whereas the simulation of the particle beam dynamics along the RFQ is based on the potential function for the area between the electrode vane tips and the corresponding equations of motion, special software codes are used to determine sets of modulation parameters by which the desired beam output properties are achieved. This section provides a brief description of the derivation of the well-known two-term potential function, the equations of motion commonly used in RFQ beam dynamics codes (which take the form of Mathieu's differential equation) and the famous LANL four-section electrode design procedure, which is the basis of the RFQ design-code PARMTEQ[11].

2.4.1 Two-Term Potential Function

The homogeneous form of the wave equation for the electric field component of a propagating electromagnetic wave in charge-free space (Eq. 2.52) can be derived directly from the Maxwell-Faraday equation and Ampère's circuital law. Considering a harmonic time dependence of the electric field $\vec{E}(t) = \vec{E_0}\sin(\omega t + \phi)$ yields a Helmholtz type equation (Eq. 2.53) with $k = \omega/c = 2\pi/\lambda$, which eventually can be written as in Eq. 2.54 [112, pp. 167 f.].

$$\Delta\vec{E} - \frac{1}{c^2}\frac{\partial^2\vec{E}}{\partial t^2} = 0 \qquad (2.52) \qquad\qquad \Delta\vec{E} + k^2\vec{E} = 0 \qquad (2.53)$$

$$\frac{\partial^2\vec{E}}{\partial x^2} + \frac{\partial^2\vec{E}}{\partial y^2} + \frac{\partial^2\vec{E}}{\partial z^2} + \left(\frac{2\pi}{\lambda}\right)^2\vec{E} = 0 \qquad (2.54)$$

When the wavelength λ is large compared to the spatial dimensions of the field variations, the Helmholtz equation finally reduces to a Laplace type equation as given in Eq. 2.55. This so-called quasistatic approximation basically corresponds to neglecting the inductive influence by the time-varying magnetic field according to the Maxwell-Faraday equation. Regarding the region between the electrode vane tips of the RFQ, which constitutes the capacitive component of the RF structure, the quasistatic approximation applies accurately since the ratio of the RF wavelength to the aperture diameter is typically in the range of 10^3.

$$\Delta\vec{E} \cong 0 \qquad (2.55) \qquad\qquad \nabla\cdot\vec{E} = -\Delta\Phi = 0 \qquad (2.56)$$

---

[11]**P**hase **A**nd **R**adial **M**otion in **T**ransverse **E**lectric **Q**uadrupole Linacs

In general, the electric field $\vec{E}(\vec{x})$ also has to satisfy the basic vector cross-product relationship $\nabla \times (\nabla \times \vec{E}) = \nabla(\nabla \cdot \vec{E}) - \Delta \vec{E}$. However, with the quasistatic approximation $\Delta \vec{E} \cong 0$ (Eq. 2.55) and Gauss's law for charge-free space ($\nabla \cdot \vec{E} = 0$), this reduces to $\nabla \times (\nabla \times \vec{E}) = 0$. Eventually, this is satisfied for the electric field being derived from a scalar potential as $\vec{E} = -\nabla \Phi$, due to the vector identity $\nabla \times \nabla \Phi = 0$. Again from Gauss's law it follows that also the potential $\Phi(\vec{x})$ has to satisfy a Laplace type equation according to Eq. 2.56.

$$\Phi(r, \theta, z, t) = U(r, \theta, z) \, \sin(\omega t + \phi) \tag{2.57}$$

$$\Delta U = \frac{1}{r} \frac{\partial}{\partial r} \left(r \frac{\partial U}{\partial r} \right) + \frac{1}{r^2} \frac{\partial^2 U}{\partial \theta^2} + \frac{\partial^2 U}{\partial z^2} = 0 \tag{2.58}$$

According to Eq. 2.57, the scalar potential $\Phi(r, \theta, z, t)$ in the cylindrical coordinates r, θ and z can be written as the product of the static potential $U(r, \theta, z)$ and a time-dependent term $\sin(\omega t + \phi)$. The corresponding Laplace equation is given by Eq. 2.58 and can finally be solved by applying the separation of variables approach ($U(r, \theta, z) = R(r) \cdot \Theta(\theta) \cdot Z(z)$), resulting in the general solution for the potential function as shown in Eq. 2.59, with $m + n = 2p + 1$ ($p = 0, 1, 2, ...$), the intervane voltage V, $k = 2\pi/\beta\lambda$, and the modified Bessel function $I_{2n}(x) = i^{-2n} \cdot J_{2n}(x)$ of the order $2n$ with $J_{2n}(x)$ being the corresponding Bessel function of the first kind as given by Eq. 2.60. A detailed derivation can be found in [130].

$$U(r, \theta, z) = \frac{V}{2} \left(\sum_n A_{0n} \, r^{2n} \cos(2n\theta) + \sum_n \sum_m A_{mn} \, I_{2n}(mkr) \cos(2n\theta) \cos(mkz) \right) \tag{2.59}$$

$$J_a(x) = \sum_{b=0}^{\infty} \frac{(-1)^b}{b! \, \Gamma(b + a + 1)} \left(\frac{x}{2} \right)^{2b+a} \quad \text{with} \quad \Gamma(b + a + 1) = \int_0^{\infty} y^{b+a} \, e^{-y} \, \mathrm{d}y \tag{2.60}$$

To simplify the infinite series expansions, the general potential function is typically reduced to lower orders for the calculation of RFQ beam dynamics. The solution of the lowest orders for each series, corresponding to the so-called two-term potential function, is shown in Eq. 2.61. Whereas the first term resembles a transverse quadrupole potential, the second term represents the longitudinal potential distribution, with the accordingly titled focusing parameter A_{01} and accleration parameter A_{10} being defined by the electrode geometry.

$$U(r, \theta, z) = \frac{V}{2} \left(A_{01} \, r^2 \cos(2\theta) + A_{10} \, I_0(kr) \cos(kz) \right) \tag{2.61}$$

Eventually, A_{01} and A_{10} as given by Eq. 2.63 and Eq. 2.64, respectively, can be calculated from the condition of the potential $U(r, \theta, z)$ being constant along the electrode vane tips as described by Eq. 2.62, with the minimum cell aperture a and the electrode modulation factor m as defined in section 2.1 and shown in Fig. 2.4.

$$U(a, 0, 0) = U\left(m \cdot a, 0, \frac{\beta\lambda}{2} \right) = \frac{V}{2} \tag{2.62}$$

$$A_{01} = \frac{1}{a^2} \frac{I_0(ka) + I_0(mka)}{m^2 I_0(ka) + I_0(mka)} \tag{2.63}$$

$$A_{10} = \frac{m^2 - 1}{m^2 I_0(ka) + I_0(mka)} \tag{2.64}$$

Finally, from the two-term potential function given by Eq. 2.61, the corresponding electric field components in Cartesian coordinates can be calculated by derivation, as indicated in Eqs. 2.65–2.67:

$$E_x = -\frac{\partial U}{\partial x} = -V A_{01} x - V A_{10} I_1(kr) \frac{xk}{2r} \cos(kz) \tag{2.65}$$

$$E_y = -\frac{\partial U}{\partial y} = V A_{01} y - V A_{10} I_1(kr) \frac{yk}{2r} \cos(kz) \tag{2.66}$$

$$E_z = -\frac{\partial U}{\partial z} = \frac{V}{2} A_{10} k I_0(kr) \sin(kz) \tag{2.67}$$

In modern beam dynamics codes, typically higher-order potential terms are used to achieve an increased accuracy of the field calculation with respect to higher-order multipole field components arising from the use of a circular vane tip profile instead of the ideal hyperbolic shape. For instance, the PARMTEQM code applies an eight-term potential function [131].

2.4.2 Equations of Motion in the RFQ

The basic equation of motion in each Cartesian direction $\kappa = x, y, z$ as given by Eqs. 2.69–2.71 can be obtained by inserting Eqs. 2.65–2.67 including the time-dependent term $\sin(\omega t + \phi)$ into the general form of Eq. 2.68, with the particle charge q and mass m. Also, the modified Bessel functions can be approximated by $I_0(kr) \approx 1$ and $I_1(kr) \approx kr/2$ for small arguments.

$$\frac{\mathrm{d}^2 \kappa}{\mathrm{d}t^2} - \frac{q}{m} E_\kappa = 0 \tag{2.68}$$

$$\frac{\mathrm{d}^2 x}{\mathrm{d}t^2} + x \left(\frac{qV}{m} A_{01} + \frac{qV k^2}{4m} A_{10} \cos(kz) \right) \sin(\omega t + \phi) = 0 \tag{2.69}$$

$$\frac{\mathrm{d}^2 y}{\mathrm{d}t^2} + y \left(-\frac{qV}{m} A_{01} + \frac{qV k^2}{4m} A_{10} \cos(kz) \right) \sin(\omega t + \phi) = 0 \tag{2.70}$$

$$\frac{\mathrm{d}^2 z}{\mathrm{d}t^2} - \frac{qV k}{2m} A_{10} \sin(kz) \sin(\omega t + \phi) = 0 \tag{2.71}$$

By introducing the normalized independent variable τ with $2\pi\tau = kz + \phi = \omega t + \phi$, the transverse equations of motion can be written in standard notation as given by Eq. 2.72 and

Eq. 2.73, corresponding to Mathieu type equations, with the focusing factor B (Eq. 2.74) and the RF defocusing factor Δ_{RF} (Eq. 2.75) [130]. Whereas the focusing factor $B \propto V A_{01} \propto V/a^2$ increases with the value of applied intervane voltage and with smaller aperture, the RF defocusing factor $\Delta_{\mathrm{RF}} \propto \sin\phi$ is typically <1, corresponding to a defocusing effect, since a negative phase ϕ is required to obtain stable longitudinal bunch motion. As shown in Fig. 2.36, with an increasingly negative value of the RF defocusing factor Δ_{RF}, the focusing factor B has to be increased accordingly to maintain transverse stability.

$$\frac{\mathrm{d}^2 x}{\mathrm{d}\tau^2} + \left(B \sin(2\pi\tau) + \Delta_{\mathrm{RF}} \right) \cdot x = 0 \tag{2.72}$$

$$\frac{\mathrm{d}^2 y}{\mathrm{d}\tau^2} + \left(-B \sin(2\pi\tau) + \Delta_{\mathrm{RF}} \right) \cdot y = 0 \tag{2.73}$$

$$B = \frac{qV\lambda^2}{mc^2} A_{01} \tag{2.74} \qquad\qquad \Delta_{\mathrm{RF}} = \frac{q}{m} \frac{V\pi^2 \sin\phi}{2c^2\beta^2} A_{10} \tag{2.75}$$
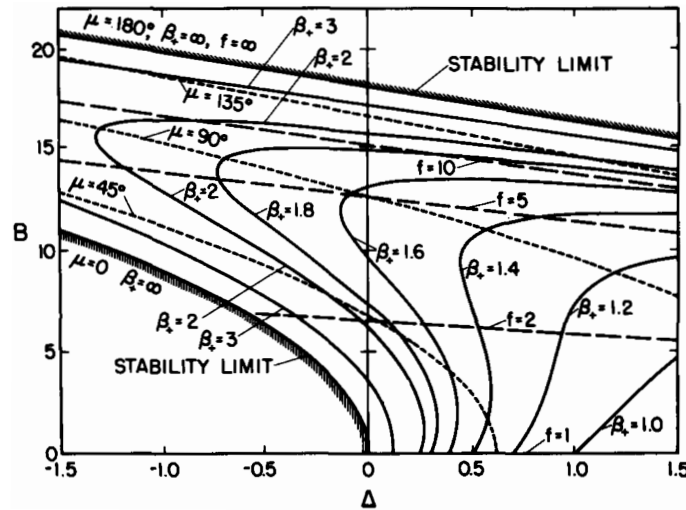
Figure 2.36: Transverse stability diagram for an RFQ, with the abscissa given by the RF defocussing factor Δ_{RF} and the ordinate being the focusing factor B [132].

By integrating over the longitudinal time-dependent electric field component $E_z \sin(\omega t + \phi)$ (see Eq. 2.67), the energy gain ΔW in one RFQ cell can be calculated according to Eq. 2.76. With the phase spread $\Delta\phi = \phi - \phi_s$ and energy spread $\Delta W = W - W_s$ relating to the synchronous phase ϕ_s and energy W_s, the basic equations of synchrotron motion can be written as in Eq. 2.77 and Eq. 2.78 [130].

$$\Delta W = \int\limits_0^{\beta\lambda/2} q\, E_z(0,0,z)\, \mathrm{d}z = \frac{qV\pi\cos\phi}{4} A_{10} \tag{2.76}$$

40

$$\frac{\mathrm{d}\Delta\phi}{\mathrm{d}\tau} = -\frac{2\pi\Delta W}{mc^2\beta_{\mathrm{s}}^2} \tag{2.77}$$

$$\frac{\mathrm{d}\Delta W}{\mathrm{d}\tau} = A_{10}\,\frac{qV\pi}{2}\left(\cos\phi - \cos\phi_{\mathrm{s}}\right) \tag{2.78}$$

This set of equations results in the longitudinal phase space trajectories typical for low-beta structures, as shown in Fig. 2.37. Whereas particles within the phase space "bucket", that is delimited by the separatrix, undergo stable synchrotron oscillations around the synchronous particle, all outside particles will lose synchronicity with the acceleration by the RF field. The size of the bucket is determined by the synchronous phase ϕ_{s} and ranges from zero (for $\phi_{\mathrm{s}} = 0$, resulting in maximum energy gain ΔW) to 360° (for $\phi_{\mathrm{s}} = -90°$, resulting in zero energy gain). A more descriptive explanation of the concept of phase focusing is provided by [111, chapter 3].
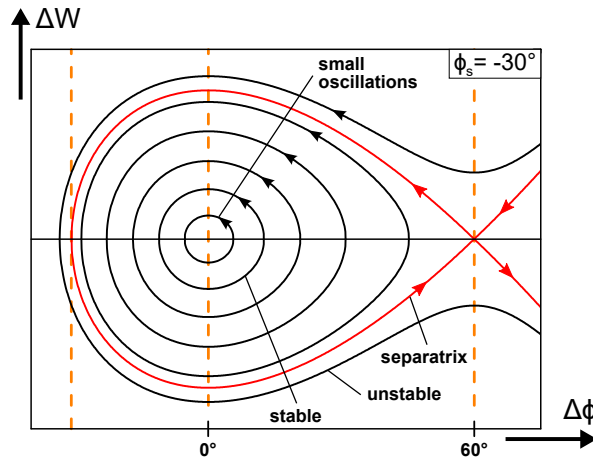
Figure 2.37: Longitudinal stability diagram for a synchronous phase of $\phi_{\mathrm{s}} = -30°$ [111].

2.4.3 LANL Four-Section Design

The LANL Four-Section Procedure (FSP) is a strategy to determine a set of electrode modulation parameters for a number of n RFQ cells (minimum cell apertures a_n, modulation factors m_n and cell lengths $\ell_{c,n}$) to achieve bunching and acceleration of a beam that is characterized by its input energy, input emittance, mass-to-charge ratio and current, for obtaining the nominal output beam parameters with a pre-determined RF operating frequency. While the Four-Section Procedure was already applied to design the proof-of-principle RFQ at LANL at the end of the 1970s [132], it is still implemented in the RFQ code PARMTEQ(M) today. One of the main principles followed by the method is to keep the charge density in the beam as constant as possible during the process of bunching in order to avoid emittance growth due to the effect of space charge, especially regarding high-current beams. After all, for the process of "adiabatic" bunching, the synchronous phase ϕ_{s} has to be gradually adjusted, so that the geometric bunch length remains constant with increasing beam energy, while the center-to-center bunch distance increases, corresponding to a bunching in phase.

A characteristic feature of the Four-Section Procedure is that the total number of RFQ cells is subdivided into four sections with each having a dedicated function [110, 63]:

- The first section, to which the DC beam is injected from the LEBT, is the so-called **radial matcher**, with the purpose to radially and transversally capture the beam. This is accomplished by applying a synchronous phase of $\phi_\mathrm{s} = -90°$ (maximum bucket size) and a large aperture radius at the first cell of up to 10 times the regular value of a, to which the aperture reduces until the end of the matcher section. As shown in Fig. 2.38, the focusing strength B accordingly increases almost linearly due to its $1/a^2$-dependency. The typical length of the radial matcher is about 4 to 10 cells ($\beta\lambda/2$).

- In the **shaper** section, a smooth pre-bunching is initiated by very slowly increasing the modulation (from $m = 1$) as well as the synchronous phase (from $\phi_\mathrm{s} = -90°$ (linearly) to about $-70°$). In the classic FSP, the focusing factor B remains constant from the shaper to the end of the RFQ.

- In the **gentle buncher** the beam is adiabatically bunched as described above. By the end of the buncher section, the synchronous phase has reached its maximum value in the range of $\phi_\mathrm{s} = -30°$ and also the modulation factor is raised to its maximum value (typically to around 2). Eventually, the end of the gentle buncher is a crucial point regarding the current limit of the RFQ, due to the aperture a being minimal and a still comparatively low beam velocity.

- In the **accelerator** section, the modulation m, aperture a and synchronous phase ϕ_s are kept constant at the respective values from the end of the buncher section. Here, a major part of the acceleration is achieved until the nominal output energy is finally reached.

However, over the years successful attempts have been made to further modify the longitudinal evolution of the beam design parameters $B(z)$, $m(z)$, and $\phi_\mathrm{s}(z)$, with benefits for the achievable RFQ length or the reduction of emittance growth [133].
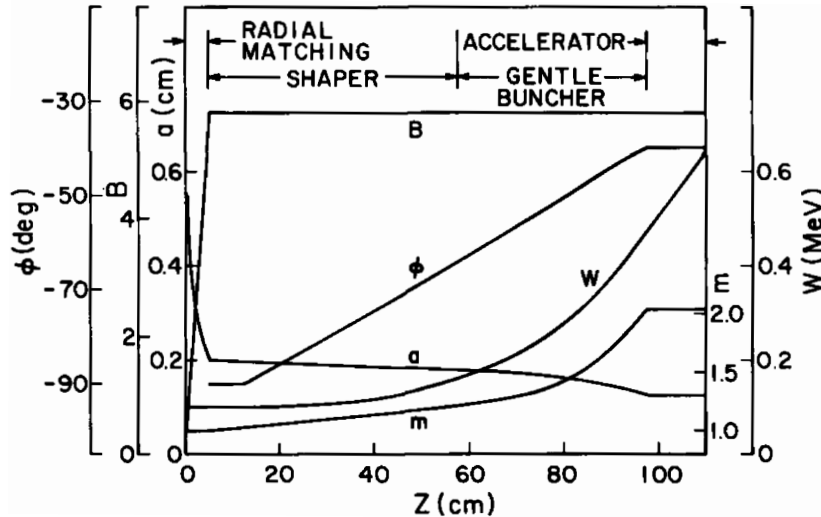
Figure 2.38: Beam dynamics design parameters of the 425 MHz LANL POP-RFQ, implementing the four-section design procedure [132].

(3) Mechanical Analysis of the 108 MHz 4-Rod RFQ at the HLI

The currently operated HLI-RFQ was commissioned at GSI in 2010 [78] as a replacement for the original RFQ [80], which was installed at the HLI during its construction in 1991 [40] and successfully operated for about 20 years. The original 4-rod RFQ with a design frequency of 108.5 MHz and a length of 3 m was capable of accelerating heavy ions with a mass-to-charge ratio of up to 8.5 (U^{28+}) from 2.5 keV/u to 300 keV/u at duty cycles from 25 % for $A/z = 8.5$ up to 50 % for $A/z = 1$. Within the scope of the CW upgrade program for the HLI [41], another 4-rod RFQ was designed and manufactured with the aim of providing CW capability for $A/z = 6$ and allowing pulsed operation with a duty cycle of 50 % up to $A/z = 8.5$ [134]. However, during commissioning and operation of the new RFQ two major issues became apparent [135], limiting the achievable performance and severely impeding stable operation:
(1) The structure is highly thermally sensitive and the resulting deviations of the resonance frequency occur suddenly and are of significant magnitude, even for very small changes of thermal load. This affects the frequency tuning with the plunger tuner, the control response and movement of which is slow compared to the timescale of the thermal detuning.
(2) During pulsed operation, there is severe power reflection with a modulated time structure. Besides limiting the achievable RF amplitude due to the high amount of power being reflected to the transmitter, this also poses another problem for the plunger tuner controller, which relies on the phase difference between forward and reflected power.
Modulated power reflection was already observed at the previously decommissioned original HLI-RFQ [136, 137]. At that time, it was suspected that the source of the modulated reflection were mechanical vibrations of the long electrode overhang segments. Therefore, the electrode rods had been additionally mechanically modified and stiffened, which lead to a mitigation of the reflected power as well as its modulation and improved operational stability. After the mechanical behavior of the newly installed RFQ during pulsed operation was analyzed based on observations of the RF signals, which is restricted to the timespan of the RF pulses, more sophisticated measurements of the electrode vibrations were conducted at GSI using a laser vibrometer [138]. This was followed by a structural-mechanical analysis based on simulations done at IAP [139] using CST Studio Suite [123] and ANSYS Workbench [140]. Besides details on the RFQ design and operating experience, the results of the analyses from the mechanical measurements and simulations are discussed in this chapter[1], as well as the results of simulations for the investigation of the thermal sensitivity.

3.1 Design Properties

The now existing 4-rod HLI-RFQ had been designed at IAP [142, 134] and manufactured by NTG Neue Technologien GmbH [58]. The electrodes with an approximate length of 2 m are mounted on 12 stems at a distance of 173 mm and a beam axis height from the bottom panel

---

[1]as published in [141]

43

of 162 mm (see Fig. 3.1 and Fig. 3.3). The 11 tuning plates are contacted with the stems by a solid silver sheet as conductor, which is pressed against the stem by wedges and a steel spring[2] (see [134, Figs. 7.8–7.10]). Given the design power consumption during CW operation, the thermal load per length amounts to 30 kW/m. All parts of the RFQ (stems, electrodes, tuning plates, plunger tuner and coupling loop) are directly water cooled, which requires a total of 72 cooling water connections [78]. The assembled RFQ tank is shown in Fig. 3.2.

In order to be compatible with the designated power amplifier, the RFQ was designed under the guideline of a power restriction to 60 kW. Necessarily, the overall capacitance had to be kept low, resulting in a thin profile of the electrode rods which have an almost rectangular shape with edge lengths of approximately 15×10 mm as shown in Fig. 3.3. The RF properties and basic geometric parameters of the HLI-RFQ are summarized in Tab. 3.1. The beam dynamics parameters are listed in Tab. 3.2.
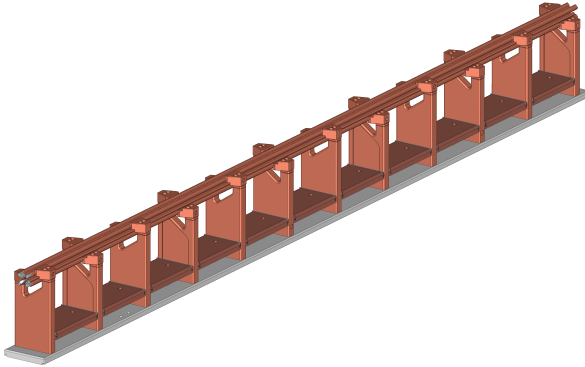
Figure 3.1: CAD model of the existing RFQ structure which was installed at the HLI in 2010.

Figure 3.2: HLI-RFQ tank during assembly at GSI [78].

RF frequency [MHz]	108.408
intervane voltage (cw) [kV]	55
intervane voltage (pulsed) [kV]	78
duty factor (pulsed) [%]	≤ 50
power (cw) [kW]	60
power (pulsed) [kW]	120
$r_{\text{electrode}}$ / r_{aperture}	0.8
shunt impedance [kΩm]	108
quality factor	3300
electrode length [m]	1.99
number of stems	12
stem distance [mm]	173
beam axis height [mm]	162
stem height [mm]	143
stem thickness [mm]	20
stem width [mm]	90

Table 3.1: RF and mechanical design properties of the HLI-RFQ[3].

mass-to-charge ratio (cw)	≤ 6
mass-to-charge ratio (pulsed)	≤ 8.5
injection energy [keV/u]	2.5
extraction energy [keV/u]	300
input beam current [mA]	≤ 5
transmission (5 mA) [%]	96
transverse acceptance [π mm mrad]	≥ 200
$\epsilon_{\text{in}}^{\text{transversal, n. rms}}$ [π mm mrad]	0.1
$\epsilon_{\text{out}}^{\text{transversal, x, n. rms}}$ [π mm mrad]	0.102
$\epsilon_{\text{out}}^{\text{transversal, y, n. rms}}$ [π mm mrad]	0.098
$\epsilon_{\text{out}}^{\text{longitudinal, rms}}$ [π MeV deg]	0.05
output energy spread [keV/u]	± 3
output phase spread [deg]	± 20
number of cells	177
minimum aperture [mm]	1.98
maximum modulation	1.97

Table 3.2: Beam dynamics parameters of the HLI-RFQ[3].

---

[2]based on the mechanism applied to the SARAF-RFQ [143]
[3]information taken from [78], [144], [134] and [142]
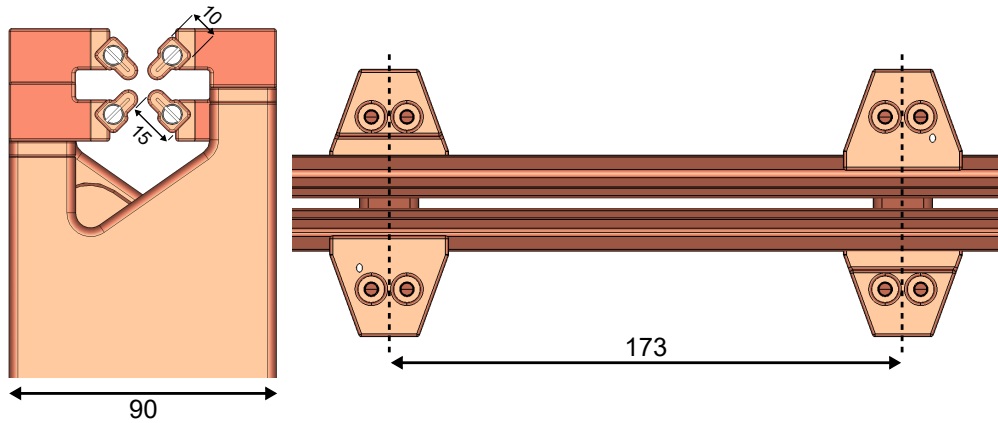
Figure 3.3: Geometry of the HLI-RFQ structure (dimensions in mm).

3.2 Operating Experience & RF Observations

This section provides a summary of the operating experience and RF observations by GSI on the existing HLI-RFQ, as presented in [78] and [135] where further information are given.

During commissioning of the new RFQ in 2010, beam tests were performed with measurements of the emittances, bunch shape, current and energy at different locations of the HLI beamline. By measuring the beam parameters before the RFQ entrance and behind the exit, the predicted performance regarding transmission and output beam quality could be demonstrated. After achieving optimum matching of the input beam into the RFQ and adjusting the default settings for the HLI beamline components, beam times with low mass-to-charge ratio ions and thus moderate RF power levels could be operated without obvious problems. The originally installed spring contacts for contacting the tuning plates with the stems showed damages or even were destroyed by impact of heat[4] at average RF power levels $< 30\,\mathrm{kW}$. In order to enable safe routine operation of the RFQ, a modified contact mechanism as mentioned in section 3.1 was applied, using solid silver sheets as conductor. Until then, the new contact mechanism proved reliability for $30\,\mathrm{kW}$ average and $110\,\mathrm{kW}$ pulsed power.

Although each component of the RFQ is directly water cooled, the resonance frequency changes by approximately $200\,\mathrm{kHz}$ from switched off RF to $50\,\%$ of the design power ($30\,\mathrm{kW}$). The corresponding temperature increase of the RF structure was estimated to 10–$20\,\mathrm{K}$. The response of the resonance frequency to changes of thermal load occurs almost instantaneously and even small variations of $<< 1\,\%$ have a significant effect. Therefore, changes of the average power during operation have to be applied slow enough to allow the frequency and plunger tuner controller to follow. When the RF power is switched off (e.g. due to RF breakdowns), the RFQ structure cools down again and is off resonance. Restarting operation thus requires to move the plunger tuner back to the initial "cold" position.

As depicted in Fig. 3.4, there is a modulated reflection of power occuring during the RF pulses with a modulation frequency of roughly $500\,\mathrm{Hz}$ and a magnitude in the range of up to $10\,\%$. On the one hand, this is problematic regarding the operation of the plunger tuner controller, which adjusts the plunger position based on the measured phase difference between forward and reflected power. On the other hand, at higher powers the achievable RF amplitude and duty cycle is limited by the significant amount of power being reflected and

---

[4]similar problems also occured at the SARAF-RFQ [145]

by the resulting heating-up of the transmitter and sparking. This also poses a major risk of damage to the RF amplifier. According to an analysis of the RF signals, the damping time constant of the modulation was estimated to 6–10 ms. Because it was suspected that the modulated power reflection is caused by a time-varying RF mismatch due to vibrations of the electrodes, the mechanical damping of the structure was increased by putting clamps on the inter-stem electrode sections. This reduced the damping time to 5–6 ms and slightly increased the modulation frequency, which both corresponds to a higher mechanical stiffness.
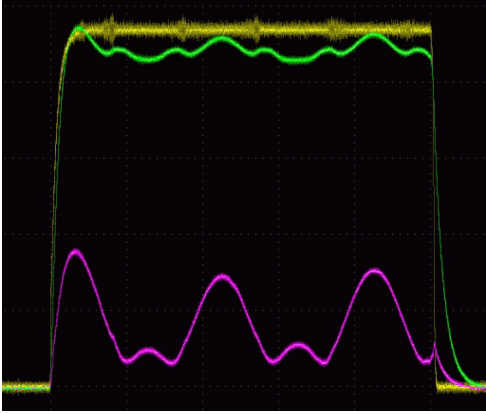
Figure 3.4: Modulation of the reflected power (magenta) with a frequency of roughly 500 Hz (period ≈ 2 ms) at an RF pulse length of 5 ms (yellow: forward power, green: tank pickup) [78].
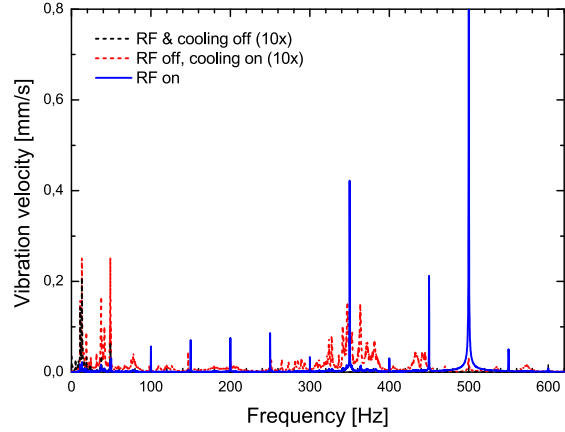
Figure 3.5: Measured frequency spectra of the electrode vibration velocity without RF and switched off cooling (dashed black line), with only cooling water running (dashed red line) and with switched on RF (blue line) [138].

At the typical pulse repetition rate of 50 Hz, the modulation amplitude shows a dependence on the pulse length. This corresponds to an interference behavior between successive pulses, assuming that the mechanical oscillations of the electrodes are triggered by the raising and falling edges of the square wave RF pulse shape, which contain a broad frequency spectrum. After all, the interference effect is so severe that operation of the RFQ is restricted to certain pulse lengths, which have to be adjusted carefully. Using a trapezoid pulse shape leads to a reduction of the modulation amplitude. During operation with a lower pulse repetition rate of 1 Hz, there is no dependence of the reflected signal on the pulse length because the vibrations are presumably damped out within the timespan between two pulses. All observations during RF operation support the assumption that the modulated power reflection is caused by electrode vibrations that are triggered by the edges of the RF pulses. It seems unlikely that the harmonic oscillation of the applied RF field can cause the excitation, since it oscillates 5 orders of magnitude faster than the observed modulation. This is also contradicted by the fact that the modulation amplitude is damped during the flattop of the pulse.

Although in CW mode the forward power does not have a pulsed time structure, no stable CW operating state can be reached. Due to the high level of thermal load during CW operation, the general thermal sensitivity leads to changes of the resonance frequency that are faster than the reaction time of the frequency controller. The resulting fluctuations of the reflected power then lead to changes of the forward power due to the reaction of the ampli-

tude controller, which is additionally affected by the movement of the plunger tuner. As a consequence, the modulation of the reflected signal is constantly excited by the fast changes of the forward power and a stable operating state cannot be reached.

After all, pulsed operation is restricted to certain pulse lengths or low repetition rates due to the modulated power reflection and the high thermal sensitivity complicates stable operation to an extent that CW operation could not be established.

3.3 Vibrometer Measurements

This section describes the method and results of the vibrometer measurements performed at GSI on the existing HLI-RFQ, according to [138] where more details are provided.

The deductions from the RF signals are limited by the fact that the observable time period is restricted to the pulse length. As an RF independent approach, direct measurements of the mechanical vibrations with a commercially available laser vibrometer were conducted.

In principle, the used Polytec OFV-525 laser vibrometer uses an interferometer to measure the Doppler frequency shift and phase modulation between a reference beam and a probe beam that is pointed onto the monitored surface and reflected back to the vibrometer [146]. The determined frequency shift is proportional to the velocity of the surface movement in the spatial direction of the probe beam, whereas the corresponding phase modulation relates to the deflection amplitude. Accordingly, the vibration velocity and amplitudes can either both be measured directly with dedicated operation modes of the vibrometer, or the amplitudes can be calculated afterwards from the measured velocity data. The Fourier transform of the measured data in the time domain finally yields the frequency spectrum of the vibration.

For the vibration measurements on the RF structure of the existing HLI-RFQ, the laser beam was pointed through a vacuum window in the tank onto the backside of an inter-stem electrode section of an upper electrode at an angle of roughly 30° (60°) with respect to its principal axes. This way, vibrations along both transversal spatial axes were measured. The investigations were conducted for standard operation conditions with an RF pulse repetition rate of 50 Hz and, additionally, at a much lower pulse repetition rate of 1 Hz in order to study the mechanical ring-down after excitation by a single pulse.

3.3.1 Results from Standard Operation Conditions

The measured frequency spectra of the vibration velocity for different scenarios are depicted in Fig. 3.5. With only the vacuum pumps running (black dashed curve, ten times enhanced), vibrations of the electrode with frequencies in the range of up to 60 Hz are excited. This is within the typical range of unavoidable mechanical low-frequency excitations $< 100\,\mathrm{Hz}$. With switched on water cooling, running directly through the stems and electrodes, and without RF (red dashed curve, ten times enhanced), a broad background up to 600 Hz appears with distinct peaks below 60 Hz and between 300 and 400 Hz. Finally, for RF operation at moderate power levels (blue compact line), the spectrum contains two major peaks at 350 and 500 Hz. Whereas the measured 500 Hz vibration is in good agreement with the previous RF observations, the other striking peak at 350 Hz could not be seen in the RF signal before. Because the vibrometer was operated unsynchronized, the pulse repetition frequency of 50 Hz

leads to artifacts in the Fourier transform, which are visible in the frequency spectrum as narrow side bands every 50 Hz. According to calculations from the velocity data, the vibration amplitude at 500 Hz is in the order of 1 μm.
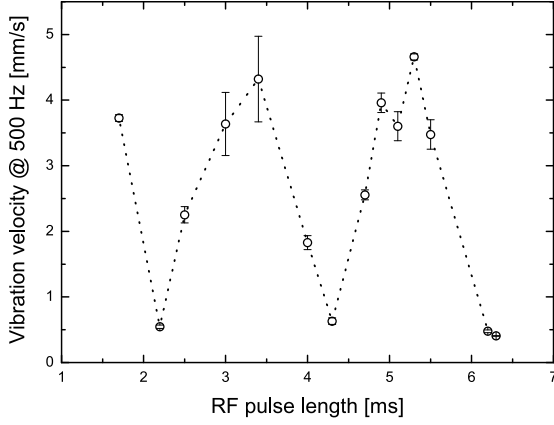

Figure 3.6: Measured vibration velocity at 500 Hz for different RF pulse lengths at a pulse repetition rate of 50 Hz [138].
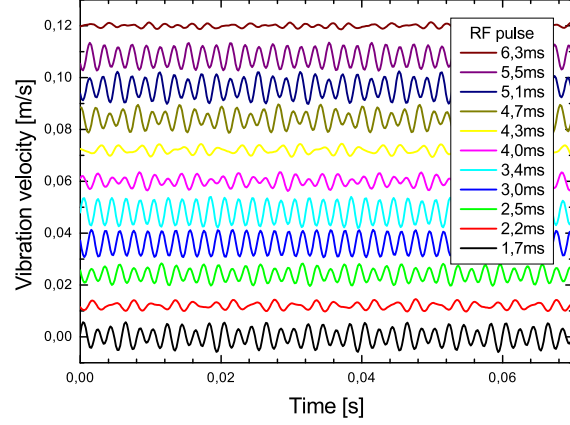
Figure 3.7: Measured vibration velocity during a time period of 3.5 pulse cycles for different pulse lengths at a repetition rate of 50 Hz [138].

Fig. 3.6 shows the measured vibration velocity at a frequency of 500 Hz as function of the pulse length at a pulse repetition rate of 50 Hz. The minima of the periodic dependence correspond to RF pulse lengths that have already been known from experience to enable stable operation, while at other pulse lengths operation is unstable or not possible. Fig. 3.7 depicts the measured vibration velocity in the time domain for different pulse lengths. Each curve shows a steady periodic behavior with a period duration of 20 ms, correlating to the pulse repetition rate of 50 Hz. At pulse lengths that enable stable operation (2.2 ms, 4.3 ms and 6.3 ms), the measured vibration velocities are visibly lower during the entire duration of the period. When the pulse length t_p is an integer multiple of the vibrational period duration t_v ($t_\mathrm{p} = n \cdot t_\mathrm{v}$, $n = 1, 2, ...$), the opposite excitations by the rising and falling edges of the RF pulses coincide with the same phase of the vibration and cancel each other out. Accordingly, for $t_\mathrm{p} = \frac{2n+1}{2} \cdot t_\mathrm{v}$ with $n = 0, 1, ...$, the opposite excitations then coincide with different vibration phases and interfere positively.

3.3.2 Ring-Down Investigations

Fig. 3.8 shows the vibration velocity in the time domain during excitation by a single RF pulse and the subsequent free decay of the mechanical oscillation, measured for different pulse lengths. Due to the low pulse repetition rate of only 1 Hz, the vibrations induced by the previous pulse have already completely subsided before the next pulse is transmitted. After the initial excitation by the rising edge, in each case the first deflection is similar, but the effect of the falling edge depends on the phase of the vibration at the end of the respective pulse duration. At a pulse length of 5.0 ms the vibration is damped by the falling edge and amplitudes after the pulse are low, whereas at 4.1 ms pulse length the falling edge interferes positively with the vibration and amplitudes after the pulse are significantly higher. The

conditions for positive and negative interference, as derived for the steady periodic oscillation during operation at a pulse repetition rate of 50 Hz (see Fig. 3.7), apparently are reverse valid for single pulse excitation. This is due to the differing phase of the vibration at the beginning of the pulse. Fig. 3.9 shows the measured frequency spectrum of the vibration velocity during the free decay after the RF pulse, exhibiting a major peak at about 350 Hz with some smaller peaks in its immediate vicinity as well as the already well known peak at 500 Hz.
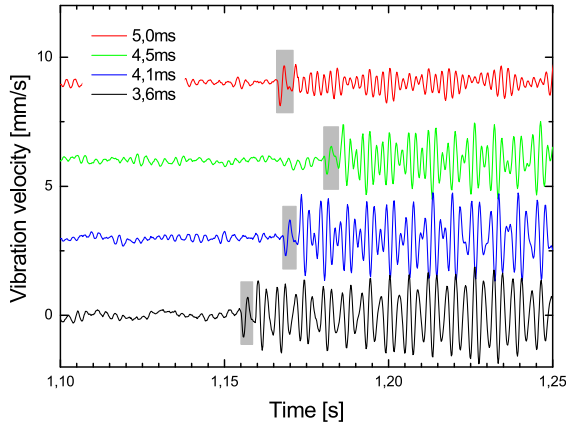
Figure 3.8: Measured velocity in the time domain for vibrations induced by a single RF pulse (marked in gray, repetition rate = 1 Hz) for different pulse lengths [138].
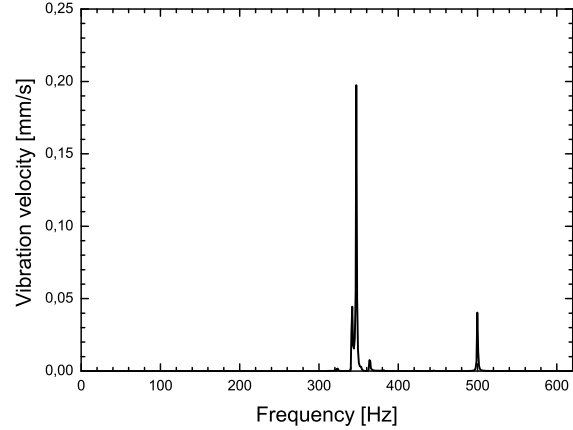
Figure 3.9: Frequency spectrum of the measured vibration velocity during the free decay after the RF pulse [138].

The measurements during the free decay of the vibrations allowed a more precise determination of the damping times, which eventually turned out to be in the order of 0.3 s for all vibration frequencies rather than the previously derived 6–10 ms from the RF observations.

3.4 Structural-Mechanical Simulations

In order to gain a better understanding of the previously experimentally investigated structural-mechanical behavior of the HLI-RFQ, simulations with CST and ANSYS were conducted [139]. From a modal analysis with ANSYS the mechanical eigenmodes of the structure were determined, which allowed to identify the measured vibrational modes at 350 Hz and 500 Hz with the latter perturbing the RF properties of the RFQ and impairing stable operation. After that, the excitation of the identified vibrational modes was studied with a harmonic response analysis, simulating the resonance response to excitations by an ideal electric quadrupole field as well as asymmetric field configurations as associated with the occurrence of a dipole component. In order to evaluate the effect of different vibrational modes on RF matching and resulting power reflection, the frequency detuning due to corresponding mechanical deformations of the electrodes was simulated with CST. Actually, the vibration simulations with ANSYS allow to calculate the magnitude of the displacement amplitudes, however, the knowledge of the mechanical damping ratio is required as an input parameter because the damping characteristics can generally not be predicted from numerical simula-

tions [147]. Finally, using the experimentally determined value of the damping time, the magnitude of the vibration was further investigated by conducting transient simulations of the mechanical response to non-harmonic excitation in order to account for the sequential shock excitations by the edges of the RF pulses.

3.4.1 Eigenmode Analysis

Fig. 3.10 shows the simulated deformation profiles (in exaggerated depiction) of the first order mechanical eigenmodes on the upper electrode. First of all, the modes can be distinguished into oscillations of either only the levitating free end of the electrode overhang (modes 1 & 2) or the entire electrode rod with the overhang typically being at rest (modes 3–12). Furthermore, a classification according to the respective vibrational plane can be made. The almost rectangular shape of the electrode profile has two planes of symmetry, perpendicular to which eigenoscillations occur. The vibrational planes are oriented to the quadrupole center either tangentially (modes 1 & 3–7) or radially (modes 2 & 8–12), as depicted in Fig. 3.11.
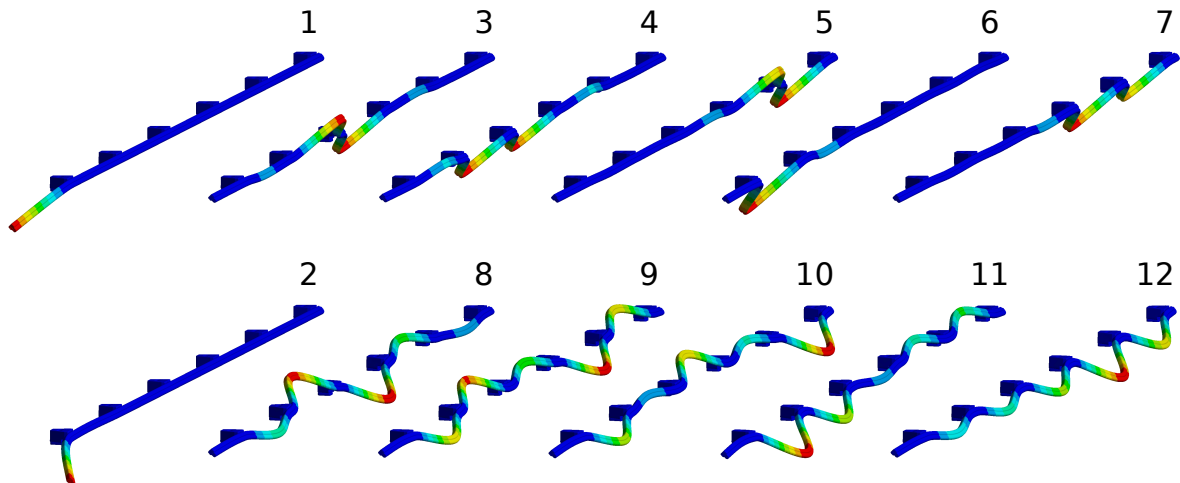
Figure 3.10: Deformation profiles of the first order mechanical eigenmodes on the electrode (1: overhang tangential, 2: overhang radial, 3–7: electrode tangential and 8–12: electrode radial).
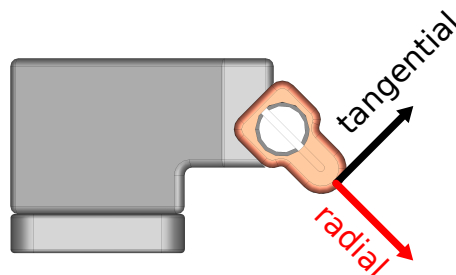
Figure 3.11: Vibrational planes of the electrodes.

The boundary conditions for the simulations with the ANSYS modal analysis solver were defined as surfaces on the imported CAD model with zero displacement (fixed supports). In order to investigate the influence of the boundary definition on the obtained eigenmode defor-

mation profiles and frequencies, simulations with differently placed boundary surfaces were conducted. Fig. 3.12 shows simulated mechanical eigenmode spectra of the upper electrode for two simulation models with different boundary definitions. In model **A**, the boundary surfaces are located directly on the trapezoid electrode mounting brackets, corresponding to the contact surfaces to the stem arms on which the mounting brackets rest. In model **B**, the boundaries are defined on the ground areas of the stems. Generally, the obtained values of the eigenmode frequencies are slightly higher in model **A** because the proximity of the zero displacement boundaries to the electrode introduces an artificial increase of mechanical rigidity. Eventually, this effect is reduced the further the boundaries are located from the electrodes and accordingly the eigenmode frequencies decrease. Whereas there are no qualitative differences between both simulation models regarding the obtained eigenmode deformation profiles of the electrodes, in model **B** the distant boundary conditions on the bottom of the stems introduce additional degrees of freedom for deformations of the stem arms and oscillation modes of the stems themselves (also see Fig. 3.14).
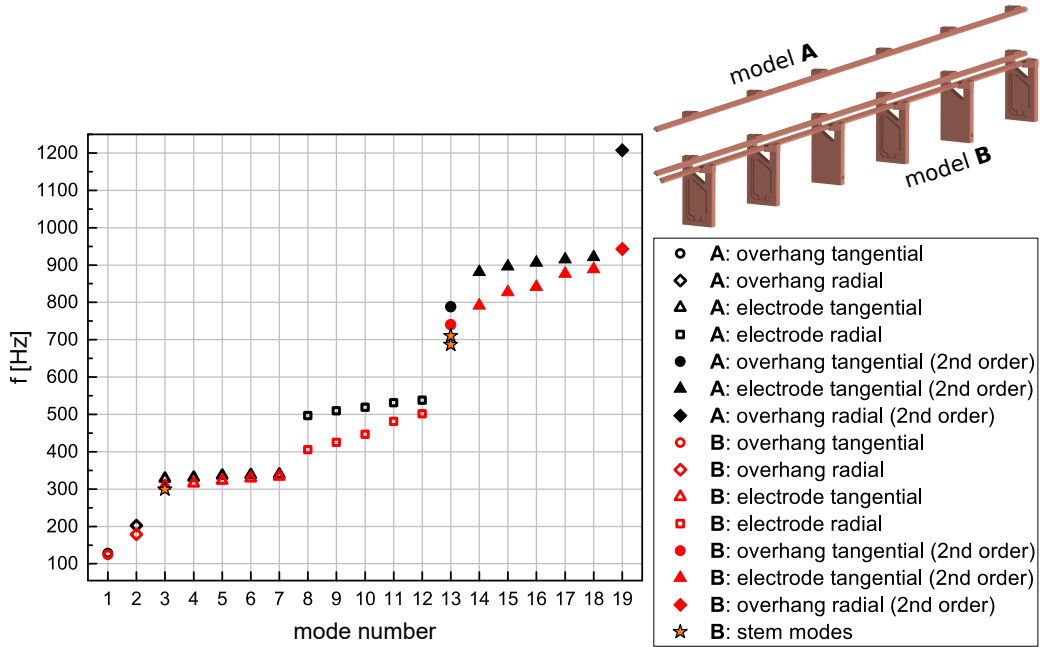
Figure 3.12: Simulated mechanical eigenmode spectra of the upper electrode for two different simulation models **A** and **B** of the HLI-RFQ.

As depicted in Fig. 3.12, the different eigenmode types occur ordered in the mode spectrum. The simulated frequencies of the first order tangential and radial overhang modes (modes 1 & 2) regarding model **A** [model **B**] are 128 [124] Hz and 202 [179] Hz, respectively. The first order tangential electrode modes (modes 3–7) range from 328 [308] to 339 [334] Hz, whereas the first order radial electrode modes (modes 8–12) are between 497 [405] and 538 [501] Hz. After that, only higher order modes occur, with a second order tangential overhang mode (mode 13) at 788 [740] Hz, second order tangential electrode modes (modes 14–18) from 882 [791] to 921 [889] Hz and a second order radial overhang mode (mode 19) at 1208 [943] Hz. The frequencies of the stem modes are 299, 687 and 710 Hz. Furthermore, higher modes (> 19, not shown in Fig. 3.12) contain second order radial electrode modes, third order modes and torsion modes of the electrodes and stems.

The deformation profiles of the first 3 orders of only radial eigenmodes are depicted in Fig. 3.13 in topview onto the radial oscillation plane. Regarding one inter-stem electrode section, the classification in nth orders is characterized by a number of n antinodes (positions with maximum displacement) and $n+1$ nodes (positions with zero displacement, including the mounting positions on the stems).
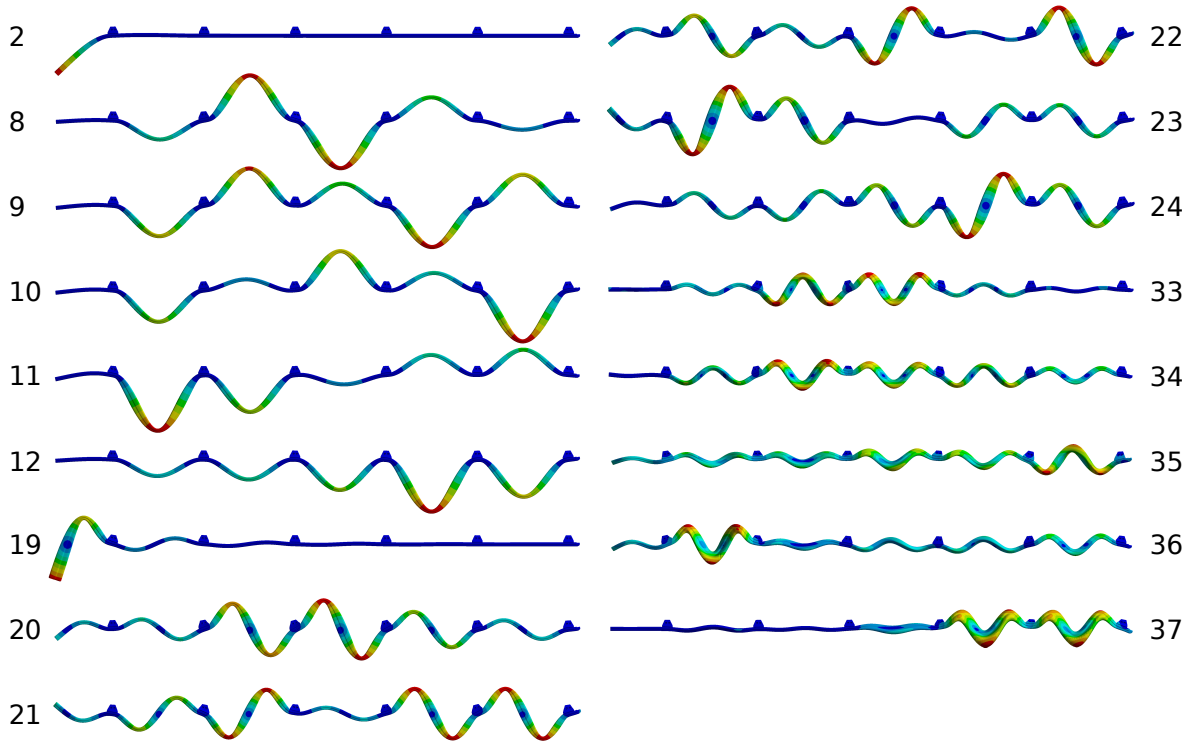
Figure 3.13: Deformation profiles of the radial mechanical eigenmodes in topview onto the the radial oscillation plane (2: first order overhang, 8–12: first order electrode, 19: second order overhang, 20–24: second order electrode, 33–37: third order electrode).

Considering the experimentally identified modes from the preceding vibrometer measurements, it can already be concluded from the simulated eigenmode spectra that the mode at 500 Hz corresponds to a radial electrode mode, whereas the mode at 350 Hz is presumably associated with tangential electrode oscillations. Regarding the eigenmode deformation profiles, it seems striking that there are only few electrode modes with unidirectional deformation, meaning that all deformations point to the same side of the respective vibrational plane. The corresponding modes 6, 7 and 12 each are the highest mode of their respective type. Because in the idealized case the electric quadrupole potential is constant along the electrodes, the resulting electric forces at the electrode surfaces point homogeneously in only one direction at all times. Accordingly, the excitation of bidirectional modes should not be possible. Regarding the simulated eigenmode frequencies of model **B**, the unidirectional radial mode 12 with 501 Hz nicely matches the measured mode at 500 Hz, whereas the corresponding tangential modes 6 and 7 with 329 and 334 Hz deviate slightly from the other measured mode at 350 Hz. Overall, model **B** seems to provide a better reproduction of the real structural-mechanical behavior compared to model **A**. This is presumably because possible deformations of the

stem arms are taken into account. However, in model **B** the screwed connections between the stem arms and electrode mounting brackets are modelled as solid body transitions. This poses a fundamental simplification of the complicated mode-dependent mechanical coupling between the screwed components, which is most likely the cause for deviations between the simulations and measurements. Exemplary, Fig. 3.14 illustrates the (unidirectional) highest first order radial electrode mode (mode 12) on both the upper and lower electrode, the first order stem mode as well as the lowest second order tangential electrode mode (mode 14).

(unidirectional) radial mode
on the upper electrode (501 Hz)

1st order stem mode (299 Hz)

(unidirectional) radial mode
on the lower electrode (529 Hz)

lowest 2nd order tangential mode
on the upper electrode (791 Hz)
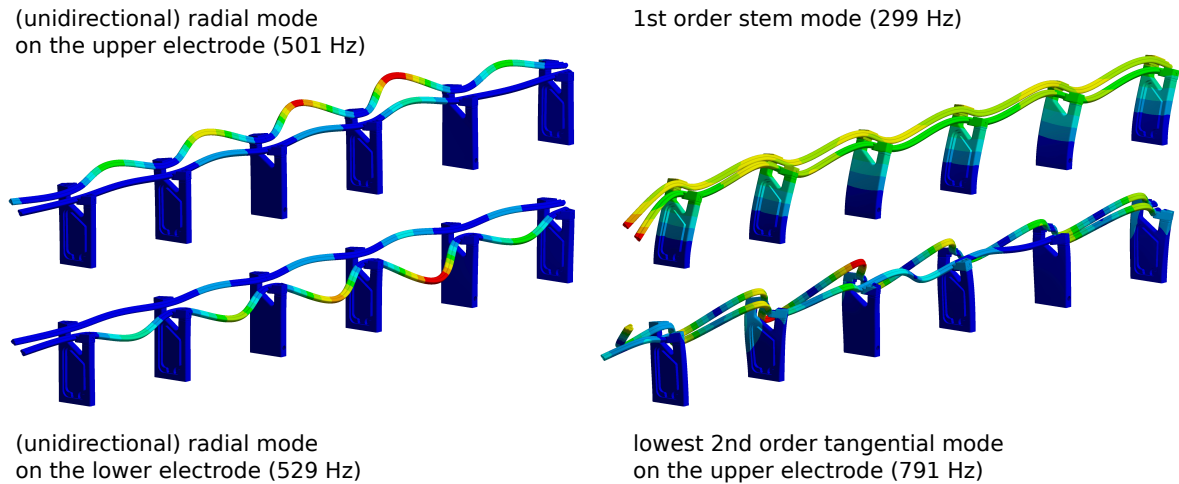
Figure 3.14: Some exemplary eigenmodes of simulation model **B** (including stem deformations).

3.4.2 Harmonic Response Analysis

In order to investigate the excitation of the identified vibrational modes, a harmonic response analysis with ANSYS was performed, from which the frequency-dependent steady-state response to a predefined harmonic load is determined. For the simulations, the load was applied as a homogeneous force to the upper electrode surface with an arbitrary but constant magnitude. As depicted in Fig. 3.15, the direction of the force is parameterized by $\lambda = F_{\text{vertical}}/F_{\text{horizontal}}$, being the ratio of vertical to horizontal excitation.

$\lambda = 1$ $\lambda = 0$

M0 M1 M2 M3 M4 M5
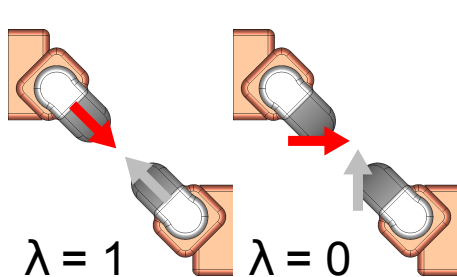
Figure 3.15: Direction of the excitation force for $\lambda = 1$ (radial excitation) and $\lambda = 0$ (horizontal excitation).
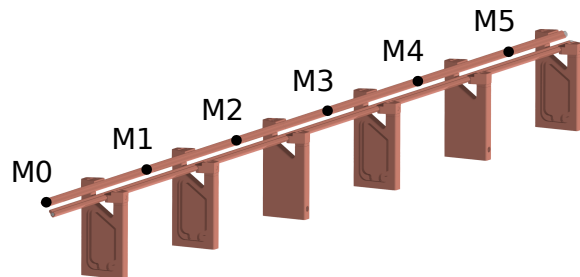
Figure 3.16: Monitoring points on the upper electrode.

For $\lambda = 1$, the excitation force points in radial direction, emulating the force associated with an ideal electric quadrupole field. $\lambda < 1$ corresponds to forces of asymmetric electric field configurations, relating to the effect of the electric dipole component (see section 2.3.5).
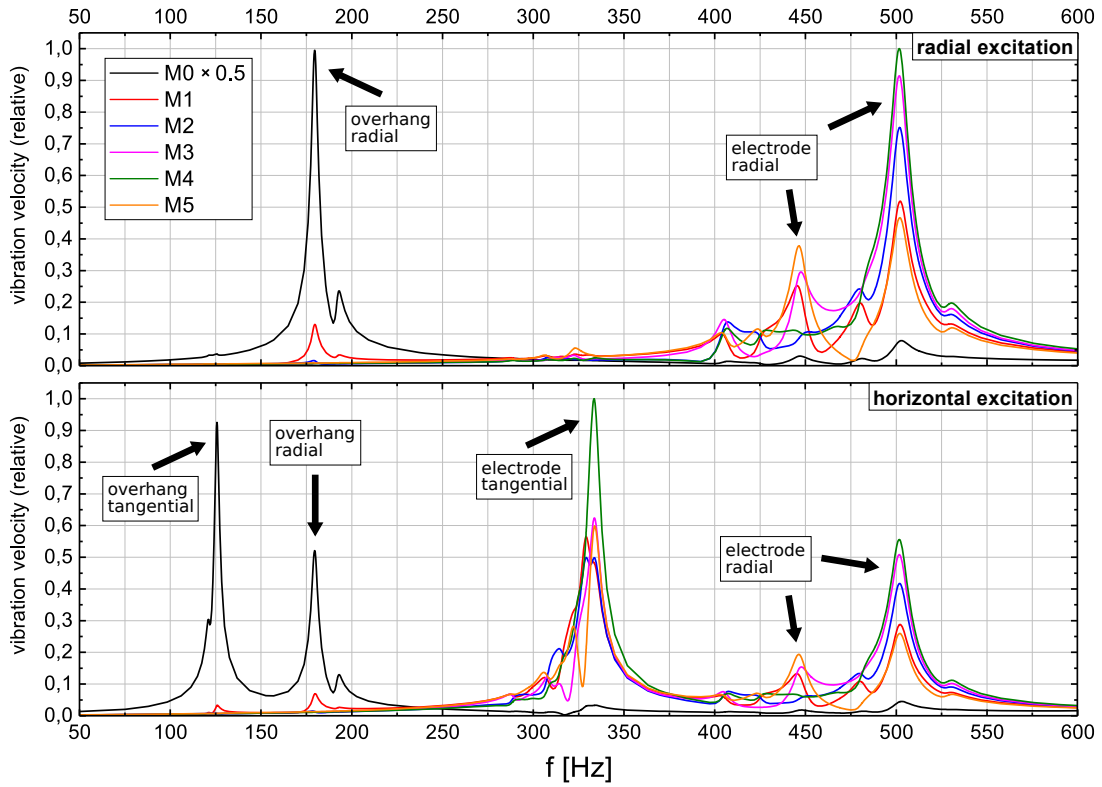
Figure 3.17: Simulated resonance response spectra at different monitoring points on the electrode for radial and horizontal excitation (the values for M0 are scaled down with a factor of 0.5).
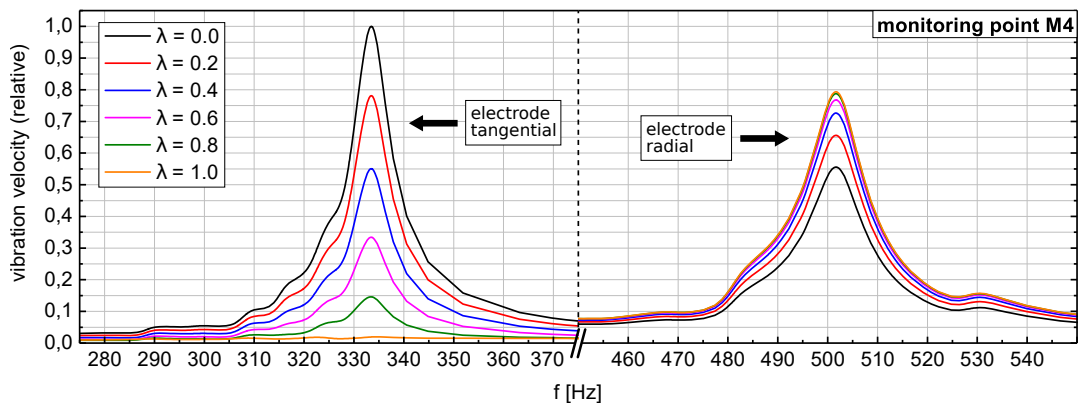
Figure 3.18: Simulated resonance response spectra for the electrode section at M4 for different excitations from $\lambda = 0$ (horizontal excitation) to $\lambda = 1$ (radial excitation).

The harmonic response analyses were conducted on model **B** as described in section 3.4.1. According to Fig. 3.16, the simulated resonance response was evaluated on six monitoring

points on the upper electrode with M0 being located at the end of the electrode overhang and M1–M5 being at the centers of the inter-stem electrode sections. The unknown value of the (constant) mechanical damping ratio was arbitrarily set to 1%. The obtained response spectra display the relative vibration velocity as function of the excitation frequency.

Fig. 3.17 shows the resonance response at each monitoring point for radial and horizontal excitation. With radial excitation ($\lambda = 1$) only the radial modes occur in the spectrum with significant peaks for the radial overhang mode at $179\,\text{Hz}$ (mode 2) and the unidirectional radial electrode mode at $501\,\text{Hz}$ (mode 12). Also, the bidirectional radial electrode modes at $405\,\text{Hz}$ (mode 8), $425\,\text{Hz}$ (mode 9), $446\,\text{Hz}$ (mode 10) and $481\,\text{Hz}$ (mode 11) are present in the spectrum with minor peaks. When looking at a certain eigenmode frequency, the magnitude of each peak roughly corresponds to the relative amount of mechanical deflection at the respective inter-stem electrode section according to the eigenmode deformation profiles as depicted in Fig. 3.13. With horizontal excitation ($\lambda = 0$) the spectrum also includes the tangential modes with major peaks for the tangential overhang mode at $124\,\text{Hz}$ (mode 1) and the unidirectional tangential electrode mode at $334\,\text{Hz}$ (mode 7). The other unidirectional tangential electrode mode at $329\,\text{Hz}$ (mode 6) occurs in the spectrum with a medium peak (only at M1 and M2). Again, also the bidirectional tangential electrode modes at $309\,\text{Hz}$ (mode 3), $315\,\text{Hz}$ (mode 4) and $323\,\text{Hz}$ (mode 5) are weakly recognizable but present.

Fig. 3.18 shows the resonance response at monitoring point M4 for different directions of the excitation ($\lambda = 0...1$), taking a closer look at the vicinity of the two major peaks which correspond to the unidirectional tangential and radial electrode modes. The increasing excitation of the tangential mode with decreasing λ (the excitation becomes more horizontal) is clearly visible, whereas the amplitude of the radial oscillation slowly decreases.

After all, the simulated response spectra nicely reproduce the experimentally obtained frequency spectra from the vibrometer measurements (compare to Fig. 3.5 and Fig. 3.9). Additionally, the response analysis strongly supports the previous assumption that there is no excitation of bidirectional modes by the longitudinally constant electric field as associated with the quadrupole potential. The excitation of tangential modes is clearly attributed to asymmetries of the electric field distribution, as in case of an existing dipole component.

Although the modulation of the electrodes causes another inherent field asymmetry, the length of one modulation cell along the electrode is typically much smaller than the longitudinal dimensions of the deformation antinodes of the mechanical eigenmode oscillations and thus an influence on their excitation seems unlikely.

3.4.3 Mechanical RF-Sensitivity

To investigate the influence of the identified vibrational modes on RF matching, the corresponding power reflection was calculated considering the respective mechanical electrode deformation. For this purpose, deformation profiles as depicted in Fig. 3.19 were applied to the electrode rods, resembling the unidirectional modes in radial and tangential direction. The directions of the corresponding traction forces on all four electrodes are shown in Fig. 3.20.

$$\frac{P_\text{r}}{P_\text{f}} = |\Gamma|^2 = \left| \frac{\beta - 1 - i\beta Q_0 \delta}{\beta + 1 + i\beta Q_0 \delta} \right|^2 \overset{\beta=1}{\approx} 1 - \frac{1}{1 + Q_0{}^2 \frac{\Delta f^2}{f_0^2}} \tag{3.1}$$

First, the frequency detuning Δf associated with the capacitance change due to the electrode deformation was simulated with CST. From that, the ratio of reflected power to forward power P_r/P_f was analytically derived using Eq. 3.1. In general, the power reflection $P_r = |\Gamma|^2 P_f$ is described by the reflection coefficient $\Gamma(\Delta f) = (\beta - 1 - i\beta Q_0 \delta)/(\beta + 1 + i\beta Q_0 \delta)$ [120, p. 98] with the resonator's unloaded quality factor Q_0, the coupling coefficient $\beta = Q_0/Q_e$ (see section 2.3.1) and $\delta = f_0/(f_0 - \Delta f) - (f_0 - \Delta f)/f_0$.
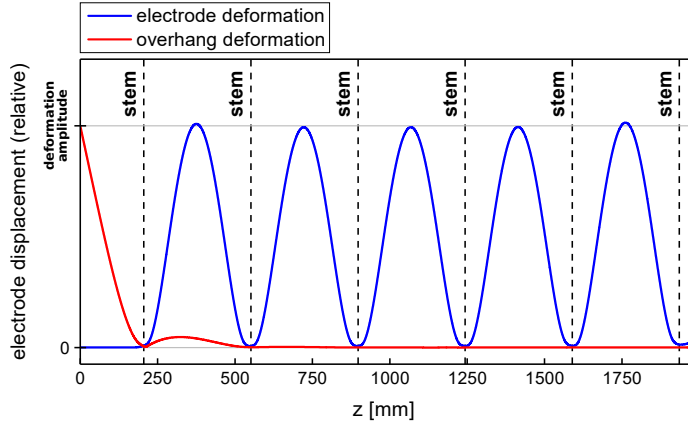
Figure 3.19: Mechanical deflection along the electrode regarding the applied deformation profiles (longitudinal coordinate: z).
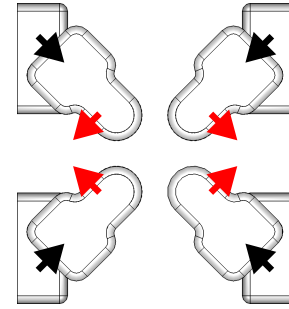
Figure 3.20: Directions of the traction forces on the electrode rods (black: radial deformation, red: tangential deformation).
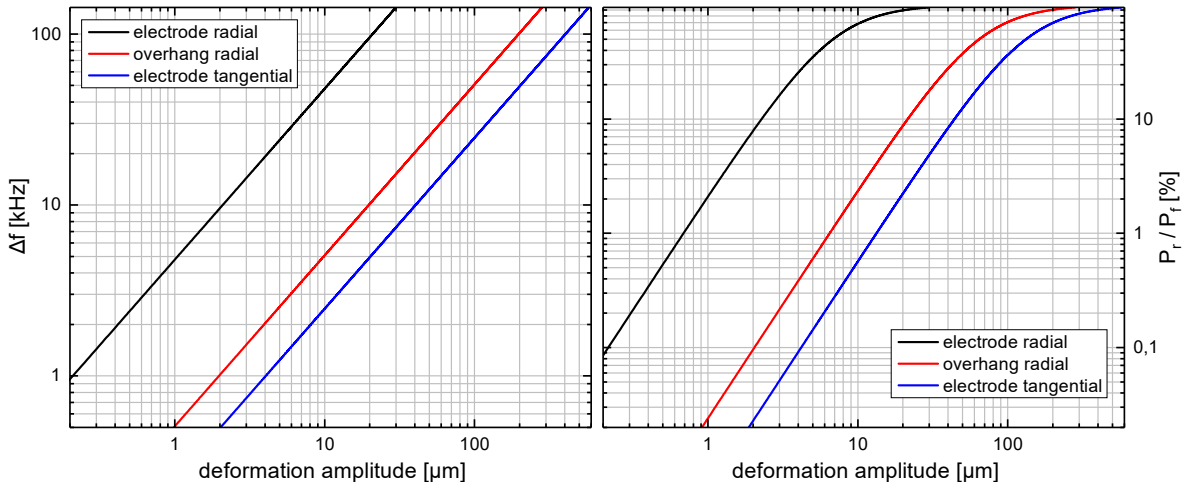
Figure 3.21: Simulated frequency detuning Δf and calculated ratio of reflected to forward power P_r/P_f (see Eq. 3.1) as functions of the (maximum) deformation amplitude for different deformation profiles according to Fig. 3.19.

For the case of critical coupling ($\beta = 1$), another analytic expression for the calculation of the reflected power can be derived from a different approach: At resonance, the dissipated power $P_c = P_f$ equals exactly the forward power which is coupled into the resonator and given by $P_f = (2\pi f_0)W(f_0)/Q_L$ with the stored energy $W(f_0)$, according to Eq. 2.15. Considering small changes in frequency and quality factor, the dissipated power $P_{\text{detuned}} \approx (2\pi f_0)W(\Delta f)/Q_L$

for the detuned case depends on the stored energy $W(\Delta f) = W(f_0)/(1 + 4Q_{\mathrm{L}}^2(\Delta f/f_0)^2)$ in the detuned resonator, according to Eq. 2.20. The reflected power $P_{\mathrm{r}} = P_{\mathrm{f}} - P_{\mathrm{detuned}}$ is then given by the difference between the (constant) forward power and the detuned dissipated power. Finally, this yields the approximation formula for the calculation of the relative reflected power as given by Eq. 3.1, which however only applies for critical coupling ($\beta = 1$).

The frequency detuning Δf and the proportion of reflected power $P_{\mathrm{r}}/P_{\mathrm{f}}$ as functions of the deformation amplitude for different vibrational modes are shown in Fig. 3.21, calculated for $Q_0 = 3300$ as specified in [134, p. 103]. Accordingly, for radial electrode deformations, the experimentally observed magnitude of the power reflection of up to 10 % would correspond to deformation amplitudes of up to approximately 2 µm, which eventually is in good agreement with the measured vibration amplitudes at 500 Hz. At an assumed deformation amplitude of 2 µm, the influence on the frequency detuning due to radial overhang and tangential electrode deformations amounts to only approximately 10 % ($\Delta f \approx 1$ kHz) and 5 % ($\Delta f \approx 0.5$ kHz), respectively, compared to the radial electrode mode with $\Delta f \approx 10$ kHz. The corresponding amount of reflected power is in the range of about $P_{\mathrm{r}}/P_{\mathrm{f}} \approx 0.1$ % for the radial overhang mode and $P_{\mathrm{r}}/P_{\mathrm{f}} \approx 0.02$ % for the tangential electrode mode, which both is considerably less than the power reflection of $P_{\mathrm{r}}/P_{\mathrm{f}} \approx 8$ % associated with the radial electrode mode. Finally, this probably poses the reason why the measured mode at 350 Hz, which was identified as a tangential electrode mode, cannot be observed in the reflected RF signal. After all, it is obvious that the unidirectional radial electrode mode (mode 12) has by far the most perturbing influence on the RF frequency stability of the RFQ resonator.
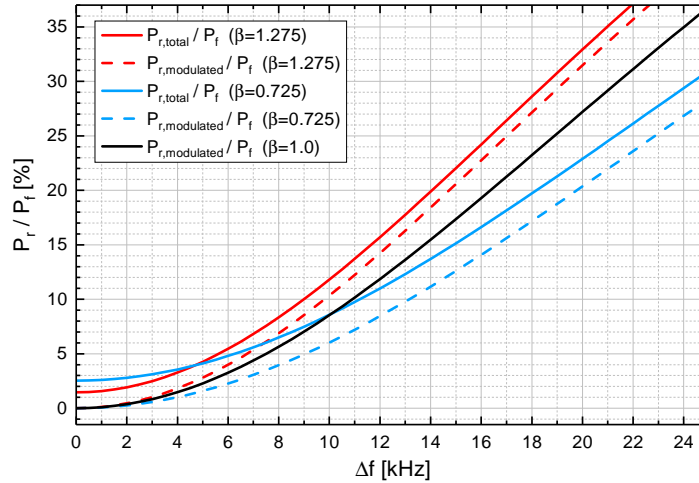
Figure 3.22: Reflected power $P_{\mathrm{r}}/P_{\mathrm{f}}$ as function of the frequency detuning Δf for different coupling scenarios (the dashed lines show the respective amount of modulated power reflection).

In order to show the effect of overcoupling ($\beta > 1$) and undercoupling ($\beta < 1$) on the reflection behavior of the detuned resonator, the magnitude of total and modulated reflected power is plotted as function of the frequency detuning Δf for different coupling scenarios in Fig. 3.22, as calculated from Eq. 3.1. The amplitude of the modulated power reflection $P_{\mathrm{r,modulated}}$ corresponds to the fraction of reflected power that results only from the time-varying frequency detuning due to the electrode vibration, whereas a constant amount of reflected power $P_{\mathrm{r,const.}}$

is caused by the initial non-critical coupling $(P_{\text{r,total}} = P_{\text{r,const.}} + P_{\text{r,modulated}})$[5]. Therefore, in case of critical coupling $(\beta = 1)$, the reflected power is entirely modulated.

On the one hand, overcoupling apparently increases both the total as well as the modulated power reflection, whereas on the other hand, undercoupling actually might provide benefits to mitigate the effects of frequency detuning since the modulated power reflection is generally reduced. The corresponding total power reflection exceeds the reference case of critical coupling only at comparatively low detuning, which however is not too problematic as this is associated with lower field amplitudes and thus lower absolute power levels.

3.4.4 Transient Vibration Analysis

A commonly used approach for the experimental determination of the mechanical damping characteristics is given by the logarithmic decrement method [148, pp. 4 ff.], in accordance to which the corresponding value of the damping ratio ζ can be calculated from a measurement of the damping time constant τ, following Eq. 3.2. The damped natural frequency $\omega_{\text{d}} = \sqrt{\omega_0{}^2 - \tau^{-2}}$ is approximately equal to the undamped natural frequency ω_0 when damping is very weak and the corresponding damping time is hence large compared to the period duration of the oscillation $(1/\tau^2 \ll \omega_0{}^2)$.

$$\zeta = \frac{1}{\sqrt{1 + (\omega_{\text{d}}\tau)^2}} = \frac{1}{\omega_0\tau} \overset{\tau^{-2} \ll \omega_0{}^2}{\approx} \frac{1}{\omega_{\text{d}}\tau} \tag{3.2}$$

In contrast to the previously conducted simulations of the mechanical resonance response to a harmonic excitation, where primarily a qualitative analysis was pursued with arbitrary values for the excitation force and damping ratio, the magnitude of the vibration can also be analyzed quantitatively, using the experimentally determined value of the damping ratio and calculating the force on the electrodes from the simulated electric field distribution.

As calculated with CST MWS, the horizontal and vertical force on the upper electrodes at 45 kW pulse power amounts to 4.23 N and 3.54 N, respectively, being different due to the non-zero dipole ratio. The correspondingly simulated resonance response spectra at an electrode section (M4) and at the overhang (M0) are shown in Fig. 3.23.
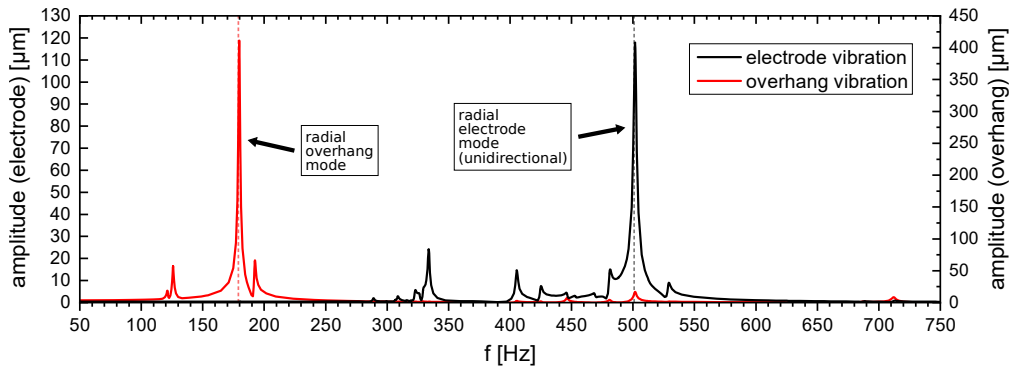
Figure 3.23: Simulated resonance response at the electrode (M4) and at the end of the overhang (M0) to harmonic excitation, in analogy to Fig. 3.17, for the force on the electrodes calculated with CST MWS ($F_{\text{horizontal}} = 4.23$ N, $F_{\text{vertical}} = 3.54$ N) and a daming ratio of $\zeta = 0.106\,\%$, corresponding to the experimentally determined value for the damping time of $\tau = 0.3$ s.

---

[5]because the reflected power is calculated for static detuning and thus corresponds to an amplitude, the time averaged power reflection is hence given by $\langle P_{\text{r,total}}\rangle = P_{\text{r,const.}} + \frac{1}{\sqrt{2}}P_{\text{r,modulated}}$, assuming harmonic modulation

Regarding harmonic excitation, the simulated amplitude of the unidirectional radial electrode mode with a displacement of almost $120\,\mu$m is however much larger than the previously determined vibration magnitude of up to $2\,\mu$m, as calculated from the vibrometer measurements (section 3.3.1) or derived from the analysis of the mechanical RF sensitivity (section 3.4.3). Accordingly, the excitation by the edges of the RF pulses, which corresponds to a periodic sequence of single mechanical shock events, is 2 orders of magnitude weaker.

To validate the previous analyses and further investigate the progression of the mechanical electrode oscillation in the time domain and its response to the pulse edges, transient mechanical simulations with ANSYS have been conducted. With the electrodes initially being completely at rest, the transient response to a number of RF pulses with a repetition rate of $50\,$Hz and a pulse length of t_p was calculated over a total period of $250\,$ms with a time resolution of $10^{-4}\,$s, corresponding to $5\,\%$ of the period duration of the expected $500\,$Hz electrode vibration and resulting in 2500 single simulation steps per evaluation.
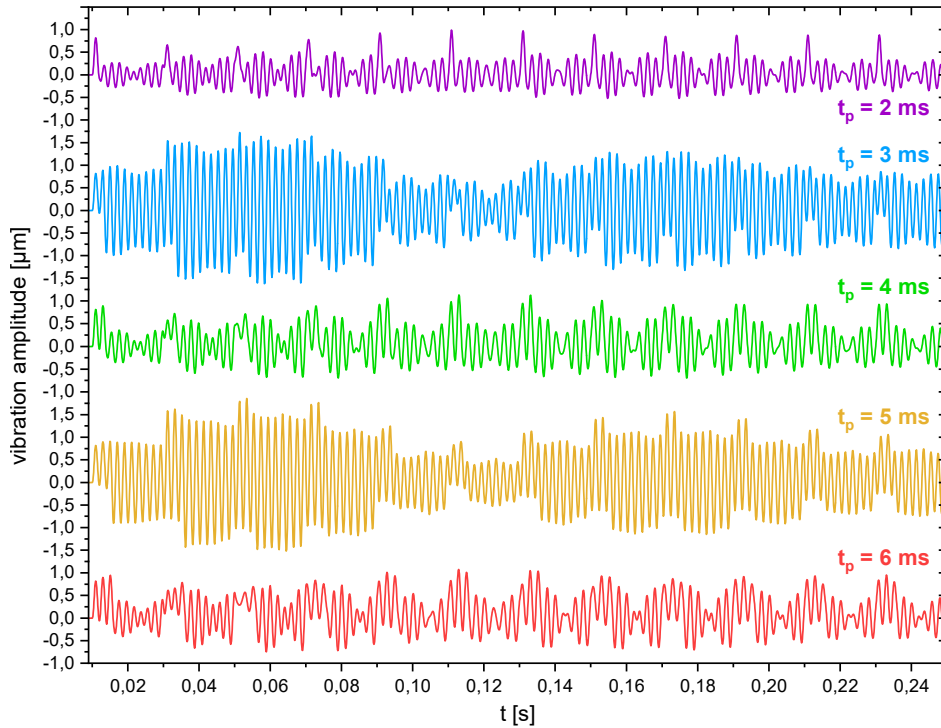
Figure 3.24: Simulated vibration amplitude at the electrode during the first $250\,$ms of a pulsed excitation with a repetition frequency of $50\,$Hz and different pulse lengths t_p.

As shown in Fig. 3.24, the simulated transient vibration amplitudes for different excitation pulse lengths nicely reproduce the interference behavior observed in the vibrometer measurements as discussed in section 3.3.1 (see Fig. 3.7), with significantly lower amplitudes for the pulse length being an integer multiple of the mechanical eigenmode period duration ($t_\mathrm{p} = 2, 4, 6\,$ms). Also, the magnitude of the simulated oscillations largely corresponds to the values from the vibrometer measurements as well as from the RF sensitivity consideration. The process of negative and positive excitation interference for pulse lengths of 2 and $5\,$ms, respectively, is shown in detail in Fig. 3.25. For $t_\mathrm{p} = 2\,$ms, the excitations of both the rising

and falling edges are typically out of phase with the vibration, which is marked by a phase jump and results in damping, causing the amplitude directly after the pulse to be lower than before. On the other hand, for $t_p = 5\,\text{ms}$ the excitations of the rising and falling edges are more often in phase to the vibration, in which case the amplitude increases after both the rising and the falling edge without causing a phase jump. In both cases of negative and positive interference, the vibration period duration is a constant $2\,\text{ms}$, corresponding to the frequency of the associated unidirectional mechanical radial electrode eigenmode of $500\,\text{Hz}$.
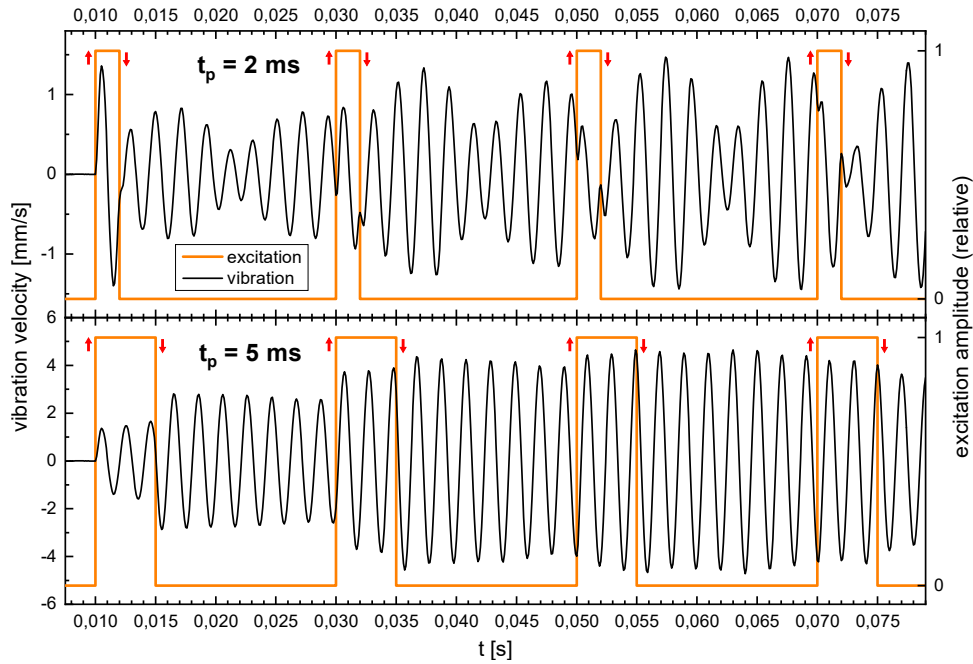
Figure 3.25: Simulated vibration velocity during the first 4 pulses of a pulsed excitation with a repetition frequency of $50\,\text{Hz}$ for $t_p = 2\,\text{ms}$ (negative interference with low vibration amplitudes) and $t_p = 5\,\text{ms}$ (positive interference with high vibration amplitudes).

3.5 Thermal Analysis

To investigate the high thermal sensitivity of the HLI-RFQ, a thermal analysis using CST Studio Suite has been conducted. In principle, the temperature distribution on the RF structure can be simulated with CST Mphysics Studio, using the imported heat loss distribution as calculated by Microwave Studio from the simulated distribution of the magnetic field. Given the temperature distribution, the resulting thermal deformation can then be simulated. Importing the thermal deformation profile back to Microwave Studio finally allows to conduct a sensitivity analysis, by which the frequency detuning of the resonator is calculated, considering the imported surface displacement of the RF structure.

A schematic overview of the heat dissipation from the lossy cavity surface to the flowing cooling water is provided by Fig. 3.26. For this idealized case, the temperature inside the heat loaded copper structure is mainly determined by three processes:

(1) The thermal conduction from the cavity surface to the cooling channel results in a linear temperature gradient which depends on the heat flow rate $\dot{Q}_i$, the total area A_i of the respective surface element i (the ratio $\dot{Q}_i/A_i$ corresponds to the dissipated power density) as well as on the material dependent value λ of the thermal conductivity. Accordingly, the total temperature difference ΔT_1 across the overall material thickness d_{copper} is given by Eq. 3.3.

(2) The heat flux $\dot{Q}_i$ from the copper material to the cooling water through a surface element with area A_i is driven by the temperature difference ΔT_2 at the transition layer between the materials. With the heat transfer coefficient α being the corresponding proportionality constant, ΔT_2 can thus be calculated according to Eq. 3.4. In general, the value of the heat transfer coefficient itself depends on the heat conductivity of the cooling water and on its internal temperature distribution, which again is connected in a complex way with the velocity distribution and hence the fluid dynamic flow properties [149].

(3) For a perfectly uniform laminar water flow, the water temperature increases linearly along the cooling channel due to the heat transfer from the copper. The temperature gradient depends mostly on the magnitude of the heat flux ($\dot{Q}_i$) and on the water flow rate $\dot{V}$, but also on the water density ρ and its (specific) heat capacity c_{W}. Accordingly, the overall temperature increase ΔT_i of the cooling water along the considered surface element i is given by Eq. 3.5.

$$\Delta T_1 = \frac{\dot{Q}_i \, d_{\mathrm{copper}}}{\lambda \, A_i} \qquad (3.3)$$

$$\Delta T_2 = \frac{\dot{Q}_i}{\alpha \, A_i} \qquad (3.4)$$

$$\Delta T_i = \frac{\dot{Q}_i}{\dot{V} \rho \, c_{\mathrm{w}}} \qquad (3.5)$$
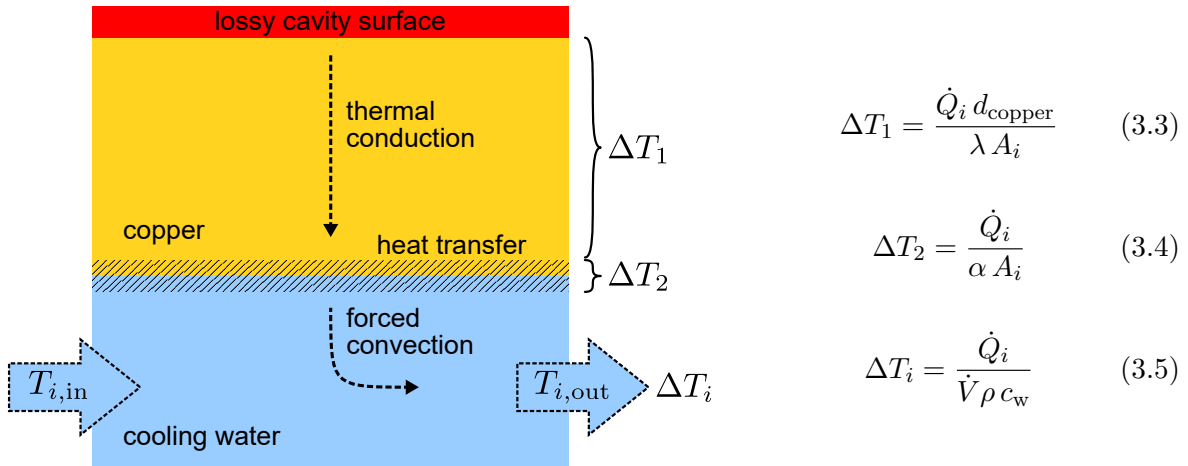
Figure 3.26: Schematic overview of the heat flow from the lossy cavity surface to the cooling water [150, p. 38].

Following the above consideration, the resulting absolute temperature $T_{i,\mathrm{s}}$ at the cavity surface, according to Eq. 3.6, is ultimately determined by the temperature $T_{i,\mathrm{in}}$ of the water inflow, which basically constitutes the boundary condition to the given thermal problem.

$$T_{i,\mathrm{s}} = T_{i,\mathrm{in}} + \frac{\Delta T_i}{2} + \Delta T_2 + \Delta T_1 \qquad (3.6)$$

However, the thermal simulations with CST Mphysics Studio are in the current software version restricted to the calculation of only the thermal conduction[6], thus neglecting the heating of the water along the cooling channels ($\dot{V} \to \infty$) and assuming perfect heat transfer ($\alpha \to \infty$). Therefore, the boundary condition for the thermal simulation has to be defined

---

[6]so far, the new Conjugate Heat Transfer solver (CHT) included in CST Studio Suite could not be successfully applied to simulate the water flow through complex routed cooling channels

as a perfectly thermally conductive source of constant temperature (T_{boundary}) on a solid body inside the cooling channels which represents the water. After all, this highly simplified simulation approach is valid for high water flow rates ($\Delta T_i \rightarrow 0$) in conjunction with low average heat flux densities ($\Delta T_2 \rightarrow 0$), which in principle applies well to accelerator structures with low RF duty cycles. In case of ΔT_i or ΔT_2 not being negligible compared to ΔT_1, thus having a noticeable effect on the surface temperature $T_{i,\text{s}}$, the influence from the heating of the cooling water and from finite heat transfer, respectively, has to be considered.

To achieve this within Mphysics Studio, a simple semi-analytical workaround approach can be applied: Since the local power loss on a certain component of the RF structure can be directly evaluated from the RF simulations in Microwave Studio, the temperature increase ΔT_i of the cooling water flowing through the associated section of the corresponding cooling channel can hence be calculated according to Eq. 3.5. To finally take into account the heating of the cooling water within the thermal simulation, the originally defined boundary temperature $T_{\text{boundary},i}$ along the concerned channel section i, which is typically set to the initial inflow temperature to the entire cooling channel, can then be increased by the averaged value $\Delta T_i/2$. Of course, the temperature difference ΔT_i calculated for one section of the cooling channel also has to be added to the boundary temperatures $T_{\text{boundary},i+n}$ of all following channel sections, since the heat deposited in the water is ideally only removed by forced convection due to the cooling water flow. To also account for the finite heat transfer, the boundary temperature can analogously be additionally increased by ΔT_2 as caluclated from Eq. 3.4, considering the surface area A_i of the respective channel section over which the heat flow $\dot{Q}_i$ is hence averaged. Whereas for a first rough approximation the described procedure can be applied averaged over an entire cooling channel, provided that the respectively associated heat flow can be determined, the RF structure can also be split up along the cooling channels into a number of sections, for each of which the corresponding semi-analytical boundary temperature can then be determined separately in order to yield a more accurate overall boundary temperature distribution. Eventually, the accuracy of this method is however limited by basically neglecting the heat flows in between the considered sections. More sophisticated commercially available software solutions concerning the simulation of thermal problems, including heat transfer properties and fluid dynamic simulations of the water flow through the cooling channels, are provided by ANSYS [140] or COMSOL [151]. Regarding the HLI-RFQ, the temperature increase ΔT_i of the cooling water by heating ranges up to values of 8.5, 4 and 16 K on the stems, tuning plates and electrodes, respectively, whereas finite heat transfer with a pessimistically assumed value of the heat transfer coefficient of $\alpha = 3500\,\text{W/m}^2\text{K}$ would correspondingly result in an increase ΔT_2 of the boundary temperature by 40, 33 and 32 K, averaged along the cooling channels (see Fig. 3.27).

In general, the mechanical behavior of 4-rod RFQs under thermal load and the resulting effect on the RF resonance frequency strongly depends on the mechanical coupling between the thermal deformations of the single components of the RF structure. In order to investigate the effect of different coupling behavior between the tuning plates and stems, as well as between the stems and the electrodes, respectively, all thermal simulations have been conducted for the four different mechanical boundary models as depicted in Fig. 3.28. Whereas in model **A** all component contacts are solid body transitions, corresponding to strong mechanical coupling between the components, in model **B** the tuning plates are completely ignored for the mechanical simulation, which practically corresponds to weak mechanical

coupling to the stems. Model **C** corresponds to the case that the tuning plates, which are fixed between two stems, prevent the thermal deformation of the stems at the respective contact surfaces. Regarding model **D**, the electrodes are basically fully mechanically decoupled from the thermal deformation of the stems, which are set to be a zero displacement boundary.
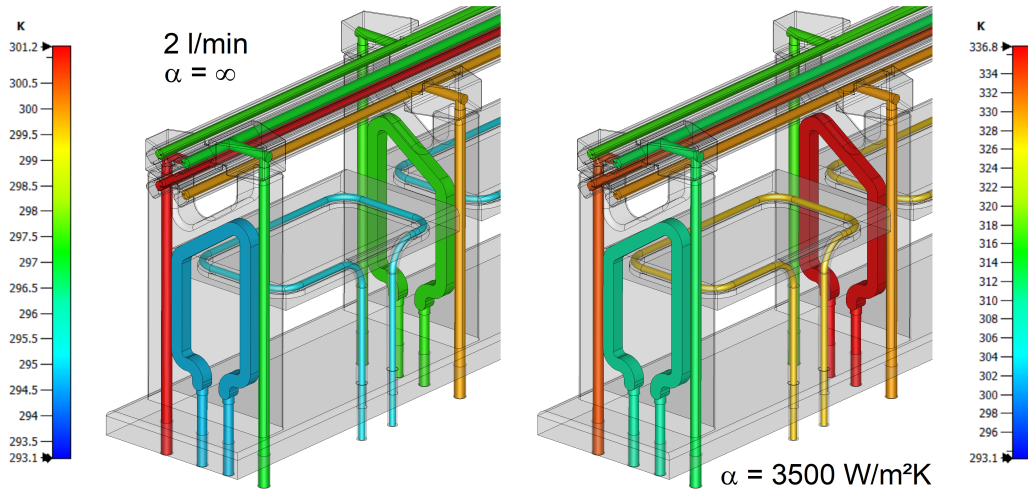

Figure 3.27: Semi-analytically determined boundary temperatures averaged along the entire length of the cooling channels for $\dot{V} = 2\,\mathrm{l/min}$, considering perfect and finite heat transfer.
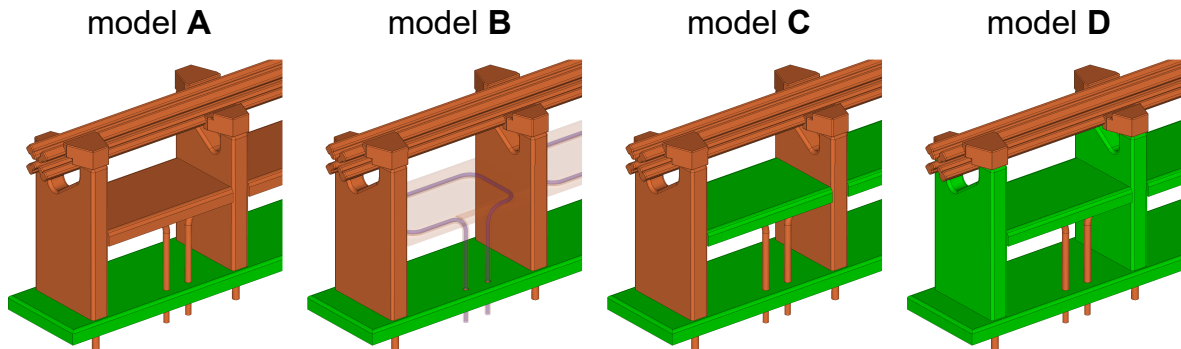
Figure 3.28: Different mechanical boundary models for the simulation of the thermal deformation, reproducing different mechanical coupling behavior at the screwed connections between the stems and electrodes as well as at the contact surfaces where the tuning plates are pressed against the stem:

model **A**: Zero displacement boundary at the bottom panel (indicated in green), solid body transition between tuning plates and stems as well as between stem arms and electrode mounting brackets (corresponding to model **B** from the vibration analysis, see section 3.4.1).

model **B**: Same displacement boundary as in model **A**, but the tuning plates are being ignored for the mechanical simulation.

model **C**: The surface of the tuning plates is also defined as zero displacement boundary, the stems are thus fixed at the corresponding contact surfaces.

model **D**: Additionally, also the stems were set to zero displacement, which ultimately only allows for deformation on the electrodes.
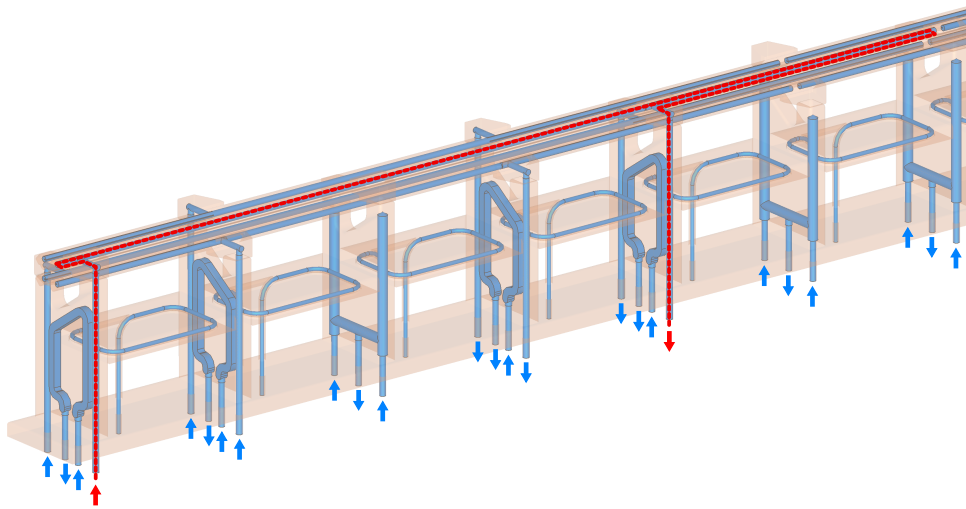
Figure 3.29: Cooling concept of the HLI-RFQ (the path of the water flow through a cooling channel of an upper electrode is highlighted by the red dashed line).
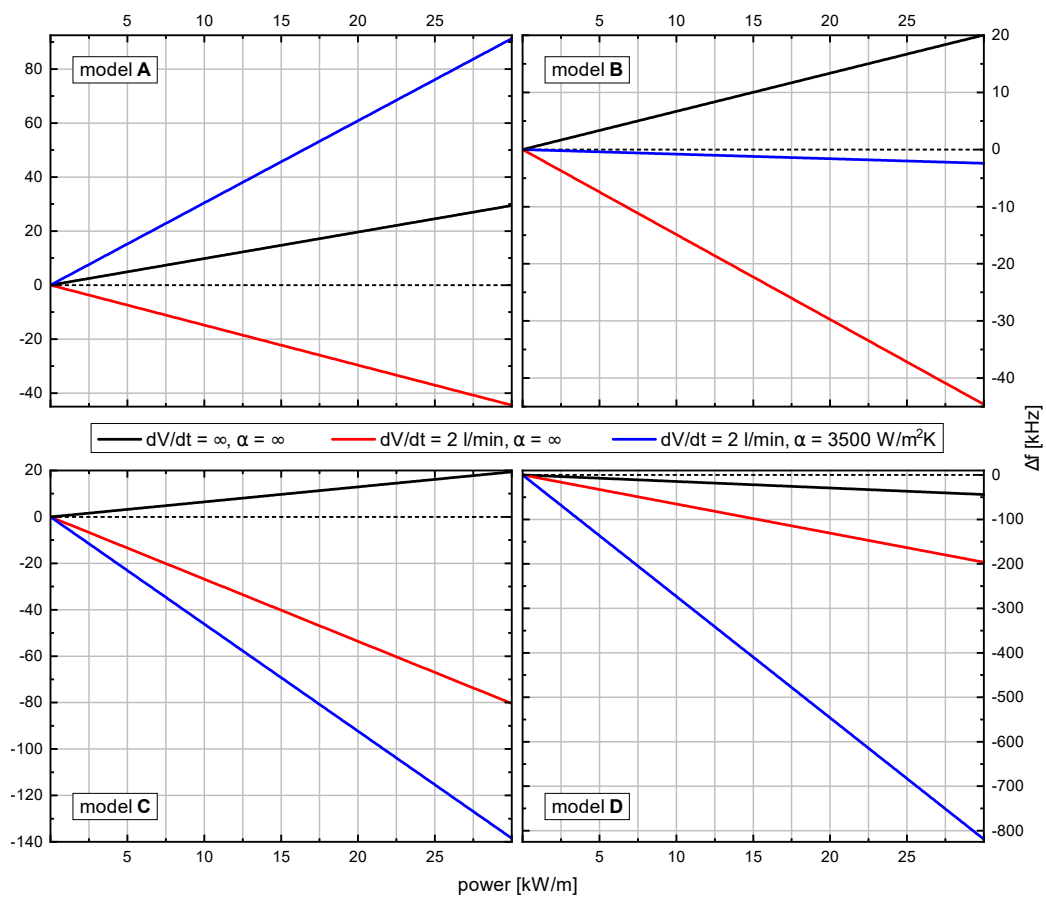
Figure 3.30: Simulated thermal frequency detuning Δf as function of the dissipated power P_c for different properties of the water flow and heat transfer, as well as different mechanical boundary models reproducing different mechanical coupling behavior between the electrode rods, stems and tuning plates according to Fig. 3.28.

The simulated thermal frequency detuning $\Delta f(P_c)$ as function of the dissipated power is shown in Fig. 3.30 for the four mechanical boundary models as well as three different cases concerning the quantity of water flow and heat transfer properties, which both have a huge and qualitative effect on the frequency detuning. The high sensitivity of the frequency on the water flow rate is due to the fact that the single cooling circuits of the electrodes extend over 5 to 6 RF resonator cells (see Fig. 3.29), which increases the overall heating of the cooling water, but also implies that the heated water has to travel a longer distance inside the copper structure. Furthermore, the influence of the heat transfer coefficient α is very significant because the cooling channels in the electrodes with a round cross-section profile of 6 mm radius provide a comparatively small surface area for heat transfer, considering the power loss density occurring on the electrodes (see Eq. 3.4). The simulated surface temperature distribution is shown in Fig. 4.19 for optimal and pessimistically assumed cooling properties.
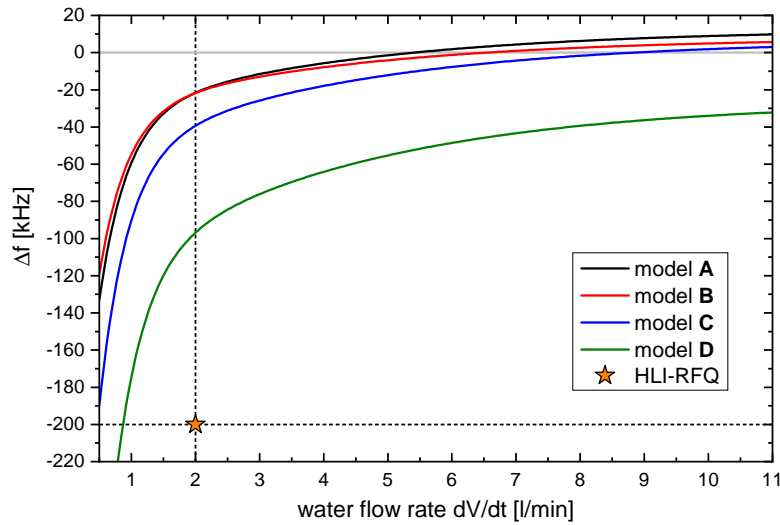
Figure 3.31: Simulated thermal frequency detuning Δf at a thermal load of 15 kW/m as function of the water flow rate, assuming perfect heat transfer, for different mechanical boundary models according to Fig. 3.28.

The influence of the thermal deformation of the RFQ structure on the resonance frequency is primarily determined by two effects: On the one hand, the electrode ends at the overhangs bend away from each other, which reduces capacitance and thus increases the resonance frequency. On the other hand, the inter-stem electrode sections tend to bend towards the center of the quadrupole due to thermal expansion, which in turn increases the capacitance and reduces the resonance frequency. Although the influence of the electrode deformation on the frequency is much greater than by the overhang (see Fig. 3.21), significant corresponding deformation amplitudes only occur at higher electrode temperatures. For this reason, the influence of the electrode deformation is typically exceeded by that of the overhang when the heat is dissipated efficiently, as with high water flow rates and good heat transfer, thus detuning the frequency upwards. Accordingly, as heat dissipation is reduced, the influence of the electrode deformation prevails and the frequency is hence tuned down, which can be clearly seen in Fig. 3.31, depicting the detuning as function of the water flow rate.

After all, at a power of 15 kW/m and a water flow rate through the RFQ components of roughly 2 l/min, the observed frequency detuning at the HLI-RFQ of -200 kHz can only be

reproduced in the simulations by model **D**, which indicates that mechanical coupling between thermal deformations of the electrodes and stems is only very weak and that the value of the heat transfer coefficient must be around $\alpha = 9250\,\mathrm{W/m^2K}$, according to Fig. 3.32.
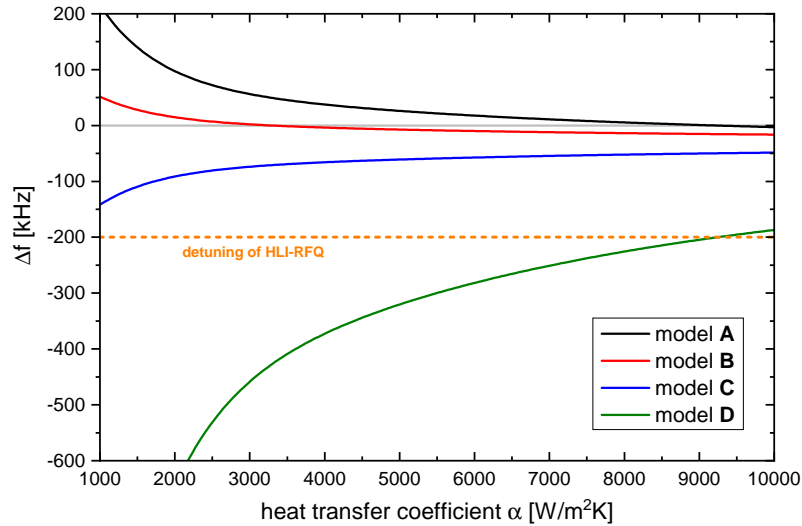
Figure 3.32: Simulated thermal frequency detuning Δf at a thermal load of $15\,\mathrm{kW/m}$ as function of the heat transfer coefficient, assuming a water flow rate of $2\,\mathrm{l/min}$, for different mechanical boundary models according to Fig. 3.28.
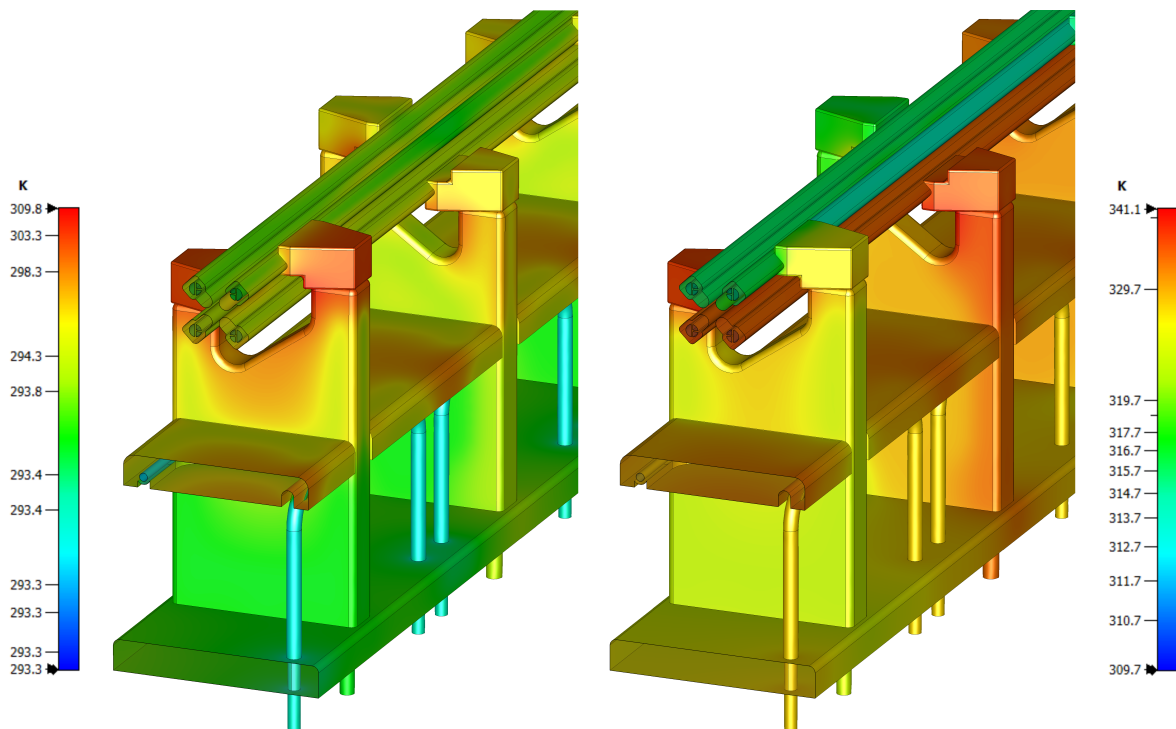
Figure 3.33: Simulated temperature distribution on the HLI-RFQ for $P_\mathrm{c} = 15\,\mathrm{kW/m}$ (*left*: perfect heat transfer and high water flow rate of $20\,\mathrm{l/min}$, *right*: finite heat transfer of $\alpha = 3500\,\mathrm{W/m^2K}$ and low water flow of $2\,\mathrm{l/min}$).

(4) Development & Test of a Newly Designed 6-Stem Prototype

Due to the problems with mechanical vibrations of the electrodes as well as the high thermal sensitivity, as both investigated in chapter (3), the existing HLI-RFQ is not suited for reliably providing beam according to the future requirements of either the CW linac or the UNILAC. Therefore, a new RF design for a completely revised 4-rod RFQ was developed with the aim to enable stable pulsed operation with high duty cycles up to CW mode at average heat loads in the order of 30–40 kW/m. The newly developed design is based on the concepts that were already applied to the RFQ designs for FRANZ ($f_0 = 175$ MHz) and MYRRHA ($f_0 = 176.1$ MHz), which have successfully proved reliability during long-term tests at very high power levels > 70 kW/m [152, 153]. Consequently, the main challenge was posed by the required adaption to the considerably lower HLI operating frequency of 108 MHz.

In general, 4-rod RFQs in the lower frequency range are prone to mechanical oscillations of the electrodes because the usually necessary larger distance between the stems facilitates mechanical deformations of the inter-stem electrode sections. Based on the experience from the preceding mechanical analysis of the existing HLI-RFQ, the newly revised design was developed with an emphasis on structural-mechanical simulations in order to efficiently suppress vibrational modes that have a perturbing effect on RF operation [154, 155]. The applicable methods for improving mechanical rigidity (e.g. thicker electrode rods, shorter stem distance) typically lead to a reduction of shunt impedance. Thus, the main design approach was to minimize the vibration amplitudes by increasing the mechanical rigidity under restriction to a reasonable decrease of shunt impedance and resulting increase of thermal load. Finally, in order to be able to extend the electrode length to over 2 m for reasons of beam dynamics and to enable power levels of more than 30 kW/m, the restriction to a maximum power consumption of 60 kW, which the design of the existing HLI-RFQ complies with, was dismissed. For the future operation of the newly developed full-length HLI-RFQ the acquisition of a new power amplifier with a sufficiently high power output around 100 kW is planned.

According to the results of relating RF and mechanical design studies, a 6-stem prototype was developed and manufactured. Unlike the commonly used 4-stem prototypes for RF tests of 4-rod RFQ designs, the configuration of the new prototype was upgraded to 6 stems with the aim to reproduce a mechanical eigenmode spectrum that is comparable to a longer structure with a higher number of stems. For the validation of the anticipated characteristics prior to RF conditioning and high-power tests of the prototype, extensive pre-tests were conducted. Both the RF and mechanical properties have been investigated by measurements of the RF frequency tuning, field flatness, Q factor, shunt impedance, dipole compensation, mechanical eigenmode spectrum [156] and mechanical damping characteristics. In order to study the vibration behavior during operation, further vibration measurements using a laser vibrometer are planned to be conducted during high-power tests, analogously to the measurements done at GSI on the existing HLI-RFQ as discussed in section 3.3.

This chapter presents the methods and results of the development and tests on the newly designed 6-stem prototype, including the initial design studies, the final RF design and its simulated properties, the pre-tests and low-level measurements as well as the RF pre-conditioning and preparations for high-power tests.

4.1 RF/Mechanical Design Studies

The basic FRANZ/MYRRHA RFQ design with its crucial geometric parameters is depicted in Fig. 4.1. The electrode rods consist of a square profile (edge length = "electrode profile") on the edge of which the actual electrode vane is placed, rotated by 45°. The square profile mainly provides the mechanical stability of the electrode rod and also contains the water cooling channels, as shown in Fig. 4.6. The rods are mounted to the stem arms by lateral trapezoid electrode mounting brackets (see Fig. 4.8 and Fig. 4.10 for a topview), whose dimension along the rod is parameterized by the "trapezoid base length". Throughout the entire process of the design studies, the distance between the square profiles of adjacent rods (= 15.2 mm) and the distance between the rods and the stem arms (= 10.9 mm) were maintained constant, according to the original specifications of the FRANZ/MYRRHA RFQ. Also, the length of the electrode overhang was kept constant at a value of 35 mm.
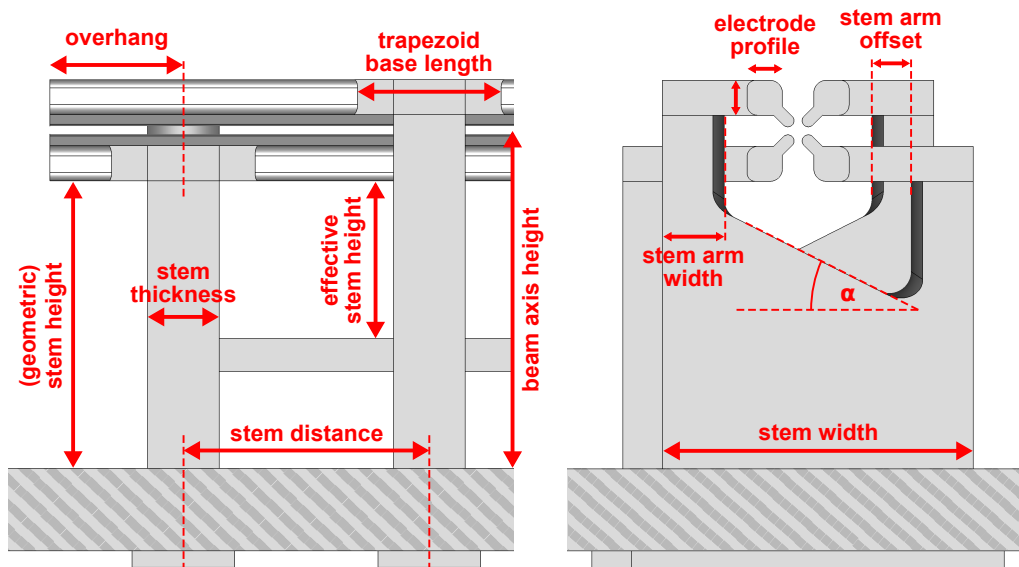
Figure 4.1: Basic geometric parameters considered for the design studies.

For the compensation of the electric dipole component a new method is applied, which was first implemented on the MYRRHA-RFQ [129]. Here, the current path to the lower electrodes is deliberately being extended by shifting the lower stem arms sideways, thus creating a stem arm offset and increasing the overall stem width. Due to the extension of the current path, the electric potential on the lower electrodes can be increased to an extend that allows to match the potential on the upper electrodes, thus effectively eliminating the dipole field (see section 2.3.5). Eventually, this method is mainly limited by the decrease of mechanical

rigidity resulting from the widening of the electrode mounting brackets as the stem arm off-set increases. Another, more conventional approach to influence the dipole magnitude is to increase the angle α of the stem cutting, which results in a steeper cutting and increases the total height of the lower stem arms. This provides more space for the magnetic field to form around the stem arm and increases charge transport to the undersupplied lower electrodes. After all, the thereby achievable moderate dipole compensation is limited by the thermal heating in the resulting acute angle opening as well as the increase of the stem arm height, which again leads to a higher susceptibility towards mechanical vibrations [139].

geometric design parameters		target properties (values)
rod geometry	stem distance	resonance frequency f_0 (108 MHz)
	$\begin{cases} \text{electrode profile} \\ \text{trapezoid base length} \end{cases}$	stem height (min.)
		shunt impedance R_{pL} (max.)
dipole compensation	$\begin{cases} \alpha \text{ (stem cutting angle)} \\ \text{stem arm offset} \end{cases}$	dipole ratio (0)
		mechanical eigenfrequencies (max.)
stem geometry	$\begin{cases} \text{stem thickness} \\ \text{stem width} \end{cases}$	

Table 4.1: Overview of the geometric design parameters and evaluated target properties.

The prototype was designed with flat electrodes without modulation, meaning that the aperture radius $r_{\mathrm{aperture}} = 4\,\mathrm{mm}$ and the electrode radius $r_{\mathrm{electrode}} = 3\,\mathrm{mm}$ are both constant along the beam axis. For each evaluated design iteration, the resonance frequency was adjusted to the nominal value of $f_0 = 108\,\mathrm{MHz}$ by varying the position of the tuning plates, which were all set to the same height without any flatness tuning. In case the resonance frequency is adjusted correctly, the distance from the tuning plates to the lower electrode rods defines the effective stem height. An overview of the basic independent variable geometric parameters considered for the design studies as well as the correspondingly evaluated target properties is given in Tab. 4.1. The shunt impedance R_{pL} was calculated according to Eq. 2.28, where U_0 was considered to be the mean vane voltage along the longitudinal axis. The stem height was always set to a value that allows a generous tuning range down to $-15\,\mathrm{MHz}$ ($f_0 = 93\,\mathrm{MHz}$) for all tuning plates being in the lowest position possible. The dipole ratio was evaluated according to Eq. 2.49.

$$A = \frac{F_0}{k\sqrt{\left(1 - \left(\frac{\Omega}{\omega}\right)^2\right)^2 + 4\zeta^2 \left(\frac{\Omega}{\omega}\right)^2}} \overset{\Omega \approx \omega}{=} \frac{F_0}{2k\zeta} = \frac{F_0}{c\omega} \tag{4.1}$$

The amplitude A of a forced mechanical vibration with viscous damping for a system with a single degree of freedom is given by Eq. 4.1, corresponding to the differential equation of motion $m\ddot{x} + c\dot{x} + kx = F_0 \sin(\Omega t)$ with mass m, damping coefficient c, (spring) stiffness coefficient k, magnitude F_0 of the harmoniously applied force with frequency Ω, the natural (angular) frequency $\omega = \sqrt{k/m}$ and the damping ratio $\zeta = c/c_0 = c/(2\sqrt{km})$ (with critical damping $c_0 = 2\sqrt{km}$) [157]. Considering the mechanical excitation of the RFQ electrodes

by the broadband edges of the RF pulses and assuming that the resonance frequencies of the mechanical eigenmodes are within the excitation bandwidth, the damper-controlled solution for $\Omega \approx \omega$ provides a rough qualitative estimation of the magnitude of the vibration amplitudes, relating to harmonic excitation. Accordingly, the vibration amplitudes are inversely proportional to the mechanical eigenmode frequency ω as well as to the corresponding damping $c(\omega)$, which again might be frequency dependent, whereas being proportional to the excitation force F_0 which relates to the applied electric field amplitude.

A more comprehensive quantitative characterization of vibrations at the electrode sections between adjacent mounting brackets is provided by the analytic approaches for forced transverse vibrations of a continuous bar with fixed ends, as discussed in [158] and [159].

Since the amount of damping cannot be predicted from numerical simulations with ANSYS, the actual vibration amplitudes could not be evaluated for the design studies. However, the mechanical eigenmode frequencies can be determined directly from the modal analysis solver and hence provide a convenient measure for the effect of a structural modification on the magnitude of the vibration amplitudes. Therefore, a main objective during the design process was to increase the frequency of the RF affecting unidirectional radial electrode mode.
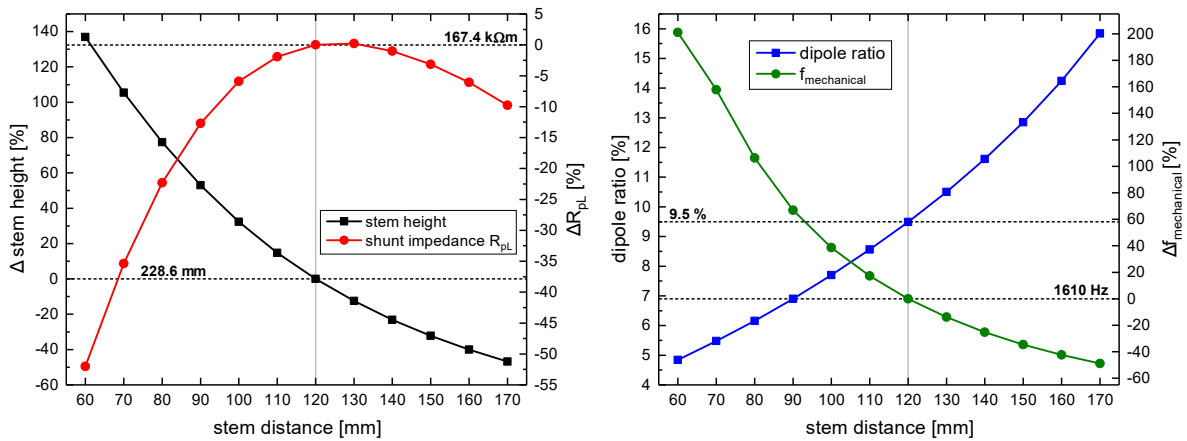
Figure 4.2: Variation of the stem distance.

First, based on the design specifications of the FRANZ/MYRRHA RFQs, an adapted reference design was derived with corresponding geometric parameters but a different stem distance, which was adapted to the lower nominal resonance frequency of $f_0 = 108\,\text{MHz}$ (see Tab. 4.2). According to Fig. 4.2, the stem distance was chosen to a value of 120 mm, close to the characteristic broad maximum of the shunt impedance curve as function of the stem distance (a similar optimization procedure for another 4-rod RFQ is presented in [160]). Thereby, the shunt impedance is maximized at the expense of the stem height increasing to almost twice its value compared to the case of a much larger stem distance $\geq 170\,\text{mm}$ as at the existing HLI-RFQ. However, since the reduction of the stem distance significantly improves the mechanical rigidity of the electrode rods, the frequency $f_{\text{mechanical}}$ of the unidirectional radial electrode eigenmode was almost doubled[1]. Another modification of the adapted reference design is the increased stem cutting angle of $\alpha = 30°$, since it already became apparent during the early stages of the design studies that this would avoid large required stem arm offsets in order to provide full dipole compensation. At the chosen value of $\alpha = 30°$, the re-

---

[1]simulated on the bottom electrode

sulting stronger thermal heating at the opening angle of the stem cutting and at the adjoining lower stem arms is still acceptable, as well as the slightly decreased mechanical rigidity due to their increased height. The remaining dipole ratio of the (uncompensated) reference design amounts to 9.5 %. This is significantly less compared to the (also uncompensated) FRANZ-RFQ design with a dipole ratio of 33.4 %, mostly because the dipole generally decreases with lower RF resonance frequencies (the frequency dependence of the dipole ratio is discussed in section 2.3.5). Based on the adapted reference design, the other geometric parameters were then further optimized, as described in the following.

	FRANZ design	MYRRHA design	reference design	prototype design
RF frequency [MHz]	175	176.1	108	108
stem distance [mm]	97	100	120	120
beam axis height [mm]	151	150	251.2	272.4
geometric stem height [mm]	128.4	127.4	228.6	247.8
effective stem height [mm]	59.7	53.4	144.1	156.4
electrode profile [mm]	15	15	15	17
trapezoid base length [mm]	54.2	54.2	54.2	89.2
stem cutting angle α [deg]	21.8	22.9	30	30
stem arm offset [mm]	0	18	0	15.9[2]
stem thickness [mm]	25	28	25	35
stem width [mm]	110	128	110	146.9
shunt impedance R_{pL} [kΩm]	79.9	82.6	167.4	146.6
dipole ratio [%]	33.4	-3.5	9.5	0.1
mechanical eigenfrequencies [Hz]:				
bottom electrode only	2081	2052	1610	2118
upper electrode only	2238	2147	1527	2085
entire structure	1332	1317	886	1087

Table 4.2: Comparison between the RFQ designs for FRANZ [152] and MYRRHA [88], the adapted reference design and the final prototype design regarding RF frequency, geometric design parameters, simulated RF properties (shunt impedance R_{pL} and dipole ratio, both simulated on a 4-stem model) and simulated RF affecting mechanical eigenfrequencies (on the electrodes only and for the entire structure, simulated on a 12-stem model).

As shown in Fig. 4.3, the shunt impedance as well as the stem height decreases almost linearly with increasing electrode profile. Both of this is due to the resulting increase in capacitance, which also leads to a linear increase of the dipole ratio. Eventually, it was decided to increase the electrode profile by 2 mm from the reference value (marked as vertical gray line) to a total of 17 mm. At that consideration, a resulting reduction of the shunt impedance by 5.2 % and a corresponding increase of the dipole ratio by 1 % seemed acceptable in order to reduce the stem height by 3.6 % and, most of all, yield a further increase $\Delta f_{\mathrm{mechanical}}$ of the mechanical eigenfrequency of the unidirectional radial electrode mode[1] by roughly 4.5 %.
Because the geometry of the trapezoid electrode mounting brackets barely affects the overall capacitance, there is only very little influence of their size on the shunt impedance, stem height and dipole ratio. However, the mechanical stiffness of the electrode rod is considerably

---

[2]for a better comparability of the resulting mechanical eigenfrequencies, this value already corresponds to the final 6-stem prototype configuration

enhanced by enlarging the mounting brackets. Therefore, the trapezoid base length was increased from its reference value of 54.2 mm to the largest possible, practically applicable, dimension of 89.2 mm. Thereby, a remarkable increase of the mechanical eigenfrequency[1] of about 18.5 % could be achieved with virtually no impairment of the RF properties.
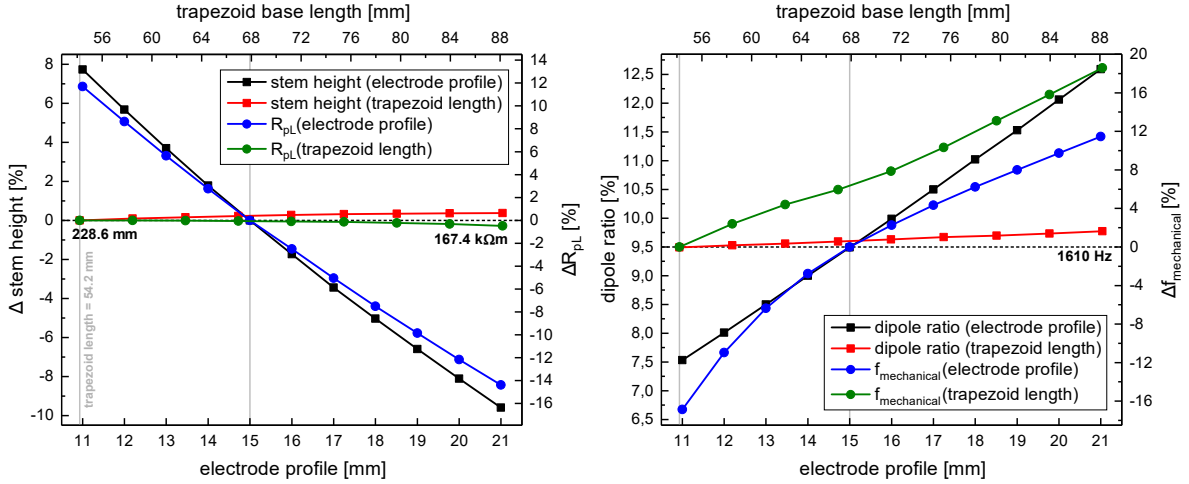
Figure 4.3: Variation of the electrode geometry (electrode profile and base length of the trapezoid electrode mounting bracket).
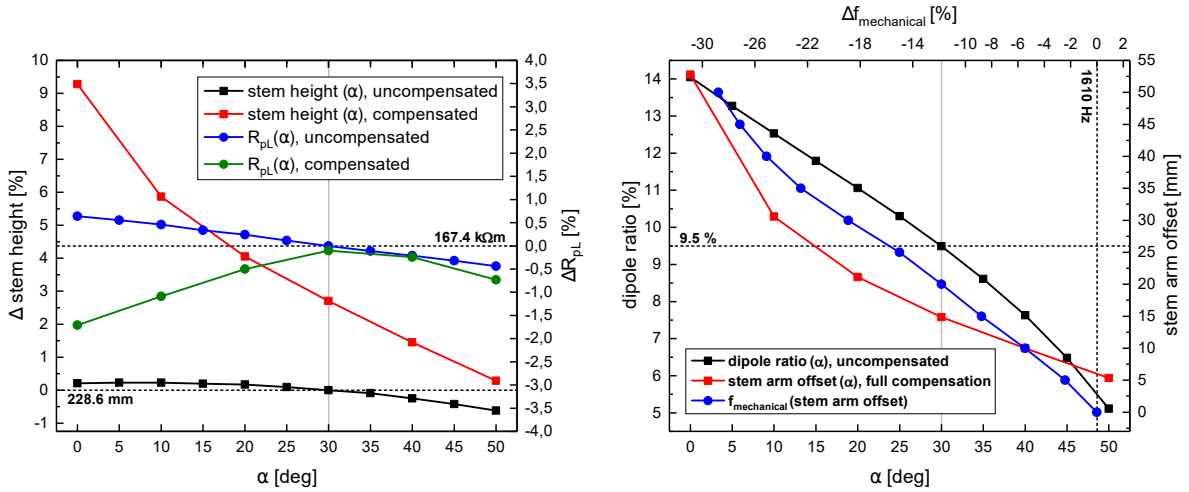
Figure 4.4: Variation of the stem cutting angle α and stem arm offset for dipole compensation.

On the left, Fig. 4.4 shows the dependence of the stem height and shunt impedance R_{pL} on the stem cutting angle α, regarding the case without any dipole compensation being applied (zero stem arm offset), as well as for full dipole compensation with correspondingly adjusted stem arm offset. The right side, on the other hand, shows the dipole ratio as function of α (again for the uncompensated case with zero offset), the required stem arm offset for full dipole compensation as function of α, and the influence of the stem arm offset on the mechanical eigenmode frequency of the unidirectional radial electrode mode[1].

Accordingly, the variation of the stem cutting angle α affects the stem height and shunt impedance only to a very small extent of about 1 %, considering the uncompensated case

with zero stem arm offset. However, this allows the dipole ratio to be reduced from 14% for $\alpha = 0$, corresponding to a horizontal stem cutting, to 9.5% for $\alpha = 30°$, which is the maximum value of the stem cutting angle as already specified for the reference design in order to limit the height and heating of the lower stem arms. With $\alpha = 30°$, the required stem arm offset for yielding full dipole compensation amounts to roughly $15\,\mathrm{mm}$. For this case, the stem height increases only slightly by 2.7% and the shunt impedance hardly changes from the reference value of $167.4\,\mathrm{k\Omega m}$. After all, the associated resulting decrease of the mechanical eigenmode frequency amounts to a considerable value of $\Delta f_\mathrm{mechanical} = -9\%$, which consequently had to be accepted in order to achieve the pursued full compensation of the electric dipole.
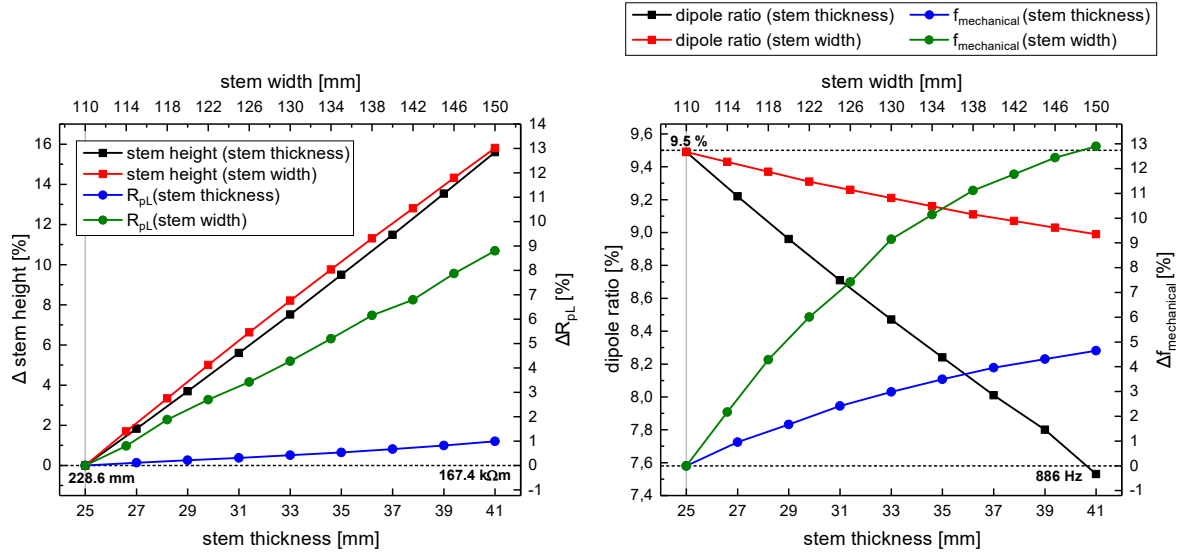
Figure 4.5: Variation of the stem geometry (stem thickness and stem width).

The influence of the stem geometry on the RF properties and unidirectional radial mechanical eigenmode frequency[3] is depicted in Fig. 4.5. On the one hand, the stem thickness was varied, effectively altering the distance between the opposing surfaces of adjacent stems while keeping the stem distance constant (which is defined as the distance between the stem centers). Considering the finally applied increase of the stem thickness to $35\,\mathrm{mm}$ from the reference value of $25\,\mathrm{mm}$, the shunt impedance is only insignificantly affected ($\Delta R_\mathrm{pL} < 1\%$) and the dipole ratio reduces by roughly 1.3%, whereas the stem height increases by about 9.5%. The corresponding increase of the mechanical eigenmode frequency amounts to 3.5%.

On the other hand, the stems were also widened laterally, while retaining all other dimensions, corresponding to an increase of the stem arm width towards the outside. This increases the cross section for the current flow on the stem arms and thus improves shunt impedance, but also significantly increases the mechanical rigidity, especially considering lateral deformations. Eventually, the stem arms have been widened by $10.5\,\mathrm{mm}$ each and hence the overall stem width increased from $110\,\mathrm{mm}$ to $131\,\mathrm{mm}$, resulting in a total of $146.9\,\mathrm{mm}$ after dipole compensation with a stem arm offset of $15.9\,\mathrm{mm}$. While again suffering an increase in stem height by 8.4%, this however increases the shunt impedance by 4.6% and the dipole ratio decreases only slightly by about 0.3%. The accordingly achieved increase $\Delta f_\mathrm{mechanical}$ of the mechanical eigenmode frequency amounts to remarkable 9.5%.

---

[3]evaluated on the bottom electrode, simulated on the full modell including the stems (entire structure)
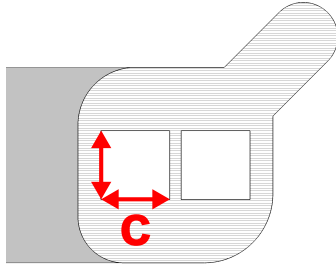
Figure 4.6: Profile of the electrode rod with square cooling channels (edge length $= c$).
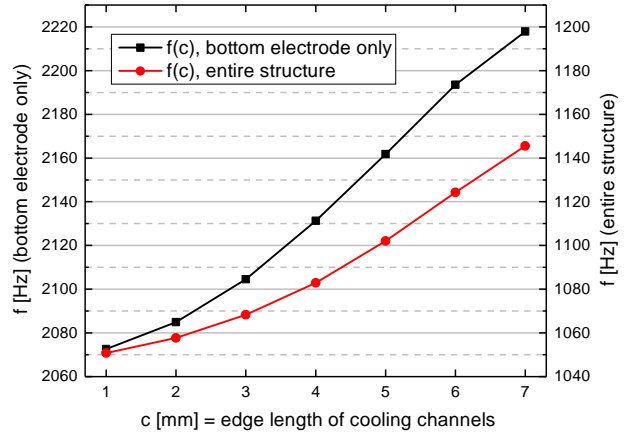
Figure 4.7: Influence of the cooling channel size on the mechanical eigenfrequencies.

Relating to the simulated eigenmode spectra on the existing HLI-RFQ, as given in section 3.4.1, the values of the frequencies differ only slightly between the applied simulation models (model **A**: upper electrode only, model **B**: entire structure). This is because the long and thin inter-stem electrode segments are mechanically much softer than the comparatively rigid stems. Hence, the mechanical oscillations take place mainly on the electrode rods, while the stem arms move along only slightly or not at all. Regarding the much stiffer electrode geometry of the basic FRANZ/MYRRHA RFQ design, a significant part of the vibration is transmitted to the stem arm or to the entire stem. This results in a much larger discrepancy between the simulated frequencies on either only the electrode rods or on the entire RFQ model, with the respective values differing by a factor of almost 2 (see Tab. 4.2).

The applied design approach of maximizing the eigenfrequencies in order to obtain lower vibration amplitudes implies the assumption that the resulting increase in frequency $\Delta\omega = \sqrt{(k + \Delta k)/(m + \Delta m)}$ is solely attributed to an increased stiffness $\Delta k > 0$, which effectively is the case when the oscillating mass remains constant or increases ($\Delta m \geq 0$). This is true for all previously conducted structural-mechanical optimizations concerning the stiffening of the electrode rods or stems, where the modification of the geometry was always associated with an increase of mass ($\Delta m > 0$). However, regarding the effect from enlarging the cooling channel size, which leads to an increase in frequency as depicted in Fig. 4.7, this assumption is violated due to the resulting reduction of mass ($\Delta m < 0$). Eventually, this is the reason why the mechanical eigenfrequencies increase, although the stiffness (k) and damping (c) obviously both decrease because of the increasing internal hollowness of the electrode rod, which most likely even leads to increased vibration amplitudes. After all, this effect cannot be predicted easily from only the frequency consideration[4]. In general, however, it can be argued that from a structural-mechanical point of view the cooling channels should be kept as small as possible, regardless of the effect on the mechanical frequencies, in order to maximize stiffness and damping. On the other hand, this of course has to be carefully considered with regard to the cooling performance. Concerning the design studies, all mechanical eigenmode simulations were conducted on a 12-stem model with rectangular cooling channels with edge lengths of 5×3 mm.

---

[4]in fact, the effect on the stiffness can be estimated from simulations of the reaction to a statically applied force

The properties of the evolved final prototype design are summarized in Tab. 4.2 and result from the non-linearly accumulated effects of the various separate parameter adjustments, an overview of which is given in Tab. 4.2. After all, the simulated mechanical eigenfrequency of the RF affecting unidirectional radial electrode mode could be increased significantly to 1087 Hz, which is more than twice compared to the existing HLI-RFQ with 501 Hz. The expected shunt impedance[5] of $110\,\mathrm{k\Omega m}$ ($= 146.6\,\mathrm{k\Omega m} \times 0.75$) corresponds well to the HLI-RFQ with $R_{\mathrm{pL}} = 108\,\mathrm{k\Omega m}$. The simulated full compensation of the electric dipole component could be achieved without difficulty. A distinctive characteristic of the prototype design are the strikingly high stems. A more detailed description of the final prototype specifications and its simulated properties is given in the following section.
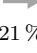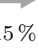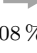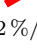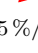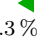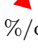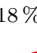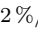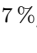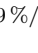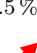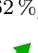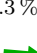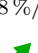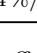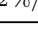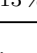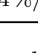
↓ varied parameters	Δh_{stem}	ΔR_{pL}	dipole ratio	$\Delta f_{\mathrm{mechanical}}$
stem distance	$-13.6\,\%/\mathrm{cm}$	$\pm 2.2\,\%/\mathrm{cm}$	$+1\,\%/\mathrm{cm}$	$-15.5\,\%/\mathrm{cm}$
electrode profile	$-1.8\,\%/\mathrm{mm}$	$-2.6\,\%/\mathrm{mm}$	$+0.5\,\%/\mathrm{mm}$	$+2.5\,\%/\mathrm{mm}$
trapezoid base length	$+0.21\,\%/\mathrm{cm}$	$-0.15\,\%/\mathrm{cm}$	$+0.08\,\%/\mathrm{cm}$	$+5.5\,\%/\mathrm{cm}$
stem arm offset	$+2\,\%/\mathrm{cm}$	$-0.5\,\%/\mathrm{cm}$	$-6.3\,\%/\mathrm{cm}$	$-6\,\%/\mathrm{cm}$
stem cutting angle α	$-0.18\,\%/10°$	$-0.22\,\%/10°$	$-1.7\,\%/10°$	$-0.9\,\%/10°$
stem thickness	$+9.5\,\%/\mathrm{cm}$	$+0.62\,\%/\mathrm{cm}$	$-1.3\,\%/\mathrm{cm}$	$+4.8\,\%/\mathrm{cm}$
stem width	$+4\,\%/\mathrm{cm}$	$+2.2\,\%/\mathrm{cm}$	$-0.13\,\%/\mathrm{cm}$	$+5.4\,\%/\mathrm{cm}$

Table 4.3: Overview of the separate effects of each parameter variation considered for the design studies on the stem height (Δh_{stem}), shunt impedance (ΔR_{pL}), dipole ratio and frequency of the unidirectional mechanical radial electrode mode ($\Delta f_{\mathrm{mechanical}}$). The specified values correspond to the change of the evaluated properties per typical order of magnitude of the respective variation.

4.2 Prototype Design & Simulated Properties

Based on the preceding design studies on 4-rod RFQ models with 4 and 12 stems for RF and structural-mechanical simulations, respectively, the final technical design for the 6-stem prototype was derived in close consultation with the chosen manufacturer NTG GmbH [58]. As stated in Tab. 4.4, the stem height had to be increased again from the 4-stem model in order to obtain the aimed frequency range by the tuning plates down to $-15\,\mathrm{MHz}$, taking into account the two additional RF cells. Also, the stem arm offset needed to be readjusted to $15.9\,\mathrm{mm}$. The position and size of the designated plunger tuner, which can be placed between two stems, was chosen to provide a dynamic tuning range of $\pm 200\,\mathrm{kHz}$.

---

[5]based on experience, the real shunt impedance can be expected to amount approximately 75 % of the simulated value

For reasons of mechanical production the final prototype structure, which is shown in Fig. 4.8 and Fig. 4.9, has some minor geometric deviations compared to its simulation model used in CST Microwave Studio, mostly affecting the rounding radii of the edges on the stems (including the stem arms) and electrode mounting brackets. Also, the profile of the electrode vane tip was flattened towards the end in order to reduce the surplus overhang capacitance. Overall, this results in very slight deviations of the final simulated RF properties from the nominal target values according to which the simulation model was optimized for, which eventually is the reason for the simulated value of the dipole ratio not being exactly zero.
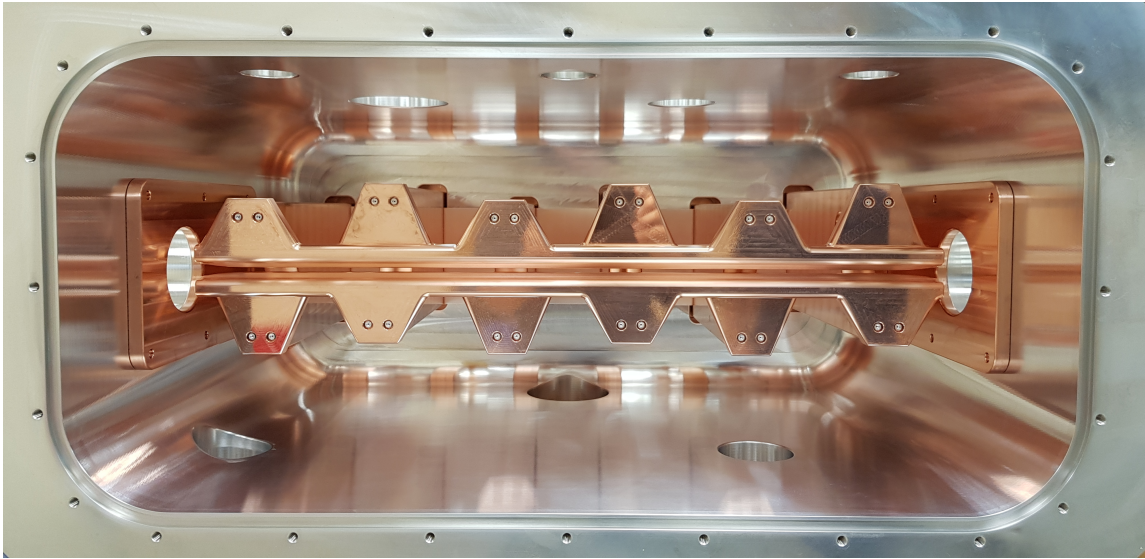

Figure 4.8: Topview of the 6-stem 4-rod RFQ prototype (photo taken by NTG GmbH).

RF design frequency [MHz]	108.0
quality factor (sim./exp.)	6680 / 5010
shunt impedance (sim./exp.) [kΩm]	145 / 109
dipole ratio [%]	0.3
mechanical electrode eigenfrequency [Hz]	985.9
RF tuning range (tuning plates) [MHz]	$92.5 - 153$
dynamic RF tuning range (plunger tuner) [kHz]	± 200
electrode length [mm]	702
$r_{\mathrm{electrode}}/r_{\mathrm{aperture}}$	0.75
beam axis height [mm]	307.3
(geometric) stem height [mm]	282.7
effective stem height [mm]	179.2
stem arm offset [mm]	15.9

Table 4.4: Final design parameters and simulated properties of the 6-stem prototype (all other geometric parameters correspond to Tab. 4.2).
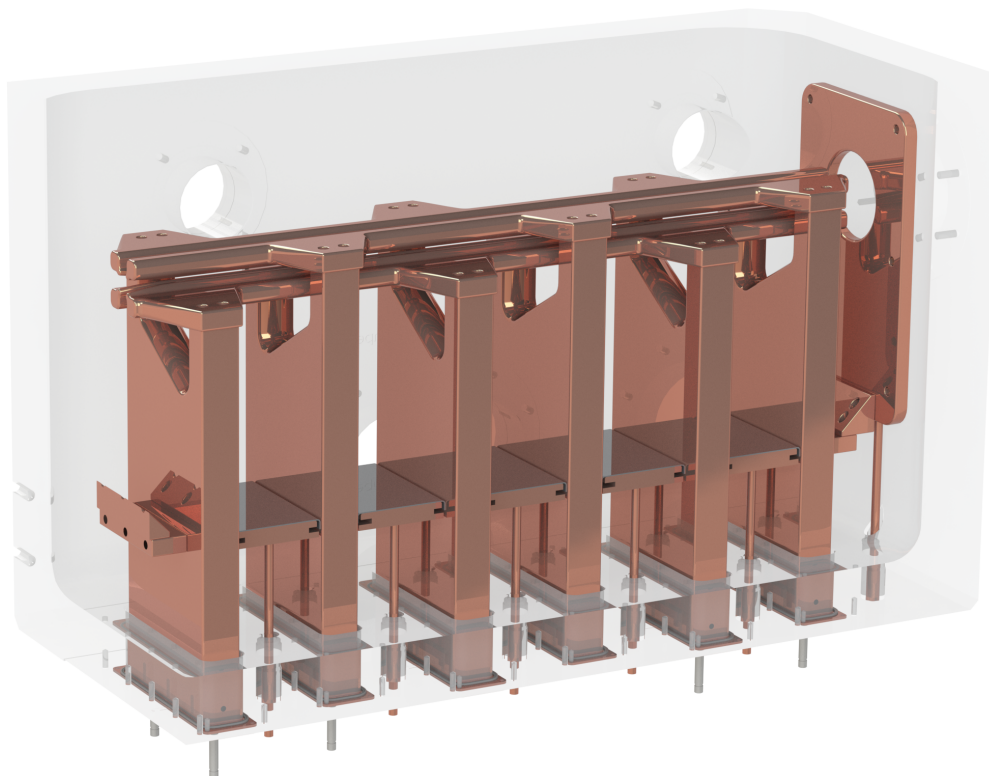
Figure 4.9: Rendered sectional view of the 6-stem 4-rod RFQ prototype (with transparent tank).

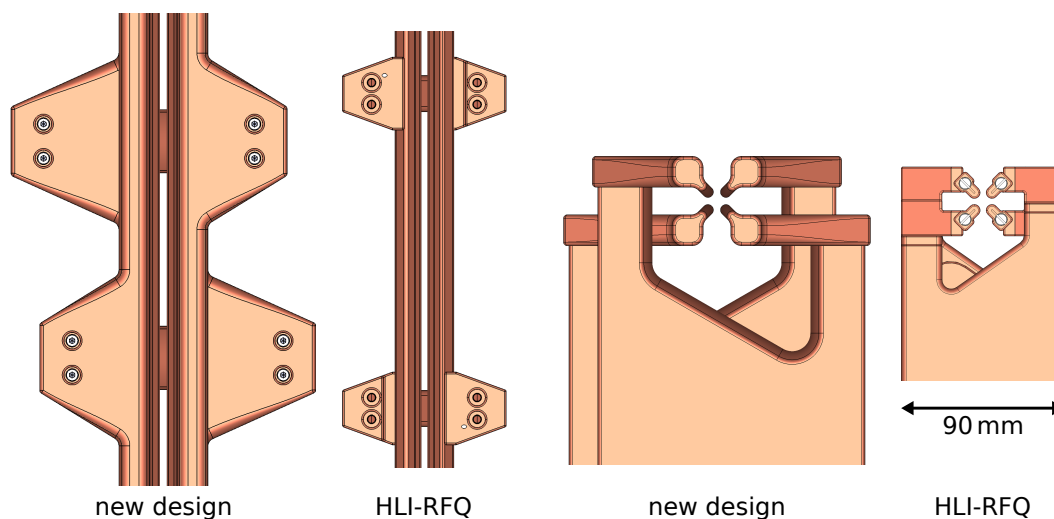| new design | HLI-RFQ | new design | HLI-RFQ |

90 mm

Figure 4.10: True-to-scale comparison between the HLI-RFQ and the newly developed prototype.

After all, the expected shunt impedance remains virtually unaffected at $R_{\mathrm{pL}} = 109\,\mathrm{k\Omega m}$ with an expected value for the quality factor of $Q = 5010$. The total tuneable frequency range is from 92.5 to 153 MHz for the tuning plates being in the lowest and highest possible position, respectively. Because the 6-stem structure has a lower overall mechanical stiffness compared

to the 12-stem simulation model as considered for the design studies, the frequency of the lowest unidirectional mechanical radial electrode eigenmode decreased from 1087 to 985.9 Hz, which is also affected by the slightly enlarged cooling channel size with edge lengths of now 8×3 mm. The substantial mechanical reinforcement of the resonator structure compared to the existing HLI-RFQ is depicted in Fig. 4.10.

As shown in Fig. 4.11, the prototype tank is fitted with a total of four ISO-F DN 100 flanges for connecting a vacuum pump and an RF coupler as well as two blind flanges at the hypothetical beam entrance and exit. An ISO-F DN 63 flange is provided for moving the plunger tuner into the cavity and three KF 40 flanges can be used for RF and vacuum diagnostics. For the purpose of vibration measurements with a laser vibrometer during RF operation, the RFQ tank is also equipped with four additional diagnostic windows (ISO-F DN 63). Whereas two of which are located on the upper cavity lid, with one targeting the overhang of the upper electrode and the other targeting the inter-stem section adjacent to the corresponding opposite electrode end, the other two windows are positioned sideways with each again being targeted to one of the same respective spots. This configuration allows to measure vibrations at the two designated points on both transversal spatial axes.
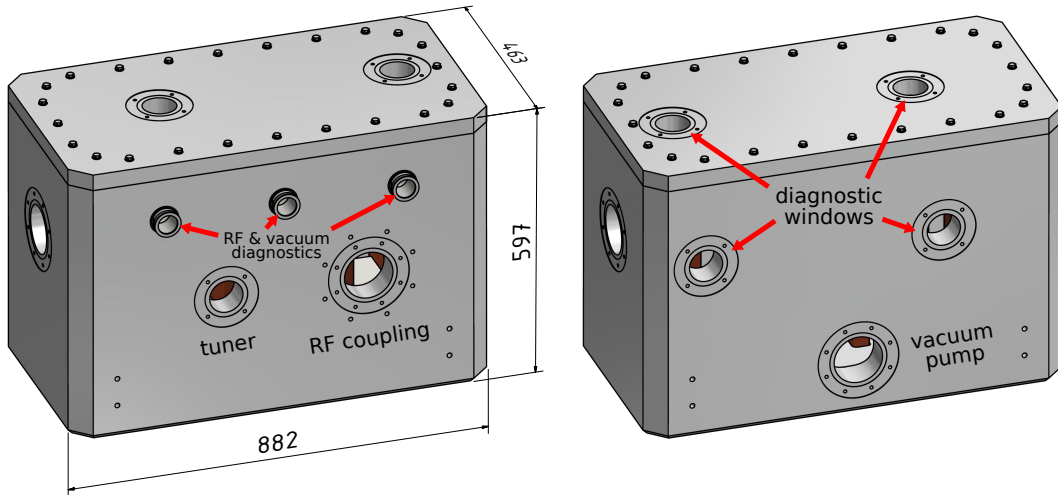

Figure 4.11: Prototype tank dimensions (in mm) and flange configuration.

According to Fig. 4.12, the order of modes in the simulated mechanical eigenmode spectrum of the 6-stem prototype shows several differences to that of the existing HLI-RFQ (see Fig. 3.12 for comparison, but be aware that here only eigenmodes on the upper electrode have been considered). First of all, the spectra of eigenmodes for the upper and lower electrode, respectively, now are substantially different, which is mainly caused by the differing geometry of the electrode mounting brackets due to the introduced stem arm offset, affecting the lower electrode. Second, in addition to the stem modes that already occurred before (Fig. 4.16), also a number of stem torsion modes can be observed (Fig. 4.15), which is a consequence of the large stem height. Third, because the square electrode profile now is very large compared to the vane tip, two more planes of symmetry emerge in vertical and horizontal orientation, thus resulting in accordingly oriented additional vibrational planes.
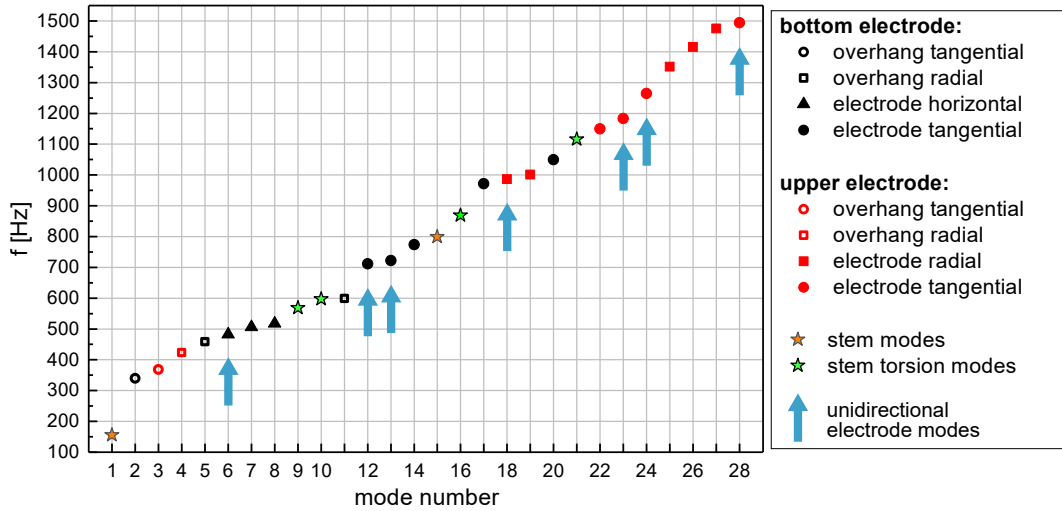
Figure 4.12: Simulated mechanical eigenmode spectrum of the 6-stem prototype.
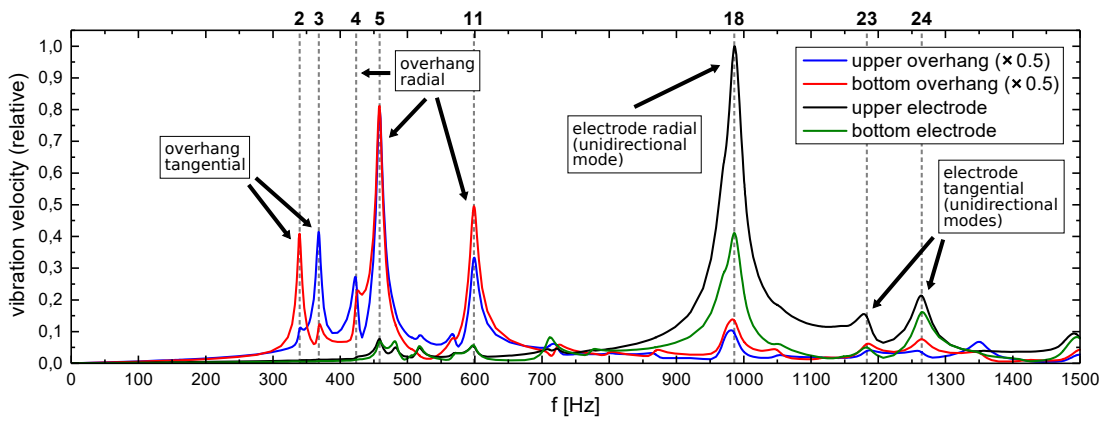

Figure 4.13: Simulated resonance response spectra for the overhang ends and the centers of the inter-stem electrode sections of the 6-stem prototype with perfect radial excitation (the values for the overhangs are scaled down with a factor of 0.5).
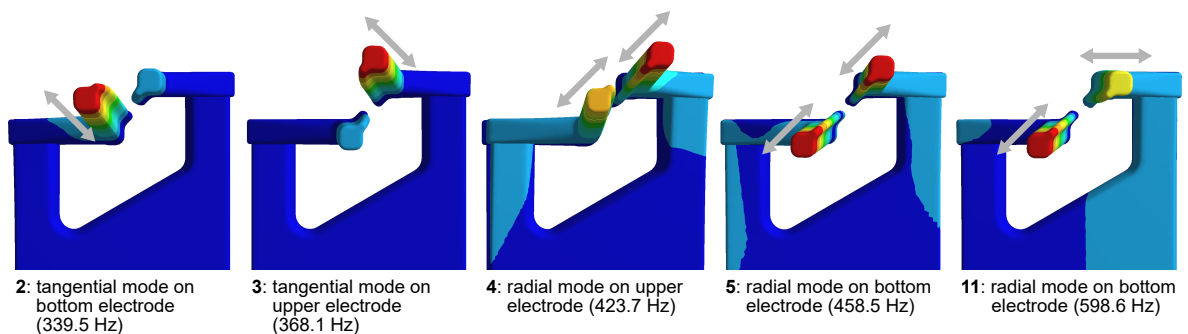

2: tangential mode on bottom electrode (339.5 Hz)

3: tangential mode on upper electrode (368.1 Hz)

4: radial mode on upper electrode (423.7 Hz)

5: radial mode on bottom electrode (458.5 Hz)

11: radial mode on bottom electrode (598.6 Hz)

Figure 4.14: Mechanical eigenmodes of the electrode overhangs (front view, the gray arrows indicate the vibrational planes).
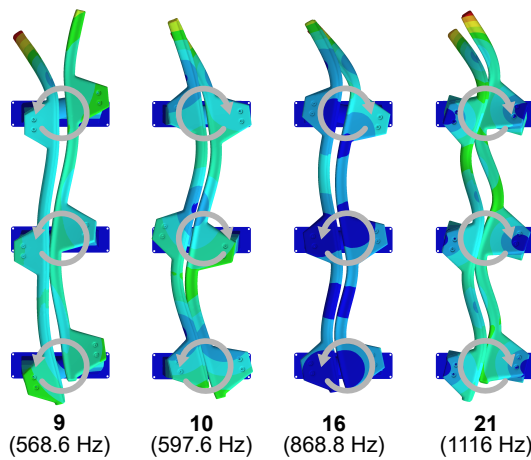
9
(568.6 Hz)

10
(597.6 Hz)

16
(868.8 Hz)

21
(1116 Hz)

Figure 4.15: Stem torsion modes (topview, the gray arrows indicate the orientation of the stem torsion).

1: first order stem mode (156 Hz)

15: second order stem mode (799 Hz)

Figure 4.16: Stem modes (sideview).

6: horizontal mode on bottom electrode (482.4 Hz)

12: tangential mode on bottom electrode (711.2 Hz)

13: tangential mode on bottom electrode (773.4 Hz)

18: radial mode on upper electrode (985.9 Hz)

23: tangential mode on upper electrode (1182.9 Hz)
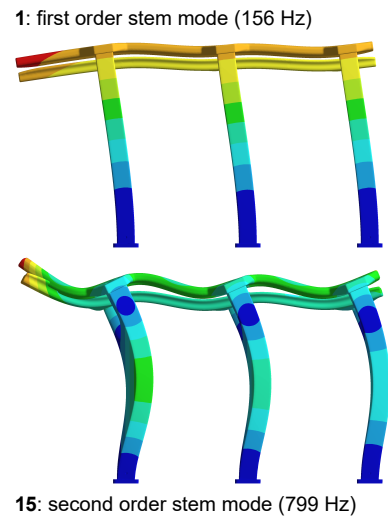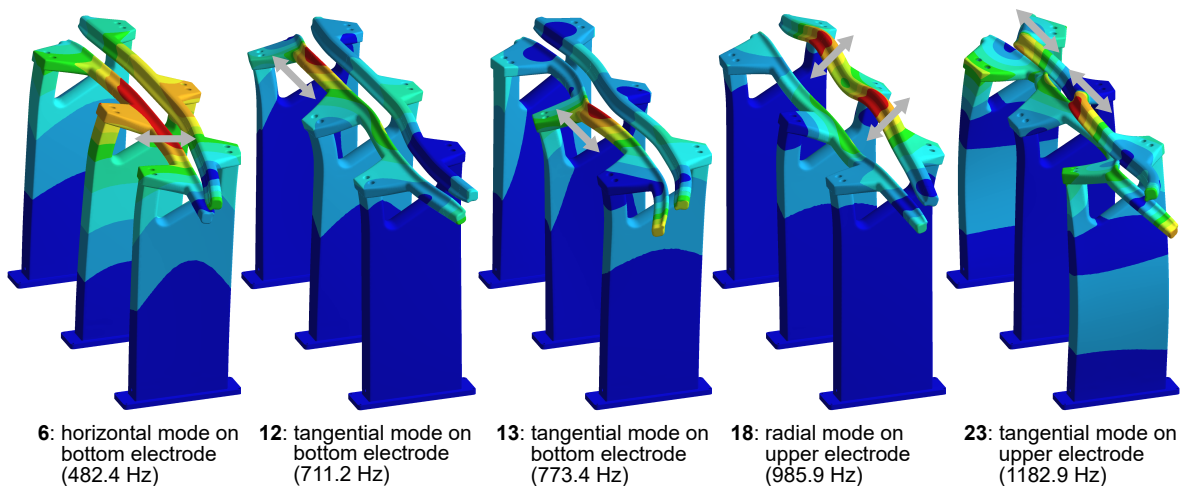
Figure 4.17: Overview of unidirectional electrode modes (perspective view, the gray arrows indicate the vibrational planes).

As shown in Fig. 4.13, perfect radial excitation as corresponding to the effect of an ideal electric quadrupole field (also see section 3.4.2) causes mechanical oscillations of the electrode overhangs in almost all their eigenmodes, which are depicted in Fig. 4.14. Considering opposite electrodes, the associated mechanical forces always act in opposite direction (antiphase excitation) and hence the comparatively weak presence of the radial mode 4 in the simulated spectrum can be explained by its in-phase deformation of the overhang ends, whereas otherwise the also radial mode 5 with corresponding antiphase deformation is most strongly being excited. The noticeable occurrence of the tangential overhang modes (modes 2 and 3) is due to the fact that the respective vibrational planes are slightly tilted relative to the tangential plane, which results from the influence of the mounting bracket and stem arm deformations on the overall deformation profile of the electrode rod. The accordingly minor but non-zero radial deformation component of the primarily tangential eigenmodes eventually leads to the

observed excitation by the ideal radially acting excitation force.

As already expected, the only electrode mode that occurs in the response spectrum with a significant amplitude is the unidirectional radial mode 18, which besides being the only unidirectional radial electrode mode also has antiphase electrode deformation, as can be seen in Fig. 4.17. Whereas mode 18 with an eigenfrequency of 985.9 Hz is primarily an oscillation mode of the upper electrode, the frequency of the corresponding eigenmode on the bottom electrode is above 1500 Hz. Regarding the striking horizontal mode 6, which oscillates predominantly on the bottom electrode but however is also associated with a significant deformation of the upper electrode, the condition of in-phase deformation for both electrodes effectively suppresses excitation by the forces associated with the electric quadrupole field. For the same reason as with the overhang oscillations, also some tangential electrode modes are weakly recognizable in the response spectrum (see modes 23 and 24).
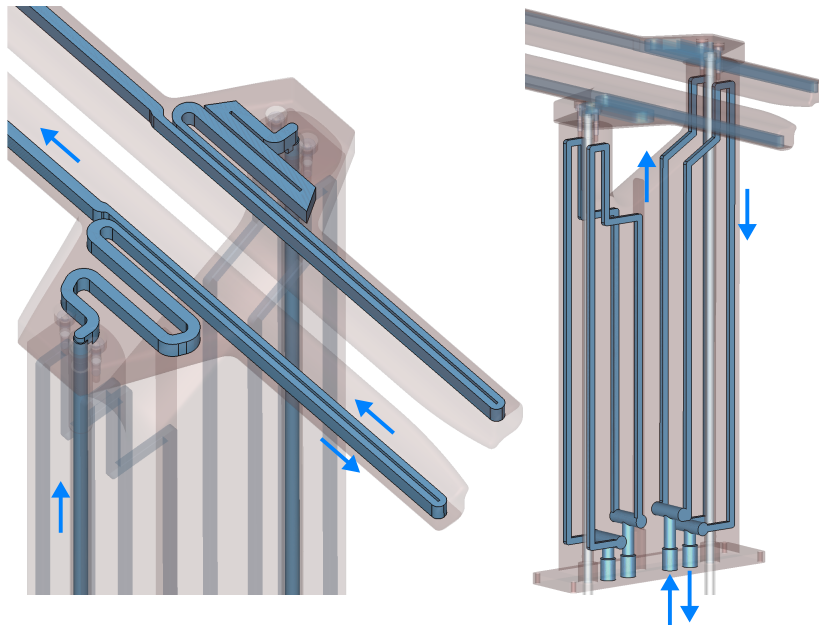

Figure 4.18: Cooling channels in the electrodes (*left*) and stems (*right*) of the 6-stem prototype (the blue arrows indicate the direction of water flow).

The routing of the water cooling channels through the electrodes and stems is shown in Fig. 4.18. Each stem is fitted with two separate cooling circuits, which are further divided into two channels that are located at a depth of 2 mm below the copper surface and reach as high as practically possible into the stem arms, which besides the opening of the acute stem cutting angle are the most heat loaded areas of the stem surface. The horizontal positions of the long vertically running channel sections were optimized by thermal simulations to a uniform temperature distribution on the stem surface, which can be seen in Fig. 4.19. In order to optimize the cooling of the large electrode mounting brackets, which carry the entire current flow from the stems to the electrodes, they have been fitted with maze-like cooling loops which feed the water from the inlet through the stem into the electrode cooling circuit. At the 6-stem prototype, each electrode is mounted on an uneven number of 3 stems, with the water in- and outflow to and from the electrodes being at the first and third stem, respectively, thus

the entire electrode being cooled by a single water circuit that spans over a total of 5 RF cells. In case of longer RFQ structures with more than 6 stems and each electrode being mounted on an even number of stems, the in- and outflow can be located at adjacent stems connected to the same electrode, reducing the number of RF cells to 3, over which each cooling channel of the electrodes extends. A dedicated feature for thermal diagnostics of the prototype is provided by additional vertical hollow channels inside the stems, through which thermo sensors can be inserted from the outside and placed at a position close to the stem cutting surface in order to measure the material temperature for comparison with simulations (see Fig. 4.42).
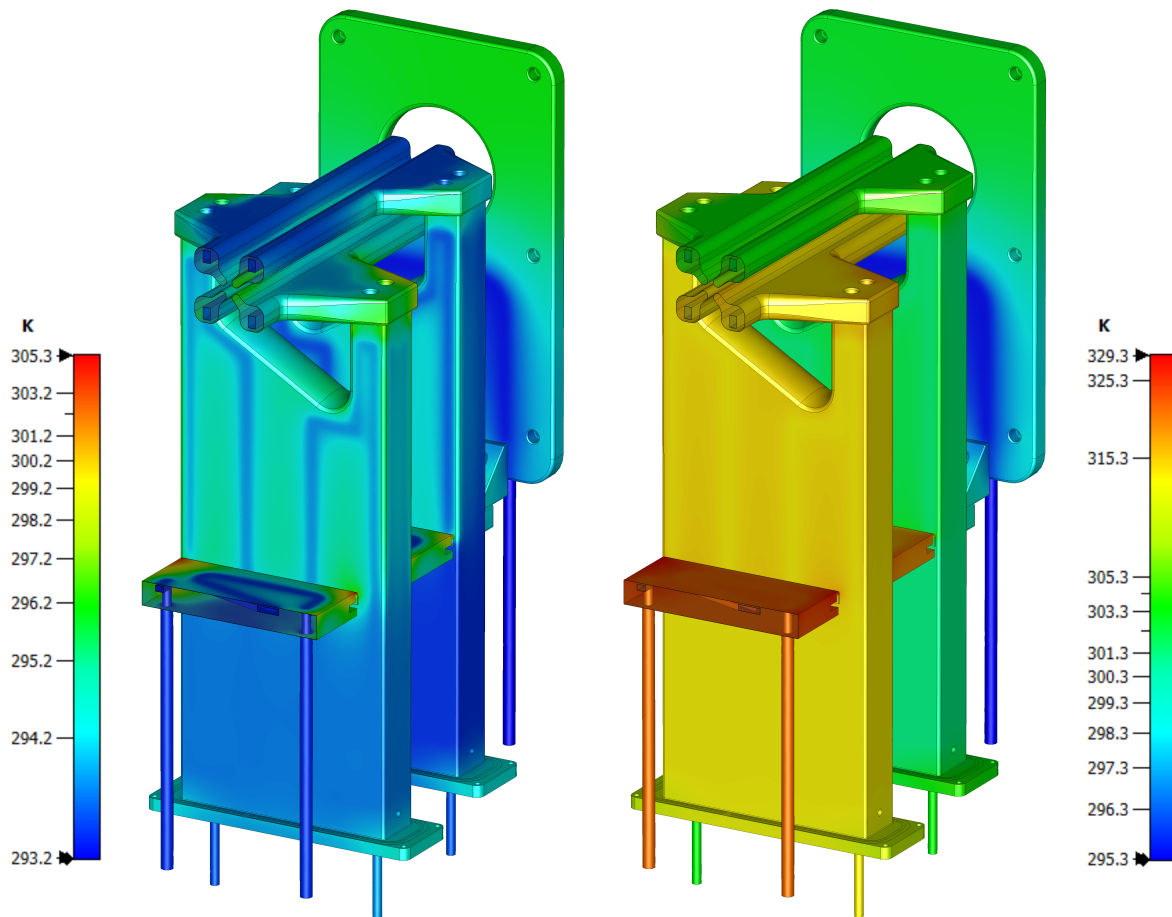

Figure 4.19: Simulated temperature distribution on the 6-stem prototype for $P_c = 30\,\mathrm{kW/m}$ (*left*: perfect heat transfer and high water flow rate of 20 l/min, *right*: finite heat transfer of $\alpha = 3500\,\mathrm{W/m^2K}$ and low water flow of 2 l/min).

In principle, the cooling channels are completely embedded within the solid copper structure, which is made possible by a new fabrication technique developed by NTG GmbH. At this, the channels are first milled into the prefabricated bottom part of the copper structure and then filled with a special wax. In the next step, the channels are closed by applying the entire surface layer of the structure by thick copper plating using electro forming, before the wax is being removed again [88]. The produced solid copper structure provides highly efficient heat conduction from the stem surface to the cooling channels, without additional material

transitions such as welding or soldering seams, which is a significant advantage regarding the production of CW RFQs with an average power loss of up to several tens of kW/m. This new technique was first used to fabricate the RFQs for FRANZ and MYRRHA.
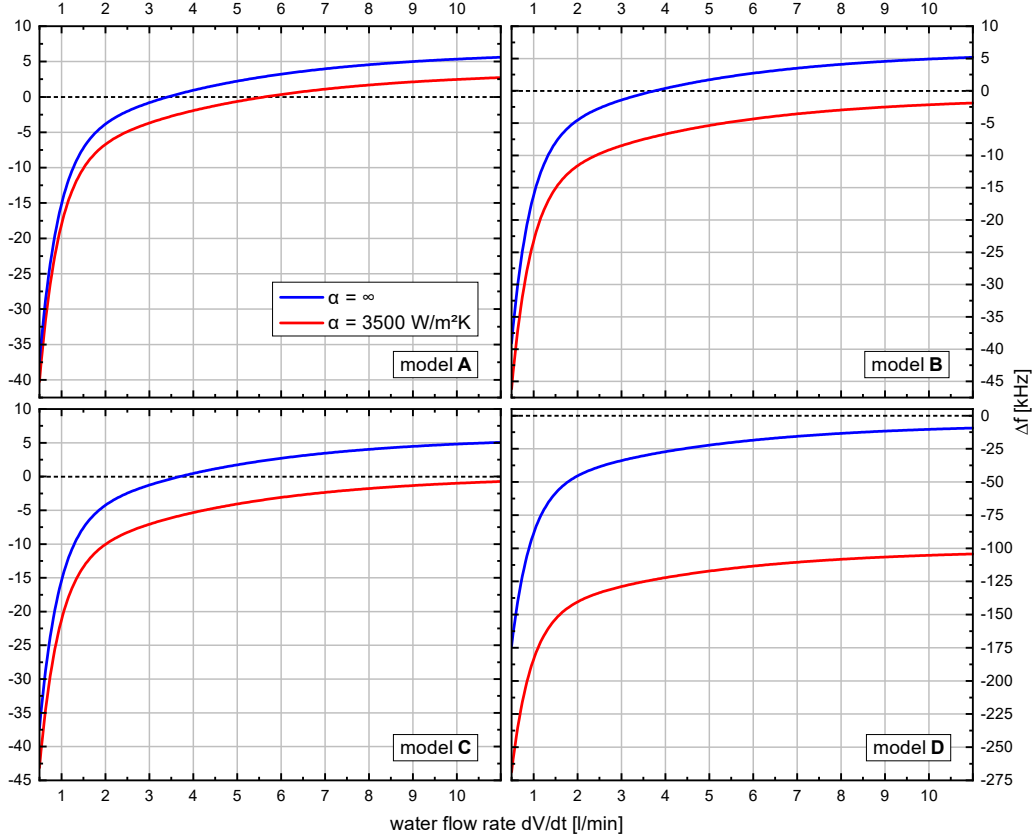

Figure 4.20: Simulated thermal frequency detuning Δf of the 6-stem prototype for $P_\mathrm{c} = 30\,\mathrm{kW/m}$ as function of the water flow rate for different mechanical boundary models as given in section 3.5 (see Fig. 3.28), considering perfect and finite heat transfer ($\alpha = \infty$, $\alpha = 3500\,\mathrm{W/m^2K}$), respectively.

According to the results of thermal simulations for $P_\mathrm{c} = 30\,\mathrm{kW/m}$ as shown in Fig. 4.19, the maximum temperature increase on the stems and electrodes, which is approximately the same, amounts to only $3\,\mathrm{K}$ ($T_\mathrm{max} = 296\,\mathrm{K}$), considering the ideal case of perfect heat transfer and a very high water flow rate, but ranges up to $23\,\mathrm{K}$ ($T_\mathrm{max} = 316\,\mathrm{K}$) for a lower flow rate of $2\,\mathrm{l/min}$ as well as a comparatively low heat transfer coefficient of $3500\,\mathrm{W/m^2K}$. Again, the warmest spots are located at the edges of the electrode mounting brackets as in case of the existing HLI-RFQ (see Fig. 4.19), but also at the corners of the tuning plates.

Compared to the simulated temperature distribution on the existing HLI-RFQ under ideal conditions ($\mathrm{d}V/\mathrm{d}t = 20\,\mathrm{l/min}$, $\alpha = \infty$, $P_\mathrm{c} = 30\,\mathrm{kW/m}$), with a maximum temperature increase of $6\,\mathrm{K}$, the corresponding value of the prototype amounts to only half of that. Considering the supposed worst case scenario ($\mathrm{d}V/\mathrm{d}t = 2\,\mathrm{l/min}$, $\alpha = 3500\,\mathrm{W/m^2K}$, $P_\mathrm{c} = 30\,\mathrm{kW/m}$), the difference of the temperature increase of $23\,\mathrm{K}$ at the prototype compared to $88\,\mathrm{K}$ at the existing HLI-RFQ is even much larger, corresponding to a factor of about 4.

The simulated frequency detuning Δf for the four different mechanical boundary models (**A**...**D**) from section 3.5 as function of the water flow rate is shown in Fig. 4.20, again for

perfect and finite heat transfer. At the existing HLI-RFQ, there are huge differences in the simulated frequency detuning between the considered boundary models and scenarios for water flow and heat transfer, with even qualitative differences of the overall deformation and resulting differing sign of the detuning, ranging from $+90$ to $-800\,\text{kHz}$ (see Fig. 3.30). At the prototype, the corresponding deviations are in general considerably smaller, with the frequency detuning at a water flow rate of $2\,\text{l/min}$ always being negative, differing by a factor of 2 to 3 between perfect and finite heat transfer. Accordingly, compared to the existing HLI-RFQ, the prototype is much less sensitive to the properties of the water flow, which eventually determine the heat transfer characteristics. At a power of $P_\text{c} = 30\,\text{kW/m}$, also the absolute values of the frequency detuning at the prototype of $+6$ and $-130\,\text{kHz}$, as simulated for ideal cooling and the worst case, respectively, are significantly less than at the existing HLI-RFQ with $+30$ and $-800\,\text{kHz}$, corresponding to a factor of 5 to 6. Consequently, also the thermal frequency sensitivity is reduced accordingly and can thus be estimated for the prototype to 1.1–$1.3\,\text{Hz/W}$, based on the value of $6.7\,\text{Hz/W}$ observed at the HLI-RFQ.

4.3 Low-Level Measurements & Pre-Tests

This section provides an overview of the low-level measurements for the investigation of the RF properties and the field distribution, the initial mechanical pre-tests concerning the vibration behavior, as well as the experimental modal analysis using a 3D laser vibrometer, which all have been conducted at IAP on the open prototype tank.

4.3.1 RF Measurements & Field Distribution

The low-level measurements of the RF resonator properties and the field distribution were conducted using a network analyzer with the power coupler and an RF pickup each being connected to one of the ports. The finally determined values for the quality factor and the shunt impedance are summarized in Tab. 4.5.

quality factor (Q_0)	5050 ± 20	(3 dB method)
shunt impedance (R_pL) [kΩm]	114.9 ± 0.5	(capacitance simulation)
	110.5 ± 2.6	(perturbation capacitance)
	109.8 ± 0.4	(R/Q-comparison)

Table 4.5: Determined values of the quality factor Q_0 and the shunt impedance R_pL from the low-level RF measurements.

At first, measurements of the quality factor by the 3 dB method were done right after the adjustment of the tuning plate positions, with the therefor used dummy tuning plates still being mounted between the stems (see Fig. 4.22). The dummy plates are made of aluminum and are contacted to the stems by copper alloy contact springs. The correspondingly measured value of the quality factor was approximately $Q_0 = 4000$. After this, the dummies have been replaced by the actual tuning plates, having the same construction and contacting mechanism as the tuning plates of the FRANZ- and MYRRHA-RFQs[6], and the measurement was

---

[6]which again are similar to the construction of the modified tuning plates for the existing HLI-RFQ (see [134, section 7.2])

repeated with the result of a significantly increased quality factor of about $Q_0 = 5050$. This is probably due to the considerably improved contacting to the stems by the firmly pressed-on silver sheet and the comparatively low electric conductivity of the aluminum dummy plates. After all, the measured value of the quality factor nicely matches the expected value from the RF simulations. Also, the value of the shunt impedance measured by the perturbation capacitance method corresponds within its error margin to the expected value and is largely consistent with the values determined by the methods of R/Q-comparison and capacitance simulation, with the latter slightly deviating upwards.
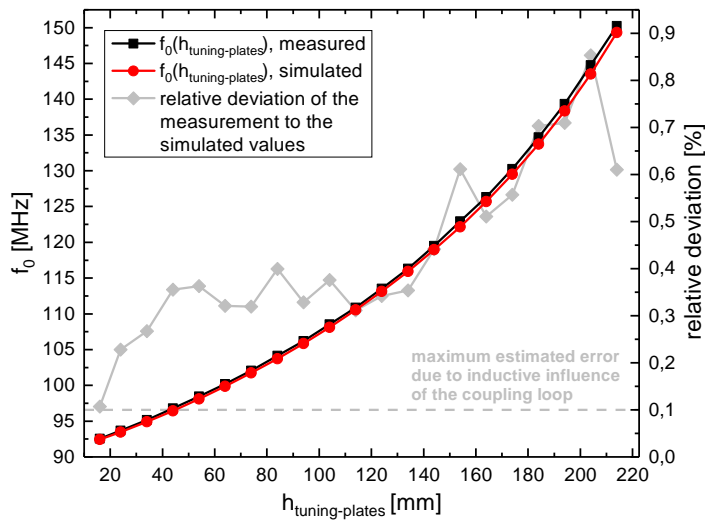

Figure 4.21: Simulated and measured RF resonance frequency f_0 for different positions of the tuning plates.
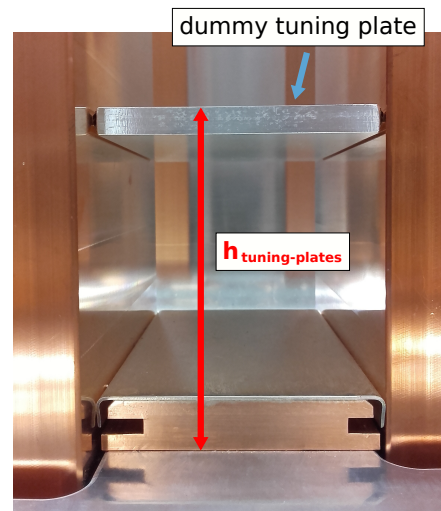

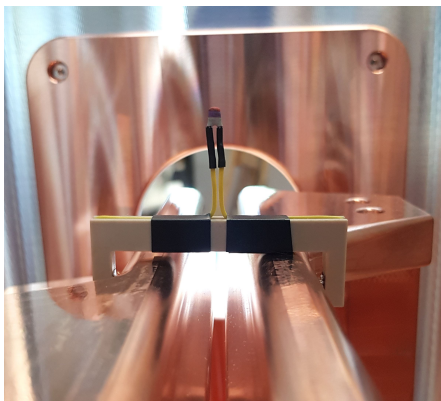**Figure 4.22:** Positioning of the dummy tuning plates.

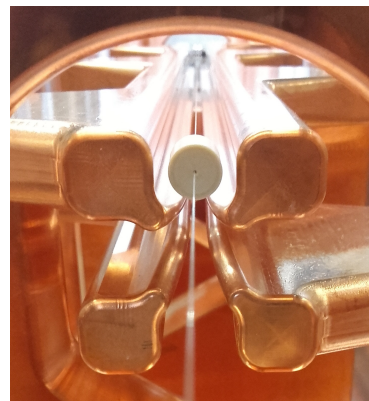**Figure 4.23:** Perturbation capacitor (1 pF) on PEEK mounting bracket[7].

Figure 4.24: Dielectric "bead" (PEEK, diameter = 1 cm, length = 1.2) moved along the longitudinal axis between the upper electrodes.

---

[7]actually, due to the additional capacitance resulting from the attachment of the wires, the measurements of the shunt impedance had to be carried out with the bare capacitor, which was clamped between the electrodes with its existing wire connections

Given the experimentally determined value of the shunt impedance of $110\,\mathrm{k\Omega m}$, the total capacitance between the $702\,\mathrm{mm}$ long quadrupole electrodes amounts to $135\,\mathrm{pF}$ (according to Eq. 2.27), which corresponds well to the value simulated with CST EM Studio of approximately $130\,\mathrm{pF}$ (also see section 2.3.2). However, the analytically derived formula for the calculation of the capacitance between ideally cylindrical quadrupole electrodes (Eq. 2.29) only yields about $35\,\%$ of the simulated value. This is mainly due to the fact that in case of the given electrode geometry with a comparatively large square rod profile (see Fig. 4.1), a significant part of the overall capacitance is not only between the electrode vane tips, as in the idealized case, but also between the opposing flat surfaces of adjacent rods as well as between other parts of the RFQ structure like the stem arms and electrode mounting brackets.
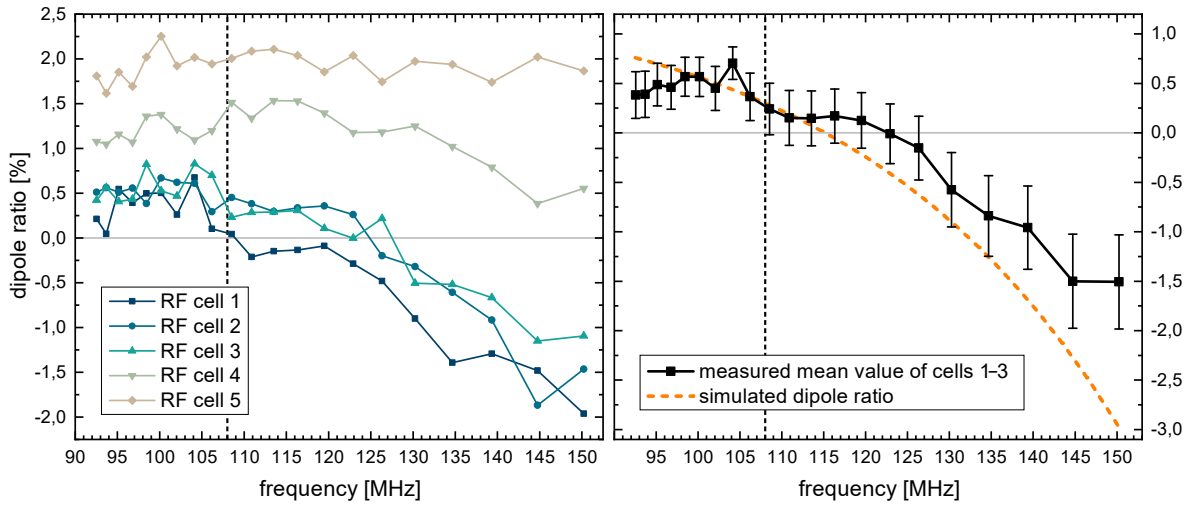

Figure 4.25: Dipole ratio as function of the RF resonance frequency, measured using a perturbation capacitor and calculated according to Eq. 4.2 (*left*: measured values for each RF cell, *right*: comparison between the mean measured value of cells 1–3 and the simulated curve of the dipole ratio).

The measured and simulated values of the RF resonance frequency as function of the tuning plate position (all plates set to the same height) are shown in Fig. 4.21, with the corresponding deviation being in the order of less than $1\,\%$. The inductive influence of the coupling loop, which has not been included in the RF simulations, affects the resonance frequency by less than $0.1\,\%$. The overall adjustable frequency range between the lowest and highest position of the tuning plates is 92.5 to almost $150\,\mathrm{MHz}$, as expected from the simulations.

A measurement of the dipole ratio in each of the five RF cells of the prototype as function of the RF resonance frequency adjusted by the tuning plates is shown in Fig. 4.25, using a $1\,\mathrm{pF}$ perturbation capacitor on a PEEK mounting bracket as depicted in Fig. 4.23. From the measured frequency shifts Δf_{top} and $\Delta f_{\mathrm{bottom}}$ resulting from the capacitor being mounted on the upper and lower electrode pair, respectively, the dipole ratio was calculated according to Eq. 4.2, following Eq. 2.49 and considering the proportionality between the frequency shift and the square of the field amplitude (see Eq. 2.36).

$$\text{dipole ratio} = \frac{\sqrt{\Delta f_{\mathrm{top}}} - \sqrt{\Delta f_{\mathrm{bottom}}}}{\frac{\sqrt{\Delta f_{\mathrm{top}}} + \sqrt{\Delta f_{\mathrm{bottom}}}}{2}} \tag{4.2}$$

For a correct measurement in a given RF cell, the capacitor has to be placed at the exact same longitudinal position at the upper and lower electrode pair, respectively. The measurement error of the applied perturbation capacitance method is hence mainly determined by the deviation of the measured perturbed frequencies due to inaccurate positioning of the capacitor mounting bracket attached by hand, which results in an error of the corresponding frequency shifts $\Delta f_{\text{top/bottom}}$ of about $0.3\,\%$ at $f_0 = 108\,\text{MHz}$.
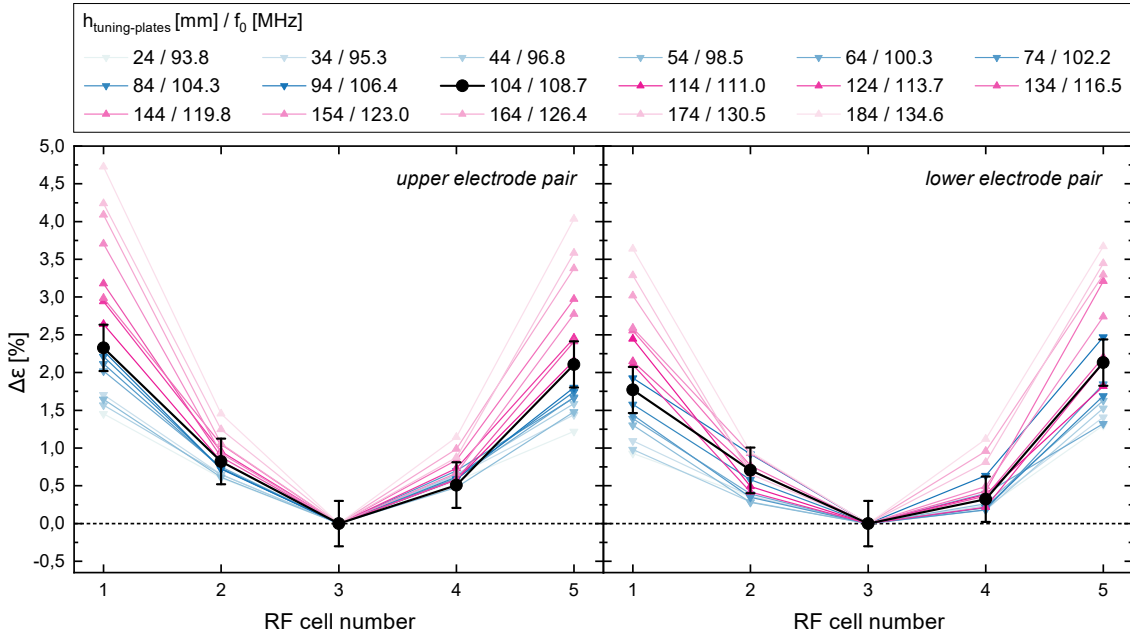

Figure 4.26: Measured deviation of the field flatness $\Delta\epsilon$ along the longitudinal axis, using a perturbation capacitor as depicted in Fig. 4.23 on the upper and lower electrode pair, for different tuning plate positions and corresponding resonance frequencies.

Overall, the measured curve of the dipole ratio as function of the frequency corresponds well to the predicted dipole compensation from the simulations, which shows that compared to the uncompensated reference design with a simulated dipole ratio of $9.5\,\%$ (see Tab. 4.2) almost full compensation is achieved. However, as can also be seen from the measurements, in some RF cells the dipole compensation deviates from the ideal case (see cells 4 & 5), with a dipole ratio of up to $2\,\%$. Based on the presumption that this was related to a tilted field distribution due to an initial mechanical misalignment of the electrodes, which was particularly striking regarding the concerned cells 4 & 5 (also see [156, Fig. 5]), the electrodes have been realigned and further investigations of the field flatness using the perturbation capacitor, but also the bead-pull method, were conducted (see Figs. 4.26 & 4.27, respectively). Despite unrelenting efforts, however, achieving an exactly symmetrical field distribution along the electrodes proved to be difficult, and both the full dipole compensation as expected for the ideal case, as well as deviations with typical values of up to $\pm 2\,\%$ could be reproduced in several attempts to mechanically realign the quadrupole electrode rods. This is due to the fact that the RF structure of the prototype with the high stems and comparatively short electrodes, each being connected to only 3 stems in total, is obviously prone to unpredictable mechanical contortion occurring during the tightening of the fixing screws between the electrode mounting brackets

and the stem arms. Eventually, this problem will likely have less of an effect at a longer RFQ structure, where the longer electrode rods and the higher number of screwed connections reduce the degrees of freedom for mechanical tilt of the single components.
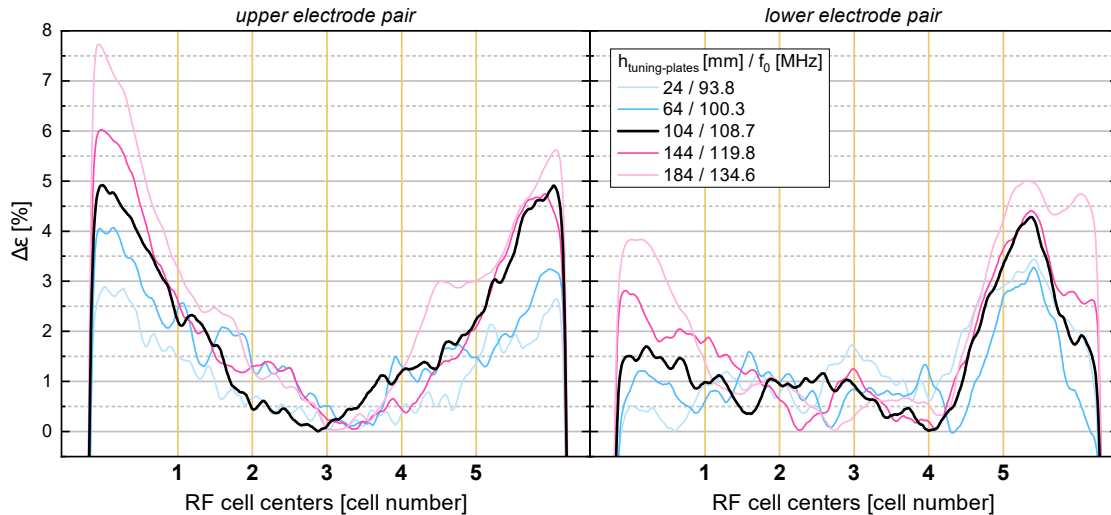

Figure 4.27: Deviation of the field flatness $\Delta\epsilon$ along the longitudinal axis, measured using the bead-pull method (see Fig. 4.24) between the upper and lower electrode pair, for different tuning plate positions and corresponding resonance frequencies.

4.3.2 Vibration Measurements

In order to experimentally investigate the vibration behavior of the 6-stem RFQ prototype structure without the presence of an electric RF field, vibration measurements were conducted with the tank being open and applying different external excitation mechanisms as well as different available vibration measurement techniques. This procedure offered the opportunity of also observing vibrational modes that are typically not excited by RF operation. The used methods for achieving mechanical excitation were as follows:

- The most simple possibility to excite the mechanical structure to vibrations is given by the broadband shock excitation due to a hit with a soft-face hammer, which basically can be executed at any arbitrary position on the RF structure or the tank.

- The RF structure of the prototype can also be directly mechanically contacted with a piezo actuator[8] which can be mounted through one of the flanges intended for diagnostic windows or for the vacuum pump, using a specially designed mounting structure as shown in Fig. 4.32. This allows the piezo actuator to be pressed against either the overhang of the upper electrode, the corresponding inter-stem electrode section adjacent to the opposite electrode end (see Fig. 4.28), or the lower part of a stem. The applied excitation signal was either a harmonic frequency sweep or noise (white, pink or brown).

- Yet another method to trigger mechanical vibrations is given by applying externally generated sound, eventually resulting in acoustic excitation. For this purpose, a PA loudspeaker, which is supposed to have a flat frequency response curve, was placed on

---

[8]model: P–225.20 PICA power piezo actuator by PI (Physik Instrumente) GmbH & Co. KG

top of the tank with the membrane directly facing the RF structure (also see Fig. 4.31). Again, the applied sound signal was a harmonic frequency sweep or noise.
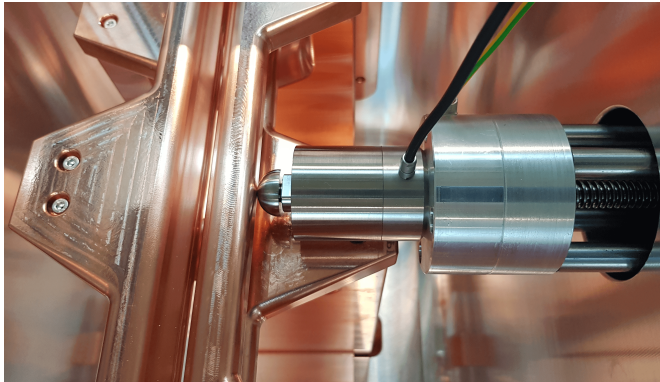

Figure 4.28: Piezo mounted against inter-stem electrode section.

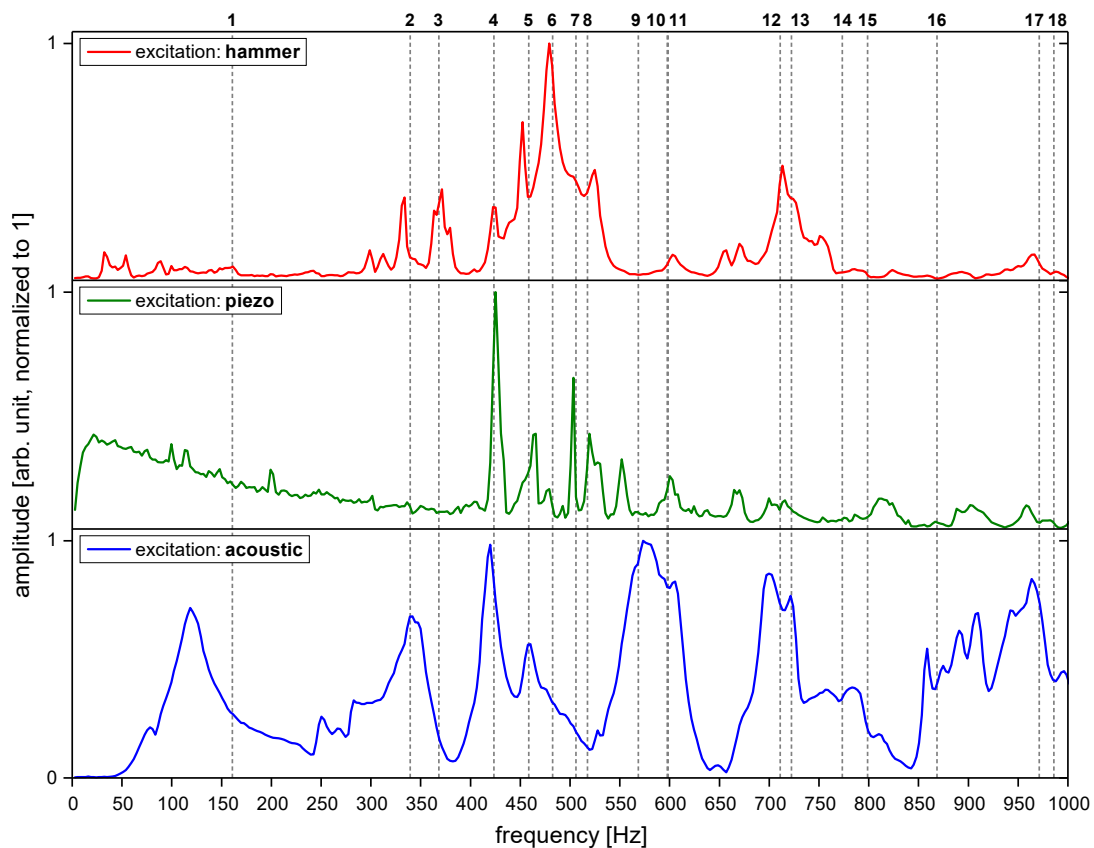**Figure 4.29:** Microphone suspended in the prototype tank.

Figure 4.30: Microphone measurements on the prototype of vibration frequency spectra for different excitations (red: lateral hammer hit on electrode, green: lateral excitation of the electrode by piezo actuator with brown noise signal, blue: acoustic excitation by frequency sweep, vertical gray dashed lines: simulated mode frequencies).
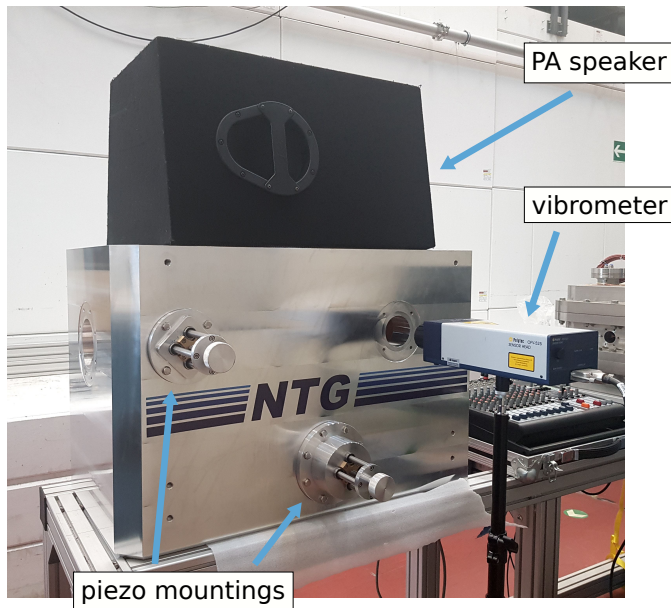
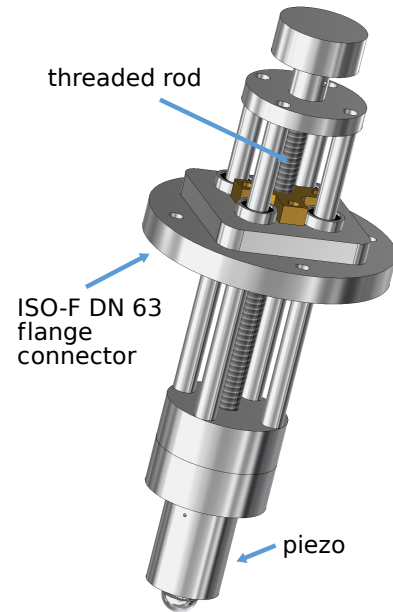**Figure 4.31:** Experimental setup for the vibration measurements.

Figure 4.32: Schematic drawing of the piezo mounting structure.

For the measurement of the excited vibrations the following methods were applied:

- As shown in Fig. 4.29, a microphone was suspended in the tank to capture the audible acoustic signal generated by the mechanical vibrations. By this, all vibrations occurring on the different parts of the structure are measured simultaneously, without being able to localize the vibration or determine its spatial direction.

- On the other hand, the piezo actuators can also be used as vibration sensors, whose output signal can be recorded after running through a preamplifier. This allows to measure the vibrational component in longitudinal direction of the piezo at the specific point where the sensor touches the structure.

- In analogy to the preceding vibrometer measurements on the existing HLI-RFQ (see section 3.3), also the Polytec OFV-525 laser vibrometer was employed and measurements were conducted by pointing the laser beam through the diagnostic windows of the prototype tank onto the corresponding electrode overhang or inter-stem section.

Some results of the numerous measurements conducted using the microphone, piezo sensor and laser vibrometer are shown in Fig. 4.30, Fig. 4.33 and Fig. 4.34, respectively, considering the typical frequency range for the occurrence of mechanical vibrations of up to 1 kHz. Only by looking at the microphone measurements, which after all is a very simple and cost-effective method, already a good agreement between the measured and simulated spectra can be observed, with frequency deviations of only a few Hz between the easily recognizable measured peaks related to the modes 2–13 and the corresponding simulated values. The generally broader peaks occurring with the acoustic excitation and measurement methods indicate a higher damping of the acoustic signal compared to the mechanical vibration of the structure.
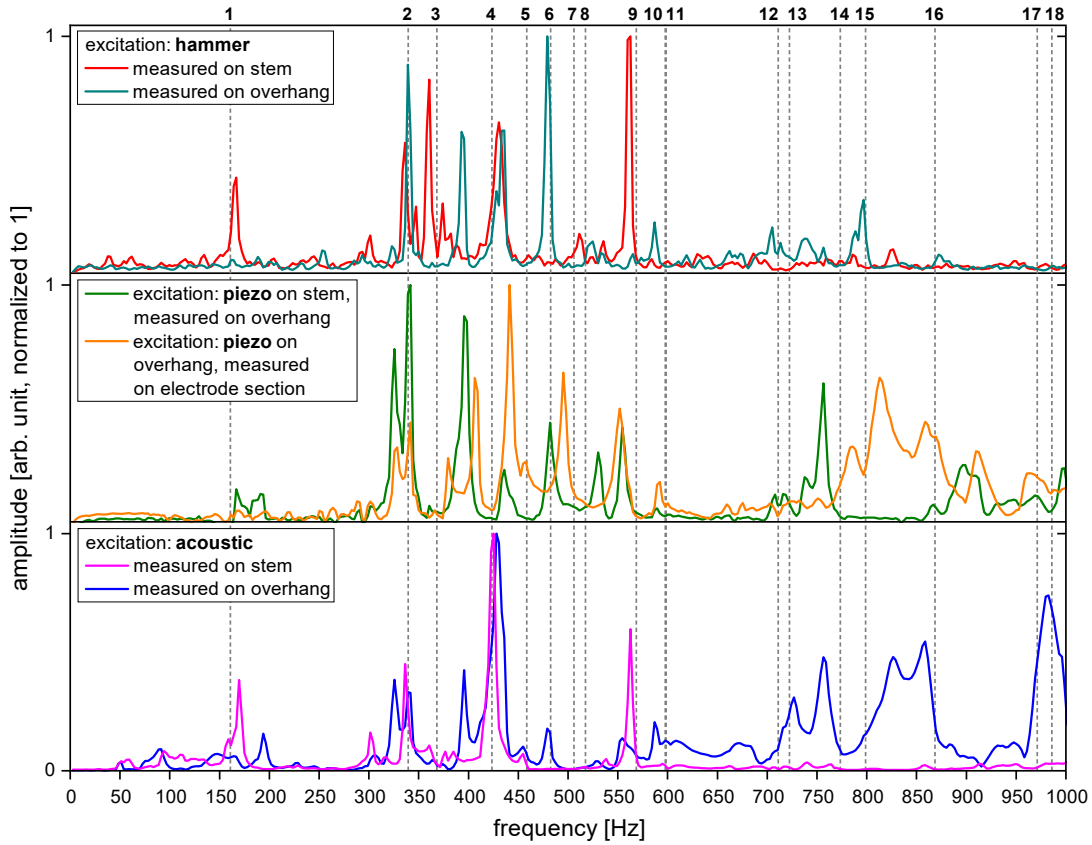
Figure 4.33: Piezo measurements on the prototype of vibration frequency spectra for different excitations (red/cyan: frontal hammer hit on stem / vertical hammer hit on electrode, green/orange: lateral excitation by piezo actuator with frequency sweep, magenta/blue: acoustic excitation by brown noise signal / frequency sweep, vertical gray dashed lines: simulated mode frequencies).

By a direct vibration measurement at the lower part of the stem, using the piezo sensor, also the first stem mode (mode 1) could be observed in the spectrum. However, with the piezo sensor/actuator being mounted to the electrode, generally some further modes appeared which typically were noticeable in the range around 400 Hz as well as a little below the second mode. After all, the fact that this only occurs at the piezo measurements leads to two different possible explanations, which eventually pose inherent problems of the applied measurement technique: On the one hand, the piezo mounting structure itself can be excited to vibrations, which then additionally occur in the mode spectrum. On the other hand, the mechanical contact of the piezos to the comparatively mechanically soft electrodes might alter their vibrational behavior and shift the frequencies of the affected eigenmodes. Although a definite conclusion could not be drawn from the conducted measurements, it can however be assumed that the measured peaks around 400 Hz correspond to a vibrational mode of the piezo mounting structure which is clamped between its screwed mounting at the flange and the electrode. This can be deduced from the observation that the concerned mode occurs for both cases of the piezo either being mounted to the electrode overhang or to the inter-stem section and, furthermore, that the occurrence and magnitude of the corresponding peak can be induced deliberately by direct excitation at the piezo mounting structure using the soft-face hammer [156]. It is also striking that the measurements with both piezos (one

as actuator, one as sensor) generally show the largest deviations to all other measurements as well as to the simulations. It can therefore be concluded that non-contacting techniques for the excitation and measurement of vibrations should in principle be preferred over piezo-based methods, as those interfere with the mechanical behavior of the investigated structure.
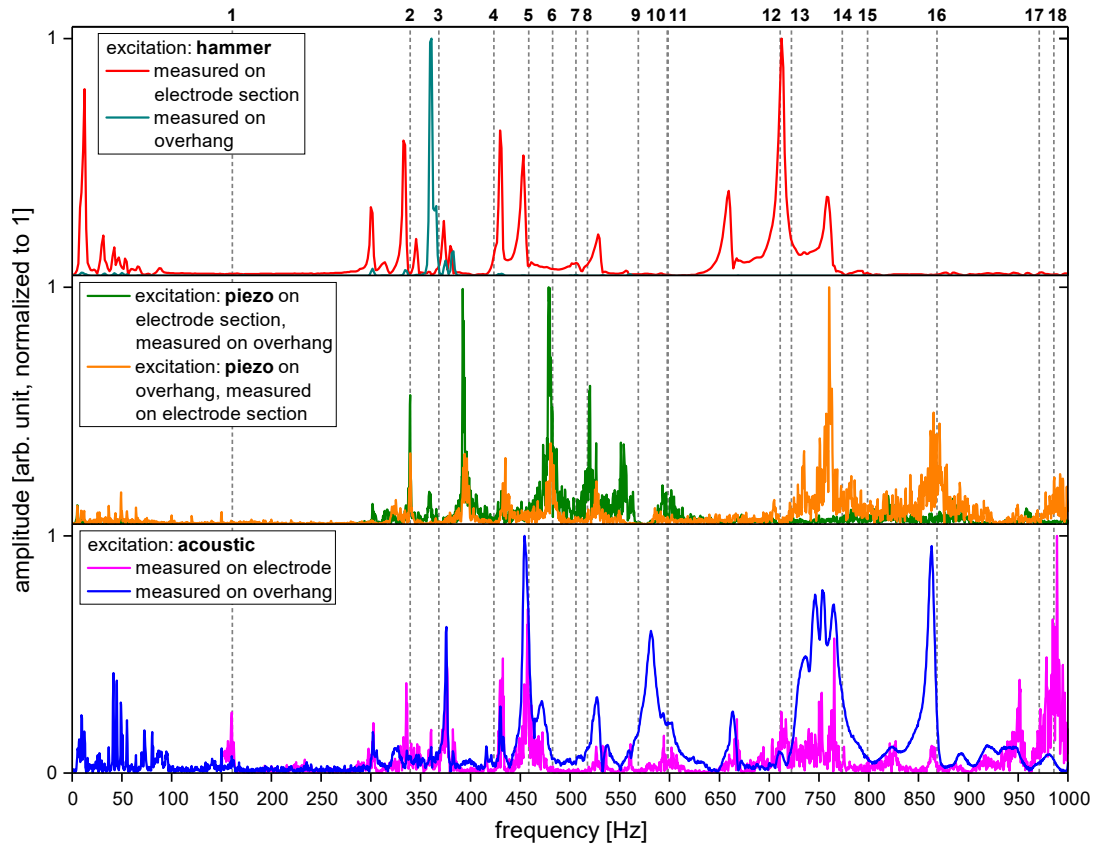

Figure 4.34: Vibrometer measurements on the prototype of vibration frequency spectra for different excitations (red/cyan: hammer hit on tank, green/orange: lateral excitation by piezo actuator with pink noise signal, magenta/blue: acoustic excitation by pink noise signal / frequency sweep, vertical gray dashed lines: simulated mode frequencies).

Eventually, it shows that a systematic excitation of specific vibrational modes could not be achieved with any of the applied excitation methods. In addition, most of the measured spectra also contain some seemingly randomly occurring minor unidentifiable peaks which are most likely associated with vibrations of the prototype tank, its mounting frame, components of the measurement setup, or even other surrounding objects. An improved experimental vibration analysis would hence require a much greater effort in terms of mechanical decoupling from the experimental environment as well as a much more sophisticated method for systematic mechanical excitation. Because with the excited vibrations, usually a number of mechanical eigenmode oscillations occur simultaneously, no reliable analysis of the typically mode-dependent damping times could be obtained, which are required to determine the corresponding vibration amplitudes from numerical simulations. The values of the damping times calculated from the measurement data are in a broad range between 30 and 700 ms,

while being noticeably lower for spectra that predominantly contain higher vibration modes, thus indicating a strong mode-dependency of the damping characteristics. Also, an accurate evaluation of the damping based on the mechanical resonance width proved to be difficult due to large deviations of the observed resonance widths of the individual peaks between different measurements. Nevertheless, every single mode in the frequency range below 1 kHz could finally be excited and identified, thus achieving an appropriate validation of the simulated mode spectrum by the 1D vibration measurements.

4.3.3 Experimental Modal Analysis

Exploiting the opportunity to employ a 3D laser vibrometer in collaboration with the research group System Reliability, Adaptive Structures, and Machine Acoustics (SAM) of the Technical University of Darmstadt, an experimental modal analysis was conducted, under the technical direction of C. Adams and the support of K. Bahrke. Typically, experimental modal analyses are used to investigate vibrations of thin-walled structures as for automotive or aeronautical applications.
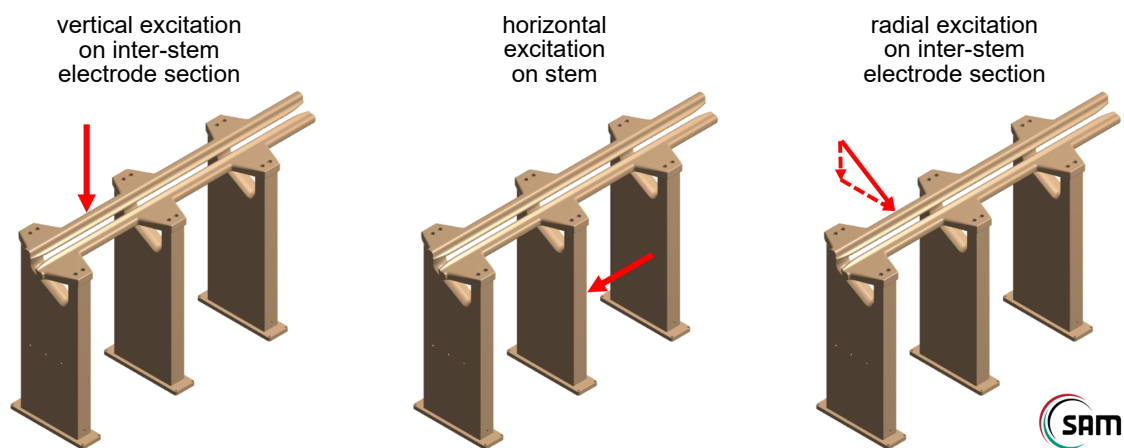

Figure 4.35: Excitation points and directions for the 3D vibrometer measurements[9].

Similar to the applied method of excitation by a soft-face hammer at the previous vibration measurements as discussed in section 4.3.2, for the 3D measurements the prototype structure was excited by an impact hammer, that basically measures the impact force during the hammer hit, to which the accordingly measured vibration amplitudes can then be normalized. To achieve excitation of as many vibrational modes as possible, three series of measurements were carried out, with excitation at different points of the structure and in different directions, as depicted in Fig. 4.35. The overall measurement setup for the used Polytec PSV-500 3D laser vibrometer is shown in Fig. 4.36. To be able to reconstruct the deformation profiles of the electrode, a virtual measuring grid was defined upon its surface in the vibrometer software. Unlike to the previous 1D vibrometer measurements, a perpendicular alignment of the laser beams from the three sensor heads relative to the electrode surface is not possible, so that optical scattering on the bare copper structure was too severe to obtain a high enough magnitude of the reflected signal. Therefor, a piece of reflective foil was attached at each

---

[9]all images marked with the SAM-logo courtesy of K. Bahrke

position corresponding to a predefined measuring point. Finally, by measuring the vibration amplitudes in the three spatial projections in direction of the laser beams from the three vibrometer sensor heads at each of the measuring points, the vibrometer software can calculate the resonance response spectra in the three orthogonal spatial directions and reconstruct the vibrational deformation profile of the electrode as function of the vibration frequency.
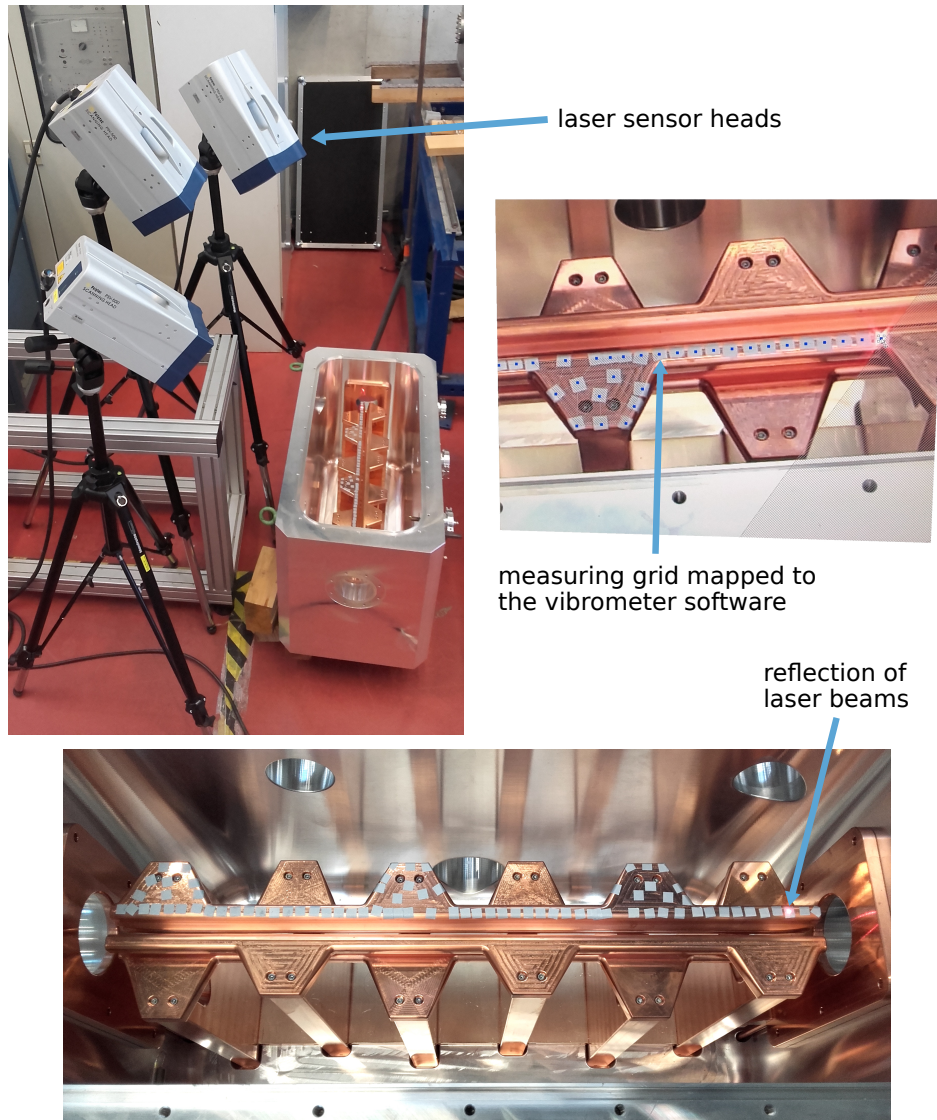

Figure 4.36: Measurement setup for the experimental modal analysis with the 3D laser vibrometer.

As can be seen in Fig. 4.37, the response spectra measured with the 3D vibrometer generally agree well with the previous 1D measurements as well as with the simulations. Also, the spatial directions, in which the peaks of the respective modes occur, largely correspond to the vibrational planes found in the simulations. As shown in Fig. 4.38, the occurrence of some of the simulated deformations could be nicely demonstrated by the measurements.

Whereas some peaks in the measured response spectra can be clearly identified as being asso-

ciated with a certain vibrational mode on the basis of both frequency (with relative deviations of less than 10 %) and by the correspondingly measured deformation profile (see modes 1, 3, 9, 11 and 13), the frequencies of other modes that can seemingly be identified only from their deformation profile however deviate considerably, as it is particularly the case for modes 6 and 18, but also to a lesser extend for modes 5, 10, 12 and 19.

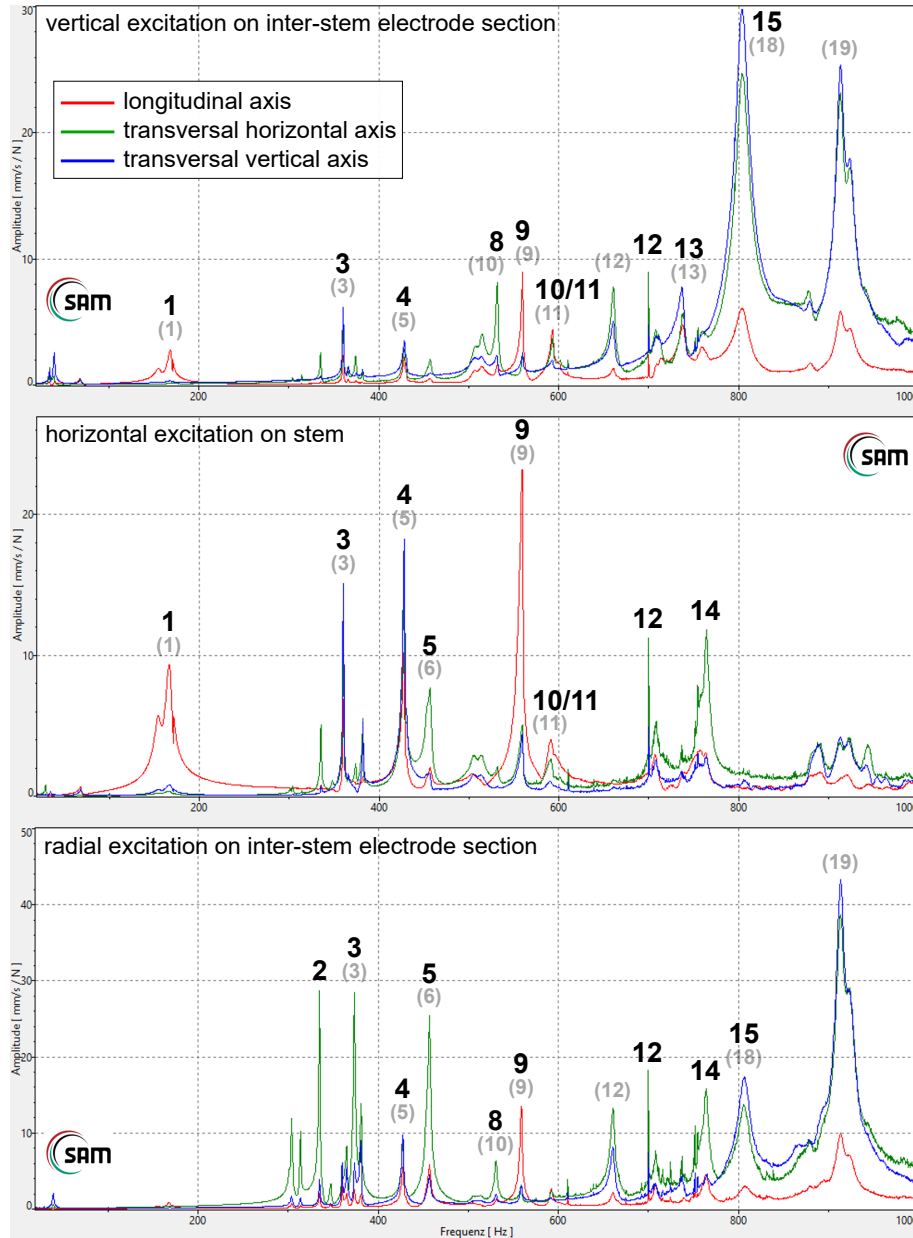

Figure 4.37: Measured frequency spectra by the 3D vibrometer for different excitations according to Fig. 4.35. The black numbers indicate the modes that correspond to the respective peaks according to the simulated mode spectrum. The gray numbers in brackets indicate the modes that correspond to the respective peaks according to the measured deformation profiles, as depicted in Fig. 4.38.
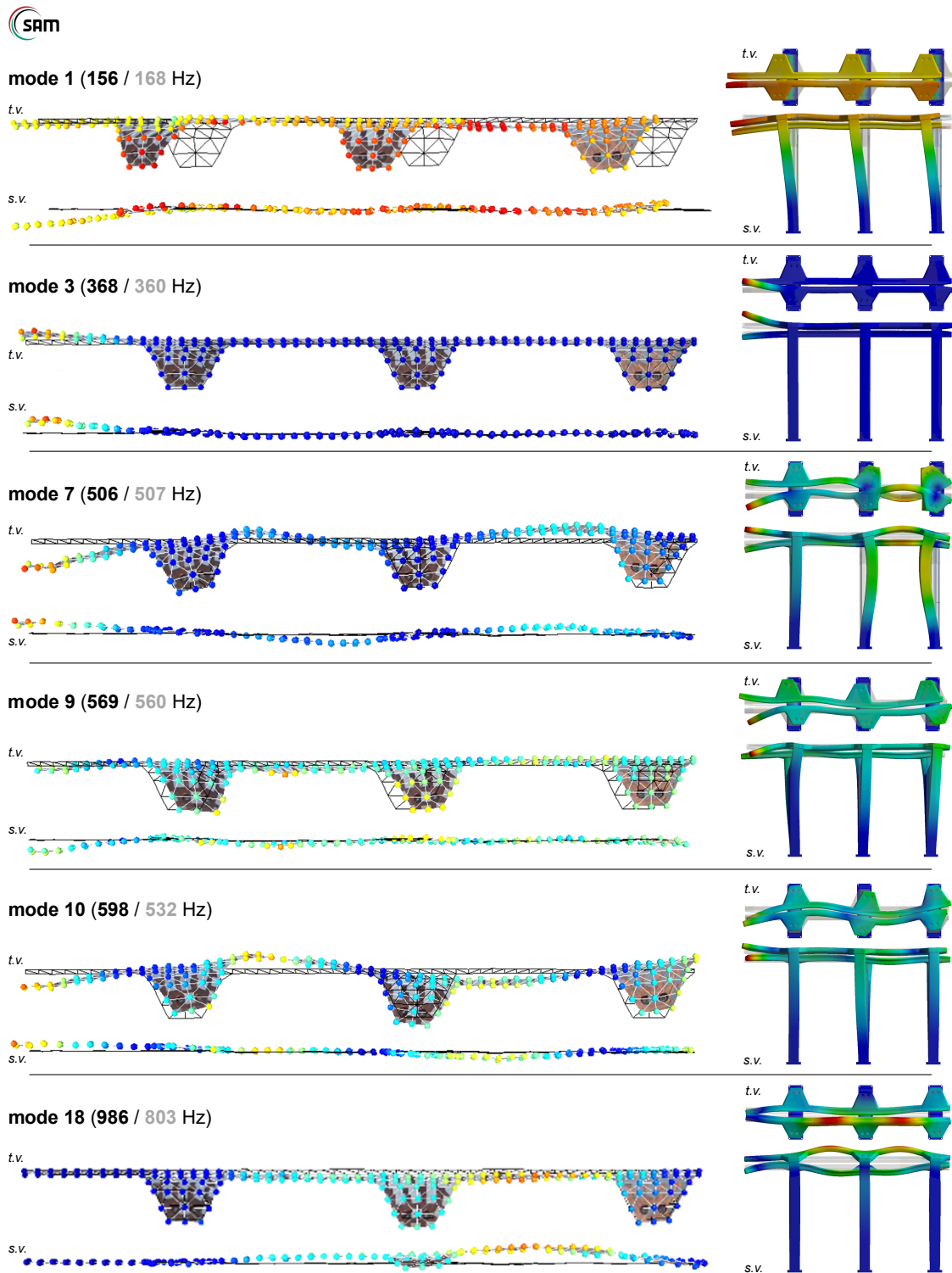
Figure 4.38: Measured deformation profiles of the upper electrode for some identified modes in topview (*t.v.*) and sideview (*s.v.*) (*left*) and the corresponding simulated deformation (*right*). The black number equals the simulated frequency of the respective mode, whereas the frequency associated with the measured deformation profile is given in gray.

After all, a possible reason for some of the observed deviations can be given by the fact that several modes might just not be correctly identified by the optical comparison between the measured and simulated deformation profiles. Because for some modes only low vibration amplitudes can be achieved by excitation with the impact hammer, which is more often the case at higher vibration frequencies, the corresponding deformation profiles are often difficult to classify due to the measured deflections being very small, which makes it complicate to assign the reconstructed representation of the deformation by the vibrometer software to one of the known deformation profiles from the simulations. However, further insights can be expected from the planned vibrometer measurements during RF operation of the RFQ prototype, especially regarding the investigation of the most critical mode 18.

Nevertheless, the data from the 3D measurements finally allowed for a more precise determination of the damping ratio than at the previous 1D measurements. The according values of the resonance width and damping ratio are summarized in Tab. 4.6 for all modes where an evaluation could be achieved. The already previously observed mode dependence of the damping can clearly be seen. Regarding the RF affecting mode 18, the measured damping ratio amounts to $\zeta = 0.93\,\%$, which corresponds to about 9 times the observed damping at the existing HLI-RFQ.

mode #	frequency f_0 [Hz]	resonance width Δf_{FWHM} [Hz]	damping ratio ζ
1	168	4.51	0.0134
3	360	0.38	0.0005
5	428	2.15	0.0025
9	560	1.87	0.0016
10	532	3.18	0.0030
11	593	3.98	0.0034
12	660	5.38	0.0040
13	738	8.43	0.0057
14	759	13.72	0.0090
18	803	15.01	0.0093
19	913	9.58	0.0050

Table 4.6: Measured resonance width Δf_{FWHM} and corresponding damping ratio ζ for some modes identified from the 3D measurements.

4.4 RF Pre-Conditioning

In preparation for the planned high-power tests at GSI, a pre-conditioning of the prototype at low powers of up to 200 W was carried out at IAP, using a low wattage broadband RF amplifier. The assembled test stand for RF operation of the prototype and vacuum/RF diagnostics is shown in Fig. 4.39. Since the frequency of the of the RF feed at GSI is fixed at 108.408 MHz and cannot be further adjusted, also a plunger tuner had to be installed for dynamic tuning of the cavity to the nominal frequency at high thermal loads.

With the coupling loop which has been adapted for installation in the prototype tank, a coupling of -45 to $-50\,\mathrm{dB}$ $(= |S_{11}| = \sqrt{P_{\mathrm{r}}/P_{\mathrm{f}}})$ is achieved. The two RF pickups have been adjusted to -30 and $-45\,\mathrm{dB}$ $(= |S_{21}| = \sqrt{P_{\mathrm{t}}/P_{\mathrm{f}}})$, respectively, to yield a reasonable amplitude of the transmitted signal at both low and high forward powers. The pre-conditioning was done without water cooling of the RFQ structure. The base pressure of the evacuated cavity was at approximately $2.5 \cdot 10^{-7}\,\mathrm{mbar}$.
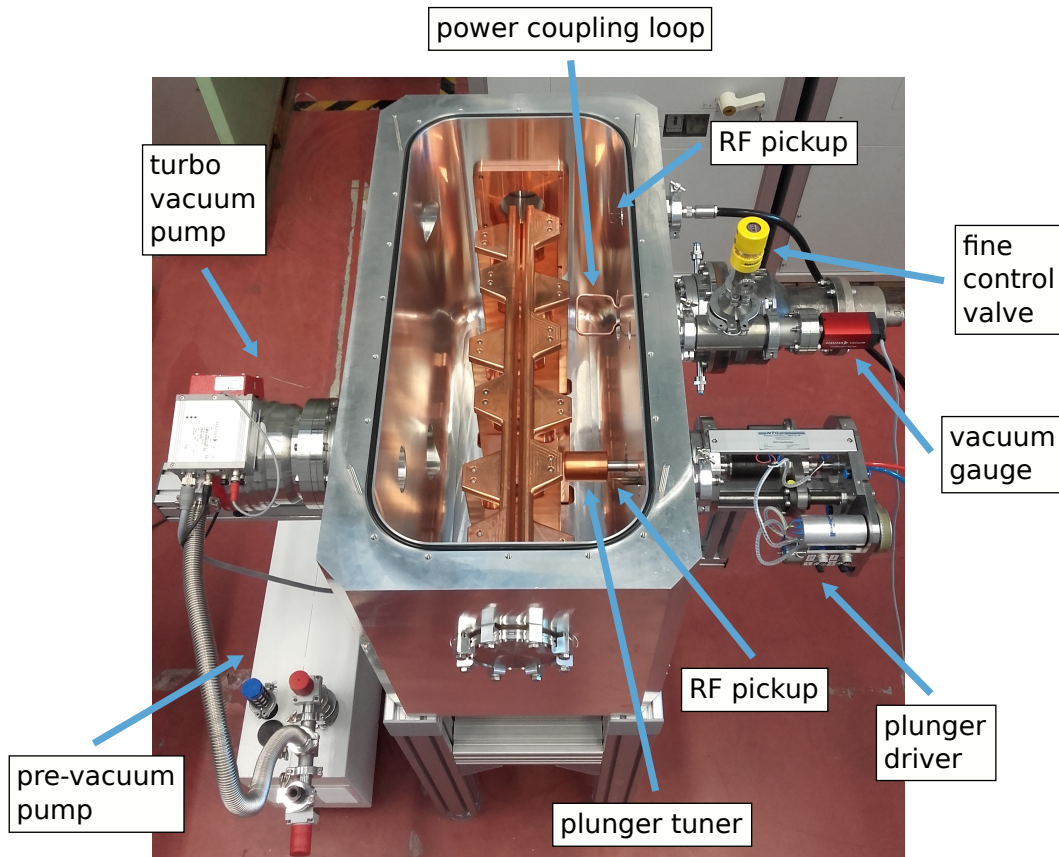

Figure 4.39: Setup of the test stand for RF conditioning and high-power tests.

Eventually, the conditioning up to $200\,\mathrm{W}$ could be carried out within 3 working days without major difficulties. The temporal progression of the forward, reflected and transmitted power $(P_{\mathrm{f}}, P_{\mathrm{r}}, P_{\mathrm{t}})$ and the pressure during conditioning is shown in Fig. 4.40. As can be seen, a significant conditioning threshold occurred between about 140 and $240\,\mathrm{mW}$, for the overcoming of which the largest part of the overall conditioning time had to be spent. After crossing the threshold, which happens abruptly and is marked by a sudden decrease of the reflected power and an associated increase of transmission, the forward power could be immediately increased to $200\,\mathrm{W}$ without further complications. Also, after the threshold once had been crossed and the structure has already been operated at higher power levels, during a restart of RF operation it can then easily be jumped just by increasing the forward power fast enough. Due to the structure not being water cooled during pre-conditioning, thermal equilibrium is hence reached very slowly, which can be observed during the long-term measurement by

the steady increase of the time span in which the reflected power rises from its base value of about $3\,\mathrm{W}$ to the maximum accepted value of $10\,\mathrm{W}$, from where the frequency was finally again readjusted manually.
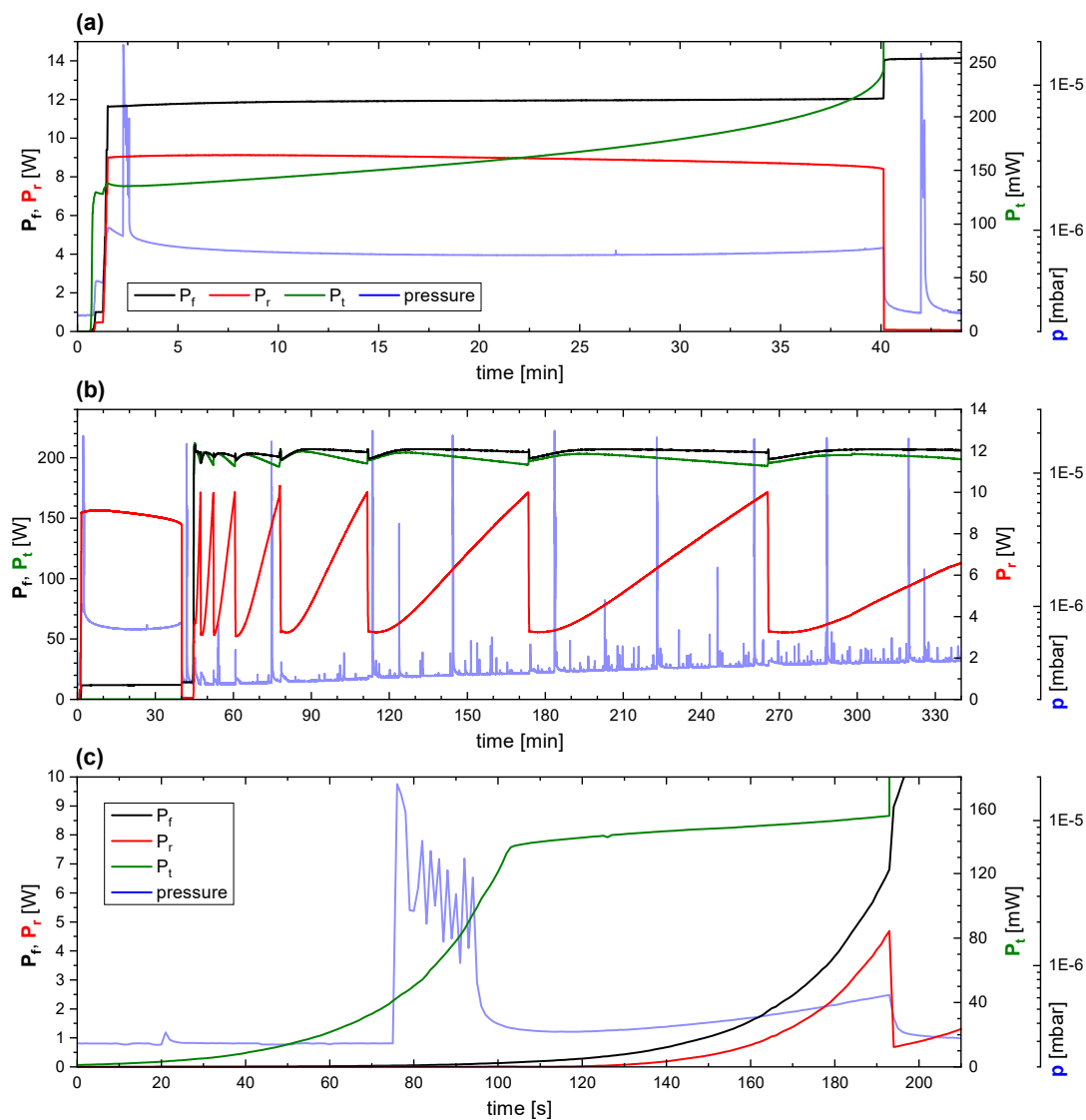
Figure 4.40: Forward power P_{f}, reflected power P_{r}, transmitted power P_{t} and pressure during low-power conditioning up to $200\,\mathrm{W}$ for different cases:

- **(a)** Slow conditioning over the persistent low-power threshold between approximately 140 and $240\,\mathrm{mW}$.
- **(b)** Long-term measurement over a duration of $5\,\mathrm{h}$, following to **(a)**.
- **(c)** Fast crossing of the low-power threshold after previous long-term operation at $200\,\mathrm{W}$.

4.5 High-Power Test Preparations

Finally, after pre-conditioning, the water cooling system was installed with a total of 50 single water connections (see Fig. 4.41), corresponding to 25 separate cooling circuits (2 in each of the 6 stems, 1 in each of the 4 electrodes, 1 in each of the 5 tuning plates, 1 in each of the 2 end-plates, 1 in the power coupler and 1 in the tuner). For monitoring the water outlet temperatures, PT100 temperature sensors are mounted at the outlet tubes of the stems, electrodes and tuning plates and connected to a read out bus system.
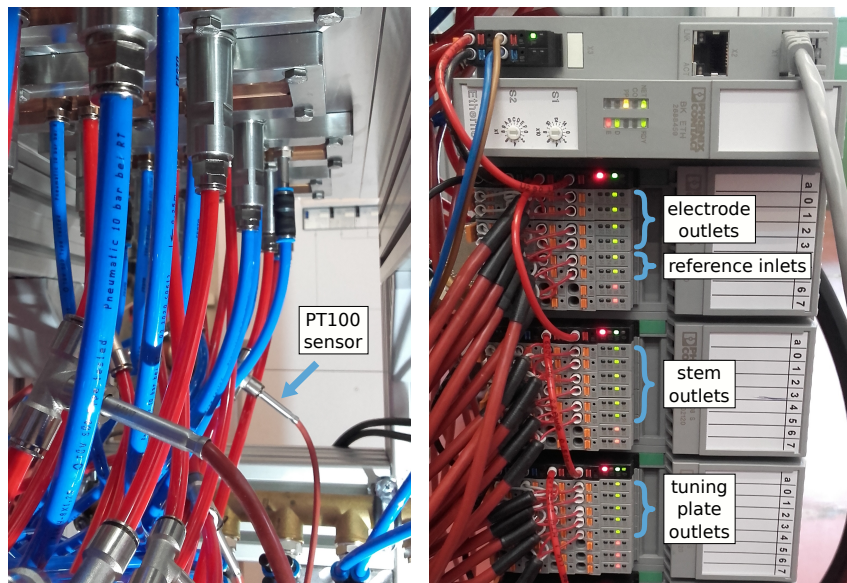

Figure 4.41: Installation of the water supply with water inlets in blue and outlets in red (*left*) and read out bus system for the temperature sensors (*right*).

The manufactured and assembled structure for positioning additional temperature sensors inside the stems is shown if Fig. 4.42. Basically, the used PT100 sensors were fixed to the copper contacting heads with a thermally conductive adhesive and can then be slid in the sensor shafts using a guiding rod until the head touches the curvature at the end of the shaft, to the surface of which it is thermally contacted by thermal paste.

The entire diagnostics read out of the temperature sensors, the pressure gauge and the power meters is done using a dedicated LabVIEW script which was developed especially for the RF conditioning of accelerator cavities [161].

After the preparations for the high-power tests had been completed, the entire test stand was finally transported to GSI (see Fig. 4.43), where the infrastructure of the RF test bunker concerning RF supply, data read out and water has to be adapted to finally be able to run the planned investigations of the RF, mechanical and thermal behavior of the RFQ prototype.
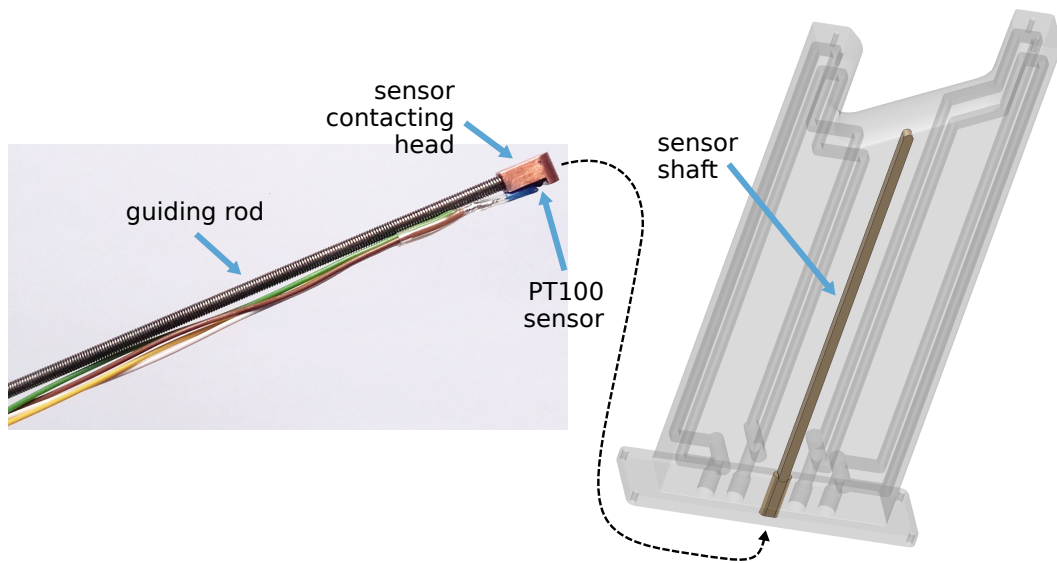
Figure 4.42: Setup of the temperature measurement inside the stems.

Figure 4.43: Prototype tank in the RF test bunker at GSI[10].

Besides conclusions regarding the application of the developed prototype design for a newly revised full-length HLI-RFQ from the planned high-power RF tests, the prototype configuration also offers outstanding possibilities for general studies concerning the comparison between measurements and corresponding thermal and structural-mechanical simulations, due to the installation of the dedicated systematically placed diagnostic windows for vibration measurements, the additional temperature sensors being mounted inside the stems, and the extensive monitoring of the cooling water temperatures by thermal sensors.

(5) Design Concept for a New Full-Length HLI-RFQ

Based on the developed prototype design and the validation of the anticipated RF and mechanical properties by the pre-tests, a preliminary new design for a revised full-length HLI-RFQ was derived, which is briefly presented in this chapter. In principle, the RF structure of the prototype could be adapted almost without further modification to the length and electrode geometry of a newly developed beam dynamics design. A comparison between the new RFQ concept and the existing HLI-RFQ is provided in the following.

5.1 Beam Dynamics Design

The preliminary new beam dynamics design presented in this section was originally developed by C. Zhang and kindly provided for publication in this thesis. Since at the time the specific beam input distribution from the LEBT of the upgraded HLI was not yet available, a generic 4D waterbag input distribution was used. The overall design approach was to pursue an as far as possible reduction of the required vane voltage while achieving similar beam characteristics to the existing HLI-RFQ. The main advantages of a lower vane voltage are on the one hand a reduced thermal load per length during CW operation, but on the other hand also a reduction of the mechanical forces on the electrodes, which eventually helps to suppress mechanical electrode vibrations.
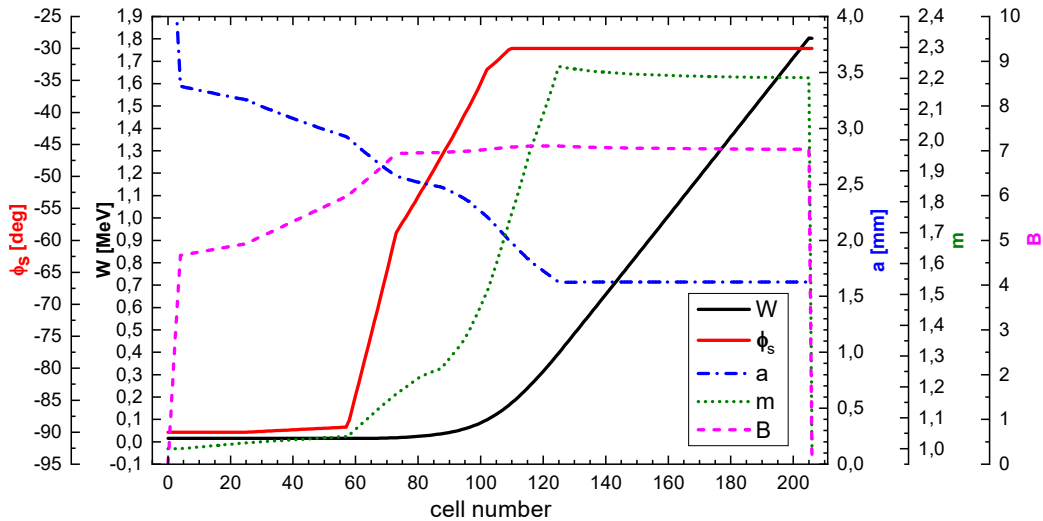

Figure 5.1: Synchronous phase ϕ_s, energy W, minimum cell aperture a, modulation factor m and radial focusing strength B along the beam axis as function of the cell number.
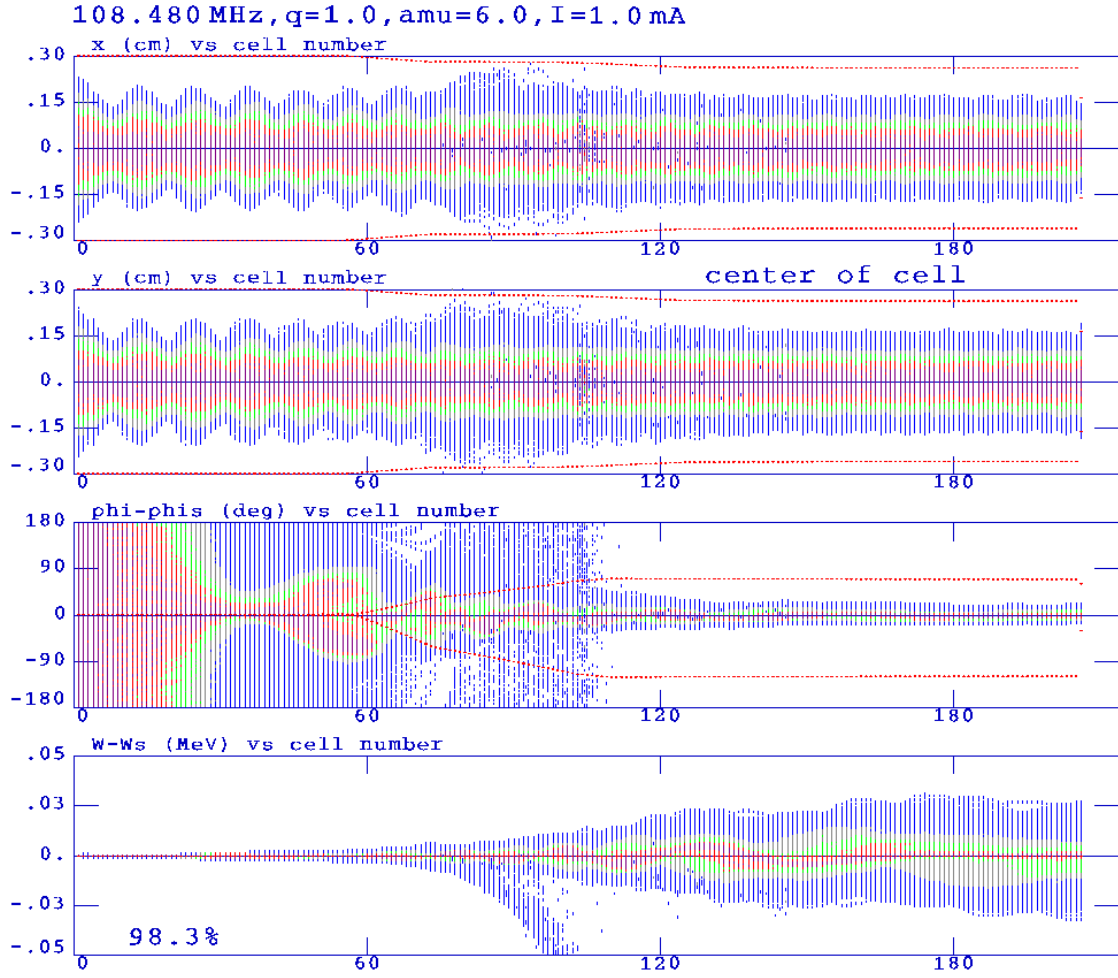
Figure 5.2: Evolution of the transversal beam particle distribution in x/y-direction, the phase spread $\Delta\phi = \phi - \phi_s$ and the energy spread $\Delta W = W - W_s$ as function of the modulation cell number, for $A/q = 6$ and $I = 1\,\text{mA}$.

RF frequency [MHz]	108.48
electrode length [m]	2.83
intervane voltage [kV]	40
number of cells	206
minimum aperture [mm]	1.63
maximum modulation	2.238
Kilpatrick factor [kV]	1.72
$r_{\text{electrode}}$ / r_{aperture}	0.8

Table 5.1: RF and electrode properties of the new beam dynamics design approach.

beam current [mA]	1
mass-to-charge ratio	6
input energy [keV/u]	2.5
output energy [keV/u]	300
$\epsilon_{\text{in}}^{\text{transversal, n. rms}}$ [$\pi\,\text{mm}\,\text{mrad}$]	0.08
$\epsilon_{\text{out}}^{\text{transversal, x, n. rms}}$ [$\pi\,\text{mm}\,\text{mrad}$]	0.086
$\epsilon_{\text{out}}^{\text{transversal, y, n. rms}}$ [$\pi\,\text{mm}\,\text{mrad}$]	0.085
$\epsilon_{\text{out}}^{\text{longitudinal, rms}}$ [$\pi\,\text{MeV}\,\text{deg}$]	0.048
transmission [%]	98.31

Table 5.2: Beam properties with the new design approach.

After all, the vane voltage could be reduced to 40 kV for the acceleration of the HELIAC design beam with a mass-to-charge ratio of $A/q = 6$ and a beam current of 1 mA [43] at the expense of the electrode length having to be increased to about 2.8 m. Also a high transmission of > 98 % was yielded. Details on the developed beam dynamics design are given in Fig. 5.1 and Fig. 5.2, and a summary of the corresponding RF and electrode properties as well as of the beam properties is provided by Tab. 5.1 and Tab. 5.2, respectively.

5.2 RF Design

A model of the developed preliminary new design for a completely revised full-length HLI-RFQ is shown in Fig. 5.3, with an overall electrode length of 2829 mm and a total of 24 stems at a distance of 120 mm (= stem center distance, see Fig. 4.1). To yield the nominal electrode length specified by the beam dynamics design, the length of the electrode overhangs was cut down to 34.3 mm (from 51 mm at the prototype) by applying a minor modification to the electrode mounting brackets at the end-stems. After all, the decrease in overhang length is beneficial for reducing the longitudinal end-field magnitude (see chapter (6)), decreasing the depth of the tub-shape of the longitudinal voltage distribution by reducing the surplus overhang capacitance, and for the mitigation of mechanical overhang vibrations. At an effective stem height of 174.9 mm to obtain the nominal resonance frequency of 108.408 MHz, the geometric stem height can finally be decreased to 265.7 mm. Also, the stem arm offset for dipole compensation was readjusted to almost exactly 15 mm. Based on the RF simulations, the expected shunt impedance is about 105 kΩm (0.75 of the simulated value), the difference of which compared to the prototype is attributed to the higher number of RF cells, the reduction in overhang capacitance and a slight difference in the ratio of $r_{\text{electrode}}/r_{\text{aperture}}$.
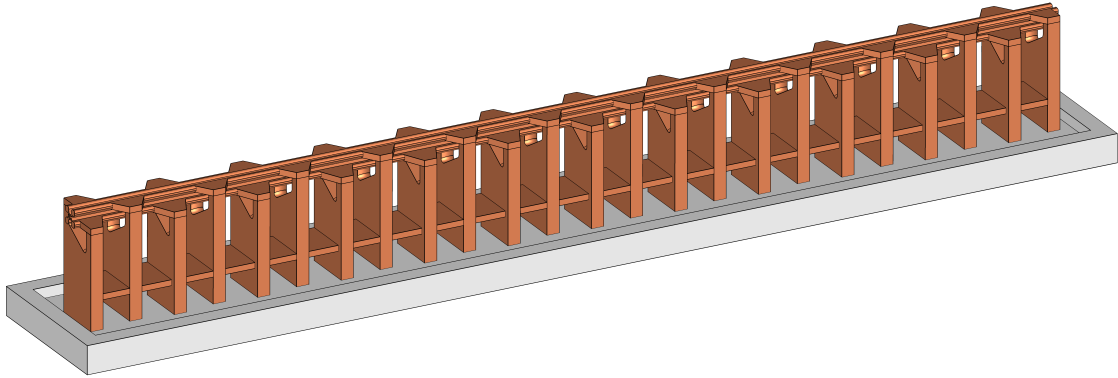

Figure 5.3: CST model of the developed new design for a completely revised full-length HLI-RFQ.

5.3 Comparison of Existing HLI-RFQ and New Design Concept

As summarized in Tab. 5.3, the key features of the new design concept compared to the existing HLI-RFQ are an almost preserved shunt impedance > 100 kΩm, a reduced intervane

voltage of 40 kV, resulting in a correspondingly decreased expected power consumption of
< 45 kW, full dipole compensation, a considerably enhanced mechanical rigidity, and a re-
duced thermal sensitivity. As shown in Fig. 5.4, the vibration amplitudes at the electrodes
are reduced by a factor of at least 20 ($\zeta = 0.106\,\%$) up to 200 ($\zeta = 0.93\,\%$).

	existing HLI-RFQ	new design concept
beam mass-to-charge ratio (cw)	6	6
design beam current [mA]	5	1
electrode length [m]	1.99	2.83
shunt impedance [kΩm]	108	105^a
quality factor	3300	5200^a
intervane voltage ($A/q = 6$) [kV]	55	40
RF power (cw) [kW]	55.7	43.1^a
$r_\text{electrode}/r_\text{aperture}$ (avg.)	0.8	0.8
dipole ratio [%]	10.2^b	$\approx 0^b$
number of stems	12	24
stem distance [mm]	173	120
beam axis height [mm]	162	290.3
mechanical damping (ζ) [%]	≈ 0.11	$0.5 - 0.93^c$
mechanical eigenfrequency [Hz]	500	786^b
thermal detuning [Hz/W]	6.7	$1.1 - 1.3^{b,c}$

Table 5.3: Comparison of the existing HLI-RFQ and the new design concept by their crucial proper-
ties regarding design beam parameters and structure geometry, as well as RF, mechanical
and thermal properties (a: expected value, b: simulated value, c: value of the prototype).
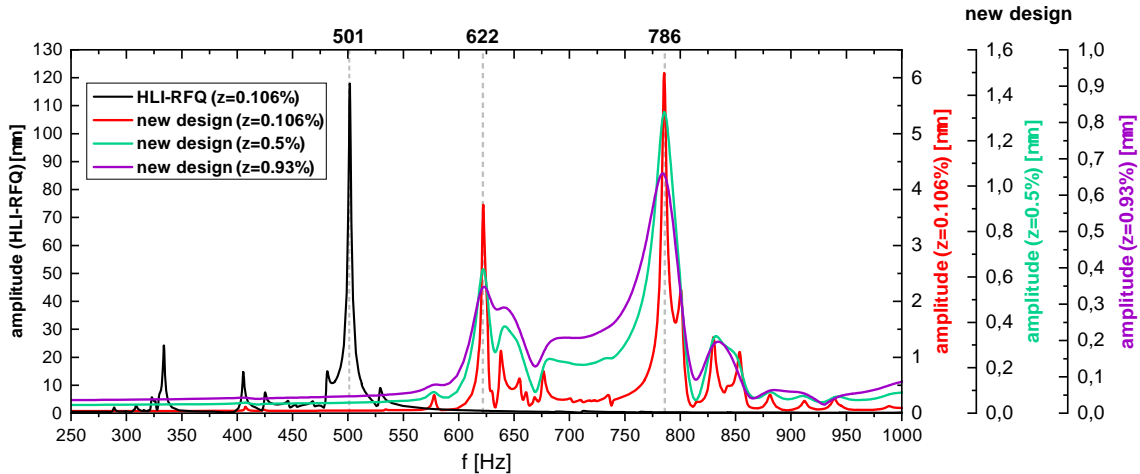

Figure 5.4: Comparison of the simulated mechanical resonance response of the existing HLI-
RFQ (upper electrode, see Fig. 3.23) and the new design (lower electrode) to radial harmonic
excitation at an intervane voltage of 50 kV, regarding different values of the damping ratio ζ. On
the new design the due to the stem arm offset wider electrode mounting brackets at the lower
electrodes result in an additional horizontal vibration mode at 622 Hz, besides the mechanical
radial main resonance at 786 Hz.

(6) Compensation of the Longitudinal End-Fields in 4-Rod RFQs

Besides the difference in length of the current paths to the lower and upper electrodes, which results in an electric dipole field as discussed in section 2.3.5, the conventional geometric structure of 4-rod RFQs has another design inherent asymmetry regarding its RF end-cells. As shown in Fig. 6.1, the current paths to the long-overhang electrode ends, which are mounted on the second-last stem, are considerably longer than to the short-overhang electrode ends, being mounted on the end-stem. In analogy to the explanation provided by Fig. 2.33, this results in a reduced potential on the short-overhang ends compared to the long-overhang ends. Furthermore, with only one adjacent stem the coupling of the end-stems to the RF structure is much weaker compared to the second-last stems. This reduces the induced current on the end-stems and additionally degrades the charging of the short overhangs.
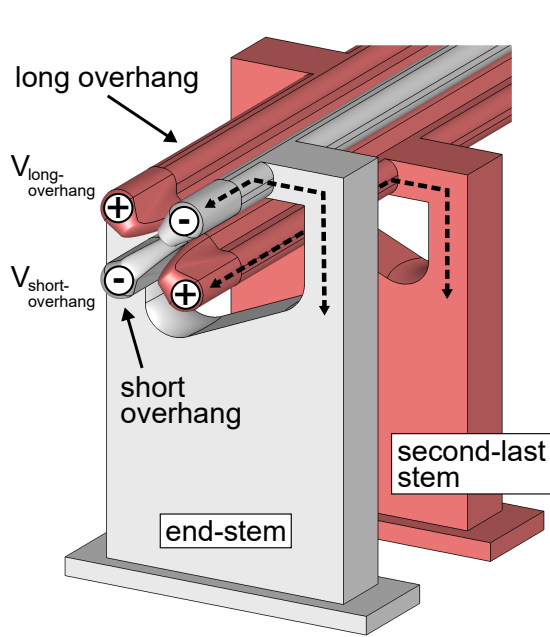

Figure 6.1: Front part of the RF structure of a 4-rod RFQ. The long overhangs are mounted on the second-last stem (red) and the short overhangs are mounted on the end-stem (gray). The corresponding potentials at the respective electrode ends are defined as $V_{\text{short-overhang}}$ and $V_{\text{long-overhang}}$. The current paths are indicated by the black dashed lines.
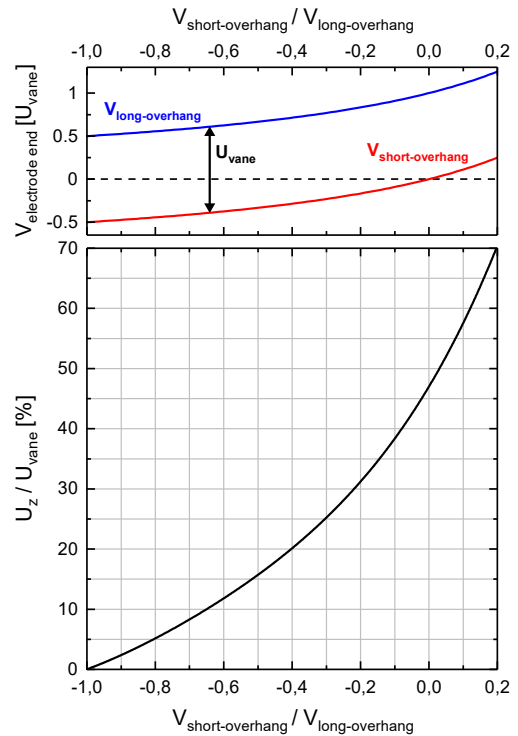

Figure 6.2: End-field voltage U_z (in relation to the vane voltage U_{vane}) as function of the potential asymmetry between the short- and long-overhang electrode ends, characterised by the ratio $V_{\text{short-overhang}}/V_{\text{long-overhang}}$.

(6) End-Field Compensation

After all, the uneven potential distribution at the electrode ends violates the quadrupole potential symmetry (since $V_{\text{long-overhang}} \neq V_{\text{short-overhang}}$) and according to section 2.3.6 results in a longitudinal electric field component ("end-fields") between the plane of the electrode ends and the end-plates at the beam entrance and exit flanges (see Fig. 6.4). The magnitude of the end-field $E_z(z)$ along the longitudinal axis is depicted in Fig. 6.3, whereas the end-field voltage U_z as function of the potential asymmetry is shown in Fig. 6.2. Eventually, these longitudinal fields might have negative effects on the nominal beam output properties like energy and emittance, but also transmission. Therefore, several approaches for a compensation of the end-fields have already been studied so far [162]. However, the applied methods for increasing the inductivity of the end-stems or increasing the potential on the short-overhang ends by applying additional capacitance only allowed a small amount of compensation to be achieved, whereas resulting in drawbacks and constraints on the RF end-cell design.
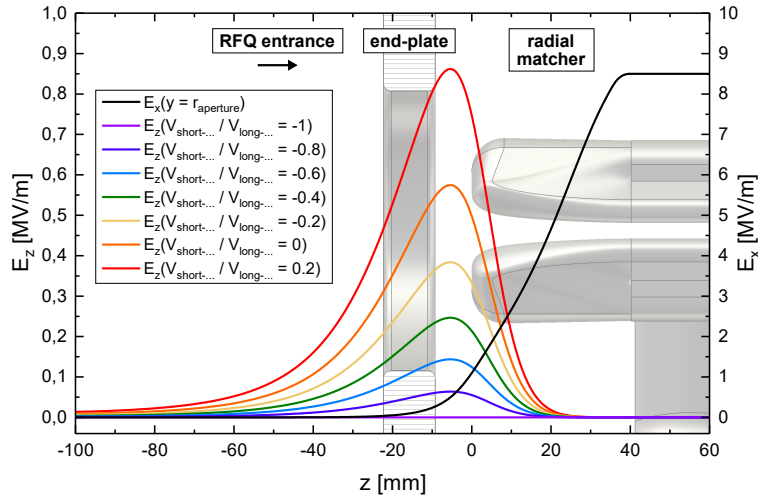

Figure 6.3: Longitudinal electric end-field $E_z(z)$ for different ratios of the potentials at the electrode ends of the long overhang ($V_{\text{long-overhang}}$) and short overhang ($V_{\text{short-overhang}}$). The transversal electric field $E_x(z)$ at aperture radius ($y = r_{\text{aperture}}$) for $U_{\text{vane}} = 40\,\text{kV}$ is given for comparison.

According to [163], the presence of a longitudinal end-field at the entrance gap causes a prebunching effect on the incoming DC beam, which mainly affects the beam output emittance and transmission. It was shown that this prebunching can be advantageously used by matching the synchronous phase of $-90°$ at the center of the first shaper cell for particles with zero energy gain in the end-field. This can be accomplished by adjusting the phase shift for the synchronous particle within the distance between the RFQ entrance and the longitudinal shaper. Therefore, the length of either the gap between the electrode ends and the end-plate or of the radial matching section has to be adapted accordingly. Overall, a correct implementation of this method even yields a reduction of emittance growth and an increase in beam transmission compared to the reference case without any end-field influence, whereas a mismatch to the nominal shaper entrance phase leads to the exact opposite.

While accordingly the end-field at the entrance gap mainly influences the beam output quality and transmission, the end-field at the RFQ exit alters the output energy by having the effect of an additional acceleration gap. This can be problematic for the beam matching to the downstream accelerating structures, especially when the deviation from the nominal

output energy exceeds the energy acceptance of the following DTL linac, which can be in the range of down to $\pm 10\,\text{keV}$. An example for this is given by the case of the FNAL-RFQ [164], which after commissioning had to be analyzed and modified with tremendous effort in order to achieve the functionality of the planned injector upgrade.
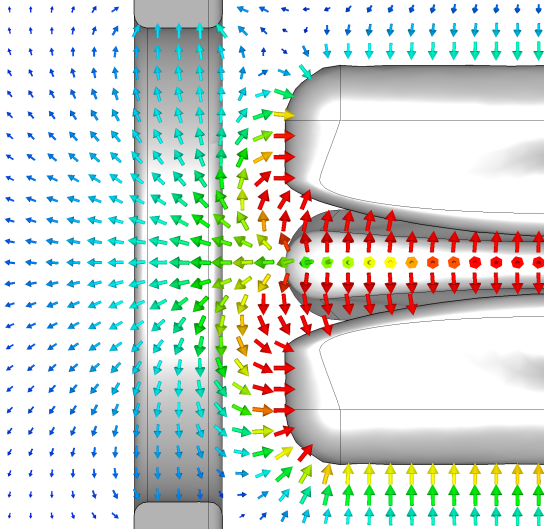

Figure 6.4: Electric field at the electrode ends without end-field compensation ($U_z/U_\text{vane} = 46.7\,\%$). The on-axis longitudinal component is clearly visible.
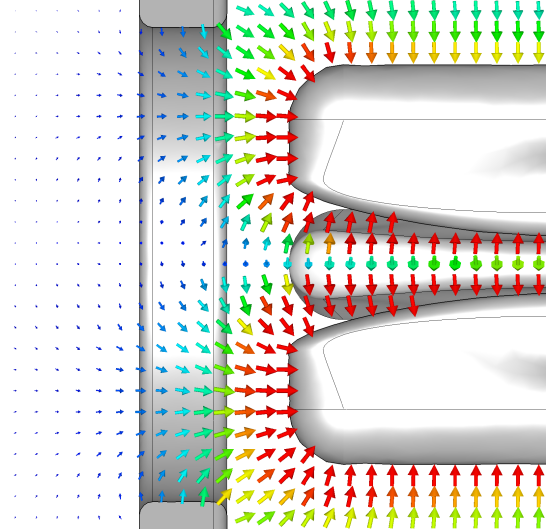
Figure 6.5: Electric field at the electrode ends with almost full compensation of the end-field ($U_z/U_\text{vane} = 0.2\,\%$).

This chapter presents a fundamentally new approach for a modification of the RF end-cell design of 4-rod RFQs[1], allowing to even out the potentials on all four electrode ends to $\pm|U_\text{vane}/2|$ as in the case of intrinsically symmetrical structures like 4-vane RFQs. By mostly restoring the desired quadrupole potential symmetry at the electrode ends using the newly developed method, an almost full compensation of the end-fields could be achieved. The electric field distribution at the entrance gap for the compensated case is shown in Fig. 6.5.

6.1 End-Fields in Conventional 4-Rod RFQs

In order to further investigate the effects of the conventional design parameters of 4-rod RFQs on the magnitude of the end-fields, simulations on a generic 6-stem model were conducted. The deployed simulation model, which is depicted in Fig. 6.6, mostly corresponds to the geometric specifications of the MYRRHA-RFQ [88] and has non-modulated flat electrodes which, however, have a radial matcher section to obtain a realistic electric field distribution in the vicinity of the electrode ends. The main properties of the simulation model are listed in Tab. 6.1. In general, the simulated values of the end-field voltage U_z show a strong dependence on the quality of the used tetrahedral simulation mesh along the integration path for E_z, which is indicated in Fig. 6.7, and good convergence could only be reached for very high local mesh refinement. After all, a short 6-stem RFQ model was chosen for the simulations in order to make optimum use of the available hardware resources, which are mainly limited by the

---

[1]as published in [165]

total RAM size. The vane voltage U_{vane} was evaluated at only one point near to the end of the matcher section in order to exclude effects of the overall field flatness on the investigated ratio U_z/U_{vane}. For each simulation step the RF resonance frequency was tuned to exactly $f_0 = 175.0\,\text{MHz}$ by adjusting the position of the tuning plates, which again were all set to the same height without flatness tuning.
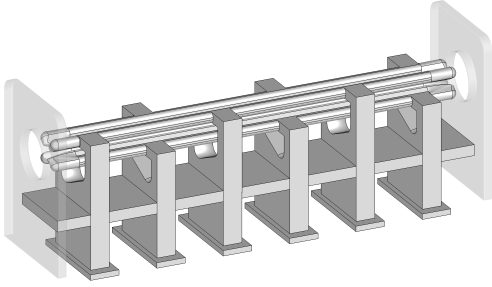

Figure 6.6: RF structure of the deployed 4-rod RFQ simulation model with 6 stems (the end-plates are shown transparent).
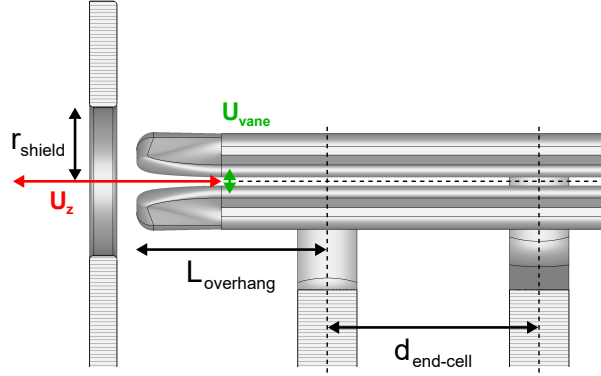
Figure 6.7: Crucial geometric design parameters affecting the longitudinal end-field, and spatial orientation of the voltages U_z and U_{vane}.

RF frequency [MHz]	175.0
stem distance (d_{stem}) [mm]	100
electrode overhang* (L_{overhang}) [mm]	55 / 90
total electrode length [mm]	610 / 680
simulated shunt impedance [kΩm]	79 / 64
electric dipole ratio [%]	34.5
electrode radius [mm]	3.4
aperture radius [mm]	4.2
RF shielding aperture radius [mm]	35

Table 6.1: Properties of the basic non-modified 6-stem simulation model (*for the second modification approach the overhang had to be extended to $L_{\text{overhang}} = 90\,\text{mm}$ in order to fit the side-stem mounting bracket on the lower electrode).

Eventually, as shown Fig. 6.7, the crucial design parameters which affect the potential distribution at the electrode ends are:

- length of the overhang L_{overhang}
- RF shield aperture radius r_{shield} in the end-plate
- RF end-cell distance $d_{\text{end-cell}}$
- longitudinal distance distance between the electrode ends and the end-plate

Throughout the parameter studies the distance between the electrode ends and the end-plates was set to a fixed value of $9.2\,\text{mm}$ without any further variation. Whereas an increased distance would result in a reduction of the end-gap capacitance, thus mitigating the end-fields

[166], this however also increases the space for longitudinal drift, which again is disadvantageous for the beam dynamics at both the entrance and exit gap. Also, the radius of the RF shield aperture affects the capacitance between the electrode ends and the end-plate, however, its influence on the end-field voltage is rather moderate ($\Delta U_z/U_{\text{vane}} \approx 3\,\%$, see Fig. 6.8). In order to minimize the emission of RF radiation through the shield aperture, its radius should generally be chosen as small as possible with regard to the transversal beam envelope.
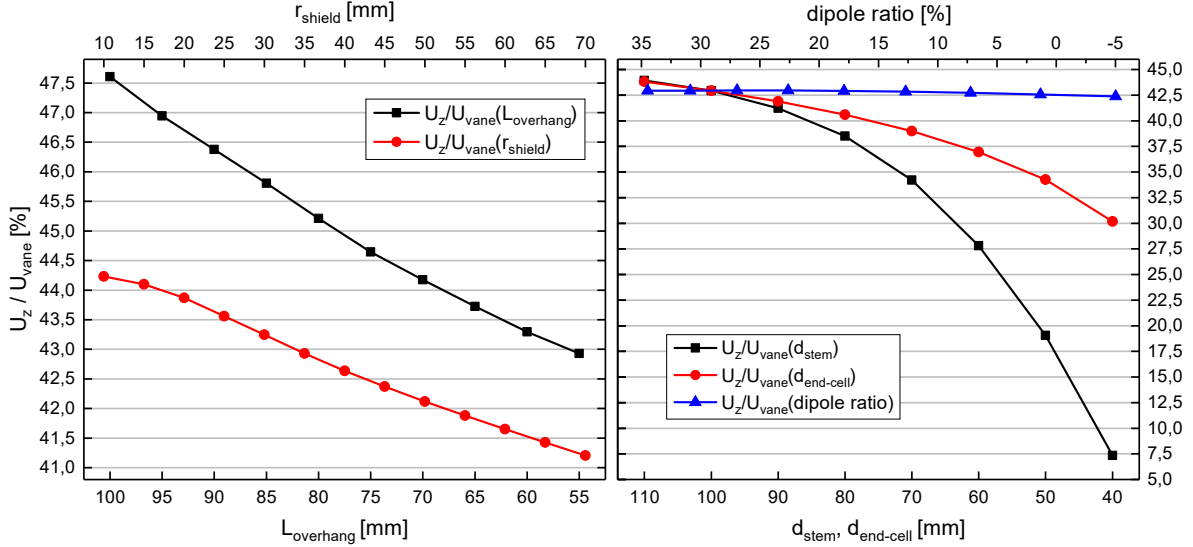

Figure 6.8: Influence of the overhang length L_{overhang} and RF shield aperture radius r_{shield} (*left*), as well as of the stem distance d_{stem}, length of the RF end-cell $d_{\text{end-cell}}$ and dipole ratio (*right*) on the on-axis longitudinal end-field voltage U_z.

As already stated in [163] and [166], the magnitude of the end-fields is affected by the length of the overhang L_{overhang} (actually, L_{overhang} corresponds to the length of the short overhang, whereas the length of the long overhang equals $L_{\text{overhang}} + d_{\text{end-cell}}$). Considering the shortest as well as the longest practically reasonable overhang length, the corresponding difference of the end-field voltage $\Delta U_z/U_{\text{vane}}$ amounts to only about 4.5 %. Because at 4-rod structures, the potential distribution at the electrode ends is affected by the electric dipole, also the dependence of the end-field voltage on the degree of dipole compensation was investigated. From this, it became apparent that the dipole only has a very minor effect on the end-fields of about $\Delta U_z/U_{\text{vane}} < 0.3\%$ for a reduction of the dipole ratio from 35 % to full compensation. Reducing the stem distance of either only the RF end-cell ($d_{\text{end-cell}}$) or for the entire structure (d_{stem}) results in better coupling to the end-stems and thus increases the induced current on them. Although by this a significant reduction of the end-fields can be achieved, both methods have the crucial drawback of resulting in very large stem heights in order to maintain the nominal RF resonance frequency, considering the required reduction of the stem distance for obtaining a substantial end-field compensation of $\Delta U_z/U_{\text{vane}} > 10\%$. Also, the shunt impedance $R_{\text{pL}}(d_{\text{stem}})$ typically degrades strongly with decreasing stem distance, considering the range below the maximum of the corresponding curve (see Fig. 4.2).

Besides the investigated aspects, also the position of the tuning plate in the RF end-cell, the overall field flatness, as well as the length of the radial matcher, which typically equals an

integer multiple of $\beta\lambda$, have a minor to negligible effect on the magnitude of the end-fields. Finally, it clearly shows that an efficient compensation of the end-fields cannot be achieved by a simple adjustment of the conventional design properties, resulting in the requirement for an extensive design modification of the RF end-cell.

6.2 Modified Design Approaches

As concluded from the previous design studies, on the one hand, the lengths of the current paths to the electrode ends have to be adjusted and, on the other hand, the induced current on the end-stems has to be increased in order to achieve an efficient compensation of the end-fields. Therefore, two different promising approaches for design modifications concerning these key demands were studied in more detail as presented in this section.

6.2.1 Adjustment of the Current Paths

For adjusting the lengths of the current paths to the long- and short-overhang electrode ends, the electrode mounting brackets at the end-stem and second-last stem can be modified according to Fig. 6.9. By this simple modification the current paths to the short overhangs are deliberately being extended by approximately $2d_1$, thus increasing the potential on the respective electrode ends. Analogously, the potential on the long-overhang electrode ends can be decreased due to a reduction of the respective current path length by about d_2.
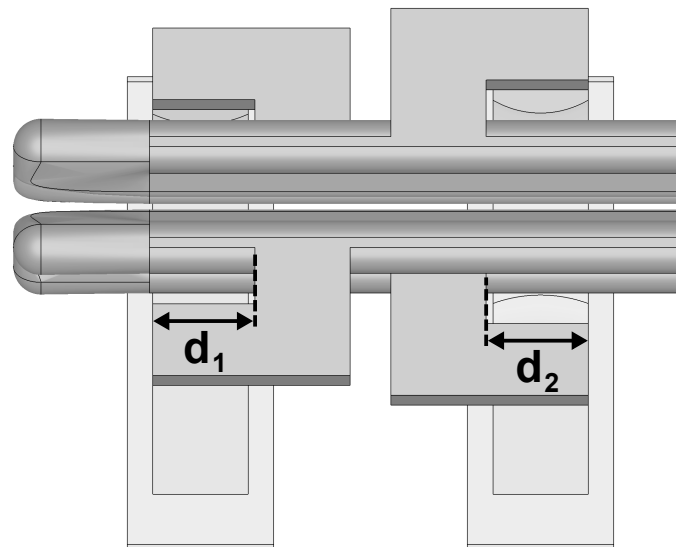

Figure 6.9: Adjustment of the current paths to the long- and short-overhang ends by modification of the electrode mounting brackets at the last two stems.

The yielded compensation of the end-field by different variations of the applied method and the corresponding effect on the shunt impedance is shown in Fig. 6.10. On the one hand, either only the mounting brackets at the end-stem (d_1 only) or at both the end-stem and

second-last stem (d_1 and d_2) can be modified. On the other hand, for both cases the modification of the end-stem mounting brackets further allows to reduce the length of the overhang uniformly with d_1, down to the maximum overhang reduction depth at which the plane of the electrode ends is at the same longitudinal position as the outer side of the end-stem.
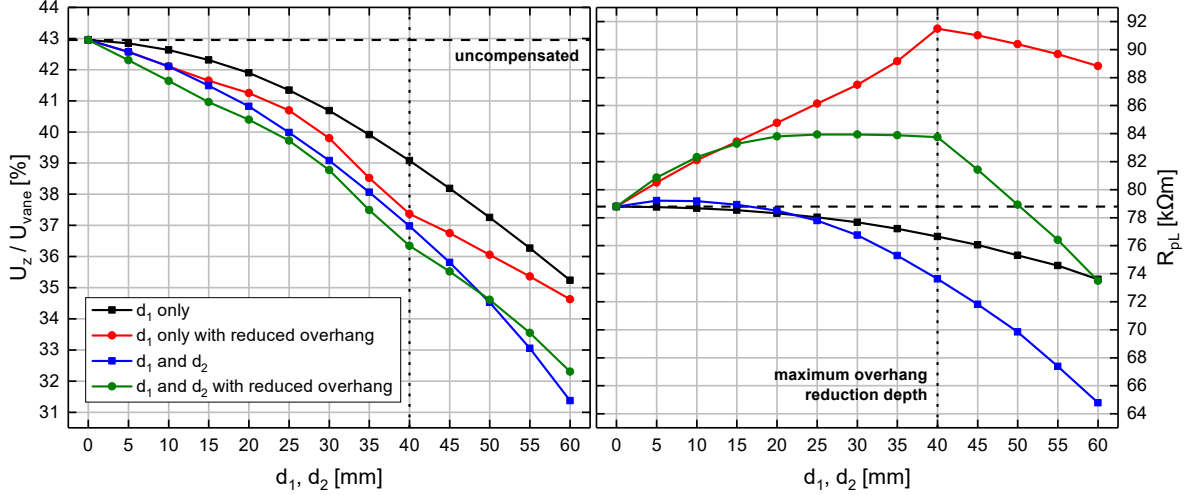

Figure 6.10: Compensation of the longitudinal end-field (expressed by the voltage ratio U_z/U_{vane}) by adjustment of the current paths according to Fig. 6.9 and corresponding influence on the shunt impedance R_{pL}.

Because a reduction of the overhang length decreases the capacitance of the RF end-cell, the shunt impedance is thereby even affected positively. For the variation of only d_1 with a corresponding reduction of the overhang length (red curve, Fig. 6.10), the end-field voltage can be decreased by $\Delta U_z/U_{\mathrm{vane}} \approx 8\,\%$ while simultaneously improving the shunt impedance by considerable 12.5 % from about 79 to 89 kΩm. However, since the overall nominal electrode length is primarily determined by the RFQ beam dynamics design, possibly the RF end-cell distance $d_{\mathrm{end\text{-}cell}}$ would have to be increased in order to compensate the overhang reduction and maintain the overall electrode length. According to Fig. 6.8, this again partially cancels the end-field compensation and also might decrease shunt impedance. Even though the uniform variation of d_1 and d_2 generally yields a slightly greater reduction of the end-field magnitude, varying only d_1 showed to be more advantageous considering the effect on the shunt impedance, regarding both cases with and without overhang reduction. Without overhang reduction, the variation of only d_1 also allows to reduce the end-field voltage by $\Delta U_z/U_{\mathrm{vane}} \approx 8\,\%$ (black curve, Fig. 6.10), which however would lead to a degradation of the shunt impedance by about 6.5 % from approximately 79 to 74 kΩm.

Considering the conducted simulations, the overall estimated impact on the shunt impedance can rather be seen as exaggerated because, compared to the 6-stem simulation model, the fraction of dissipated power in the modified RF end-cells decreases for longer RFQ structures with a higher number of RF cells. Although the total amount of compensation achieved by the investigated adjustment of the current paths seems not particularly high, being in the order of $\Delta U_z/U_{\mathrm{vane}} \approx 8\text{--}12\,\%$, the method eventually proved to be suitable for the compensation of minor remaining deviations from the desired quadrupole potential distribution after applying the concept of inductively coupled side-stems as discussed in the following section.

6.2.2 Inductively Coupled Side-Stems

With the primary aim to achieve an increase of the induced current at the end-stems, the concept of inductively coupled side-stems was developed. As depicted in Fig. 6.11, the side-stems are positioned lateral to the end-stem and connected to the long electrode overhangs. Since the side-stems are inductively coupled to the end-stem, as illustrated in Fig. 6.12, this basically creates an additional RF cell besides the actual end-cell. While increasing the induced current on the end-stem by providing another coupling cell for the end-cell, this method also offers the benefit of eliminating the current path length from the second-last stem to the long-overhang electrode ends, which are now charged directly by the current flow from the side-stems. Also, this generally has a positive influence on the overall field flatness because the normally intrinsically higher capacitance of the RF end-cells is effectively canceled out (see section 2.3.4 for further explanation).
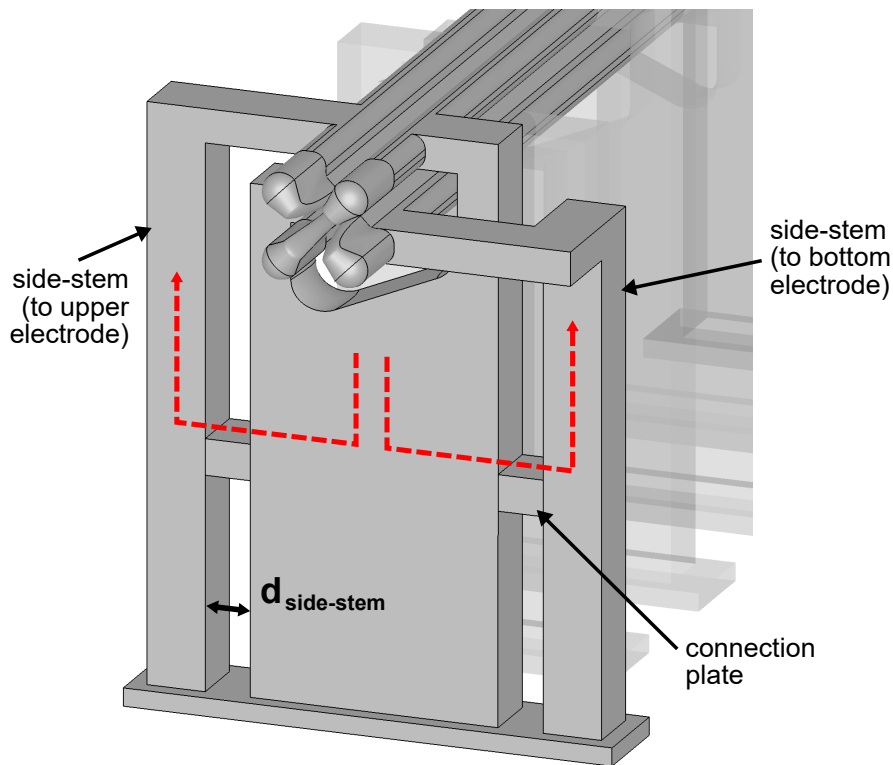

Figure 6.11: Inductively coupled side-stems lateral to the end-stem (the path and orientation of the electric current is indicated by the red dashed lines).

Analogously to the regular stems being connected by tuning plates, in the used simulation model the side-stems are connected to the end-stem by connection plates, which also were set to the same height as the tuning plates. Considering a hypothetical technical implementation, the connection plates can either be movable like the tuning plates or fixed at a certain position, depending on the practical technical feasibility and benefit for a possible adjustability of the end-field magnitude. Different mounting options for the connection of the side-stem to the bottom electrode are shown in Fig. 6.13 and are discussed in the following.
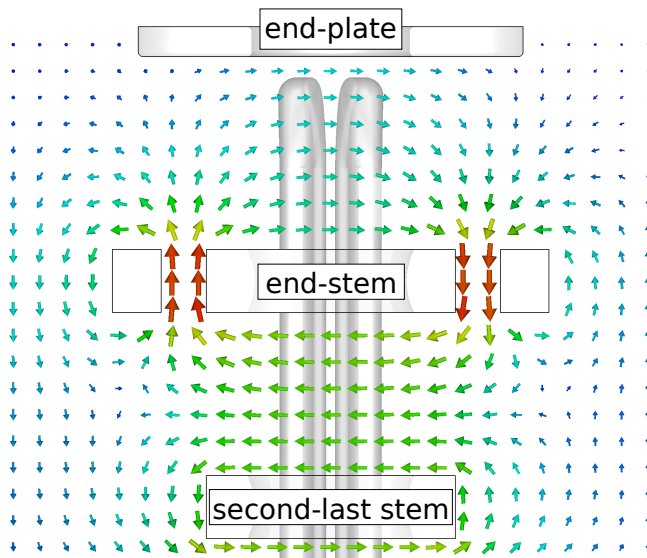
Figure 6.12: Magnetic field around the last two stems and the additional side-stems, which are positioned lateral to the end-stem.
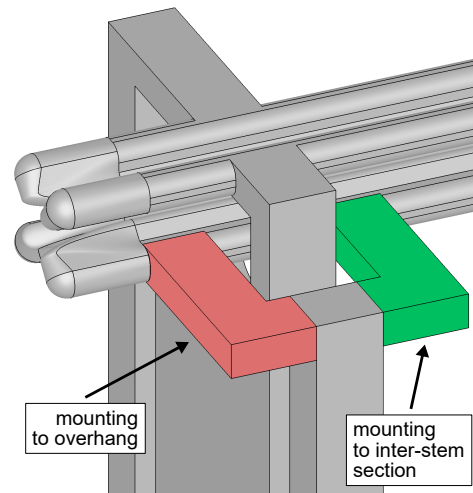

Figure 6.13: Different options for the mounting of the side-stem to the bottom electrode (green: mounting bracket connected to the inter-stem electrode section, red: mounting bracket connected to the overhang, both: "fork mounting").
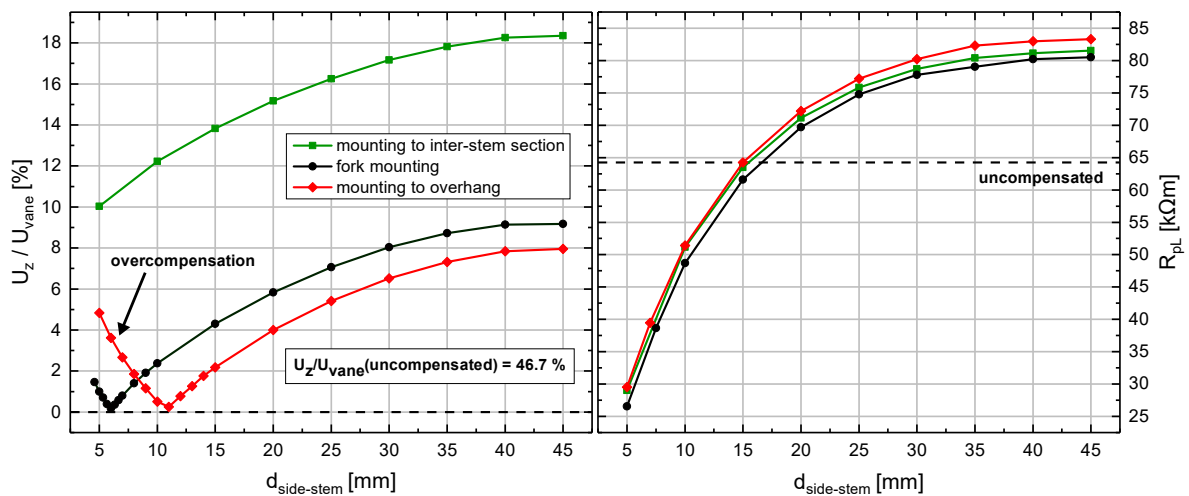

Figure 6.14: Compensation of the longitudinal end-field (expressed by the voltage ratio U_z/U_{vane}) as function of the side-stem distance $d_{\mathrm{side\text{-}stem}}$ and corresponding influence on the shunt impedance R_{pL}.

The achieved end-field compensation by the side-stem method is shown in Fig. 6.14 as function of the distance $d_{\mathrm{side\text{-}stem}}$ between the side-stems and the end-stem. The applied method yields an almost full compensation on the 6-stem simulation model from the uncompensated value of the end-field voltage of $U_z/U_{\mathrm{vane}} = 46.7\,\%$ down to nearly zero. Whereas even over-compensation can be achieved easily, however, in the compensated cases with close-to-zero end-field voltage a very small residual end-field still remains due to minor asymmetries of the end-stem, side-stems and the electrode mountings. Because the side-stems basically pro-

vide an additional current path to the long-overhang electrode ends, the shunt impedance is affected positively for large enough distances to the end-stem with less compensation effect. Positioning the side-stems closer to the end-stem results in stronger coupling and better compensation of the end-field, but however increases the overall power dissipation and accordingly results in a decrease of shunt impedance. Eventually, the power dissipated on a single side-stem roughly amounts to 50 % of the power loss on one regular stem, considering the case of preserved shunt impedance with $R_{\text{pL,compensated}}(d_{\text{side-stem}} = 15\,\text{mm}) \approx R_{\text{pL,uncompensated}}$. For a typical average overall power dissipation of $35\,\text{kW/m}$, assuming CW operation, the power loss on one side-stem amounts to about $1.7\,\text{kW}$. The corresponding heat load still seems reasonably coolable, provided that water cooling channels are routed directly through the side-stems and an efficient technical cooling concept is implemented, as in the case of the HLI-RFQ prototype or the MYRRHA-RFQ[2]. After all, the proposed side-stems even simplify the direct cooling of the long electrode overhangs and additionally stabilize them mechanically, thus preventing both thermal deformation as well as mechanical vibrations.

6.3 Full End-Field Compensation

For achieving full end-field compensation without a reduction of shunt impedance, a combination of the side-stem method and current path adjustment proved to be effective. For this purpose, the side-stem distance must first be chosen to the value $d_{\text{side-stem}}^{\star}$, at which the resulting shunt impedance $R_{\text{pL,compensated}}(d_{\text{side-stem}}^{\star}) \approx R_{\text{pL,uncompensated}}$ is equal to its value for the uncompensated case without side-stems. Finally, the small remaining end-field with its voltage U_z/U_{vane} being in the order of a few percent can then further be compensated by carefully adjusting the current paths to the four electrode ends.
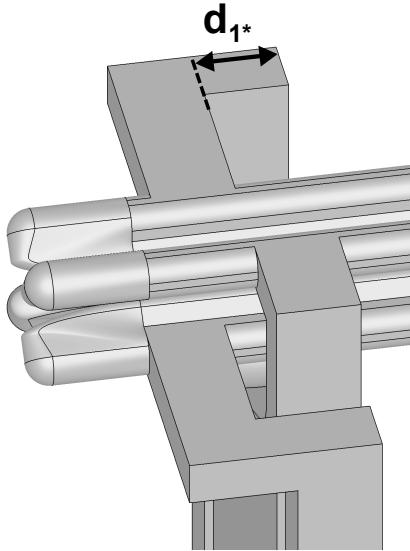

Figure 6.15: Adjustment of the current path to the electrode end of the upper long overhang by variation of the corresponding side-stem mounting bracket (parameterized by d_{1*}).
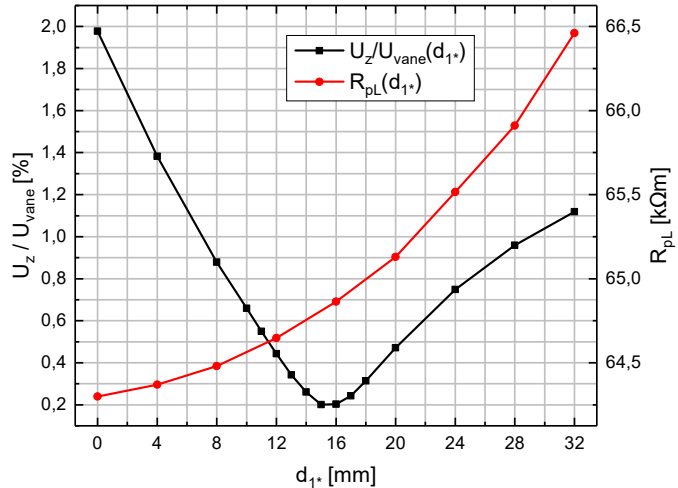
Figure 6.16: Compensation of the longitudinal end-field by the side-stem method with $d_{\text{side-stem}}^{\star} = 15\,\text{mm}$ ($R_{\text{pL}} \approx R_{\text{pL,uncompensated}}$) and additional adjustment of the current path only to the upper long-overhang electrode end by modification of the side-stem mounting bracket, according to Fig. 6.15.

---

[2]also see [88, Fig. 3]

Fig. 6.16 shows the almost full compensation down to an end-field voltage of $U_z/U_{\mathrm{vane}} \approx 0.2\,\%$, where additionally to the implementation of the side-stems only the current path to the upper long overhang was adjusted as depicted in Fig. 6.15. Overall, the initial value of the shunt impedance of $R_{\mathrm{pL}} \approx 65\,\mathrm{k\Omega m}$ is mostly preserved by the applied modification procedure.

In order to demonstrate the end-field compensation by the developed method on a longer 4-rod structure with a higher number of RF cells, other than the previously investigated short 6-stem model, the evolved modification procedure was applied to a design-identical 4-rod RFQ model with an electrode length of 3 m and 30 stems, typical for 4-rod RFQs. At this, a significant reduction of the uncompensated end-field magnitude of $U_{z,\mathrm{uncompensated}}/U_{\mathrm{vane}} = 51.7\,\%$ down to $U_{z,\mathrm{compensated}}/U_{\mathrm{vane}} = 2.6\,\%$ could be achieved easily. However, yielding further compensation turned out to be considerably more complicated because with a higher number of RF cells some of the effects which could be considered negligible at the previous investigations on the 6-stem model, like the electric dipole or effects of the field flatness, now have a noticeable influence on the end-field. Accordingly, the relevant parameter space for the fine-adjustment of the end-field is much larger, which makes full compensation with $U_{z,\mathrm{compensated}}/U_{\mathrm{vane}} \approx 0$ harder to achieve. After all, no negative influence on the shunt impedance, field flatness or mode separation could be observed for the implementation of the developed method at the 3 m long RFQ model. As shown in Fig. 6.17, the field distribution along the RFQ structure can even be improved by mounting the side-stems, due to the reduction of the redundant overhang capacitance.
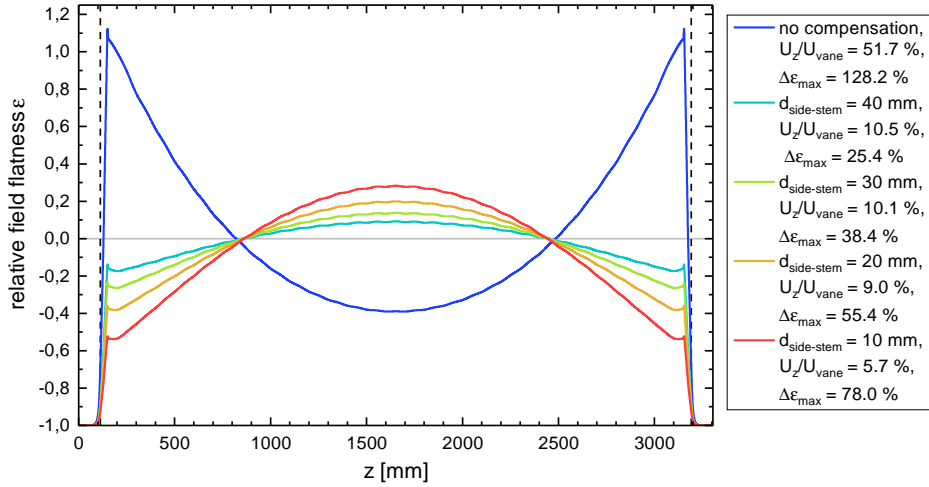

Figure 6.17: Relative field flatness $\epsilon(z)$ for different degrees of the end-field compensation by the side-stem method on a 3 m long RFQ model (with non-modulated electrodes and without flatness tuning, all tuning plates are positioned at the same height). The positions of the electrode ends are marked by the vertical black dashed lines.

After all, it could be shown that the method of inductively coupled side-stems in conjunction with minor modifications of the electrode mounting brackets for adjusting the current paths to the electrode ends is a suitable approach for obtaining an almost full compensation of the longitudinal electric end-fields in 4-rod RFQs without perturbing the RF performance or overall field flatness. A summary of the achieved maximum compensation and the associated influence on the shunt impedance for the individually and combined applied methods on the

6-stem simulation model, as well as the maximum total compensation on the 3 m long RFQ model is given in Tab. 6.2.

method	U_z/U_{vane} [%]		decrease of shunt
	uncompensated	compensated	impedance R_{pL} [%]
current path adaption	43.0	31.4	−17.7
side-stems	46.7	0.3	−14.1
combined method	46.7	0.2	0
combined method (3m-RFQ)	51.7	2.6	0

Table 6.2: Comparison of the developed methods for the compensation of the longitudinal end-field, regarding the achievable degree of compensation and influence on the shunt impedance.

Eventually, the adopted approach of actually compensating the end-fields in 4-rod RFQs by modifying the structure of the RF end-cells has to be compared to the possibility of making advantageous use of the prebunching effect in the end-field at the RFQ entrance, as proposed in [163]. For this, apparently only minor design changes are necessary for achieving the therefor required adaptation of the drift length in the entrance gap, while resulting in improvements of the beam transmission and emittance growth. Since the end-field at the RFQ exit mainly acts as an acceleration gap, its effect can simply be taken into account for the beam dynamics design in order to meet the nominal output energy, which from this point of view would even make the end-field compensation at the RFQ exit obsolete. However, the newly developed method for the end-field compensation at 4-rod RFQs, using the proposed side-stem concept, offers some unique benefits that finally can be summarized as follows:

- Because the longitudinal component of the end-fields can be compensated almost entirely, the resulting overall field distribution with likewise compensated dipole largely corresponds to the desired ideal quadrupole symmetry. This helps reaching design beam performance without requiring further considerations about the effects of the mentioned field deviations.

- The yielded end-field compensation is mostly independent of the overall capacitance between the end-plate and the electrode ends, which allows the radius r_{shield} of the shield aperture as well as the lengths of the entrance and exit gaps to be chosen as small as possible. This is an important advantage for the acceleration of very heavy ion beams at low energies and high currents [167], where it is crucial to keep the length of the transition section between the RFQ and the following accelerating structure as short as possible [168].

- By basically eliminating the excessive overhang capacitance, the overall field flatness can be improved.

- The installation of side-stems might even be applied with the purpose of improving the shunt impedance of 4-rod RFQs.

(7) Summary & Outlook

After several years of operating experience and considerable efforts to analyze and mitigate the severe problems arising from the high thermal sensitivity as well as from the occurring electrode vibrations, it became apparent that the pursued operating modes, such as CW acceleration of beams with $A/q = 6$ or pulsed acceleration for $A/q = 8.5$ at average heat loads of the quadrupole structure of up to $30\,\mathrm{kW/m}$, cannot be achieved with the existing 4-rod HLI-RFQ. For this reason, the decision was made to develop a completely revised design concept for a new HLI-RFQ to eventually replace the existing structure. The numerical simulations and experimental investigations conducted for this purpose are the primary subject of this thesis and the applied methods and achieved results are summarized in the following.

Since the primary objective of the ongoing HLI upgrade efforts is to provide a CW beam for the HELIAC accelerator, which is planned as a dedicated new linear accelerator for super-heavy elements research at GSI, an overview of the history of the exploration of heavy and super-heavy elements is given in section 1.1, starting from the historically first-ever artificial production of a transuranium element at Berkeley in 1940, over the discovery of six super-heavy elements at GSI from 1981 to 1996, to the discovery of the heaviest elements known today between 1998 and 2006 in Dubna. As can be noticed, this considerable progress was made possible by the continuous development and innovations in the field of particle accelerator technology. Due to the typically very low production rates of super-heavy nuclei, further developments for the acceleration of heavy ion beams with a focus on CW operation are thus highly required to enable the exploration of the predicted island of stability, which is briefly discussed in section 1.2. An overview of the existing GSI facility and the planned and currently under construction FAIR accelerator, the High Charge State Injector HLI, as well as the planned HELIAC project is given in sections 1.3, 1.4 and 1.5, respectively.
After the limitations of electrostatic pre-acceleration of low-energy ion beams and related methods for longitudinal bunching in order to accomplish the injection to a downstream drift tube accelerator constituted a major bottleneck for the achievable accelerator performance regarding beam intensity and quality, the concept of the RFQ was finally proposed in 1969, the basic operating principle of which is explained in section 2.1. After the RFQ principle had been successfully tested in 1974 at Protvino and later in 1980 at Los Alamos using 4-vane type resonator structures, in the following years RFQs became a standard device for the acceleration of low-energy ion beams and are being used in most of today's ion accelerators. As presented in section 2.2, over the years also a variety of different applicable resonator concepts evolved, with the 4-rod type RFQ mainly having being developed since the mid 1980s at IAP in Frankfurt. Because of the distinct advantages of 4-rod structures in terms of flexibility and simplicity of the frequency and field tuning, as well as comparatively low manufacturing costs and simple maintenance, the 4-rod type resonator can despite of all problems with the existing 4-rod HLI-RFQ be considered to be the most suitable choice of RFQ structure regarding the operational requirements of the HLI. The basic resonator char-

acteristics of RFQs are outlined in section 2.3 and a brief digression into the basics of RFQ beam dynamics and electrode design is provided by section 2.4.

Whereas the method of introducing a stem arm offset for achieving dipole compensation in 4-rod RFQs, originally being developed for the MYRRHA-RFQ, could directly be applied to the developed design for a newly revised HLI-RFQ, a completely new approach to compensate the other characteristic field error occurring in 4-rod RFQs, namely the longitudinal end-fields, was developed in the context of this thesis, as presented in chapter (6).
The conducted studies on the formation of the end-fields clearly showed that the uneven potential distribution at the quadrupole electrode ends, causing the longitudinal field component, is attributed to unequal current path lengths to the electrode ends as well as to significantly lower induced charging currents on the end-stems compared to the second-last stem. After all, both problems could successfully be addressed by a modification of the electrode mounting brackets and the introduction of so-called side-stems next to the end-stem. Finally, a reduction of the end-field from initially about 50 % (ratio of voltage in the end-field to intervane voltage) to almost zero can be achieved, while entirely preserving the shunt impedance. An experimental confirmation of the proposed principle is still to be obtained.

7.1 Conclusions from the Structural-Mechanical & Thermal Investigations

Prior to the prototype development for a new RFQ structure, an extensive simulation-based analysis was carried out to investigate the mechanical and thermal problems of the existing HLI-RFQ, the properties of which are stated in section 3.1. The starting point and reference case for the conducted simulations were the observations and measurements previously done at GSI, as summarized in sections 3.2 and 3.3. From a modal analysis with ANSYS, the measured vibrational modes at 350 Hz and 500 Hz could quickly be identified, and two criteria for the excitation of mechanical electrode eigenmodes by the electric quadrupole field became clearly evident: On the one hand, the vibrational plane of the eigenmode oscillation needs to have a radial component with respect to the quadrupole center, meaning that the vibration must be at least partially parallel to the vector of the electric force on the electrode. On the other hand, the deformation profile of the eigenmode has to point unidirectionally to one side of the vibrational plane since also the direction of excitation by the electric force is constant along the electrode. As shown in section 3.4.2, these deductions could later be validated by a harmonic response analysis, where it was shown that only the radial mode at 500 Hz is excited by the quadrupole field, whereas the excitation of the tangential mode at 350 Hz is clearly attributed to an asymmetry of the quadrupole field distribution caused by the characteristic electric dipole component of 4-rod structures. From an analysis of the RF-sensitivity to the observed excited mechanical eigenmodes using CST MWS, as given in section 3.4.3, also the fact that the tangential vibration at 350 Hz cannot be observed in the reflected RF signal could finally be clarified, which is due to its effect on the RF frequency detuning being in the order of only 5 % compared to the radial mode. The value of the vibration amplitudes derived from these simulations of about 2 μm is in good agreement with the measured values from the preceding vibrometer measurements at GSI. This was additionally confirmed by transient

vibration simulations with ANSYS, where also the previously assumed excitation mechanism by the edges of the RF pulses could nicely be reproduced, as presented in section 3.4.4.

From the conducted thermal analysis using CST Mphysics Studio, as shown in section 3.5, also the unexpectedly high thermal sensitivity of the HLI-RFQ could be roughly reproduced. Therefor, it is absolutely necessary to include all crucial thermal processes besides mere heat conduction in the simulations, like the heating of the cooling water along the cooling channels and the finite heat transfer from the copper material to the flowing cooling water. However, since in the current software version of CST both these effects cannot be taken into account, a semi-analytical workaround was applied. From this it could be shown that both processes have a considerable and non-negligible effect on the temperature distribution and resulting frequency detuning. For the case of 4-rod structures, also the properties of the mechanical coupling between the thermal deformations of the single components at the screwed connections between the electrodes and stems have a significant influence on the value of the simulated frequency detuning, which was investigated by applying different mechanical boundary conditions. After all, the observed frequency detuning of $-200\,\text{kHz}$ at a power dissipation of $30\,\text{kW}$ could be reproduced with an average heat transfer coefficient of $\alpha = 9250\,\text{W/m}^2\text{K}$ and completely suppressed mechanical coupling between the electrodes and stems, considering a water flow rate of $2\,\text{l/min}$ as used during operation of the real HLI-RFQ. Nevertheless, for a more accurate thermal analysis it would be highly recommended to apply more sophisticated simulation software like ANSYS or COMSOL that are capable to take into account the heating of the cooling water and the fluid dynamics in the cooling channels, as well as the properties of the heat transfer at material transitions.

7.2 Summary of the RFQ Development & Outlook

The prototype design was developed on the basis of the already successfully tested RFQs for FRANZ and MYRRHA. As described in section 4.1, the basic geometric design parameters of the RF structure were adjusted and optimized by RF and mechanical design studies in order to yield the nominal operation frequency of $108.408\,\text{MHz}$ and achieve maximum mechanical rigidity with an as low as possible reduction of shunt impedance. Therefor, the crucial parameter of the stem distance was chosen to a value of $120\,\text{mm}$, close to the maximum of the corresponding shunt impedance curve (as function of the stem distance), which eventually allowed to yield almost the same value of the shunt impedance as at the existing HLI-RFQ ($\approx 105\text{--}110\,\text{k}\Omega\text{m}$), despite of a significantly increase in capacitance due to the structural reinforcement of the RF structure. In the same way, all other geometric properties of the RF structure were optimized, concerning the geometry of the electrodes and their mounting brackets, as well as the stem geometry. The target parameters considered for the optimization were the resulting stem height, the shunt impedance, the influence on the dipole ratio, and the frequency of the unidirectional radial mechanical electrode eigenmode, which was tried to raise as high as possible. After all, the mechanical eigenfrequencies could be increased to values close to those of the FRANZ- and MYRRHA-RFQs, thus being significantly higher compared to the existing HLI-RFQ (by a factor from 1.5 to 2), while achieving full dipole compensation and obtaining a comparatively large but tolerable stem height of $> 250\,\text{mm}$. Based on the conducted design studies, a 6-stem prototype with an additionally optimized

cooling concept and an electrode length of 702 mm was manufactured by NTG GmbH, the simulated RF and mechanical properties of which are presented in chapter 4.2. While with a fully functional water cooling system the prototype is designed for high-power RF tests, it is also equipped with some unique features for vibration measurements and temperature diagnostics, such as four dedicated diagnostic windows in the tank for measurements with a laser vibrometer, as well as sensor shafts in the stems to monitor their inside temperature.

Due to the substantially improved cooling system, the simulated thermal sensitivity (frequency detuning per unit of dissipated power) could be significantly reduced by a factor of about 5 to 6 compared to the existing HLI-RFQ (from 6.7 to 1.1–1.3 Hz/W).

Eventually, as shown in section 4.3, extensive RF and mechanical pre-tests were conducted to validate the crucial simulated properties prior to the planned high-power tests. By applying different methods of measurement, the simulated quality factor ($Q \approx 5000$) and shunt impedance ($R_{\mathrm{pL}} \approx 110 \, \mathrm{k\Omega m}$) could finally be validated. Also, the achievement of an almost full compensation of the dipole to a ratio of less than 1 % was confirmed by measurements of the voltage distribution on the upper and lower electrode pair. In order to investigate the mechanical eigenmode spectrum of the prototype structure, different methods for the measurement and excitation of vibrations have been applied. Whereas the excitation was induced either acoustically by a PA speaker or mechanically by a piezo actuator or a soft-face hammer, the corresponding vibrations were measured with a microphone, a piezo sensor and a laser vibrometer, which had previously been used to measure the vibrations on the existing HLI-RFQ. After all, it could be observed that the measured spectra agree well with the corresponding simulations, thus confirming the anticipated mechanical reinforcement. Additionally, an experimental modal analysis using a 3D laser vibrometer was conducted, which finally allowed to experimentally investigate the eigenmode deformation profiles of the electrodes, but also to more accurately determine the mode-dependent damping times.

After tuning the RFQ structure to the HLI-frequency of 108.408 MHz, making the tank vacuum-tight and installing the diagnostics devices, a pre-conditioning up to 200 W was performed at IAP (see section 4.4), where besides a minor conditioning threshold between 140 and 240 mW within the typically critical low-power range, the cavity accepted the power ramp-up quickly and without noticeable problems. As shown in section 4.5, after the completion of the pre-tests and pre-conditioning, the prototype tank was prepared for the transport to GSI, where high-power tests with thermal loads of more than 30 kW/m and further vibration measurements during RF operation are to be carried out soon.

A new preliminary beam dynamics design and a correspondingly adapted model of the developed RFQ design with an electrode length of 2.8 m for the CW acceleration of a 1 mA heavy ion beam with $A/q = 6$, according to the HELIAC specifications, is finally presented in chapter (5). By a reduction of the required intervane voltage to only 40 kV, the overall power consumption could be reduced to only 43 kW. Additionally, this reduces the electric force on the electrodes and helps to mitigate vibrations. From a comparison between the existing HLI-RFQ and the new design, it can be seen that only by the mechanical reinforcement of the structure the vibration amplitudes can be expected to reduce by a factor of 100 to 200, considering the measured damping properties of the prototype.

(8) Appendix

Bibliography

[1]   D.C. HOFFMAN, F.O. LAWRENCE, J.L. MEWHERTER, F.M. ROURKE: *Detection of Plutonium-244 in Nature.* Nature Vol. 234, pp. 132–134, 1971, http://doi.org/10.1038/234132a0.

[2]   J. LACHNER, I. DILLMANN, TH. FAESTERMANN, U. GERSTMANN, G. KORSCHINEK, CH. LIERSE VON GOSTOMSKI, M. POUTIVTSEV, G. RUGEL, A. TÜRLER: *Attempt to Detect Primordial* ^{244}Pu *on Earth.* Physical Review C 85, 015801 (2012), http://doi.org/10.1103/physrevc.85.015801.

[3]   D.F. PEPPARD, M.V. GERGEL, G.W. MASON, J.F. MECH, M.H. STUDIER, J.C. SULLIVAN: *Isolation of Microgram Quantities of Naturally-occuring Plutonium and Examination of its Isotopic Composition.* Journal of the American Chemical Society, 1951, 73, 6, 2529–2531, http://doi.org/10.1021/ja01150a034.

[4]   E. MCMILLAN, P.H. ABELSON: *Radioactive Element 93.* Physical Review 57, 1185 (1940), http://doi.org/10.1103/physrev.57.1185.2.

[5]   A.B. GARRETT: *The Chemistry of Elements 93, 94, 95 and 96 (Neptunium, Plutonium, Americium and Curium).* The Ohio Journal of Science: Volume 47, Issue 3 (May, 1947), http://hdl.handle.net/1811/5752.

[6]   S.G. THOMPSON, A. GHIORSO, G.T. SEABORG: *The New Element Berkelium (Atomic Number 97).* Physical Review 80, 781 (1950), http://doi.org/10.1103/physrev.80.781.

[7]   S.G. THOMPSON, A. GHIORSO, G.T. SEABORG, K. STREET, JR.: *The New Element Californium (Atomic Number 98).* Physical Review 80, 790 (1950), http://doi.org/10.1103/physrev.80.790.

[8]   S.G. THOMPSON, G.R. CHOPPIN, A. GHIORSO, B.G. HARVEY: *Transcurium Isotopes Produced in the Neutron Irradiation of Plutonium.* Physical Review 93, 908 (1954), http://doi.org/10.1103/physrev.93.908.

[9]   B.G. HARVEY, R. CHOPPIN, A. GHIORSO, S.G. THOMPSON: *Further Production of Transcurium Nuclides by Neutron Irradiation.* Physical Review 93, 1129 (1954), http://doi.org/10.1103/physrev.93.1129.

[10] E.O. LAWRENCE, M.S. LIVINGSTON: *The Production of High Speed Light Ions Without the Use of High Voltages.* Physical Review 40, 19 (1932), http://doi.org/10.1103/physrev.40.19.

[11] R.J. SILVA: *Fermium, Mendelevium, Nobelium, and Lawrencium.* The Chemistry of the Actinide and Transactinide Elements, Third Edition, Volume 3, Chapter 13, Springer Science + Business Media B.V., ISBN 978-1-40203-598-2, 2008.

[12] R.C. BARBER, N.N. GREENWOOD, A.Z. HRYNKIEWICZ, Y.P. JEANNIN, M. LEFORT, M. SAKAI, I. ULEHLA, A.H. WAPSTRA, D.H. WILKINSON: *Discovery of the Transuranium Elements.* Progress in Particle and Nuclear Physics, Volume 29, pp. 453–530, 1992, http://doi.org/10.1016/0146-6410(92)90008-p.

[13] M.G. ITKIS, E. VARDACI, I.M. ITKIS, G.N. KNYAZHEVA, E.M. KOZULIN: *Fusion and Fission of Heavy and Superheavy Nuclei (Experiment)*. Nuclear Physics A 944 (2015) 204–237, http://doi.org/10.1016/j.nuclphysa.2015.09.007.

[14] P. ARMBRUSTER: *On the Production of Heavy Elements by Cold Fusion: The Elements 106 to 109*. Annual Review of Nuclear and Particle Science, Vol. 35, pp. 135–194, 1985, http://doi.org/10.1146/annurev.ns.35.120185.001031.

[15] S. HOFMANN: *The Discovery of Elements 107 to 112*. European Physics Journal Web of Conferences, Volume 131, 06001 (2016), http://doi.org/10.1051/epjconf/201613106001.

[16] D. BÖHNE: *The UNILAC, Development and Present Status*. Proceedings of LINAC1976 (pp. 2–11, A01), Chalk River, Ontario, Canada, http://accelconf.web.cern.ch/l76/papers/a01.pdf.

[17] S. HOFMANN: *Synthesis of Superheavy Elements by Cold Fusion*. Russian Chemical Reviews, Volume 78, Number 12, 1123–1138 (2009), http://doi.org/10.1070/rc2009v078n12abeh004076.

[18] V. UTYONKOV, S. DMITRIEV, J. HAMILTON, M. ITKIS, K. MOODY, Y. OGANESSIAN, J. ROBERTO, K. RYKACZEWSKI, D. SHAUGHNESSY, M. STOYER: *Discovery of Elements 113 – 118*. Proceedings of the International Symposium on Exotic Nuclei EXON-2016 (pp. 210–218), Kazan, Russia, 2017, http://doi.org/10.1142/9789813226548_0032.

[19] J.-L. BASDEVANT, J. RICH, M. SPIRO: *Fundamentals in Nuclear Physics: From Nuclear Structure to Cosmology*. Springer Science+Business Media, Inc., ISBN 978-0-38701-672-6, 2005.

[20] P. MÖLLER: *The Limits of the Nuclear Chart Set by Fission and Alpha Decay*. European Physics Journal Web of Conferences, Volume 131, 03002 (2016), http://doi.org/10.1051/epjconf/201613103002.

[21] Y. OGANESSIAN: *Nuclei in the "Island of Stability" of Superheavy Elements*. Journal of Physics: Conference Series, Volume 337 (2012), 012005, http://doi.org/10.1088/1742-6596/337/1/012005.

[22] S. HOFMANN, G. MÜNZENBERG: *The Discovery of the Heaviest Elements*. Reviews of Modern Physics, Volume 72, Number 3, 733–767 (2000), http://doi.org/10.1103/revmodphys.72.733.

[23] A. SOBICZEWSKI, K. POMORSKI: *Description of Structure and Properties of Superheavy Nuclei*. Progress in Particle and Nuclear Physics, Volume 58, pp. 292–349, 2007, http://doi.org/10.1016/j.ppnp.2006.05.001.

[24] CH. SCHMELZER, D. BÖHNE: *GSI, a new Heavy-Ion Research Facility*. Proceedings of LINAC1970 (pp. 981–992), Batavia, Illinois, USA, http://accelconf.web.cern.ch/l70/papers/i-4.pdf.

[25] L. GROENING, S. MICKAT, A. ADONIN, W. BARTH, X. DU, CH.E. DÜLLMANN, H. HÄHNEL, R. HOLLINGER, E. JÄGER, M.S. KAISER, U. RATZINGER, A. RUBIN, P. SCHARRER, B. SCHLITT, G. SCHREIBER, A. SEIBEL, R. TIEDE, H. VORMANN, C. XIAO, C. ZHANG : *Upgrade of the UNILAC for FAIR*. Proceedings of HIAT2015 (pp. 139–143, TUA1I02), Yokohama, Japan, 2015, http://accelconf.web.cern.ch/accelconf/hiat2015/papers/tua1i02.pdf.

[26] L. DAHL, P. SPAEDTKE: *The Low Energy Beam Transport of the New GSI High Current Injector*. arXiv:physics/0008086, 2000, http://arxiv.org/abs/physics/0008086.

[27] U. RATZINGER, K. KASPAR, E. MALWITZ, S. MINAEV, R. TIEDE: *The GSI 36 MHz High-Current IH-Type RFQ and HIIF-Relevant Extensions*. Nuclear Instruments and Methods in Physics Research, A 415 (1998) 281–286, http://doi.org/10.1016/s0168-9002(98)00395-7.

b

[28] U. RATZINGER, R. TIEDE: *A New Matcher Type Between RFQ and IH-DTL for the GSI High Current Heavy Ion Prestripper Linac.* Proceedings of LINAC1996 (pp. 128–130, MOP31), Geneva, Switzerland, 1996, `http://accelconf.web.cern.ch/l96/papers/mop31.pdf`.

[29] R. TIEDE, G. CLEMENTE, H. PODLECH, U. RATZINGER, C. ZHANG: *KONUS Beam Dynamics Designs Using H-Mode Cavities.* Proceedings of HB2008 (pp. 223–230, WGB11), Nashville, Tennessee, USA, 2008, `http://accelconf.web.cern.ch/hb2008/papers/wgb11.pdf`.

[30] P. SCHARRER, W. BARTH, M. BEVCIC, CH. E. DÜLLMANN, L. GROENING, K.-P. HORN, E. JÄGER, J. KHUYAGBAATAR, J. KRIER, A. YAKUSHEV: *An Upgrade for the 1.4 MeV/u Gas Stripper at the GSI UNILAC.* Proceedings of IPAC2016 (pp. 1394–1396, TUPMR058), Busan, Korea, 2016, `http://accelconf.web.cern.ch/ipac2016/papers/tupmr058.pdf`.

[31] J. GLATZ, L. GROENING: *Beam Acceleration in the Single-Gap Resonator Section of the UNILAC Using Alternating Phase Focusing.* Proceedings of EPAC2002 (pp. 897–899, WEPLE119), Paris, France, 2002, `http://accelconf.web.cern.ch/e02/papers/weple119.pdf`.

[32] A. SEMCHENKOV, A. BELOV, T. BELYAKOVA, W. BRÜCHLE, E. JÄGER, M. KAPARKOVA, F. KLOS, V. KUKHTIN, E. LAMZIN, C. MÜHLE, M. SCHÄDEL, E. SCHIMPF, S. SYTCHEVSKY, A. TÜRLER, A. YAKUSHEV: *The TransActinide Separator and Chemistry Apparatus (TASCA) at GSI – Optimization of Ion-Optical Structures and Magnet Designs.* Nuclear Instruments and Methods in Physics Research, B 266 (2008) 4153–4161, `http://doi.org/10.1016/j.nimb.2008.05.132`.

[33] D. SCHARDT: *Five Years Tumor Therapy with Heavy Ions at GSI Darmstadt.* Recent Advances in Multidisciplinary Physics – Proceedings of the First International Meeting on Applied Physics APHYS-2003 (pp. 253–257), Badajoz, Spain, 2005, `http://doi.org/10.1016/b978-008044648-6.50041-0`.

[34] O. BOINE-FRANKENHEIM: *The FAIR Accelerators: Highlights and Challenges.* Proceedings of IPAC2010 (pp. 2430–2434, WEYRA01), Kyoto, Japan, 2010, `http://accelconf.web.cern.ch/ipac10/papers/weyra01.pdf`.

[35] D. ONDREKA, C. DIMOPOULOU, H.C. HÜTHER, H. LIEBERMANN, J. STADLMANN, R.J. STEINHAGEN: *Recommissioning of SIS18 After FAIR Upgrades.* Proceedings of IPAC2019 (pp. 932–935, MOPTS035), Melbourne, Australia, 2019, `http://doi.org/10.18429/jacow-ipac2019-mopts035`.

[36] H. VORMANN, W. BARTH, L. DAHL, A. KOLOMIETS, S. MINAEV, U. RATZINGER, R. TIEDE, W. VINZENZ, S. YARAMYSHEV: *Advanced UNILAC Upgrade for FAIR.* Proceedings of LINAC2010 (pp. 142–144, MOP040), Tsukuba, Japan, 2010, `http://accelconf.web.cern.ch/linac2010/papers/mop040.pdf`.

[37] C. ZHANG, M. BASCHKE, L. GROENING, O. KESTER, S. MICKAT, H. PODLECH, U. RATZINGER, R. TIEDE, H. VORMANN: *HSI RFQ Upgrade for the UNILAC Injection to FAIR.* Proceedings of IPAC2016 (pp. 877–879, MOPOY016), Busan, Korea, 2016, `http://accelconf.web.cern.ch/accelconf/ipac2016/papers/mopoy016.pdf`.

[38] R. HOLLINGER, A. ADONIN, J. PFISTER: *High Current Ion Sources for the FAIR Accelerator Facility.* Proceedings of RUPAC2012 (pp. 436–438, TUPPB054), Saint-Petersburg, Russia, 2012, `http://accelconf.web.cern.ch/rupac2012/papers/tuppb054.pdf`.

[39] C. KLEFFNER, A.M. ALMOMANI, S. APPEL, R. BEREZOV, F. FILS, P. FORCK, H. HÄHNEL, M. KAISER, K. KNIE, C. MUEHLE, S. PUETZ, U. RATZINGER, A. SCHNASE, G. SCHREIBER, M. SCHUETT, A. SEIBEL, T. SIEBER, V. SRINIVASAN, M. SYHA, J. TRUELLER, W. VINZENZ, C. WILL: *Status of the FAIR Proton Linac.* Proceedings of LINAC2018 (pp. 787–789, THPO046), Beijing, China, 2018, `http://doi.org/10.18429/jacow-linac2018-thpo046`.

[40] J. Klabunde: *The High Charge State Injector for GSI*. Proceedings of LINAC1992 (pp. 570–574, TH1-02), Ottawa, Ontario, Canada, 1992, `http://accelconf.web.cern.ch/accelconf/l92/papers/th1-02.pdf`.

[41] P. Gerhard, L. Groening, W. Hartmann, S. Mickat, K. Tinschert, H. Vormann, K.-O. Voss: *Status and Perspectives of the CW Upgrade of the UNILAC HLI at GSI*. Proceedings of HIAT2015 (pp. 183–185, WEA1C03), Yokohama, Japan, 2015, `http://accelconf.web.cern.ch/accelconf/hiat2015/papers/wea1c03.pdf`.

[42] M. Schwarz, W. Barth, M. Basten, M. Busch, F. Dziuba, V. Gettmann, M. Heilmann, S. Mickat, M. Miski-Oglu, H. Podlech, U. Ratzinger, R. Tiede, S. Yaramyshev: *Further Steps Towards the Superconducting CW-Linac for Heavy Ions at GSI*. Proceedings of IPAC2016 (pp. 896–898, MOPOY023), Busan, Korea, 2016, `http://accelconf.web.cern.ch/accelconf/ipac2016/papers/mopoy023.pdf`.

[43] M. Schwarz, S. Yaramyshev, K. Aulenbacher, W. Barth, M. Basten, M. Busch, C. Burandt, T. Conrad, F. Dziuba, V. Gettmann, G. Gusarova, M. Heilmann, E. Khabibullina, T. Kulevoy, T. Kuerzeder, S. Lauber, J. List, M. Miski-Oglu, H. Podlech, S. Polozov, A. Rubin, K. Taletskiy, A. Ziiatdinova: *Reference Beam Dynamics Layout for the SC CW Heavy Ion HELIAC at GSI*. Nuclear Instruments and Methods in Physics Research, A 951 (2020) 163044, `http://doi.org/10.1016/j.nima.2019.163044`.

[44] W. Barth, K. Aulenbacher, M. Basten, M. Busch, F. Dziuba, V. Gettmann, M. Heilmann, T. Kürzeder, M. Miski-Oglu, H. Podlech, A. Rubin, A. Schnase, M. Schwarz, S. Yaramyshev: *First Heavy Ion Beam Tests with a Superconducting Multigap CH Cavity*. Physical Review Accelerators and Beams, 21, 020102 (2018), `http://doi.org/10.1103/physrevaccelbeams.21.020102`.

[45] M. Basten: *Entwicklung und Inbetriebnahme Zweier Supraleitender 2017 MHz CH-Strukturen für das HELIAC-Projekt*. PhD thesis, Goethe University Frankfurt, 2019, `http://nbn-resolving.org/urn:nbn:de:hebis:30:3-517672`.

[46] T. Conrad, K. Aulenbacher, W. Barth, M. Basten, M. Busch, F. Dziuba, V. Gettmann, M. Heilmann, T. Kürzeder, S. Lauber, J. List, M. Miski-Oglu, H. Podlech, A. Rubin, A. Schnase, M. Schwarz, S. Yaramyshev: *Cavity Designs for CH3 to CH11 of the Superconducting Heavy Ion Accelerator HELIAC*. Proceedings of SRF2019 (pp. 396–398, TUP005), Dresden, Germany, 2019, `http://doi.org/10.18429/jacow-srf2019-tup005`.

[47] J.D. Cockcroft, E.T.S. Walton: *Experiments with High Velocity Positive Ions*. Proceedings the Royal Society A, Volume 129, Issue 811 (pp. 477–489), 1930, `http://doi.org/10.1098/rspa.1930.0169`.

[48] J.D. Cockcroft, E.T.S. Walton: *Experiments with High Velocity Positive Ions – (I) Further Developments in the Method of Obtaining High Velocity Positive Ions*. Proceedings the Royal Society A, Volume 136, Issue 830 (pp. 619–630), 1932, `http://doi.org/10.1098/rspa.1932.0107`.

[49] J.D. Cockcroft, E.T.S. Walton: *Experiments with High Velocity Positive Ions – (II) The Disintegration of Elements by High Velocity Protons*. Proceedings the Royal Society A, Volume 137, Issue 831 (pp. 229–242), 1932, `http://doi.org/10.1098/rspa.1932.0133`.

[50] R.J. Van de Graaff, K.T. Compton, L.C. Van Atta: *The Electrostatic Production of High Voltage for Nuclear Investigations*. Physical Review 43, Volume 43, Number 3 (pp. 149–157), 1933, `http://doi.org/10.1103/physrev.43.149`.

[51] R. Wideröe: *Über ein neues Prinzip zur Herstellung hoher Spannungen*. Archiv für Elektrotechnik, Band 21 (pp. 387–406), 1928, `http://doi.org/10.1007/bf01656341`.

d

[52] F. Hinterberger: *Small Accelerators – Electrostatic Accelerators.* Proceedings of the CERN Accelerator School, Zeegse, Netherlands, 24 May – 2 June 2005, (CERN-2006-012, pp. 95–112, 2006), `http://doi.org/10.5170/cern-2006-012.95`.

[53] A. Nassiri, B. Chase, P. Craievich, A. Fabris, H. Frischolz, J. Jacob, E. Jensen, M. Jensen, R. Kustom, R. Pasquinelli: *History and Technology Developments of Radio Frequency (RF) Systems for Particle Accelerators.* IEEE Transactions on Nuclear Science, Volume 63, Number 2 (pp. 707–749), 2016, `http://doi.org/10.1109/tns.2015.2485164`.

[54] M. Vretenar: *High Power Hadron Machines – The Radio-Frequency Quadrupole.* Proceedings of the CERN Accelerator School, Bilbao, Spain, 24 May – 2 June 2011, (CERN-2013-001, pp. 207–223, 2013), `http://doi.org/10.5170/cern-2013-001.207`.

[55] M. Ferrario, M. Migliorati, L. Palumbo: *Advanced Accelerator Physics – Space Charge Effects.* Proceedings of the CERN Accelerator School, Trondheim, Norway, 19 – 29 August 2013, (CERN-2014-009, pp. 331–356, 2014), `http://doi.org/10.5170/cern-2014-009.331`.

[56] I.M. Kapchinsky, V.A. Teplyakov: *A Linear Ion Accelerator with Spatially Uniform Hard Focusing.* SLAC-TRANS-0099 (August 1969), translated from the Preprint ITEP-673 (March 1969), published in: Pribory i. Tekhnika Eksperimenta, 119, Number 2, pp. 19–22, 1970, `http://www.slac.stanford.edu/pubs/slactrans/trans01/slac-trans-0099.pdf`.

[57] A.M. Lombardi: *Small Accelerators – The Radio Frequency Quadrupole (RFQ).* Proceedings of the CERN Accelerator School, Zeegse, Netherlands, 24 May – 2 June 2005, (CERN-2006-012, pp. 201–207, 2006), `http://doi.org/10.5170/cern-2006-012.201`.

[58] NTG Neue Technologien GmbH & Co. KG, `http://www.ntg.de/en`.

[59] V.A. Teplyakov: *RFQ Focusing in Linacs.* Future Perspectives in High Energy Physics (Proceedings of the 1990 ICFA Seminars, Protvino, USSR, 9–14 October 1990), ISBN 978-9-81453-953-1.

[60] J.E. Stovall, K.R. Crandall, R.W. Hamm: *Performance Characteristics of a 425 MHz RFQ Linac.* 6th Conference on the Application of Accelerators in Research & Industry, Denton, Texas, USA, 1980, Los Alamos Report LA-UR-80-3140, `http://permalink.lanl.gov/object/tr?what=info:lanl-repo/lareport/LA-UR-80-3140`.

[61] S. Mathod, P. Bourquin, A. Briswalter, Th. Callamand, J. Carosone, N. Favre, J.M. Geisser, A. Lombardi, V. Maire, M. Malabaila, D. Pugnat, Ph. Richerot, B. Riffaud, C. Rossi, M. Timmins, A. Vacca, G. Vandoni, M. Vretenar: *Mechanical Design, Brazing and Assembly Procedures of the Linac4 RFQ.* Proceedings of IPAC2010 (pp. 807–809, MOPD054), Kyoto, Japan, 2010, `http://accelconf.web.cern.ch/accelconf/ipac10/papers/mopd054.pdf`.

[62] M. Schütt, M. Syha, U. Ratzinger: *RF Measurements and Tuning of the 325 MHz Ladder-RFQ.* Proceedings of IPAC2019 (pp. 925–927, MOPTS033), Melbourne, Australia, 2019, `http://doi.org/10.18429/jacow-ipac2019-mopts033`.

[63] M. Schütt: *Design and Development of a 325 MHz Ladder RFQ.* PhD thesis, Goethe University Frankfurt, 2017, `http://nbn-resolving.org/urn:nbn:de:hebis:30:3-457482`.

[64] A. Kipper, H. Deitinghoff, O. Engels, A. Firjahn-Andersch, J. Madlung, A. Schempp, H. Vormann: *The High Current Spiral-RFQ Prototype.* Proceedings of LINAC1992 (pp. 416–418, TU4-42), Ottawa, Ontario, Canada, 1992, `http://accelconf.web.cern.ch/accelconf/l92/papers/tu4-42.pdf`.

[65] R.L. Poirier, R. Baartman, P. Bricault, K. Fong, S. Koscielniak, R. Laxdal, A.K. Mitra, L. Root, G. Stanford, D. Pearce: *CW Performance of the TRIUMF 8 Meter Long RFQ for Exotic Ions.* arXiv:physics/0008210, 2000, `http://arxiv.org/abs/physics/0008210`.

[66] G. Liu, J.E. Chen, H. Du, S.L. Gao, Y. He, P.Y. Jiang, Z.S. Li, X.N. Li, Y.R. Lu, Z. Wang, J.W. Xia, X.Q. Yan, Y.Q. Yang, X.J. Yin, Y.J. Yuan, X.H. Zhang, H.W. Zhao, K. Zhu: *RF and Field Measurements of the SSC-Linac RFQ.* Science China – Physics, Mechanics & Astronomy, Volume 57, Number 6, 2014, `http://doi.org/10.1007/s11433-014-5418-0`.

[67] A. Lombardi, V. Andreev, L. Badan, G. Bassato, A. Battistella, L. Bertazzo, G. Bezzon, G. Bisoffi, E. Bissiato, N. Dainese, D. Daney, M. De Lazzari, S. Canella, M. Cavenago, F. Cervellera, F. Chiurlotto, M. Communian, D. Conventi, H. Dewa, A. Facco, P. Favaron, S. Gambalonga, G. Galeazzi, M. Lollo, I. Kulik, M.F. Moisio, S. Marigo, V. Palmieri, A. Pisent, M. Poggi, F. Poletto, A.M. Porcellato, M. Rigato, F. Scarpa, T. Shirai, S. Stark, F. Stivanello, V. Zviagintsev: *PIAVE the Legnaro New Positive Ion Injector Based on Superconducting RFQs.* Proceedings of LINAC2000 (pp. 356–360, TU205), Monterey, California, USA, 2000, `http://accelconf.web.cern.ch/l00/papers/tu205.pdf`.

[68] D.D. Armstrong, W.D. Cornelius, R.A. Jameson, F.O. Purser, T.P. Wangler: *RFQ Development at Los Alamos.* International Symposium on Heavy-Ion Accelerators and Their Applications to Inertial Fusion, Tokyo, Japan, 1984, Los Alamos Report LA-UR-84-498, `http://permalink.lanl.gov/object/tr?what=info:lanl-repo/lareport/LA-UR-84-0498`.

[69] N. Bultman, G. Morgan, P. Pozdeyev, J. Stovall, Y. Yamazaki, L.M. Young, Q. Zhao: *Design of the FRIB RFQ.* Proceedings of IPAC2013 (pp. 2866–2868, WEPFI075), Shanghai, China, 2013, `http://accelconf.web.cern.ch/accelconf/ipac2013/papers/wepfi075.pdf`.

[70] D. Leitner, C. Benatti, J. Häuser, O. Kester, S.W. Krause, F. Marti, D. Morris, S. Nash, J. Ottarson, G. Perdikakis, M. Portillo, R.J. Rencsok, T. Ropponen, A. Schempp, J. Schmidt, E. Tanke, L. Tobos, N. Usher, D. Wang, X. Wu, Q. Zhao, H. Zimmermann: *Commissioning Results of the REA RFQ at MSU.* Proceedings of PAC2011 (pp. 1912–1914, WEP226), New York, New York, USA, 2011, `http://accelconf.web.cern.ch/accelconf/pac2011/papers/wep226.pdf`.

[71] W. Ma, Y. He, C. Li, L. Lu, L. Shi, L. Sun, X. Xu, Z. Zhang, H. Zhao: *Design and Simulation of a High Intensity Heavy Ion RFQ Accelerator Injector.* Proceedings of LINAC2016 (pp. 999–1001, THPLR064), East Lansing, Michigan, USA, 2016, `http://accelconf.web.cern.ch/accelconf/linac2016/papers/thplr064.pdf`.

[72] R. Ferdinand, G. Congretel, A. Curtoni, O. Delferriere, A. France, M. Di Giacomo, D. Leboeuf, J. Thinel, JC. Toussaint: *SPIRAL 2 RFQ Design.* Proceedings of EPAC2004 (pp. 2026–2028, WEPLT076), Lucerne, Switzerland, 2004, `http://accelconf.web.cern.ch/accelconf/e04/papers/weplt076.pdf`.

[73] J. Maus, A. Bechtold, A. Schempp: *Measurements at the MAFF IH-RFQ Test Stand at the IAP Frankfurt.* Proceedings of LINAC2010 (pp. 491–493, TUP040), Tsukuba, Japan, 2010, `http://accelconf.web.cern.ch/accelconf/linac2010/papers/tup040.pdf`.

[74] T. Sieber, D. Habs, O. Kester, A. Kolbe, A. Schempp: *Design and Status of the RFQ for REX-ISOLDE.* Proceedings of LINAC1998 (pp. 777–779, TH4006), Chicago, Illinois, USA, 1998, `http://accelconf.web.cern.ch/accelconf/l98/papers/th4006.pdf`.

[75] G. Bezzon, P. Bourquin, A. Lombardi, A.M. Lombardi, G. Parisi, A. Pisent, M. Vretenar, M. Weiss: *Construction and Commissioning of the RFQ for the CERN Lead-Ion Facility.* Proceedings of LINAC1994 (pp. 722–724, TH-12), Tsukuba, Japan, 1994, `http://accelconf.web.cern.ch/AccelConf/l94/papers/th-12.pdf`.

f

[76] M. Vossberg, J. Alessi, B. Hofmann, D. Raparia, J. Schmidt, A. Schempp, L. Snydstrup, C. Zhang: *The New EBIS RFQ for BNL*. Proceedings of LINAC2008 (pp. 139–141, MOP033), Victoria, British Columbia, Canada, 2008, `http://accelconf.web.cern.ch/accelconf/linac08/papers/mop033.pdf`.

[77] B. Hofmann, O. Kester, A. Schempp: *A RFQ-Decelerator for HITRAP*. Proceedings of PAC07 (pp. 1437–1438, TUPAN020), Albuquerque, New Mexico, USA, 2007, `http://accelconf.web.cern.ch/accelconf/p07/papers/tupan020.pdf`.

[78] P. Gerhard, W. Barth, L. Dahl, A. Orzhekhovskaya, A. Schempp, K. Tinschert, W. Vinzenz, H. Vormann, M. Vossberg, S. Yaramyshev: *Commissioning of a New CW Radio Frequency Quadrupole at GSI*. Proceedings of IPAC2010 (pp. 741–743, MOPD028), Kyoto, Japan, 2010, `http://accelconf.web.cern.ch/accelconf/ipac10/papers/mopd028.pdf`.

[79] H. Podlech, M. Grieser, R.v. Hahn, R. Repnow, D. Schwalm: *Electrodynamic Calculations of the 4-Rod-RFQ Resonator for the Heidelberg High Current Injector*. Proceedings of PAC2001 (pp. 3069–3071, RPAH096), Chicago, Illinois, USA, 2001, `http://accelconf.web.cern.ch/p01/papers/rpah096.pdf`.

[80] J. Friedrich, N. Angert, U. Bessler, H. Deitinghoff, J. Klabunde, H. Klein, A. Schempp, R. Veith: *Properties of the GSI HLI-RFQ Structure*. Proceedings of PAC1991 (pp. 3044–3046), San Francisco, California, USA, 1991, `http://accelconf.web.cern.ch/accelconf/p91/pdf/pac1991_3044.pdf`.

[81] A. Schempp, U. Bessler, M. Björkhage, H. Deitinghoff, J. Friedrich, C.J. Herrlander, A. Källberg, A. Kipper, H. Klein, K. Langbein, J. Madlung, G. Riehl, A. Soltan, K. Volk: *The CRYRING RFQ for Heavy Ion Acceleration*. Proceedings of EPAC1990 (pp. 1231–1233), Nice, France, 1990, `http://accelconf.web.cern.ch/accelconf/e90/pdf/epac1990_1231.pdf`.

[82] A. Plastun, V. Andreev, A. Butenko, V. Koshelev, T. Kulevoy, V. Kuzmichev, D. Liakin, A. Sitnikov: *RF Design of the Nuclotron-NICA 145.2 MHz RFQ*. Proceedings of LINAC2016 (pp. 595–597, TUPLR060), East Lansing, Michigan, USA, 2016, `http://accelconf.web.cern.ch/accelconf/linac2016/papers/tuplr060.pdf`.

[83] Z. Zhang, Y. Guo, Y. He, M. Hoff, H. Jia, A. Lampert, C. Li, D. Li, Y. Liu, L. Lu, G. Pan, A. Shi, L. Shi, J. Staples, L. Sun, S. Virostek, W. Wang, X. Wang, J. Wu, Q. Wu, X. Xu, B. Zhang, C. Zhang, J. Zhang, H. Zhao, T. Zhu: *Development of the Injector II RFQ for China ADS Project*. Proceedings of IPAC2014 (pp. 3280–3282, THPME027), Dresden, Germany, 2014, `http://doi.org/10.18429/jacow-ipac2014-thpme027`.

[84] J.M. Steimel, C. Baffes, P. Berutti, J.-P. Carneiro, A. Edelen, J. Edelen, M. Hoff, T. Khabiboulline, A. Lambert, D. Li, T. Luo, L. Prost, V. Scarpine, V.L.S. Sista, J. Staples, A. Shemyakin, S. Virostek: *Beam Commissioning Status and Results of the FNAL PIP2IT Linear Accelerator RFQ*. Proceedings of LINAC2016 (pp. 1002–1004, THPLR065), East Lansing, Michigan, USA, 2016, `http://accelconf.web.cern.ch/accelconf/linac2016/papers/thplr065.pdf`.

[85] A.M. Almomani, M. Heilmann, U. Ratzinger: *RF Tuning Tests on the Coupled FRANZ RFQ-IH-DTL*. Proceedings of IPAC2017 (pp. 2224–2226, TUPVA063), Copenhagen, Denmark, 2017, `http://accelconf.web.cern.ch/accelconf/ipac2017/papers/tupva063.pdf`.

[86] E. FAGOTTI, L. ANTONIAZZI, L. BELLAN, B. BOLZON, D. BORTOLATO, P. CARA, N. CHAUVIN, M. COMUNIAN, H. DZITKO, T. EBISAWA, A. FACCO, D. GEX, M. GIACCHINI, R. GOBIN, F. GRESPAN, R. HEIDINGER, A. JOKINEN, A. KASUGAI, K. KONDO, A. MARQUETA, P. MEREU, M. MONTIS, I. MOYA, A. PALMIERI, G. PHILLIPS, A. PISENT, G. PRUNERI, K. SAKAMOTO, F. SCANTAMBURLO, T. SHINYA, M. SUGIMOTO, M. WEBER: *Beam Commissioning of the IFMIF EVEDA Very High Power RFQ.* Proceedings of IPAC2018 (pp. 2902–2907, THXGBF2), Vancouver, British Columbia, Canada, 2018, `http://accelconf.web.cern.ch/ipac2018/papers/thxgbf2.pdf`.

[87] P. FISCHER, A. SCHEMPP: *Tuning a CW 4-Rod RFQ.* Proceedings of LINAC2006 (pp. 728–730, THP064), Knoxville, Tennessee, 2006, `http://accelconf.web.cern.ch/accelconf/l06/papers/thp064.pdf`.

[88] H. PODLECH, A. BECHTOLD, K. KÜMPEL, C. LOREY, N. PETRY, A. SCHEMPP, P. SCHNEIDER, C. ZHANG: *The MYRRHA-RFQ – Status and First Measurements.* Proceedings of IPAC2017 (pp. 2243–2245, TUPVA071), Copenhagen, Denmark, 2017, `http://accelconf.web.cern.ch/accelconf/ipac2017/papers/tupva071.pdf`.

[89] R.A. GOUGH: *Design and Operation of the LBL Heavy Ion RFQ Linac.* Proceedings of LINAC1984 (pp. 68–70, MOB0008), Seeheim, Germany, 1984, `http://accelconf.web.cern.ch/accelconf/l84/papers/mob0008.pdf`.

[90] J.S. SCHMIDT, B. KOUBEK, A. SCHEMPP: *Tuning of the New 4-Rod RFQ for FNAL.* Proceedings of IPAC2011 (pp. 2580–2582, WEPS041), San Sebastián, Spain, 2011, `http://accelconf.web.cern.ch/accelconf/ipac2011/papers/weps041.pdf`.

[91] A. SCHEMPP, H. KLEIN, K.H. PAPE, P. SCHASTOK, S.H. WANG: *RFQ-Injector for HERA.* Proceedings of PAC1985 (pp. 3252–3255), Vancouver, British Columbia, Canada, 1985, `http://accelconf.web.cern.ch/p85/pdf/pac1985_3252.pdf`.

[92] A. SCHEMPP, M. FERCH, H. KLEIN: *A Light Ion Four Rod RFQ Injector.* Proceedings of PAC1987 (pp. 267–269), Washington, D.C., USA, 1987, `http://accelconf.web.cern.ch/p87/pdf/pac1987_0267.pdf`.

[93] E. BOLTEZAR, H. HASEROTH, C.E. HILL, F. JAMES, W. PIRKL, J. STOVALL, M. WEISS: *Status and First Beam Measurements on the CERN RFQ.* Proceedings of HEACC1983 (pp. 520–522), Batavia, Illinois, USA, 1983, `http://cds.cern.ch/record/146357/files/heacc83_546-548.pdf`.

[94] J.L. VALLET, M. VRETENAR, M. WEISS: *Field Adjustment, Tuning, and Beam Analysis of the High-Intensity CERN RFQ.* Proceedings of EPAC1990 (pp. 1234–1236), Nice, France, 1990, `http://accelconf.web.cern.ch/accelconf/e90/pdf/epac1990_1234.pdf`.

[95] A. BECHTOLD: *Eine integrierte RFQ-Driftröhrenkombination für ein Medizin-Synchrotron.* PhD thesis, Goethe University Frankfurt, 2003, `http://nbn-resolving.org/urn:nbn:de:hebis:30-0000003478`.

[96] H. LI, X. CAO, W. CHEN, S. FU, T. HUANG, S. LIU, Y.J. LV, F. OUYANG, Y.C. XIAO K. XUE: *The Status of CSNS Front End.* Proceedings of LINAC2018 (pp. 771–773, THPO039), Beijing, China, 2018, `http://doi.org/10.18429/jacow-linac2018-thpo039`.

[97] T. MORISHITA, K. HASEGAWA, K. HIRANO, T. HORI, Y. KONDO, F. NAITO, H. OGURI, T. SUGIMURA, A. TAKAGI, S. YAMAZAKI: *High-Power Test Results of the RFQ III in J-PARC Linac.* Proceedings of LINAC2014 (pp. 649–652, TUPP095), Geneva, Switzerland, 2014, `http://accelconf.web.cern.ch/accelconf/linac2014/papers/tupp095.pdf`.

[98] Q.Z. XING, J. BILLEN, J.C. CAI, L. DU, C.K. GONG, X.L. GUAN, J. LI, J. STOVALL, C.X. TANG, X.W. WANG, L. YOUNG, S.X. ZHENG: *Tuning and Cold Test of a Four-Vane RFQ with Ramped Inter-Vane Voltage for the Compact Pulsed Hadron Source.* Chinese Physics Letters, Volume 30, Number 5, 052901, 2013, `http://doi.org/10.1088/0256-307x/30/5/052901`.

h

[99] D. Schrage, D. Baca, D. Casillas, W. Clark, T. Davis, A. Gonzales, G. Gonzales, H. Haagenstad, S. Hidalgo, E. Kettering, F. Krawczyk, G. Leeches, F. Martinez, J. Mitchell, D. Montoya, A. Naranjo, B. Ormond, R. Reinert, A. Rendon, P. Roybal, O. Smith, J. Tafoya, L. Young: *CW RFQ Fabrication and Engineering.* Proceedings of LINAC1998 (pp. 679–683, WE1003), Chicago, Illinois, USA, 1998, `http://accelconf.web.cern.ch/accelconf/l98/papers/we1003.pdf`.

[100] C. Rossi, L. Arnaudon, G. Bellodi, J. Broere, O. Brunner, M. Desmons, A. France, A.M. Lombardi, J. Marques Balula, P. Martinez Yanez, J. Noirjean, C. Pasquino, O. Piquet, U. Raich, F. Roncarolo, M. Vretenar: *Commissioning of the Linac4 RFQ at the 3 MeV Test Stand.* Proceedings of IPAC2013 (pp. 3951–3953, THPWO082), Shanghai, China, 2013, `http://accelconf.web.cern.ch/accelconf/ipac2013/papers/thpwo082.pdf`.

[101] O. Piquet, A.C. Chauveau, D. Chirpaz-Cerbat, M. Desmons, A. Dubois, A.C. France, A. Gaget, P. Hamel, Y. Le Noa, L. Napoly, M. Oublaid, G. Perreu, B. Pottin: *ESS RFQ: Construction Status and Power Couplers Qualification.* Proceedings of IPAC2019 (pp. 855–857, MOPTS008), Melbourne, Australia, 2019, `http://doi.org/10.18429/jacow-ipac2019-mopts008`.

[102] S. Fu, J. Fang, S. Fang, X. Guan, Z. Guo, J. Li, Z. Luo, H. Ouyang, J. Qiao, T. Xu, W. Xu, Z. Zhang: *R&D Status of a 3.5MeV RFQ Accelerator for ADS Study in China.* Proceedings of LINAC2002 (pp. 154–156, MO450), Gyeongju, Korea, 2002, `http://accelconf.web.cern.ch/l02/papers/mo450.pdf`.

[103] P-Y. Beauvais: *Recent Evolutions in the Design of the French High Intensity Proton Injector (IPHI).* Proceedings of EPAC2004 (pp. 1273–1275, TUPLT053), Lucerne, Switzerland, 2004, `http://accelconf.web.cern.ch/accelconf/e04/papers/tuplt053.pdf`.

[104] E. Fagotti, M. Comunian, F. Grespan, S. J. Mathot, A. Palmieri, A. Pisent, C. Roncolato: *Fabrication and Testing of TRASCO RFQ.* Proceedings of LINAC2008 (pp. 151–153, MOP038), Victoria, British Columbia, Canada, 2008, `http://accelconf.web.cern.ch/accelconf/linac08/papers/mop038.pdf`.

[105] Y.W. Kang, A.V. Aleksandrov, W.E. Barnett, M.S. Champion, M. Crofford, B. Han, S.-W. Lee, C. Peters, J. Price, T. Roseberry, J.P. Schubert, A.P. Shishlo, M.P. Stockli, C. Stone, R.F. Welton, D. Williams, A.P. Zhukov: *Construction, Test, and Operation of a New RFQ at the Spallation Neutron Source SNS.* Proceedings of IPAC2018 (pp. 1113–1116, TUPAL046), Vancouver, British Columbia, Canada, 2018, `http://doi.org/10.18429/jacow-ipac2018-tupal046`.

[106] J.W. Staples, S.R. Abbott, R.J. Caylor, R.A. Gough, D.R. Howard, R.A. MacGill: *A Compact Proton RFQ Injector for the Bevalac.* Proceedings of LINAC1988 (pp. 48–50, MO3-05), Williamsburg, Virginia, USA, 1988, `http://accelconf.web.cern.ch/accelconf/l88/papers/mo3-05.pdf`.

[107] D. Schrage, L. Young, B. Campbell, J.H. Billen, J. Stovall, F. Martinez, W. Clark, G. Bolme, S. Gibbs, D. King, P. O'Shea, T. Butler, J. Rathke, R. Micich, J. Rose, R. Richter, G. Rosato: *BEAR RFQ-Beam Experiment Aboard a Rocket.* Nuclear Instruments and Methods in Physics Research Section B: Beam Interactions with Materials and Atoms, Volumes 40–41, Part 2, 1989, pp. 949–953, `http://doi.org/10.1016/0168-583X(89)90514-4`.

[108] H.W. Pommerenke, A. Bilton, A. Grudiev, A.M. Lombardi, S. Mathot, E. Montesinos, M. Timmins, M. Vretenar, U. van Rienen: *RF Design of a High-Frequency RFQ Linac for PIXE Analysis.* Proceedings of LINAC2018 (pp. 822–825, THPO058), Beijing, China, 2018, `http://doi.org/10.18429/jacow-linac2018-thpo058`.

[109] M. Vretenar, A. Dallocchio, V.A. Dimov, M. Garlasché, A. Grudiev, A.M. Lombardi, S. Mathot, E. Montesinos, M. Timmins: *A Compact High-Frequency RFQ for Medical Applications.* Proceedings of LINAC2014 (pp. 935–938, THPP040), Geneva, Switzerland, 2014, `http://accelconf.web.cern.ch/accelconf/linac2014/papers/thpp040.pdf`.

[110] B. Koubek: *Design Studies and Prototype Development of a 325 MHz 4-Rod RFQ.* PhD thesis, Goethe University Frankfurt, 2014, `http://nbn-resolving.org/urn:nbn:de:hebis:30:3-357114`.

[111] D. Koser: *Design of Normal-Conducting Rebuncher Cavities for the MYRRHA Injector Linac.* Master's thesis, Goethe University Frankfurt, 2015.

[112] T.P. Wangler: *RF Linear Accelerators.* 2nd Completely Revised and Enlarged Edition, Wiley-VCH Verlag GmbH & Co. KGaA, ISBN 978-3-52740-680-7, 2008.

[113] L.M. Young: *Segmented Resonantly Coupled Radio-Frequency Quadrupole (RFQ).* Proceedings of PAC1993 (pp. 3136–3138), Washington, D.C., USA, 1993, `http://accelconf.web.cern.ch/p93/pdf/pac1993_3136.pdf`.

[114] T. Sieber: *Entwicklung von 4-Rod- und IH- Radio-Frequenz-Quadrupol (RFQ)-Beschleunigern für radioaktive Ionenstrahlen bei REX-ISOLDE und MAFF.* PhD thesis, Ludwig Maximilian University of Munich, 2001, `http://nbn-resolving.de/urn/resolver.pl?urn:nbn:de:bvb:19-4557`.

[115] U. Ratzinger: *The New GSI Prestripper Linac for High Current Heavy Ion Beams.* Proceedings of LINAC1996 (pp. 288–292, TU202), Geneva, Switzerland, 1996, `http://accelconf.web.cern.ch/l96/papers/tu202.pdf`.

[116] J.S. Schmidt: *Tuning and Optimization of the Field Distribution for 4-Rod Radio Frequency Quadrupole Linacs.* PhD thesis, Goethe University Frankfurt, 2014, `http://nbn-resolving.org/urn:nbn:de:hebis:30:3-346791`.

[117] U. Bessler, J. Klabunde, A. Schempp, T. Sieber, P. Spätke: *Experiments with Heavy-Ion Beams and RF-Tests with the 27 MHz High-Current Spiral-RFQ-Prototype.* Proceedings of LINAC1996 (pp. 56–58, MOP04), Geneva, Switzerland, 1996, `http://accelconf.web.cern.ch/accelconf/l96/papers/mop04.pdf`.

[118] M. Vretenar: *RF for Accelerators – Low-Beta Structures.* Proceedings of the CERN Accelerator School, Ebeltoft, Denmark, 8 – 17 June 2010, (CERN-2011-007, pp. 319–340, 2011), `http://doi.org/10.5170/cern-2011-007.319`.

[119] M. Schütt, M. Obermayer, U. Ratzinger, A. Schnase: *Development and Measurements of a 325 MHz Ladder-RFQ.* Proceedings of LINAC2016 (pp. 578–580, TUPLR053), East Lansing, Michigan, USA, 2016, `http://accelconf.web.cern.ch/linac2016/papers/tuplr053.pdf`.

[120] H. Podlech: *Entwicklung von normal- und supraleitenden CH-Strukturen zur effizienten Beschleunigung von Protonen und Ionen.* Habilitation thesis, Goethe University Frankfurt, 2008, `http://nbn-resolving.org/urn:nbn:de:hebis:30:3-364687`.

[121] J.D. Jackson: *Classical Electrodynamics.* Third Edition, John Wiley & Sons, Inc., ISBN 978-0-47130-932-1, 1998.

[122] F. Chill: *Untersuchungen zu den Einflussfaktoren auf die Strom- und Spannungsverteilung im 4-Rod RFQ.* Diploma thesis, Goethe University Frankfurt, 2011.

[123] CST Studio Suite, Dassault Systèmes (DS), `http://www.3ds.com/products-services/simulia/products/cst-studio-suite`.

[124] A. Firjahn-Andersch: *Untersuchungen an einem 2-Strahl-RFQ für ein Funneling-Experiment.* PhD thesis, Goethe University Frankfurt, 1998.

[125] W.D. Kilpatrick: *Criterion for Vacuum Sparking Designed to Include RF and DC.* The Review of Scientific Instruments, Volume 28, Number 10, pp. 824–826, (1957).

[126] C.Y. Tan, A. Schempp, J.S. Schmidt: *Simple Lumped Circuit Model Applied to Field Flatness Tuning of Four-Rod Radio Frequency Quadrupoles.* Physical Review Special Topics – Accelerators and Beams, 17, 012002 (2014), `http://dx.doi.org/10.1103/physrevstab.17.012002`.

[127] L.C. Maier, J.C. Slater: *Field Strength Measurements in Resonant Cavities.* Journal of Applied Physics, Volume 23, Number 1, 68–77 (1952), `http://doi.org/10.1063/1.1701980`.

[128] H. Klein: *RF Engineering for Particle Accelerators – Basic Concepts I.* Proceedings of the CERN Accelerator School, Exeter College, Oxford, UK, 3–10 April 1991, (CERN 92-03, Vol. 1, pp. 97–124, 1992), `http://cds.cern.ch/record/211448/files/cern-92-03-v1-v2.pdf`.

[129] K. Kümpel, A. Bechtold, C. Lenz, N.F. Petry, H. Podlech, C. Zhang: *Dipole Compensation of the 176 MHz MYRRHA RFQ.* Proceedings of IPAC2017 (pp. 2240–2242, TUPVA070), Copenhagen, Denmark, 2017, `http://accelconf.web.cern.ch/accelconf/ipac2017/papers/tupva070.pdf`.

[130] M. Weiss: *Second General Accelerator Physics Course – Radio-Frequency Quarupole.* Proceedings of the CERN Accelerator School, Aarhus, Denmark, 15 – 26 September 1986, (CERN-1987-010, pp. 196–230, 1987), `http://doi.org/10.5170/cern-1987-010.196`.

[131] J.H. Billen, R.C. Crandall, G.H. Neuschaefer, D.L. Schrage, T.P. Wangler, L.M. Young: *RFQ Design Codes.* Los Alamos Report LA-UR-96-1836, revised on December 7, 2005.

[132] K.R. Crandall, R.H. Stokes, T.P. Wangler: *RF Quadrupole Beam Dynamics Design Studies.* Proceedings of LINAC1979 (pp. 205–216), Montauk, New York, USA, 1979, `http://accelconf.web.cern.ch/l79/papers/s4-1.pdf`.

[133] C. Zhang, A. Schempp: *Beam Dynamics Studies on a 200 mA Proton Radio Frequency Quadrupole Accelerator.* Nuclear Instruments and Methods in Physics Research, A 586 (2008) 153–159, `http://doi.org/10.1016/j.nima.2007.12.001`.

[134] M. Vossberg: *Der neue RFQ für den Hochladungsinjektor der GSI.* PhD thesis, Goethe University Frankfurt, 2011, `http://nbn-resolving.org/urn:nbn:de:hebis:30-109069`.

[135] P. Gerhard, W. Barth, L. Dahl, W. Hartmann, G. Schreiber, W. Vinzenz, H. Vormann: *Experience with a 4-Rod CW Radio Frequency Quadrupole.* Proceedings of LINAC2012 (pp. 825–827, THPLB07), Tel-Aviv, Israel, 2012, `http://accelconf.web.cern.ch/accelconf/linac2012/papers/thplb07.pdf`.

[136] J. Friedrich, N. Angert, U. Bessler, H. Deitinghoff, J. Klabunde, H. Klein, A. Schempp, R. Veith: *Performance of the GSI HLI-RFQ.* Proceedings of LINAC1992 (pp. 609–611, TH4-03), Ottawa, Ontario, Canada, 1992, `http://accelconf.web.cern.ch/accelconf/l92/papers/th4-03.pdf`.

[137] W. Vinzenz: *Resonanzfrequenzanalyse HLI RFQ.* HLI20047HF, GSI Internal Report, 1997.

[138] P. Gerhard, L. Groening, K.-O. Voss: *In Situ Measurement of Mechanical Vibrations of a 4-Rod RFQ at GSI.* Proceedings of LINAC2014 (pp. 553–555, TUPP057), Geneva, Switzerland, 2014, `http://accelconf.web.cern.ch/accelconf/linac2014/papers/tupp057.pdf`.

[139] D. Koser, P. Gerhard, L. Groening, O. Kester, H. Podlech: *Structural Mechanical Analysis of 4-Rod RFQ Structures in View of a Newly Revised CW RFQ for the HLI at GSI.* Proceedings of IPAC2017 (pp. 4142–4144, THPIK021), Copenhagen, Denmark, 2017, `http://accelconf.web.cern.ch/accelconf/ipac2017/papers/thpik021.pdf`.

[140] ANSYS Workbench, ANSYS Inc., http://www.ansys.com.

[141] D. KOSER, P. GERHARD, H. PODLECH: *Mechanical Vibration Analysis of the 4-Rod RFQ at the High Charge State Injector at GSI.* Nuclear Instruments and Methods in Physics Research, A 917 (2019) 47–55, http://doi.org/10.1016/j.nima.2018.10.162.

[142] M. VOSSBERG, W. BARTH, L. DAHL, A. SCHEMPP, C. ZHANG: *The New GSI HLI-RFQ for CW-Operation.* Proceedings of LINAC2010 (pp. 494–496, TUP041), Tsukuba, Japan, 2010, http://accelconf.web.cern.ch/accelconf/linac2010/papers/tup041.pdf.

[143] J. RODNIZKI, Z. HORVITS: *RF and Heat Flow Simulations of the SARAF RFQ 1.5 MeV/Nucleon Proton/Deuteron Accelerator.* Proceedings of LINAC2010 (pp. 506–508, TUP045), Tsukuba, Japan, 2010, http://accelconf.web.cern.ch/accelconf/linac2010/papers/tup045.pdf.

[144] A. SCHEMPP: *Design of the HLI 4-Rod Radio Frequency Quadrupole Accelerator Electrodes for $T_i = 2.5\,keV/u$.* Conceptual Design Report, 2008.

[145] I. MARDOR, D. BERKOVITS, K. DUNKEL, I. GERTS, A. GRIN, S. HALFON, G. LEMPERT, A. NAGLER, M. PEKELER, A. PERRY, C. PIEL, J. RODNIZKI, P. VOM STEIN, L. WEISSMAN: *The SARAF CW 40 MeV Proton/Deuteron Accelerator.* Proceedings of SRF2009 (pp. 74–80, MOODAU04), Berlin, Germany, 2009, http://accelconf.web.cern.ch/accelconf/srf2009/papers/moodau04.pdf.

[146] Manual for *Polytec Single-Point Vibrometer Sensor Head OFV-525*, Polytec GmbH, http://www.polytec.com.

[147] S.H. CRANDALL: *The Role of Damping in Vibration Theory.* Journal of Sound and Vibration, (1970) 11 (1), pp. 3–18, 1970, http://doi.org/10.1016/S0022-460X(70)80105-5.

[148] M.J. CASIANO: *Extracting Damping Ratio from Dynamic Data and Numerical Solutions.* NASA/TM–2016–218227, Marshall Space Flight Center, Huntsville, Alabama, 2016, http://ntrs.nasa.gov/archive/nasa/casi.ntrs.nasa.gov/20170005173.pdf.

[149] P. VON BÖCKH, T. WETZEL: *Heat Transfer – Basics and Practice.* Springer-Verlag Berlin Heidelberg, ISBN 978-3-64219-182-4, 2012, http://doi.org/10.1007/978-3-642-19183-1.

[150] D. MÄDER: *Die CH-Sektion des 17 MeV Injektors für MYRRHA.* PhD thesis, Goethe University Frankfurt, 2014, http://nbn-resolving.org/urn:nbn:de:hebis:30:3-372055.

[151] COMSOL Multiphysics, COMSOL Inc., http://www.comsol.com.

[152] R. TIEDE, M. HEILMANN, D. MÄDER, O. MEUSEL, H. PODLECH, U. RATZINGER, A. SCHEMPP, M. SCHWARZ: *A Coupled RFQ-IH-DTL Cavity for FRANZ: A Challenge for RF Technology and Beam Dynamics.* Proceedings of HB2016 (pp. 404–408, WEAM1Y01), Malmö, Sweden, 2016, http://accelconf.web.cern.ch/accelconf/hb2016/papers/weam1y01.pdf.

[153] C. ZHANG, H. PODLECH: *New Reference Design of the European ADS RFQ Accelerator for MYRRHA.* Proceedings of IPAC2014 (pp. 3223–3225, THPME008), Dresden, Germany, 2014, http://doi.org/10.18429/jacow-ipac2014-thpme008.

[154] D. KOSER, P. GERHARD, L. GROENING, O. KESTER, H. PODLECH: *Prototype Design of a Newly Revised CW RFQ for the High Charge State Injector at GSI.* Proceedings of IPAC2016 (pp. 889–891, MOPOY020), Busan, Korea, 2016, http://accelconf.web.cern.ch/accelconf/ipac2016/papers/mopoy020.pdf.

[155] D. KOSER, P. GERHARD, L. GROENING, O. KESTER, H. PODLECH: *Advanced Design Optimizations of a Prototype for a Newly Revised 4-Rod CW RFQ for the HLI at GSI.* Proceedings of LINAC2016 (pp. 586–588, TUPLR057), East Lansing, Michigan, USA, 2016, http://accelconf.web.cern.ch/accelconf/linac2016/papers/tuplr057.pdf.

l

[156] D. Koser, P. Gerhard, O. Kester, K. Kümpel, H. Podlech: *Initial Measurements on a New 108 MHz 4-Rod CW RFQ Prototype for the HLI at GSI.* Proceedings of IPAC2018 (pp. 946–948, TUPAF089), Vancouver, British Columbia, Canada, 2018, `http://doi.org/10.18429/jacow-ipac2018-tupaf089`.

[157] C.M. Harris, A.G. Piersol: *Harris' Shock and Vibration Handbook.* Fifth Edition, McGraw-Hill, ISBN 978-0-07137-081-3, 2002.

[158] S.G. Kelly: *Mechanical Vibrations: Theory and Applications.* First Edition, Cengage Learning, ISBN 978-1-43906-212-8, 2011.

[159] S.S. Rao: *Vibration of Continuous Systems.* John Wiley & Sons, Inc., ISBN 978-0-47177-171-5, 2007.

[160] H. Podlech, D. Gorelov, W. Hartung, F. Marti, U. Ratzinger, X. Wu, R.C. York: *Electromagnetic Design of an 80.5 MHz RFQ for the RIA Driver Linac.* Proceedings of EPAC2002 (pp. 942–944, THPLE065), Paris, France, 2002, `http://accelconf.web.cern.ch/accelconf/e02/papers/thple065.pdf`.

[161] S. Zimmermann: *Automatisierung von HF-Leistungstests der MYRRHA CH-Driftröhrenkavitäten.* Master's thesis, Goethe University Frankfurt, 2020.

[162] J.S. Schmidt, B. Koubek, A. Schempp: *Field Optimized 4-Rod RFQ Model.* Proceedings of IPAC2014 (pp. 3238–3240, THPME013), Dresden, Germany, 2014, `http://doi.org/10.18429/jacow-ipac2014-thpme013`.

[163] M. Schütt, M. Syha, U. Ratzinger: *Compensation of Longitudinal Entrance and Exit Gap Field Effects in RFQ's of the 4-Rod Type.* Nuclear Instruments and Methods in Physics Research, A 928 (2019) 58–64, `http://doi.org/10.1016/j.nima.2019.02.071`.

[164] J.S. Schmidt, D.S. Bollinger, K.L. Duel, P.R. Karns, B. Koubek, S.S. Kurennoy, W.A. Pellico, V.E. Scarpine, A. Schempp, B.A. Schupbach, C.Y. Tan: *Investigations of the Output Energy Deviation and Other Parameters During Commissioning of the Four-Rod Radio Frequency Quadrupole at the Fermi National Accelerator Laboratory.* Physical Review Special Topics – Accelerators and Beams, 17, 030102 (2014), `http://dx.doi.org/10.1103/physrevstab.17.030102`.

[165] D. Koser, K. Kümpel, H. Podlech, C. Zhang: *A New Method to Compensate the Longitudinal Component of the End-Fields in 4-Rod RFQ Accelerators.* Nuclear Instruments and Methods in Physics Research, A 961 (2020) 163635, `http://doi.org/10.1016/j.nima.2020.163635`.

[166] J.S. Schmidt, B. Koubek, A. Schempp: *Simulations on the Boundary Fields of 4-Rod RFQ Electrodes.* Proceedings of IPAC2013 (pp. 3803–3805, THPWO020), Shanghai, China, 2013, `http://accelconf.web.cern.ch/accelconf/ipac2013/papers/thpwo020.pdf`.

[167] C. Zhang, H. Podlech: *Efficient Focusing, Bunching, and Acceleration of High Current Heavy Ion Beams at Low Energy.* Nuclear Instruments and Methods in Physics Research, A 879 (2018) 19–24, `http://doi.org/10.1016/j.nima.2017.09.059`.

[168] C. Zhang, H. Podlech: *Frequency Jump at Low Energies.* Proceedings of IPAC2018 (pp. 3176–3178, THPAF082), Vancouver, British Columbia, Canada, 2018, `http://doi.org/10.18429/jacow-ipac2018-thpaf082`.

Acknowledgements

n